Three-Dimensional Analysis of Multi-Phase Flow between Rotating Disks with Grooved Friction Surfaces

by

Pengchuan Wang

A dissertation submitted in partial fulfillment
of the requirements for the degree of
Doctor of Philosophy
(Mechanical Engineering)
in The University of Michigan
2018

Doctoral Committee:

Professor Nikolaos D. Katopodes, Co-Chair
Professor Anna G. Stefanopoulou, Co-Chair
Professor Kenneth P. Powell
Professor William W. Schultz

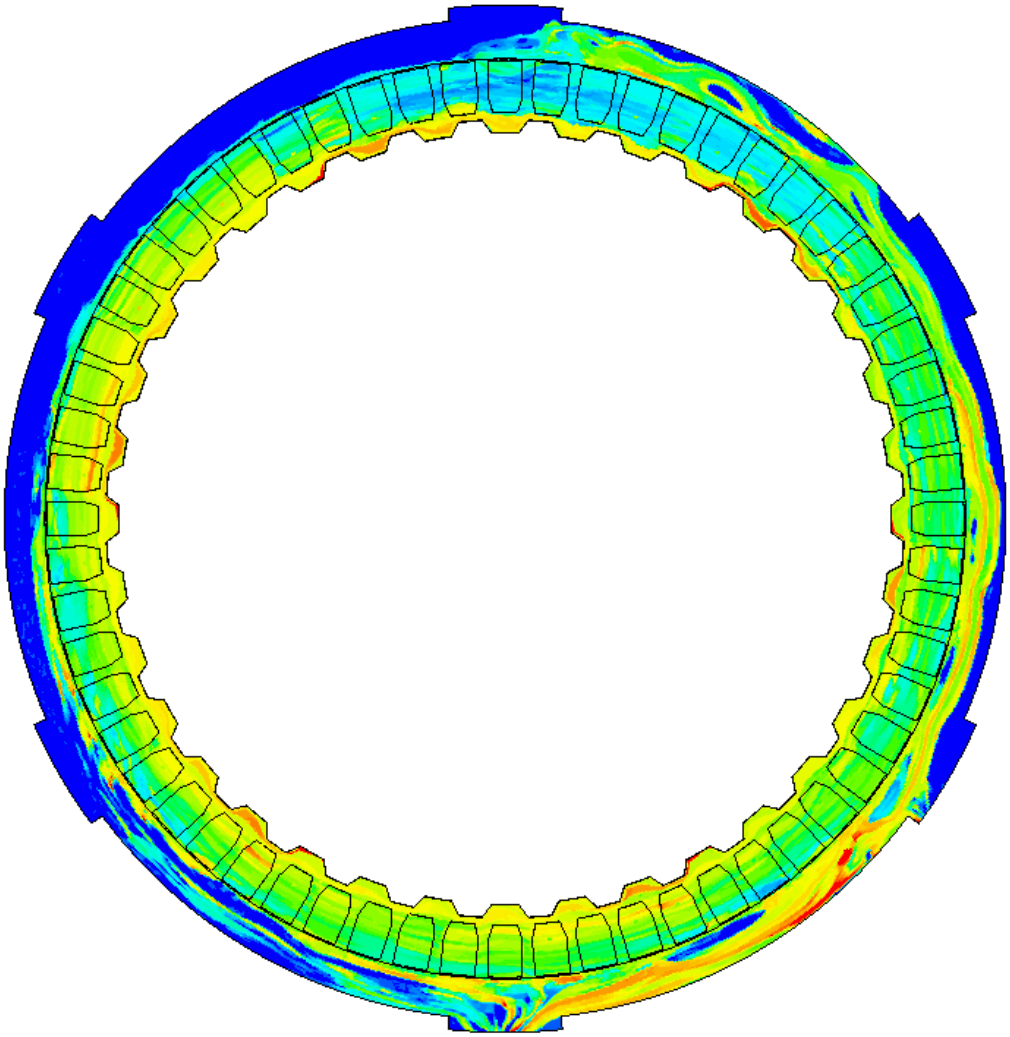
Volume Fraction of ATF
0
0.2
0.4
0.6
0.8
1

Pengchuan Wang

pechwang@umich.edu

ORCID iD: 0000-0002-3956-2698

To my mom and dad

ACKNOWLEDGEMENTS

My doctoral study has been a long and challenging journey. It would not have been possible without the support of many people.

First, I would like to express my sincere appreciation to my advisor, Prof. Nikolaos Katopodes, for his tremendous encouragement, endless support, and consistent trust in me during my doctoral study. He is always generous in speaking highly of me in front of people, showing his strong support. His inspiration and respect made the dissertation research a pleasant experience. The good advice, support and friendship has been invaluable for me at both academic and personal level. It is my great honor to be his student in my life, and I could not have imagined having a better advisor and mentor.

Besides that, I would like to thank the rest of my thesis committee: Prof. Anna Stefanopoulou, Prof. Ken Powell, and Prof. Bill Schultz, for their insightful comments, and excellent review of my thesis. I truly appreciate their time and effort to guide my work.

Next, I would like to thank Dr. Yuji Fujii for his constant guidance, and the foresight of such an interesting and challenging subject. He always has high expectations of me, which drives me to get over obstacles one after another. He inspires me, challenges me, sustains me, and makes my journey to the success.

Most importantly, I would like to thank my parents for providing me with such a valuable opportunity to study overseas. I would also thank them for their unconditional support, patience and understanding. Without them, I could not have

overcome the obstacles and difficulties during the past several years.

I would like to thank my sponsors, Ford Motor Company, Dynax Corporation and F.C.C. Co., Ltd., for their technical support, funding, and making available their experimental facilities.

I would always remember all those who have helped me in the past, and I will be always willing to give back.

TABLE OF CONTENTS

LIST OF FIGURES

Figure

LIST OF TABLES

Table

LIST OF ABBREVIATIONS

ATF automatic transmission fluid

CFD computational fluid dynamics

DOF degree of freedom

FP friction plate

MRF multiple reference frame

PDF probability density function

SIMPLE Semi-Implicit Method for Pressure-Linked Equations

SP separator plate

SRF single reference frame

VOF volume of fluid

ABSTRACT

A multi-physics model is developed for predicting the dynamic behavior of a wet clutch in an automatic transmission system. The prediction and control of clutch dynamics are of major significance in fuel efficiency. Therefore, the optimal operational characteristics are sought to reduce the viscous drag and improve the shift quality. The model simulates clutch operations under open and engagement conditions. Various CFD models are reported in the literature, but they are often limited to the analyses of SAE #2 test data, which do not reflect an actual clutch control strategy. The present work overcomes previous limitations by constructing comprehensive computational fluid dynamics (CFD) models, accounting for detailed design geometries.

The model consists of various modules depending on the status of wet clutches, which are linked by the dynamic behavior of multiple rotating disks. For open clutches, a multiphase CFD model is developed to simulate wet clutch behavior, accounting for detailed design geometry. The model employs the volume of fluid (VOF) method to capture the interface between the automatic transmission fluid (ATF) and air entrained in the gap between clutch plates. Model setup and simulation parameters, including initial conditions, boundary conditions, and relaxation factors are evaluated in terms of convergence rates. A statistical model is developed to account for the chaotic axial movement of plates in a clutch pack. The model can predict the difference in the drag torque with or without fixed clutch plates.

The engagement process is modeled using the open clutch solution as an initial

condition. A squeeze-film flow model is developed based on an iterative method to reflect the real control strategy. The iterative scheme allows use of the actuator piston force as an input to the computation of the ATF film change. Given the external force responsible for plate movement, the squeeze velocity is calculated by trial-and-error until the external force is balanced by internal fluid stresses. The results are validated using analytical solutions under various boundary conditions. The model captures the flow in micro-channels created by the grooves on the friction material surface. The model also explicitly accounts for the effects of the plate mass on the squeeze film process. The flow through the porous friction material is simulated using Darcy's law. The influence of surface roughness and mechanical contact are simulated based on the real contact area. The heat generated at the interface between friction and separator plates is computed through both conduction and convention processes. Finally, these models are combined with the baseline squeeze-film flow model to create an integrated clutch engagement model.

A series of experiments for calibration and validation of the model were performed at two testing facilities in Japan. Extensive visualization tests were performed to investigate the formation of bubbles in the interface, and validate the volume fraction computed by the model. Convergence of the open clutch model is demonstrated, capturing the peak drag location as a function of rotating speed, until the phase fraction drops to a small value. The simulation results from the statistical model compare satisfactorily with experimental data. An advanced engagement bench test is conducted using in-vehicle clutch slip and pressure profiles for specifically replicating the torque and inertia phases of shifting. It is shown that the CFD model together with the advanced clutch bench testing provide a valuable insight into in-vehicle clutch engagement behaviors.

CHAPTER I

Introduction

1.1 Motivation and Background

Modern automobiles aim at providing transportation at higher efficiency with reduced environmental impact. Every component in a vehicle is carefully examined for an opportunity to improve fuel economy. Among them, an automatic transmission system undergoes continuous design refinements. The main function of the transmission system is to transfer drive torque from the engine to the wheels based on the driver's demand and operating conditions. In a typical automatic transmission design, multiple planetary gear sets are connected in a complex manner to achieve a desired number of gear ratios. Wet clutches are commonly utilized to couple or de-couple gear elements to alter torque paths for automatic ratio-changing (*Winchell and Route* (1961)).

Figure 1.1 illustrates a transmission system which includes 5 clutch packs in a nested structure. There are two main operating modes for clutches: the open clutch and the engagement mode. When the clutch is open, the ATF is supplied from the oil pump, travels through the center shaft, and flows radially to lubricate all the internal components. The ATF enters each clutch pack from its inner hub, travels through the frictional interface, and is discharged from the drain holes of the clutch housing. Under any driving conditions, two to three clutch packs are typically open, shearing

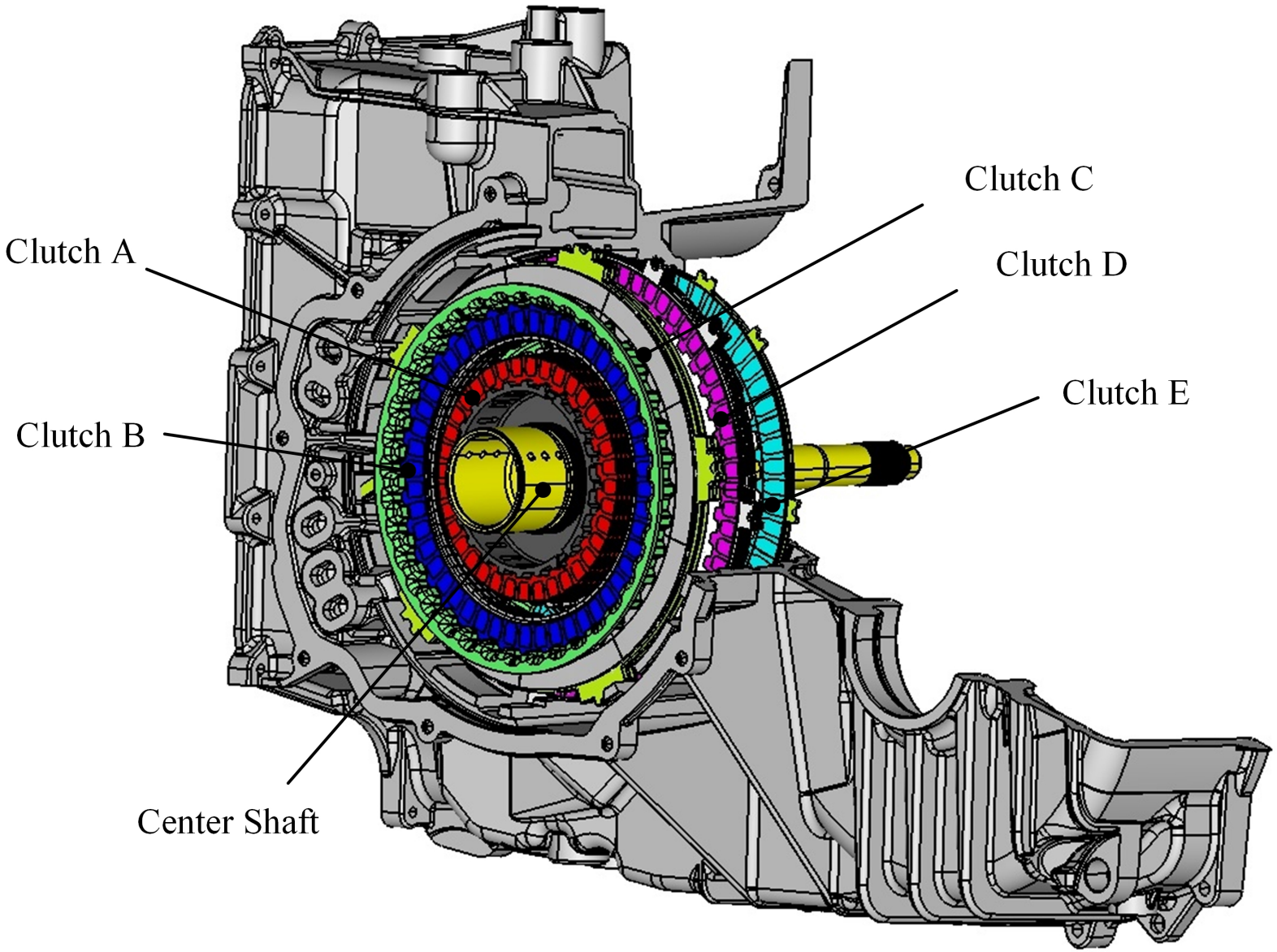

Figure 1.1: Illustration of clutch packs in an automatic transmission (*Wang et al.* (2017b))

the ATF for viscous drag, and thus affecting the overall drive-train efficiency. When a clutch is commanded for engagement, heat is generated by the frictional force between the sliding plates. A sufficient amount of the ATF must be channeled to the plate surfaces for cooling in order to avoid thermal damage and maintain stable frictional performance (*Froslie et al.* (1960)).

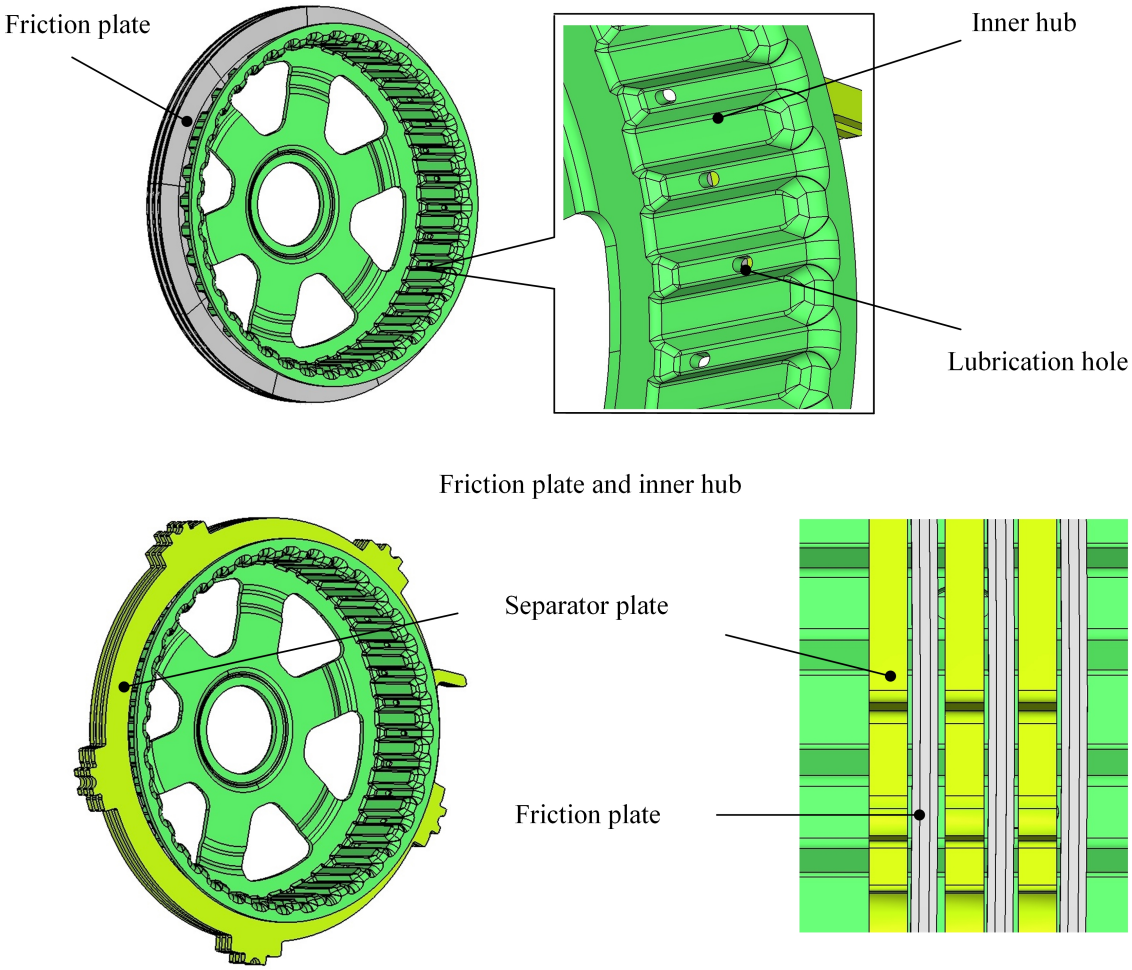

Figure 1.2: Detailed structure of Clutch C

Figure 1.2 shows the detailed structure of clutch C. Multiple friction and separator plates are alternatively placed around the inner hub. More specifically, friction plates are mounted to the inner hub through spline teeth, while separator plates are directly splined to the outer structure or the transmission case. A rotational motion of the

inner hub generates a centrifugal force that pushes the ATF into the clutch pack through lubrication holes on the hub. When the clutch is open, the friction plates can rotate independently of the separator plates. When the clutch is engaged, the friction and separator plates become securely coupled to ground the gear components attached to the inner hub of the transmission case in this example. The separator plates also act as a sink that dissipates the heat generated at the frictional interfaces during engagement.

The structure of a clutch pack is complex, with design considerations extending from fluid-structure interactions to friction material and ATF properties. Figure 1.3 illustrates different clutch plate designs. Automotive companies continue to look for new clutch plate designs to reduce the viscous drag torque. In order to reduce this drag torque, various design factors must be taken into consideration. These include the groove number and shape, the plate clearance, waves, the wave height and pattern, the lubrication oil flow, drainage, etc. Grooves between segments of the friction paper provide conduits for the ATF to pass through the plates. A large groove area may be preferred for cooling purposes, but reduces the frictional contact area, affecting the structural integrity of the friction material. A larger plate clearance reduces the velocity gradient of the ATF between plates, and also promotes air entrainment. The large clearance reduces drag torque, but an increased stroke distance tends to degrade engagement control robustness. Some plates may be gently waved in the circumferential direction, aiming at a uniform plate distribution for reducing drag torque. If the viscosity of the ATF is low, the drag torque becomes smaller.

The clutch remains one of the most critical components in the transmission system where opportunities continue to exist for design improvements. Clutch designs are required to meet the challenges of improving fuel efficiency and shift quality at the same time. When the clutch is open, the ATF within the clearance is sheared, and the resulting viscous drag contributes to a measurable loss of fuel efficiency. When a clutch

	
No groove	Radial groove
	
Shaped dot groove	Parallel groove
	
Waffle shape groove	T shape groove

Figure 1.3: Friction plate groove designs

is actuated for engagement, the clutch torque transfer process is highly non-linear, characterized by hydrodynamic lubrication and fluid-structure interaction. This slip torque is directly transferred to a transmission output shaft, affecting both the drivability of the vehicle and the comfort of occupants (*Fujii et al.* (2014)). The clutch geometry appears simple, but it remains difficult to predict its dynamic behavior due to the various new features and the complexity of physical mechanisms at the frictional interface. The computational time and memory requirements are still a huge challenge. Although there is a significant advancement in analytical methodologies, the clutch design process still largely relies on a trial-and-error approach. There are no established models available that can accurately predict the behavior of a wet clutch under all conditions. The development of a high fidelity clutch model which can replicate accurate clutch behaviors, while accounting for detailed design features, is highly desirable to provide engineering insight into clutch development processes.

1.2 Problem Definition and Objectives

The relative motion between the friction and separator plates in an open clutch causes viscous drag torque as the ATF flows through the interface. In Figure 1.4, the relationship between the drag torque and the rotating speed is illustrated.

The drag torque curve can be divided into four regimes based on torque transfer mechanisms. In regime (I), a well-developed ATF film is present between the plates because the centrifugal pumping at the interface is small due to the low rotating speed. The drag torque increases monotonically with the rotating speed. This is because the velocity gradient between the friction and separator plates is increasing, and the drag torque is proportional to the velocity gradient. For a typical clutch pack, the maximum drag torque occurs at a slip speed just below 1000 rpm. The peak torque level is around 5 to 10 Nm, depending on clutch pack designs and operating conditions. The radial velocity of the fluid decreases as the fluid approaches the

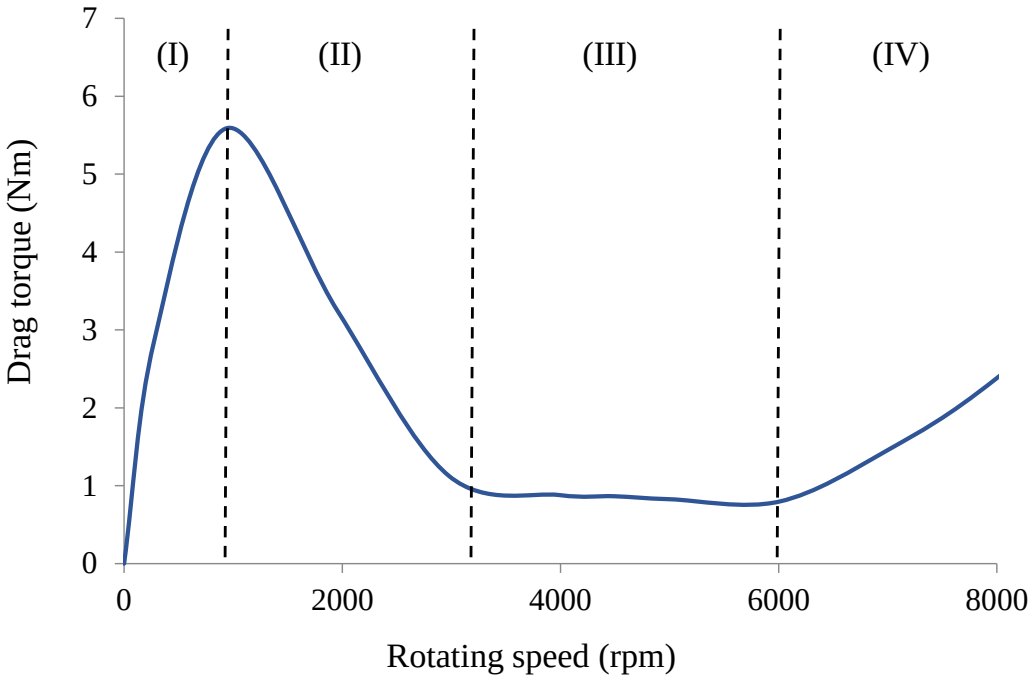

Figure 1.4: A typical drag torque curve

outer radius to satisfy conservation of mass. As the rotating speed increases, the fluid starts to lose the freedom to slow down as it approaches the outer radius since the centrifugal force becomes dominant and drives the fluid outward. As a result, air enters the domain between the plates; this results in aeration which changes the flow from single-phase to two-phase. In regime (II), as the rotating speed becomes higher, more air enters the gap between the plates. The average viscosity of the mixture becomes smaller, and the drag torque decreases with sliding speed.

In regime (III), the interface is mostly filled with air because of the large centrifugal pumping effect. Drag torque remains small and becomes insensitive to slip speed. In regime (IV), according to recent experimental results, when the rotating speed becomes larger than 6000 rpm, the drag torque rises again. At high rotation speeds, the clutch plates start fluttering, resulting in increased friction due to mechanical contact between the plates. This increase in torque may have a significant effect on the design of new clutch plates, especially for high speed transmissions.

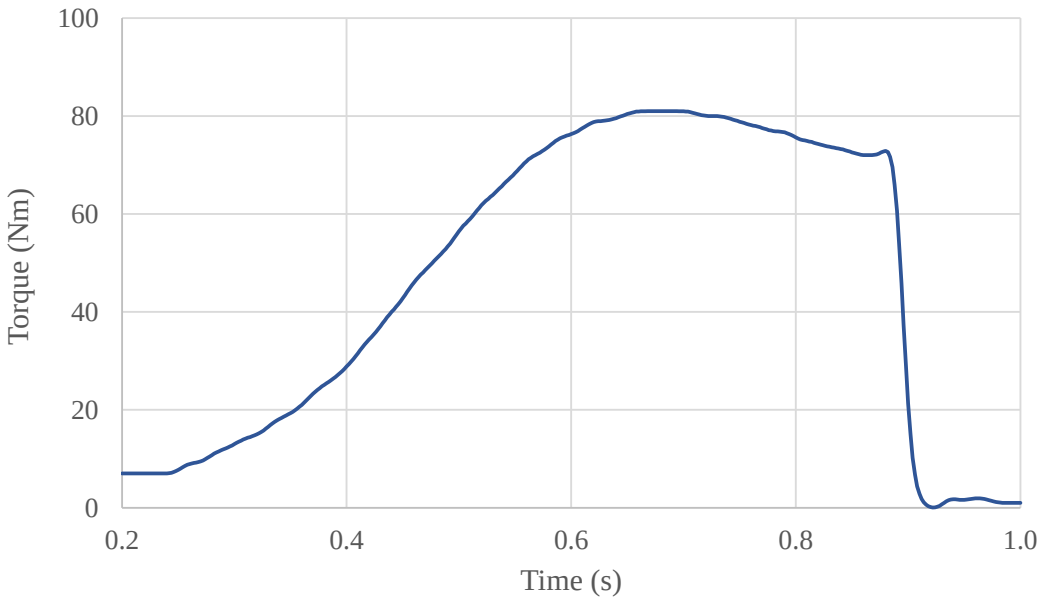

Figure 1.5: Engagement torque characteristic curve

For the engagement process, the general clutch torque behavior is shown in Figure 1.5. This torque is different from drag torque in open clutch status, it is the differential torque transferred from the friction plate to separator plate. The curve can be divided into three stages. As the open clutch is commanded for engagement, there is a complete ATF film within the interface. The clearance between friction and separator plates decreases, and the hydrodynamic torque increases since the velocity gradient within the interface becomes larger. This torque is transferred purely through viscous shear. This stage is called hydrodynamic lubrication. As the distance reduces further, at some point, asperity contact is made, and a friction torque is developed. Thus, the engagement torque is transferred through both hydrodynamic torque and mechanical contact. This is defined as partial lubrication. Large amounts of heat are generated due to the asperity contact. Finally, friction and separator plates are completely engaged, and there is no relative speed between them. This ends the boundary lubrication stage, and the torque is transferred solely through mechanical contact. All of these processes are summarized in Figure 1.6. During the engagement process,

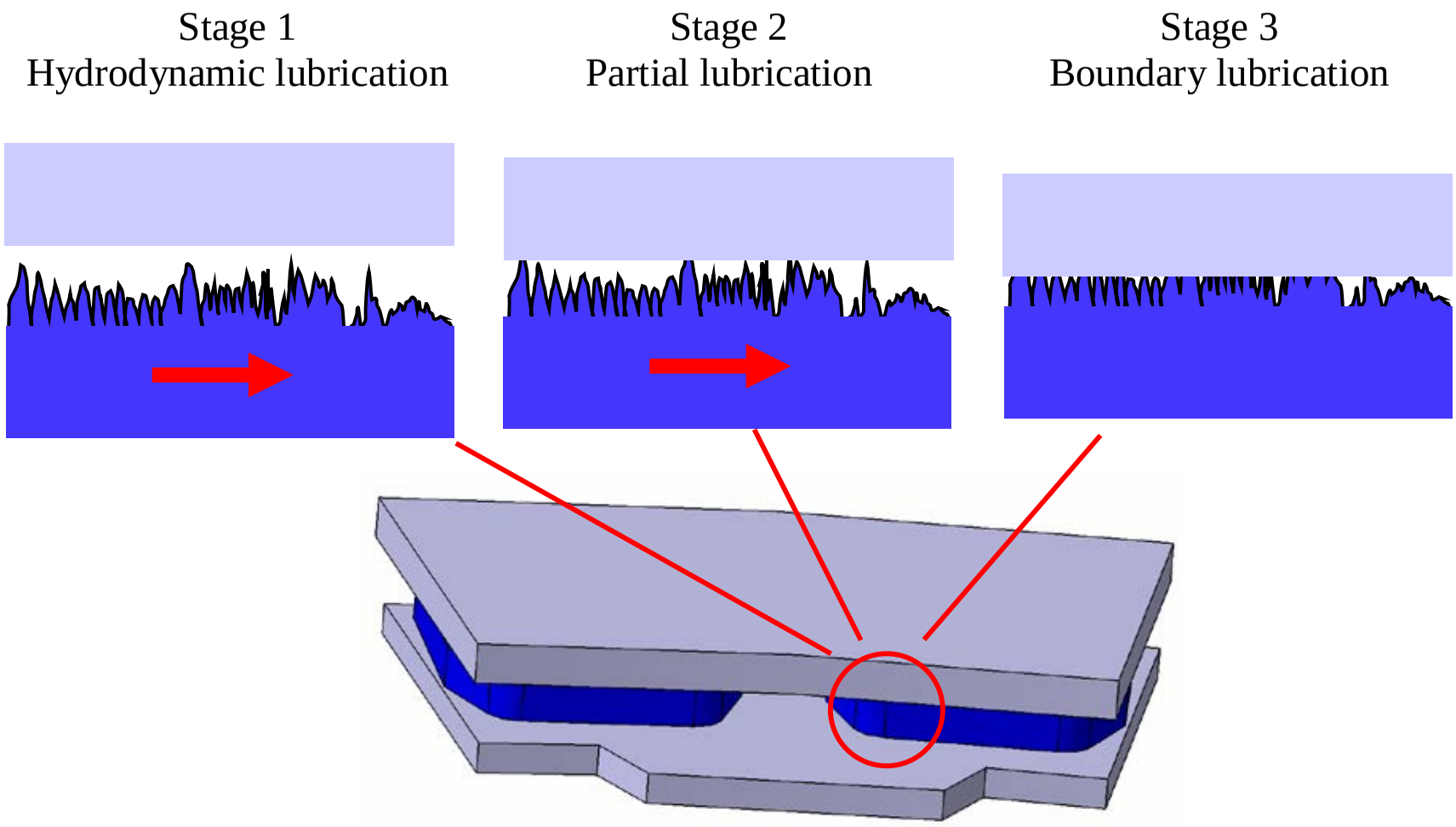

Figure 1.6: Illustration of engagement process

the oil viscosity changes as a result of the ATF temperature change, which is affected by both fluid and solid friction. In addition, the permeability of the friction material also affects the engagement process. The ATF can enter the friction material and seep out, which accelerates the squeeze process.

The primary objective of this research is to advance the state-of-the-art of CFD modeling of a wet clutch in an automatic transmission, and develop simulation tools and advanced knowledge for design and control improvements. The research targets two key areas, as follows.

1. Investigate and characterize the fluid-structure interactions to develop model and methodologies for simulations.

2. Develop and validate open clutch and engagement CFD models.

Because of the complexity of the physical mechanisms at the clutch frictional interface, several modules are developed separately. The main tasks are listed below:

1. Enhanced knowledge of clutch interface flow behaviors.

2. Develop and validate open clutch models, capturing the location and magnitude of the peak drag torque. The results of the open clutch model can be used as the initial condition for engagement modeling. (Chapter 3)

3. Develop a statistical model to investigate the effects of the plate movement on open clutch drag. (Chapter 4)

4. Implement the base line squeeze film model with an iterative numerical scheme. During the engagement process, the flow is squeezed out by the translational motion of the clutch plates. (Chapter 5)

5. Construct secondary modules to capture heat transfer, asperity contact and porous media flow. These processes have significant effects on the engagement behavior, and need to be addressed individually. (Chapter 5)

6. Validate the model with advanced bench test procedures, and deploy the CFD model to capture in-vehicle hydrodynamic effects.

CHAPTER II

Literature Review

The construction of a multi-physics model for wet clutches requires the integration of several physical processes. Open clutch analysis involves the flow between two rotating disks, and an interaction between multiphase fluid and clutch plates. Air bubbles are introduced at a high rotating speed, significantly affecting drag torque level. Clutch engagement involves a squeeze film process, transient moving-boundary partial lubrication, heat transfer, porous media flow, etc. Each component has a large effect on the wet clutch behavior. During the past several decades, numerous experimental and theoretical studies have been conducted to predict the behavior of wet clutches. The following review is by no means exhaustive. The focus is placed on recent developments in clutch dynamics, and key components of the physical processes are given a greater emphasis.

2.1 Open Clutch Modeling

The research on the flow between two parallel plates is the foundation for the viscous torque analysis within clutch interfaces. The pioneers *Cochran* (1934), *Batchelor* (1951), *Stewartson* (1953), *Savage* (1964), *Matsch and Rice* (1968), *Mellor et al.* (1968), *Gorin and Shilyaev* (1976), *Szeri et al.* (1983), *Serre et al.* (2004), and *Poncet et al.* (2005) studied the flow between two coaxial flat plates, providing explicit

pressure and velocity distributions for different cases. Cochran determined the nature of the flow field over the rotating disks. Batchelor established that the core of the fluid between the plates, away from the boundary layer on the disks, rotates with constant angular velocity. Szeri reported that the centrifugal force causes the fluid to increase its radial velocity near the rotating plate, while back flow was present near the stationary plate to compensate the centrifugal flow effect.

Schade (1971), *Lloyd* (1974), and *Fish* (1991) attempted to study the flow behavior within wet clutch systems. They evaluated the effect of groove patterns and depths, fluid flow rate, friction material, as well as clearance and viscosity on wet clutch plates. The importance of plate waviness in reducing drag torque was also discussed.

One of the most important factors that affects the drag torque is aeration. After air enters the interface, the equivalent viscosity of the flow becomes smaller. *Kato* (1993) was the first to propose a two-phase flow model to include the rupture of the ATF film due to cavitation. He also extended the turbulent flow model of *Hashimoto et al.* (1984) to calculate the pressure distribution and drag torque in the ATF film between the clutch plates. The assumption in Kato's model was that the rupture of the ATF film started from the inner radius. However, subsequent studies showed that the air should enter the interface through the outer radius.

Kitabayashi et al. (2003) experimentally investigated some of the key factors that closely relate to the viscous drag torque, such as the frictional facing area, wave height, number of grooves, and the ATF flow rate. He also proposed a theoretical model to calculate drag torque based on Newton's law of viscosity. However, this model was only applicable for single-phase flow, and limited to low speed range. The model was only suitable for predicting the rising part of the typical drag torque curve.

Yuan et al. (2003) attempted to improve the model performance by adding surface tension, and treating surface tension and viscosity of the ATF as adjustable

parameters. Although the simulation appears to match the experimental data, the model did not account for realistic boundary conditions, and was limited to simplified geometries.

Aphale et al. (2006, 2010) investigated the effects of clearance, different groove patterns and number of grooves. A CFD model was developed to study the drag torque behavior and optimize the design of grooves. In their model, only the friction material area was included, excluding the detailed design features, which could not present the real environment of the fluid within the interface. Based on previous results, *Aphale* (2007) extended his model to study drag reduction for different given conditions and other clutch parameters. The CFD analysis and experiments showed that surface modification of the clutch plates helped aeration incipience at low rotation rates, thus reducing the drag and increasing the overall fuel efficiency.

Yuan et al. (2007) proposed an improved hydrodynamic model with the inclusion of the effect of surface tension. To capture the effect of air entrainment, the concept of an equivalent film radius was utilized to divide the fluid and air regions through a hypothetical boundary. The model formulation was only applicable to non-grooved flat plates. The ATF viscosity was treated as a tuning parameter to match experimental observations. Although this model provided a relatively simple analytical framework, the concept of an equivalent radius had no physical justification in the clutch system where fluid was dispersed over the clutch surface.

Hu et al. (2009) derived expressions for the fluid pressure and velocity distributions by solving the simplified three-dimensional Navier-Stokes equations based on a laminar flow assumption. The solution showed that the centrifugal oil flow acceleration dominated the shrinking of the oil film. The equivalent radius was introduced to describe the effective oil film area, and calculate the drag torque after oil film shrinking. Simulation results were validated with experiments, and agreed well with test data.

Yuan et al. (2010) developed a two-phase CFD model to study the aeration process for a flat clutch plate using the VOF method. The simulation indicated that the aeration process is initiated near the plate where the rotational speed is small. The study confirmed that the drag torque was reduced sharply beyond a certain critical speed due to aeration.

Yuan et al. (2011) and *Hu et al.* (2012) conducted visualization experiments to study the drag torque behaviors within the single-plate wet clutches. Through experiments, they showed that the rupture of the ATF film began from the outer radius, and extended toward the inner radius. Oil and air mist was formed, and ATF flowed only along the rotating disk after rupture. The effect of the contact angle of friction plate was also studied.

Takagi et al. (2011a,b) developed a three-dimensional, single-phase CFD model for clutch plates. Effects of clearance, flow rate and groove numbers were studied at a low slip condition. The single phase assumption limits the models capability to predict the peak torque location with respect to slip speed.

Iqbal et al. (2013a,b, 2014) conducted an experimental characterization of drag toque in a multi-plate wet clutch on a SAE #2 test stand. The relationship between supplied flow rate and rotational speed was studied. Based on the experimental results, a mathematical model based on the continuity and Navier-Stokes equations was derived, considering laminar flow in the gap between the disks to estimate the drag torque in open multi-disk wet clutches. The flow pressure and velocity fields were investigated. This model quantified the volume fraction of fluid, and predicted the evolution of film shape.

Wu et al. (2015) presented a two-phase CFD model to predict the drag torque behavior an a grooved two-disk system. The results show that the presence of the grooves accelerated the transition from single-phase to a two-phase flow. The effect of rotating speed, number of grooves were studied to reduce to drag torque level.

Pahlovy et al. (2016) studied air bubble formation in the oil film by using a visualization bench test with high speed cameras. He concluded that air bubbles were generated due to the pressure drop and cavitation at low speeds. Based on this processes, an analytical drag torque model was developed by combining a new expression of volume friction of ATF.

Wang et al. (2017b) presented a two-phase multiple reference frame (MRF) CFD model to predict the drag torque behavior, accounting for detailed design features and realistic environment of the fluid within the interface. The model employed the VOF method to determine the air-oil interface inside a computational domain. Model setup and simulation parameters, including initial conditions, boundary conditions, and relaxation factors were evaluated in terms of model convergence behavior.

Hou et al. (2017) and *Hu et al.* (2018) experimental investigated the drag torque rise at high circumferential speed. The results showed that the torque rise was due to the wobbling vibration and mechanical contact of the friction plates. The rotation of the separator plates also had an impact on the drag torque behavior. Then a mathematical model was established to predict the torque increment at high speed. The fluid hydrodynamic actions are coupled simultaneously with the kinematic position of the friction plate using the rigid-body impact model.

In most analytical and numerical studies, one of the basic assumptions is that the plates are uniformly distributed within the clutch pack. In reality, however, the clutch plates continuously move back and forth in the axial direction. Given the total clearance, the distribution of the gaps can be different at any time, affecting the drag torque behavior. This phenomenon has been widely recognized by the automotive industry for years without a firm theoretical understanding.

Li et al. (2013) derived a simplified Navier-Stokes equation to calculate the drag torque. The equivalent radius was used after air entered the interface. A non-uniform coefficient was introduced to take care of the non-uniform gap within the actual clutch

pack.

Recently, *Wang et al.* (2017a) described a statistical method for modeling the distribution of the plates in a clutch pack. The proposed method employed order statistics to represent the dynamically-changing plate positions. The model could predict the difference in drag torque with or without fixed clutch plates. The simulation results compare satisfactorily with experimental data.

2.2 Engagement Modeling

The first stage of clutch engagement is a squeeze film process. The study of squeeze film flow has a long history, and is recognized as an important and complex fluid mechanics problem since it appears in many practical applications such as printing, thrust bearing, band braking, and wet clutch engagement. The squeeze behavior is affected by many parameters, such as geometry, material properties, surface roughness of the plate, physical properties of the fluid, and dynamic motion of the plate. The clutch engagement characteristics significantly affect the quality of automatic transmission shifting. It is very important to characterize the clutch engagement behavior accurately under a wide range of operating conditions.

Hays (1963) conducted a theoretical analysis of squeeze film flow between flat and curved rectangular plates. A simplified two-dimensional Reynolds equation was used to analyze the effect of surface curvature on squeeze film behavior. Hays found that the load capacity would be reduced if there were a concave or convex curvature on the plate. Furthermore, a convex surface was found to be more sensitive to this effect than a concave one.

Moore (1965) summarized the history of squeeze film studies. Fundamental equations were provided to include the effects of inertia, variable viscosity, surface tension, dynamic loading, and surface roughness. Different shapes of plates were also studied. The squeeze velocity and load capacity were expressed in terms of the applied force

and geometric parameters.

As the distance between two plates becomes smaller, asperity contact takes place. *Greenwood and Williamson* (1966) studied several contact relations, such as the real contact area, the number of micro contacts, and the load and conductance between two flat surfaces associated with the separation of planes. The total contact area and the number of micro contacts depend on the load only, and the asperity height was assumed to follow a Gaussian distribution.

One of the earliest attempts to analyze the flow between two clutch plates was made by *Wu* (1970, 1971), *Levy et al.* (1970) and *Ting* (1975). In their studies, the engagement behavior is divided into three phases, namely squeeze film flow, mixed asperity contact, and consolidating contact. Wu developed an analytical model to analyze squeeze film behaviors between clutch plates. This model considered the porosity of one disk, and the inertia due to the centrifugal force on the fluid, both in the film and the porous region. The load capacity and pressure distribution were presented. Levy described a measuring technique and an appropriate device for determining the surface temperature in disk clutches. The results showed that the surface temperature was considerably higher. Ting found that positive skewness decreases film pressure while negative skewness increases the pressure.

Patir and Cheng (1978, 1979) developed a modified Reynolds equation that included the effects of surface roughness. The modified Reynolds equation used pressure and shear flow factors to account for the effect of surface roughness and asperity contact on the flow. During the partial lubrication phase, the oil flow area is disturbed and reduced due to the increasing asperity contact area.

Zagrodzki (1985, 1990) analyzed the temperature distribution on the clutch plate, and showed that the thermal deformation had a large effect on the pressure distribution. He concluded that the thermal behavior can be reduced by lowering the elastic modulus of the friction material.

Natsumeda and Miyoshi (1994) simulated the wet clutch engagement process numerically. Both hydrodynamic and boundary lubrications were studied in this paper. The model investigated the effect of permeability, surface roughness, and waviness on the initial stage of engagement. The heat generated in the ATF was estimated as the product of the sliding velocity, and the shear stresses at the surfaces. The Gaussian distribution was used to simulate the surface roughness in the asperity contact model. However, it was observed that this assumption might be flawed since the distribution of asperity became skewed as the asperity summits were worn away during the running-in process.

Yang et al. (1995) developed an asymmetric model to study the heat transfer process and hydrodynamic behavior during the engagement in a wet clutch. The model includes the heat balance for the separator plate, friction materials, core plate, and ATF or air in the clearance between the separator plate and friction material. The momentum balance for ATF within the friction lining was also considered. The effect of various important factors affecting the interface temperatures have been examined, such as rotating speed, spline teeth, non-uniform contact, etc. Their predictions of interface temperature compared favorably with experimental measurements.

Berger et al. (1996, 1997) applied analytical tools and the finite-element method to study the effect of applied load and permeability on wet clutch engagement under isothermal conditions. The groove effect and slip conditions were also included in this study. The average flow factor was adopted to include the effect of surface roughness. The results showed that wider grooves reduced the torque peak and increased the engagement time. However, the model required a considerable simplification in the plate geometry.

Razzzaque and Kato (1999) reported a numerical study of the hydrodynamic behavior of the coolant during a hydrodynamic lubrication process. To simplify the derivation process, smooth, perfectly aligned disks, and isothermal, laminar and

steady-state conditions were assumed, and only one interface was considered. By using a finite-difference method, the viscous torque, flow rate and axial force were calculated to evaluate the effects of groove geometry and orientation, with consideration of inertial effects.

Jang and Khonsari (1999) conducted a comprehensive transient thermal hydrodynamic analysis on the wet clutch engagement process. The model calculated the temperature and torque behavior by including the effect of surface roughness, waviness, permeability and grooves. It showed that the temperature change had an effect on the torque behavior.

Davis et al. (2000) extended Berger's isothermal model to include the fluid thermal effects to analyze the onset of thermoelastic instability in a wet clutch. In his model, the modified Reynolds equation and thermal diffusion were solved simultaneously to obtain torque and temperature characteristics during the engagement process. The model took into account the surface roughness, the porosity, and the deformability of the friction material. By including thermal effects, the engagement time became shorter, and the peak drag was reduced. The results correlated well with the experimental data.

Xiang and Kremer (2001) developed a closed-form model to evaluate the thermal performance during engagement process. The model predicted the averaged temperature and peak value at the interface. Correction factors were used to adjust the heat transfer coefficients to obtain relatively accurate results. However, the model was limited to simplified geometries.

Both the clutch plate and the band brake share the same fundamental physics during the engagement process. *Fujii et al.* (2001a,b) derived a mathematical model to predict the dynamic engagement behavior for the wet band brake. The effect of squeeze film, asperity contact, porous media, heat transfer and loading pressure distribution were taken into consideration. The band engagement characteristics were

experimentally evaluated to validate the analytical model.

Mansouri et al. (2001) conducted simulations of wet clutch engagement including drive torque. The drive torque was continuously transferred from the engine to the wheels during a gear-shift. A dynamic model for frictional brake torque was developed, and the friction coefficient was obtained through experiments.

Gao et al. (2002a,b) studied the combined effects of surface roughness, skewness, and friction coefficient versus velocity characteristic on the engagement for new, run-in, and glazed wet friction materials. A Weibull asperity height distribution was utilized in the asperity contact model instead of a Gaussian distribution. The results showed that the engagement time predicted by the Weibull distribution was greater than that obtained from the Gaussian distribution.

Jen and Nemecek (2008) developed a numerical model using the separation of variables method to compute the temperature distribution in the steel plate. However, the analytical results did not agree well with the experimental data due to the non-linear behavior of the engagement process.

Miyagawa et al. (2009) carried out a numerical simulation to examine the effect of radial and circumferential grooves on the friction surface temperature and torque response in a multi-disk wet clutch. The simulation results showed that the temperature of the friction plate can be better controlled by the simultaneous use of radial and circumferential grooves.

Ompusunggu et al. (2011) presented an analytical model to study the friction material degradation effects on the dynamic engagement behavior. A 3-degree of freedom (DOF) lumped model was used to simulate the clutch system. The effects of dynamic sliding velocity and changing normal load were taken into account in this friction model. The results showed that the velocity profile and torsional vibration were affected by the degradation effect.

Cho et al. (2011) created a CFD model to simulate the transient clutch behavior

during engagement process. A new iterative scheme was developed to reflect the real control strategy. The numerical results were validated using analytical solutions of the Reynolds equation for simplified geometry. Later, *Cho* (2012) developed a more comprehensive model to include multi-physics aspects. However, due to the large computational cost, the iterative scheme was not used in the final model.

Jang et al. (2011) developed a three-dimensional governing equation to study the effects of grooves of a wet clutch during the engagement stage. The model took into account the compressibility, the surface roughness and permeability of the friction material, and the contribution of radial grooves or waffle-shape grooves.The variation of the friction coefficient with the velocity was taken into consideration. However, to account for the possibility of cavitation in the grooves, any negative pressure was simply set to be zero in the Reynolds equation.

Madhavan et al. (2012) developed a CFD model to simulate the flow and thermal performance during the engagement process. The model accurately predicted the temperature and pressure change compared with test data. It also showed that the improved flow uniformity could lead to a more uniform temperature distribution within wet clutches.

Iqbal et al. (2015) developed a mathematical friction model to study the vibrational and dynamic behavior of wet friction clutches during a dynamic engagement cycle. The model took into account the viscous effects and the delay in actuation pressure due to filling action of the ATF in the chamber. A traditional SAE #2 test stand was used to validate the model results in both the time and frequency domain. The experimental observations confirmed that the amplitude of shudder vibration was independent of the applied contact pressure.

Miao et al. (2017) utilized a turbulent CFD model to investigate the effect of groove patterns on the flow characteristics for engagement process. Two different groove patterns were compared. It concluded that the cooling effect of the radial

groove pattern was more effective.

Kim and Shim (2017) proposed a lumped heat transfer model for wet multi-plate clutch. The correlations of the heat convection coefficient with various design parameters were presented. The coefficients of the correlations were determined by the non-dominated sorting genetic algorithm. The results were validated with the experimental data, which showed a good agreement.

Though several attempts have been made, clutch engagement remains a challenging problem. To accurately model the effects of all the design variables and complex flow geometry is a daunting modeling task. There are no established models available that can accurately predict the behavior of a wet clutch under all conditions. The development of a high fidelity clutch model which can replicate accurate clutch behaviors, accounting for detailed design features, is desired to provide engineering insight into clutch development processes, and improve the fidelity of a drive cycle simulation for up-front examination of drivetrain efficiency.

CHAPTER III

Open Clutch Modeling

In this section, CFD models for both single-phase and two-phase flow are developed for investigating open clutch drag torque behavior. The models include detailed design features to capture the complexity of fluid-structure interactions, and reflect real working conditions in the transmission system. A series of studies are conducted to evaluate the number of inner iterations, time steps, initial and boundary conditions in terms of convergence behavior. Selecting appropriate settings is critical for achieving mass and momentum balance in a dispersed two-phase flow towards stable convergence. The model's capability is validated with clutch drag test data. The model successfully captures the location and magnitude of the peak drag torque. The total drag torque is decomposed into viscous and pressure elements to quantify the torque transfer mechanisms for a given groove design. Interface visualization tests are conducted to investigate fluid-structure interactions as a function of rotational speed. The use of the VOF method in the model captures the overall aeration process as observed in the tests. This CFD model offers physical insight into complex open clutch behaviors, and provides a valuable means for drag improvements, and complementing hardware-based clutch design processes.

3.1 Mathematical Formulation of Physical Processes

To capture the drag torque characteristics, a mathematical model is derived below. Figure 3.1 shows the basic geometry of a single clutch plate. The left part corresponds to a top view, and the right one is a cross sectional view. Only one friction plate and one separator plate are taken into consideration. The top plate, i.e. the friction plate, and the friction lining are shown in brown in Figure 3.1. The bottom plate is a separator plate. The dimensions of these two plates are the same. The inner and outer radii are denoted by r_1 and r_2. The top plate is rotating with a rotating speed ω, and the bottom plate is stationary. The distance between these two plates is h, and is assumed to be constant. The gap is full with ATF, and a complete oil film is formed between the plates, which is shown as a blue rectangle in Figure 3.1.

The fluid in the gap is in motion due to the rotation of the top disk. Compared with the dimensions of the clutch plates, the clearance is very small, and the ATF film is very thin. The flow between the plates is assumed to be laminar, and in a steady state. It is also assumed that the fluid pressure does not change across the film thickness. Compared with the viscous forces acting on the fluid, the gravitational and inertial forces are very small, and can be ignored. The rate of change of the velocity components in the radial and axial directions is negligible compared with that in the tangential direction. The temperature change is small, and the viscosity is assumed to be constant.

Under these assumptions, *Hamrock et al.* (2004) and *Iqbal et al.* (2014) derived the simplified Navier-Stokes equations for incompressible flow in cylindrical coordinates, which are shown below

$$\mu \frac{\partial^2 v_r}{\partial z^2} = \frac{\partial p}{\partial r} - \frac{\rho v_\theta^2}{r} \tag{3.1}$$

$$\mu \frac{\partial^2 v_\theta}{\partial z^2} = \frac{1}{r} \frac{\partial p}{\partial \theta} \tag{3.2}$$

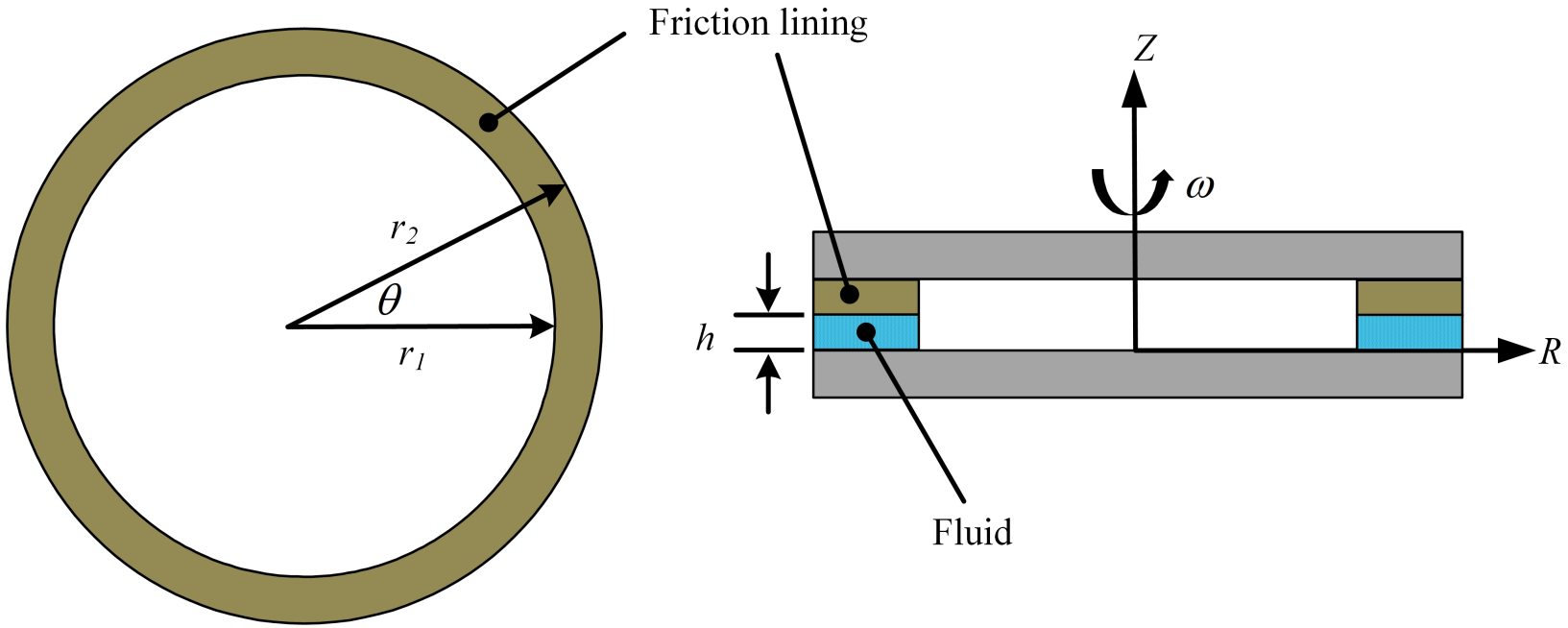

Figure 3.1: Non-grooved clutch plate geometry

where ρ is the ATF density, μ is the ATF viscosity, p is the fluid pressure, v_r is the velocity component in the radial direction and v_θ is the velocity component in the circumferential direction. Equation (3.2) shows that as the upper disk is rotating, the pressure gradient is balanced by the viscous stress, resulting in a steady radial flow. The continuity equation written in cylindrical coordinates is shown below

$$\frac{\partial \rho}{\partial t} + \frac{1}{r}\frac{\partial}{\partial r}(r\rho v_r) + \frac{1}{r}\frac{\partial}{\partial \theta}(\rho v_\theta) + \frac{\partial}{\partial z}(\rho v_z) = 0 \tag{3.3}$$

It is assumed that the tangential velocity is constant in the circumferential direction. Hence

$$\frac{\partial v_\theta}{\partial \theta} = 0 \tag{3.4}$$

Besides that, the ATF is assumed to be incompressible, and the density is constant. Therefore, the density can be eliminated to obtain a simplified equation as follows

$$\frac{1}{r}\frac{\partial}{\partial r}\big(r v_r\big) + \frac{\partial v_z}{\partial z} = \frac{1}{r}v_r + \frac{\partial v_r}{\partial r} + \frac{\partial v_z}{\partial z} = 0 \tag{3.5}$$

Due to the no-slip assumption, the boundary conditions for the flow between two plates are shown below

$$\begin{aligned} v_\theta &= r\omega \qquad \text{at} \qquad z = h \\ v_\theta &= 0 \qquad \text{at} \qquad z = 0 \\ v_r &= 0 \qquad \text{at} \qquad z = 0 \text{ and } z = h \end{aligned}$$

Since the ATF film between the plates is very thin, the pressure is assumed to be constant in the circumferential and axial directions. The ATF film thickness is assumed

to be constant as well

$$\frac{\partial p}{\partial \theta} = 0 \qquad \frac{\partial p}{\partial z} = 0 \qquad \frac{\partial h}{\partial \theta} = 0$$

Furthermore, it is assumed that the pressure is only a function of the radius, r. Furthermore, the inlet and outlet boundary conditions are correspond to constant pressure, fixed at atmospheric conditions, i.e.

$$p(r_1) = p(r_2) = 0$$

Substituting these boundary conditions into Equation (3.2), the following equation is obtained

$$\mu \frac{\partial^2 v_\theta}{\partial z^2} = \frac{1}{r}\frac{\partial p}{\partial \theta} = 0 \tag{3.6}$$

Integrating Equation (3.6) using the corresponding boundary conditions, an expression for the tangential velocity is found, as follows

$$v_\theta = \frac{\omega}{h} r z \tag{3.7}$$

Substituting Equation(3.7) into Equation (3.1), we obtain

$$\mu \frac{\partial^2 v_r}{\partial z^2} = \frac{\partial p}{\partial r} - \frac{\rho r \omega^2 z^2}{h^2} \tag{3.8}$$

Integrating Equation(3.8) twice, an expression for the radial velocity is obtained, as follows

$$v_r = \frac{1}{2\mu}\frac{dp}{dr}\Big(z^2 - zh\Big) - \frac{\rho r \omega^2}{12\mu}\Big(\frac{z^4}{h^2} - zh\Big) \tag{3.9}$$

Substituting Equation (3.9) into the continuity equation, we obtain

$$\Big(\frac{z^2 - zh}{2\mu}\Big)\frac{1}{r}\frac{d}{dr}\Big(r\frac{dp}{dr}\Big) - \frac{\rho\omega^2}{6\mu}\Big(\frac{z^4}{h^2} - zh\Big) + \frac{\partial v_z}{\partial z} = 0 \tag{3.10}$$

Integrating Equation (3.10) over z direction with the boundary condition $v_z = 0$ at $z = 0$, an expression for the axial velocity is obtained, as follows

$$v_z = \Big(\frac{3z^2h - 2z^3}{12\mu}\Big)\frac{1}{r}\frac{d}{dr}\Big(r\frac{dp}{dr}\Big) + \frac{\rho\omega^2}{6\mu}\Big(\frac{z^5}{5h^2} - \frac{z^2h}{2}\Big) \tag{3.11}$$

Since $v_z = 0$ at $z = h$ as well,

$$v_z = \Big(\frac{3h^3 - 2h^3}{12\mu}\Big)\frac{1}{r}\frac{d}{dr}\Big(r\frac{dp}{dr}\Big) + \frac{\rho\omega^2}{6\mu}\Big(\frac{h^5}{5h^2} - \frac{h^3}{2}\Big) = 0 \tag{3.12}$$

The pressure distribution in the radial direction can be obtained from Equation (3.12), as follows

$$\frac{1}{r}\frac{d}{dr}\Big(r\frac{dp}{dr}\Big) = \frac{3}{5}\rho\omega^2 \tag{3.13}$$

Integrating Equation (3.13) with the boundary condition for pressure, the expression for the pressure in the radial direction becomes available, i.e.

$$p = \frac{3}{20}\rho\omega^2 r^2 - \frac{3}{20}\rho\omega^2\frac{r_1^2 - r_2^2}{ln(r_1) - ln(r_2)}ln(r) + \frac{3}{20}\rho\omega^2\frac{r_1^2 ln(r_2) - r_2^2 ln(r_1)}{ln(r_1) - ln(r_2)} \tag{3.14}$$

Equation (3.9) and (3.11) require the derivative of the pressure. Thus, differentiating Equation (3.14) with respect to r, we obtain

$$\frac{dp}{dr} = \frac{3}{10}\rho\omega^2 r - \frac{3}{20}\rho\omega^2\frac{1}{r}\frac{r_1^2 - r_2^2}{ln(r_1) - ln(r_2)} \tag{3.15}$$

The drag torque is caused by the viscous shear of the ATF. The shear stress acting

on the rotating plate is shown below

$$\tau_{\theta z} = \mu \frac{\partial v_\theta}{\partial z} = \frac{\mu \omega r}{h} \tag{3.16}$$

Integrating the shear stress over the plate, the drag torque can be expressed as follows

$$T = 2\pi \int_{r_1}^{r_2} r \tau_{\theta z} r dr = \frac{\pi \mu \omega}{2h} \big(r_2^4 - r_1^4\big) \tag{3.17}$$

where r_1 and r_2 are the inner and outer radii. Equation (3.17) is used to predict the drag torque acting on the plate when the fluid within the interface is treated as a single phase. It also shows that for the same geometry, high rotating speed, high viscosity and small clearance lead to a large drag torque.

The volumetric flow rate, Q, in this case can be calculated by integrating the radial velocity at the outlet to obtain the following expression

$$Q = 2\pi r \int_0^h v_r dz = 2\pi r \big(- \frac{h^3}{12\mu} \frac{dp}{dr} + \frac{\rho r \omega^2 h^3}{40\mu} \big) \tag{3.18}$$

Substituting Equation (3.15) into Equation (3.18),

$$Q = 2\pi r \bigg(- \frac{h^3}{12\mu} \Big(\frac{3}{10} \rho \omega^2 r - \frac{3}{20} \rho \omega^2 \frac{1}{r} \frac{r_1^2 - r_2^2}{ln(r_1) - ln(r_2)} \Big) + \frac{\rho r \omega^2 h^3}{40\mu} \bigg) \tag{3.19}$$

Combing terms in Equation (3.19), the final expression for the flow rate is shown below

$$Q = \frac{\rho r \omega^2 h^3}{40\mu} \frac{r_1^2 - r_2^2}{ln(r_1) - ln(r_2)} \tag{3.20}$$

There is no pressure term in Equation (3.20), indicating that the flow rate, Q, is only determined by the radial fluid motion driven by the centrifugal force, when zero

pressure boundary conditions are specified at the inlet and outlet. This flow rate is also a result of the pumping capacity of the clutch system. When the ATF supply at the inlet is larger than the flow rate, the interface is filled with ATF, and there is always a complete fluid film within the interface. When the flow rate is larger than the continuous oil supply, air will enter the domain, and two-phase flow is established in the interface.

3.2 Single-phase Model

3.2.1 CFD model setup

The analytical model is limited to simple geometries. As the geometry becomes more complex, there is a need to develop a high-resolution CFD model. Figure 3.2 shows the domain of an open clutch CFD simulation. The spline teeth of the friction plate are removed, and the computational domain represents only the fluid without the solid structure. In Figure 3.2, the top surface is the friction plate, which is treated as a wall boundary with a constant rotating speed ω. The bottom surface is the separator plate, which is set to be a stationary wall. In order to reduce the computational time, only part of the clutch plate is included, and periodic boundary conditions are applied to the side surfaces of the domain. The inner radius of the plate corresponds to the inlet, and a zero-pressure boundary condition is assumed. The outer radius corresponds to the outlet, and zero pressure is assumed there as well. This zero-pressure boundary condition is very common in clutch modeling, which is the same with the analytical solution. The inlet boundary condition can also be replaced by a fixed flow rate. In that case, instead of defining pressure conditions, the flow rate is provided. When multi-phase flow is simulated, the phase fraction at the inlet and outlet sections are needed as well.

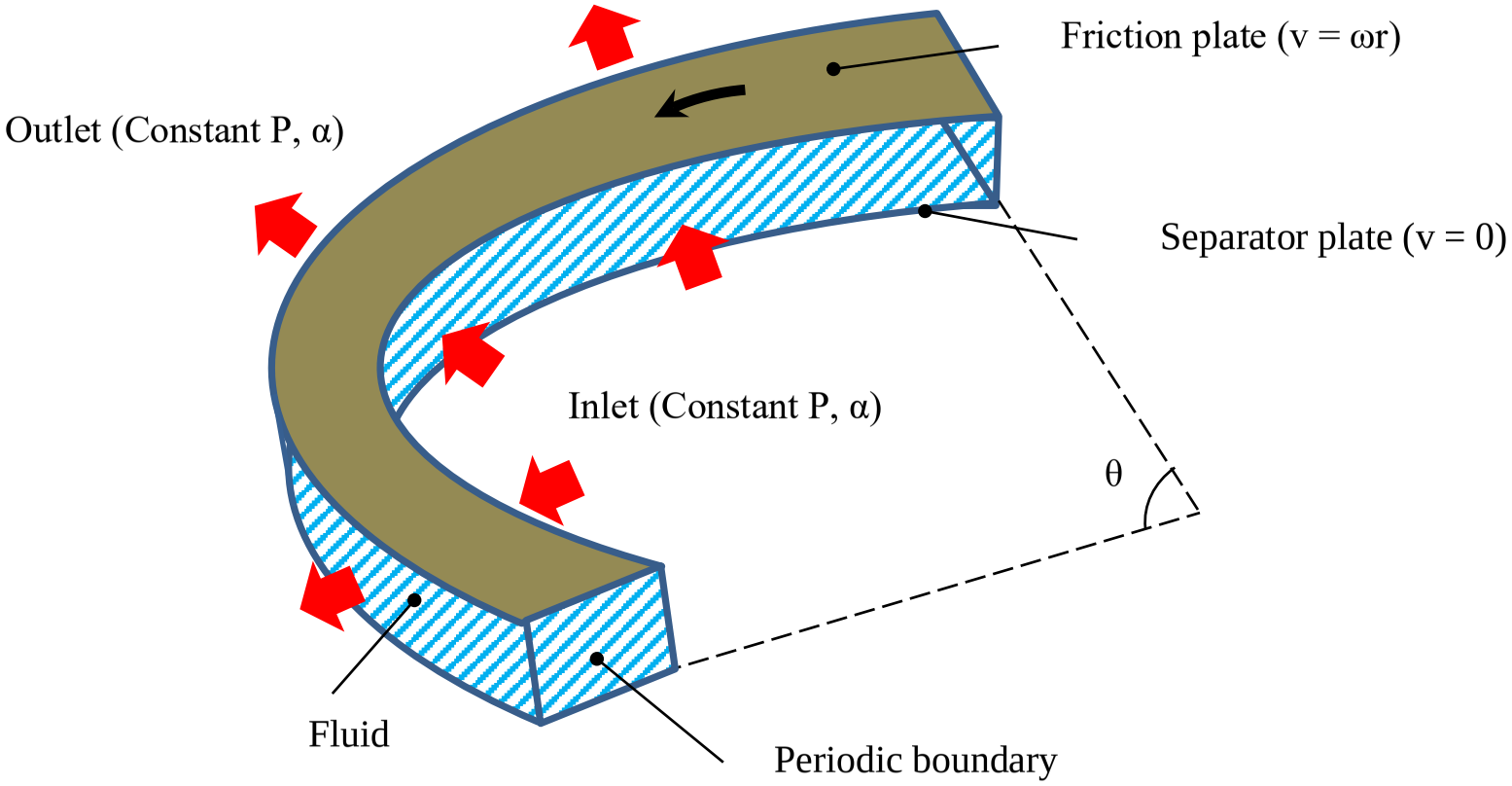

Figure 3.2: The computational domain for single-phase model

3.2.2 Analytical validation of CFD codes

The analytical solution described in the previous section is used to validate the CFD model. In this research, several available CFD codes were evaluated for application to clutch modeling. Among these, three were studied in detail, FLUENT, STAR-CCM+, and OpenFOAM. Among these three, OpenFOAM is an open source code, while the others are commercial codes. A single phase simulation with a non-grooved plate was employed using these codes independently. The results are summarized in Figure 3.3, and compared with the analytical solution. Simulation results are represented by color symbols, and the analytical solutions are represented by solid lines. Figure 3.3 shows that the simulation results from OpenFOAM and Star-CCM+ agree well with the analytical solution for the velocity and pressure fields.

There are some minor differences between the simulation results and the analytical solutions in the axial velocity distribution. This is due to the assumption made for the pressure distribution. The pressure is assumed to be constant in the axial direction during the derivation of the analytical solution. This is a reasonable assumption, and it simplifies the derivation process. However, there is no such assumption in the CFD simulation. The pressure distributions from OpenFOAM and STAR-CCM+ are the same, and they agree well with the analytical solution. Compared with the analytical solution, FLUENT results are not satisfactory. The reason is the different definition of the pressure boundary condition. In FLUENT (*Fluent* (2009)), a pressure inlet boundary condition is used to define the total pressure at the inlet boundary. However, the pressure outlet boundary condition corresponds to static pressure, and this different definition produces poor results. This also indicates that any CFD simulation is very sensitive to the boundary conditions specified.

In summary, both OpenFOAM and STAR-CCM+ provide reasonable results. On the other hand, FLUENT cannot produce accurate results due to the incorrect pressure definition, even for this simple case. Therefore, for the purposes of this project,

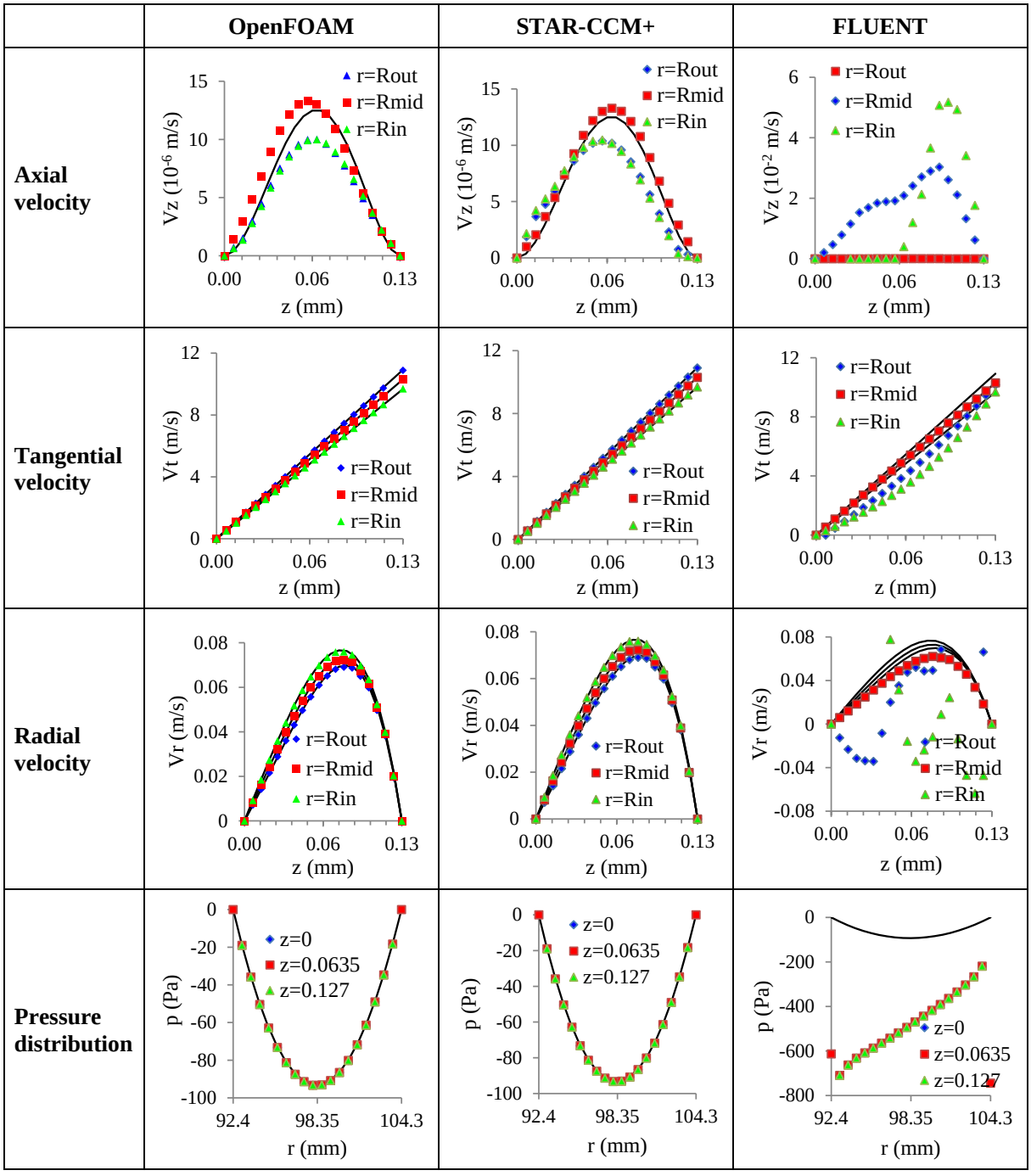

Figure 3.3: Validation of CFD software

OpenFOAM and STAR-CCM+ were selected as references, and a start-point for software development.

The inclusion of detailed geometric features in clutch simulation has recently become possible due to the advancement of CFD technology. Figure 3.4 shows a contour map for pressure and tangential velocity distributions on the friction plate for both non-grooved and grooved plates. The pressure shown in the contour map is defined as the kinematic pressure, which is the pressure divided by the density of the ATF. Figure 3.4 shows that, for the non-grooved plate, the smallest pressure occurs at the center of the friction plate, which is consistent with the analytical solution. However, for the grooved plate, the extreme pressure values are larger, and the pressure range is wider, compared with flat plate. This is due to the fluid structure interaction within the grooves. Due to the rotation, grooves guide the fluid within the interface, which increases the pressure intensity. The third column in Figure 3.4 shows that the maximum velocity occurs on the friction plate. The tangential velocity component is larger at the outer radius. For the grooved plate, the distribution is nearly the same as that for the flat plate. All plots show symmetric results, which agrees with the assumption in the analytical solution derivation process. This also shows that CFD methods have the ability to capture the flow behavior in the clutch interface.

3.2.3 Rotating Reference Frame

In clutch systems, since the friction plate is rotating, it is advantageous to solve the problem in a moving (or non-inertial) reference frame. For a flat plate, there is no difference whether the friction or the separator plate is rotating, and the use of a rotating reference frame is optional. However, for a grooved plate, since some of the groove surfaces are perpendicular to the rotating direction, the rotating velocity cannot be directly assigned to these surfaces without using a rotating reference frame. For otherwise the simulation results in a discontinuous velocity distribution. Figure

	Pressure distribution (m^2/s^2)	Velocity distribution (m/s)
Flat	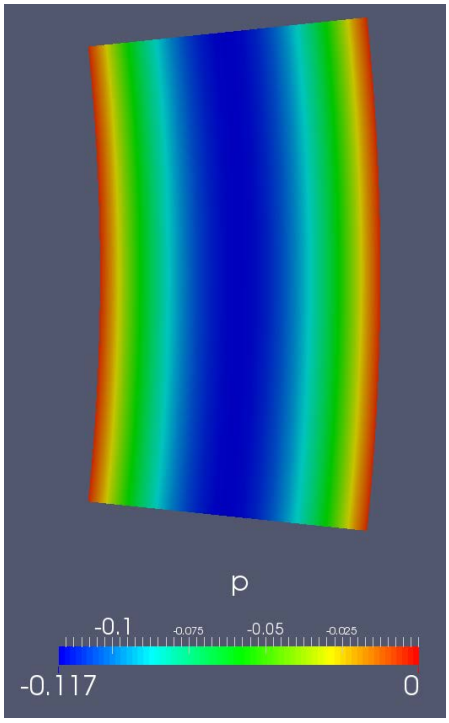	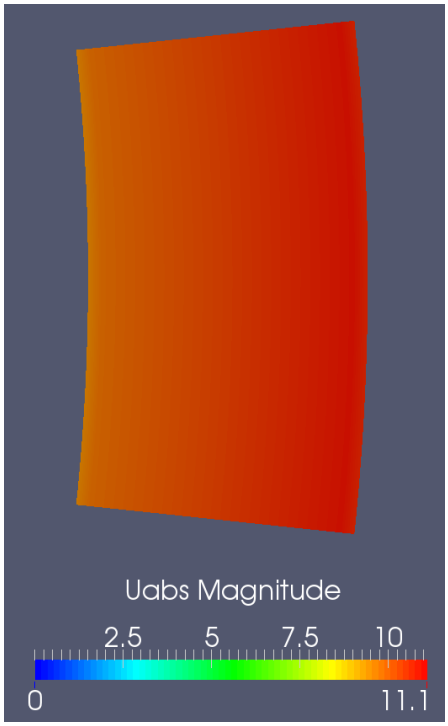
Grooved	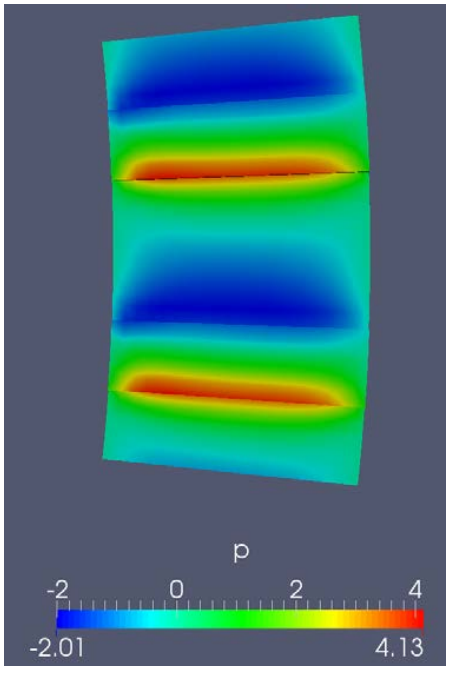	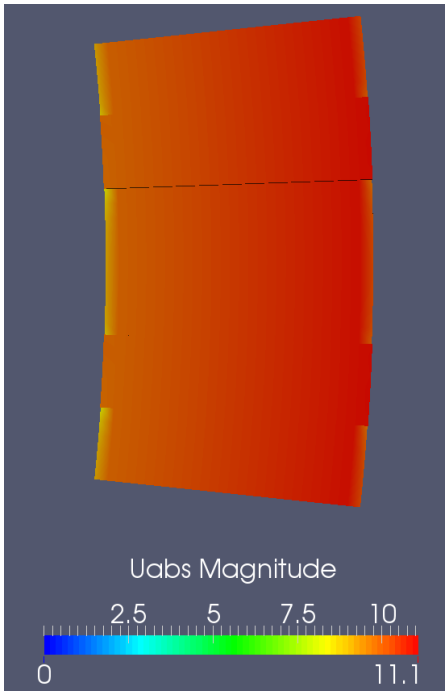

Figure 3.4: Results for single phase model

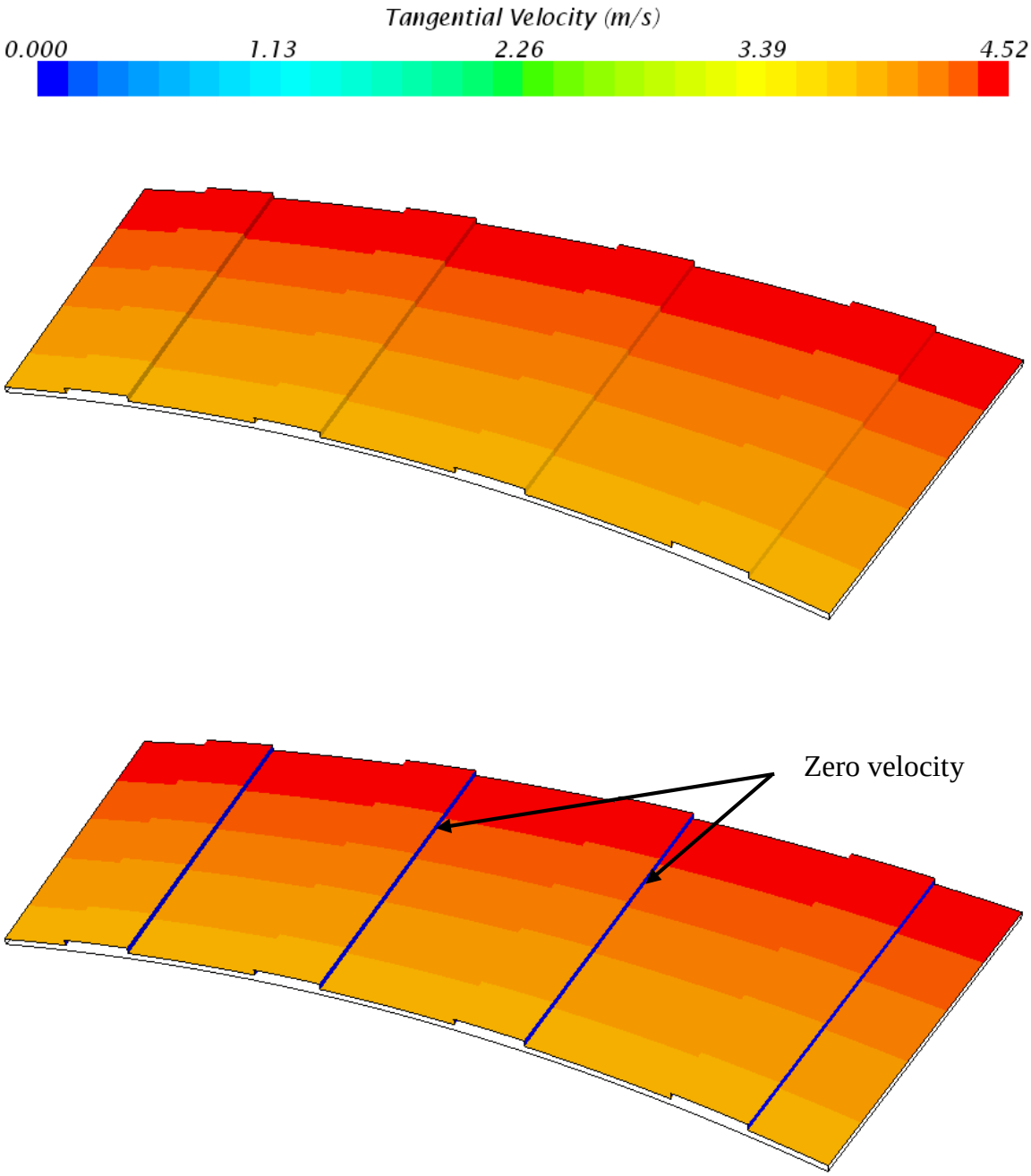

Figure 3.5: Rotating reference frame vs. non-rotating reference frame

3.5 shows the simulation results with 500 rpm with and without a rotating reference frame. The tangential velocity is represented by the color map. The top figure corresponds to the case with a rotating reference frame, and the tangential velocity is continuous on the friction plate. The bottom figure shows the velocity computed without a rotating reference frame. The velocity distribution on the surface is almost identical except that the side walls of the grooves have zero velocity, shown in blue, which makes the velocity distribution discontinuous and unrealistic. This is due to the inability of the model to assign a rotating velocity to these surfaces due to their orientation. Therefore, the use of a rotating reference frame is necessary for grooved plates.

For simple geometries, it is possible to refer the entire computational domain to one moving reference frame. This is known as the single reference frame (SRF) approach. However, for complex geometries, it may not be possible to use a single reference frame. In such cases, the domain can be broken into multiple zones with well defined interfaces between these zones. This approach is called the MRF. For the single-phase model, the SRF is capable of providing accurate results. For the multi-phase model, however, additional simulation zones need to be included in order to include detailed design features, thus a MRF must be utilized to discretize the computational domain.

3.2.4 Application of the single phase clutch model

To check the consistency of the simulation results, different sizes of the computational domain were used, by increasing the number of dots in the modeled sector of the disk, and the simulation results are compared in Figure 3.6. The drag torque increases linearly with the rotating speed while the flow rate has a quadratic relationship with the speed. The behaviors agree well with the analytical solution. For different sizes of the simulation domain, the torque and flow rate are the same, indi-

cating that the simulations are insensitive to domain size. In this case, the smaller domain has computational advantages, since it requires a smaller computational time and memory. However, the general recommendation is to model the entire plate, so that the effects of asymmetric features are not missed when computational capability permits.

Although the single-phase CFD model has some limitations, and is only valid at low speeds, it can be used to study the primary effects of different design parameters, such as the number of grooves and their depth. Figure 3.7 shows the torques acting on both the friction and separator plates for different geometries. In a non-grooved plate, the drag torque acting on the friction and separator plate is the same, since the torque is due to pure viscous shear. However, in a grooved plate, drag torque is transmitted through fluid pressure acting on the groove walls, in addition to the viscous shear over the friction material surface. The torque generated due to the pressure difference is called pressure torque, which does not exist for a non-grooved plate, where the entire surface area is parallel to the rotational direction. The bottom image in Figure 3.7 shows the pressure and viscous torques exerted on the friction and separator plates, respectively. Due to the conservation of angular momentum, the drag torque acting on the flat separator plate is smaller than the torque acting on the grooved friction plate.

Figure 3.8 shows the radial velocity distributions with respect to groove depth. The shape is different from Figure 3.3 due to the presence of grooves. It shows that the radial velocity becomes larger as the groove depth increases since grooves provide an additional channel for the fluid to move across the plate surface quickly. As the groove depth increases, the pumping effect of the plate becomes larger, leading to a higher radial velocity.

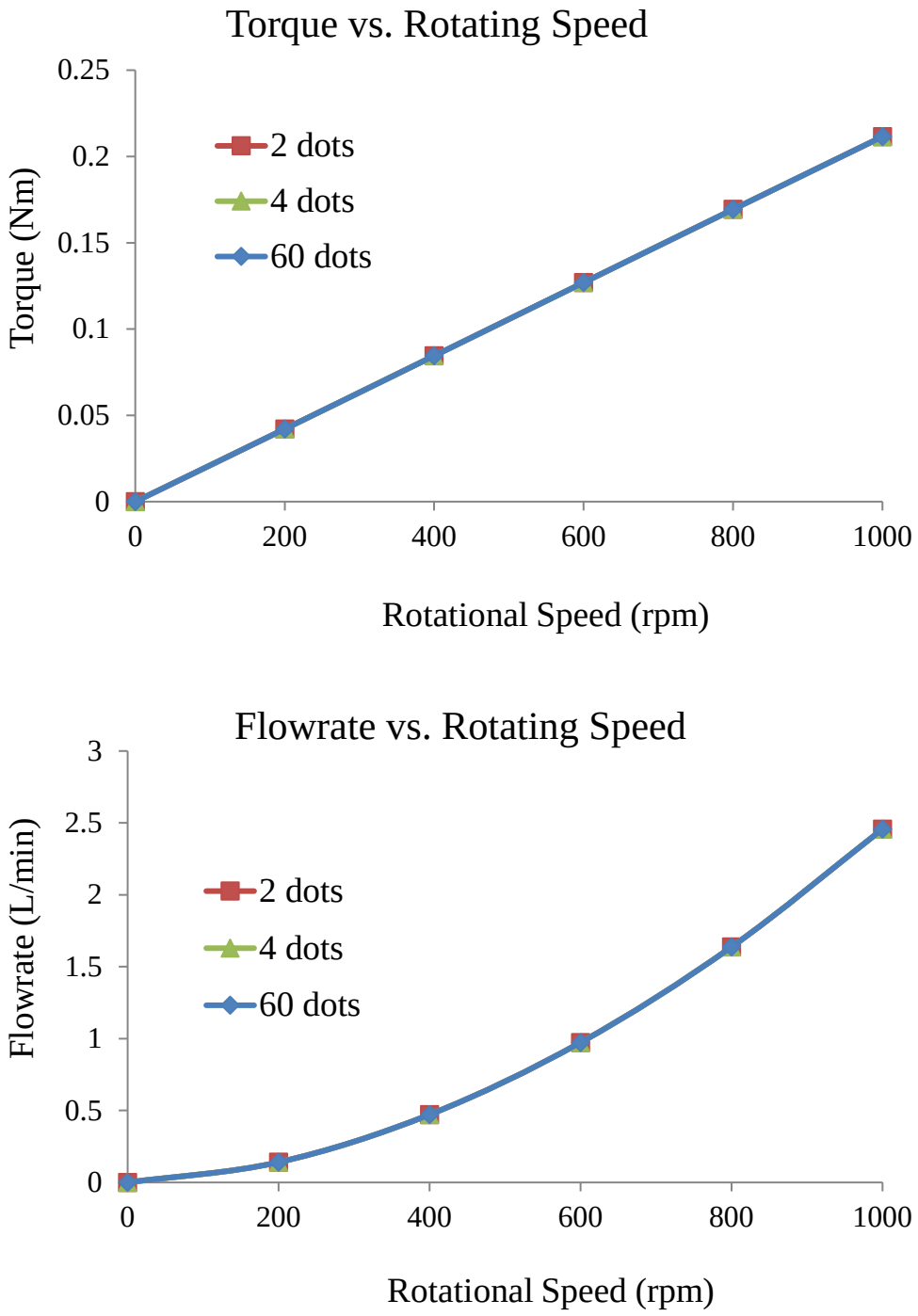

Figure 3.6: Effect of computational domain sizes

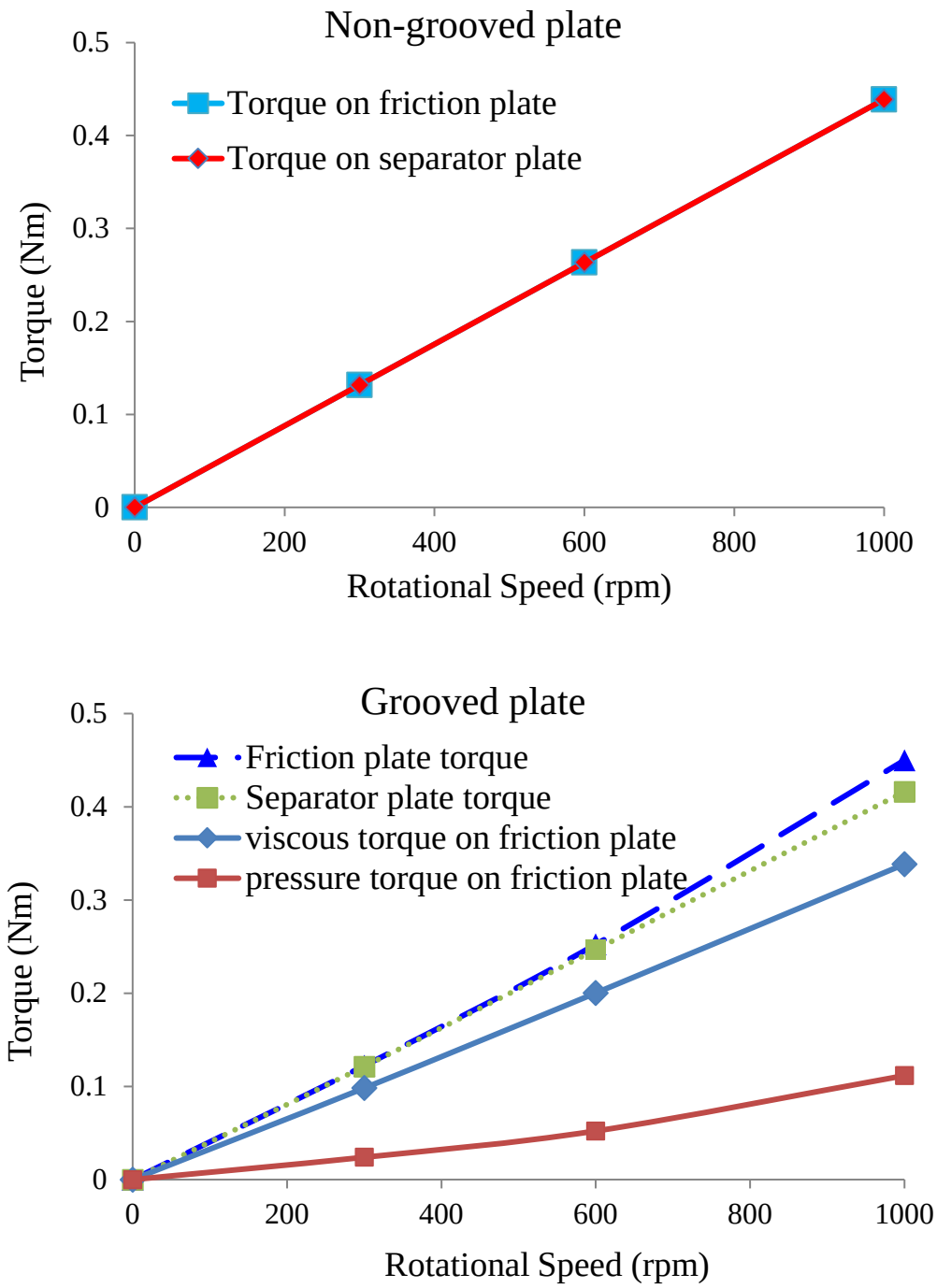

Figure 3.7: Torque behavior for non-grooved and grooved plates

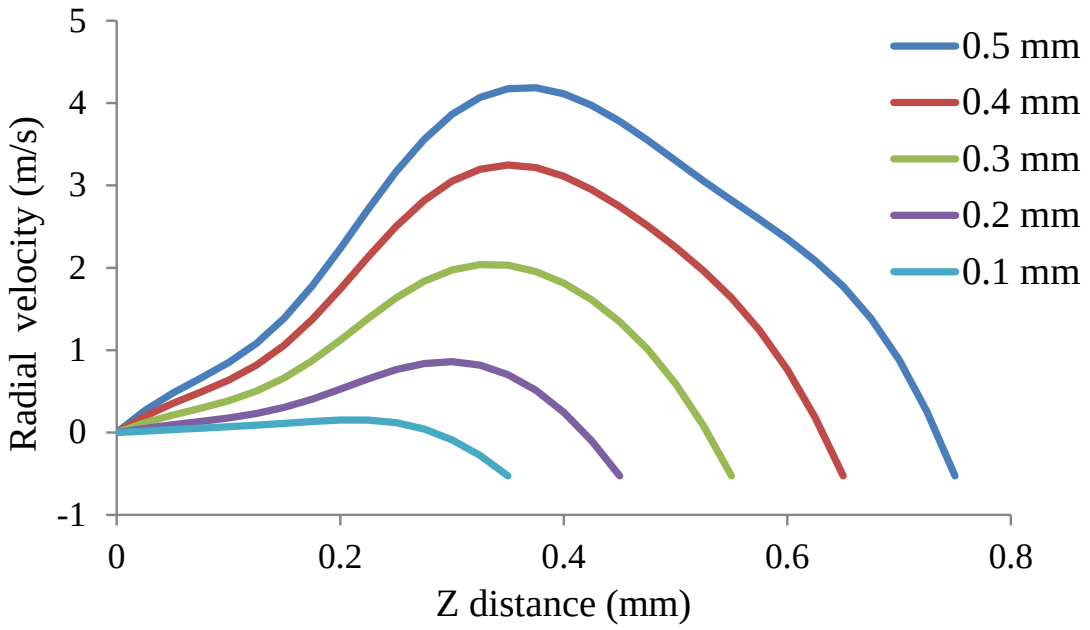

Figure 3.8: Groove depth design assessment

3.3 Two-phase Model

The computational domain for two-phase model is shown in Figure 3.9, representing a single fluid interface of a clutch pack between the inner hub and outer structure. The domain includes the friction plate, the frictional material area, the spline teeth geometry, the space between the friction plate and outer structure, and the drainage holes on the housing. The inner boundary of the domain corresponds to the spline teeth area of the friction plate. There are six evenly spaced ATF inlet holes at the spline teeth area, where a fixed flow rate boundary condition is applied. The outer boundary of the model corresponds to the clutch housing with six drainage holes where wall type and outlet boundary conditions are used, respectively. The top drainage hole is designated as the air inlet, where air enters the domain. It is assumed that this hole does not allow ATF fluid to leave the domain. The ATF and air mixture can exit or enter the domain through any of the remaining holes. This

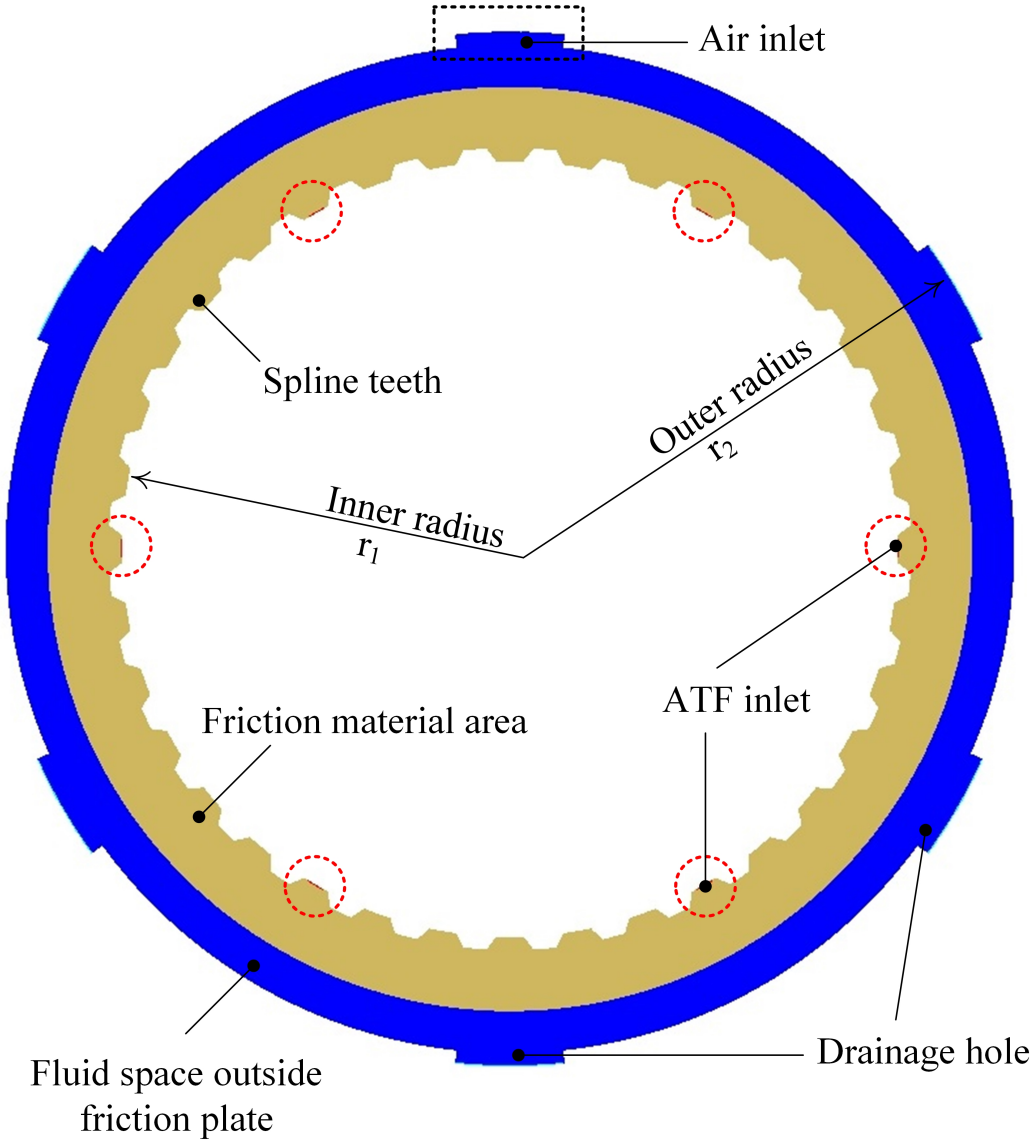

Figure 3.9: The computational domain for two-phase model

assumption is found to improve the stability of the fluid velocity in the simulation. A structured mesh of hexahedral cells is selected and generated in order to improve the numerical accuracy. The complete mesh contains more than four million hexahedral cells. A part of the mesh and a typical hexahedral grid is shown in Figure 3.10.

The flow is modeled as a laminar, two-phase flow at room temperature (40 °C). A segregated solver is used to solve the governing equations sequentially. The VOF method is used to determine the interface between the ATF and air. Each cell is described by a phase fraction, α, defined as the percentage of the local fluid volume that each phase occupies. The equations for conservation of mass and linear momentum are then written as follows (*Behzadi et al.* (2004))

$$\frac{\partial \alpha_k \rho_k}{\partial t} + \nabla \cdot \left(\alpha_k \rho_k \boldsymbol{u}_k\right) = 0 \tag{3.21}$$

$$\alpha_k \rho_k \Big(\frac{\partial \boldsymbol{u}_k}{\partial t} + \boldsymbol{u}_k \cdot \nabla \boldsymbol{u}_k\Big) = -\alpha_k \nabla \rho_k + \nabla \cdot \alpha_k \boldsymbol{T}_k + \alpha_k \boldsymbol{f}_k \tag{3.22}$$

where ρ is the density of phase k, $\boldsymbol{u}$ is the corresponding velocity, p is the pressure, $\boldsymbol{T}$ is the stress tensor, and $\boldsymbol{f}$ is the sum of external forces. The phase fraction, α, is conserved and bounded. A sharp interface cannot be maintained if $\nabla \cdot \boldsymbol{U}\alpha_k$ is diffusive.

The discretization of the governing equations is shown below. It represents the steady-state conservation equation for a quantity ϕ, such as pressure, phase fraction and velocity components, in integral form for an arbitrary control volume V.

$$\oint \rho \phi \boldsymbol{u} \cdot d\boldsymbol{A} = \oint \Gamma_\phi \nabla \phi \cdot d\boldsymbol{A} + \oint_V S_\phi dV \tag{3.23}$$

where $\boldsymbol{A}$ is the surface area vector, Γ_ϕ is the diffusion coefficient for ϕ , and S_ϕ is the source term. At each iteration, the variable ϕ is calculated for each cell using an

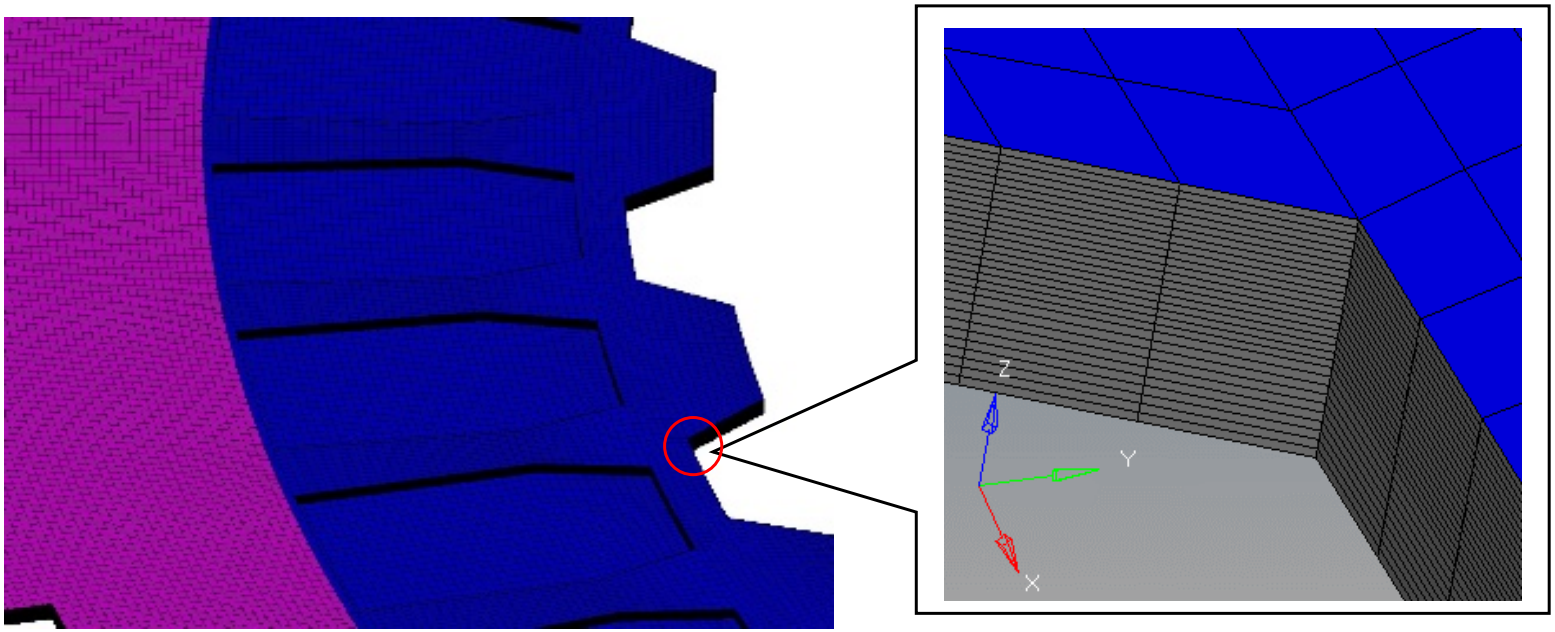

Figure 3.10: Mesh view and zoomed grid cell

adjustable parameter λ, which is commonly referred to as a relaxation factor, i.e.

$$\phi^{new,used} = \phi^{old} + \lambda(\phi^{new,predicted} - \phi^{old}) \tag{3.24}$$

where λ is the relaxation factor for pressure, which can also be applied to the VOF method and velocity. The relaxation factor is a constraint for adjusting a dependent or auxiliary variables from one solution to the next during the iteration process. The relaxation factor maintains the stability of the coupled, non-linear system of equations. If $\lambda < 1$, the process represents under-relaxation. The speed of convergence may be slow, but this increases the stability of the calculation. In contract $\lambda > 1$, results in over-relaxation. This may accelerate the convergence, but tends to decrease the stability of the calculation. For transient simulations, the governing equations must be discretized in both space and time. The spatial discretization for the time-dependent equations is identical to the steady-state case. Temporal discretization involves the integration of the differential equations using a time step Δt. The time step is determined by the Courant number

$$\boldsymbol{C}_r = \frac{u\Delta t}{\Delta x} \tag{3.25}$$

where u is the magnitude of the fluid velocity, Δt is the time step, and Δx is the cell size. When an explicit solver is used, the time step Δt is selected to keep the Courant number smaller than 1. A detailed discussion about selecting the appropriate time step is discussed in the next section.

The governing equations are discretized implicitly with respect to the velocity and pressure variables. A second-order, central-difference approximation is used to replace the derivatives in the momentum equation, i.e.

$$[\frac{\partial \phi}{\partial x}]_i^n = \frac{\phi_{i+1}^n - \phi_{i-1}^n}{2\Delta x} + O(\Delta x^2) \tag{3.26}$$

The Semi-Implicit Method for Pressure-Linked Equations (SIMPLE) algorithm is used to introduce the pressure field into the continuity equation to enforce mass conservation, and to determine the pressure field. The cell face value of the velocity is calculated through momentum-weighted averaging by introducing weighting factors. Then, the flux through each face of the cell, J_f, can be written as follows

$$J_f = \hat{J}_f + d_f\big(p_{c0} - p_{c1}\big) \tag{3.27}$$

where p_{c0} and p_{c1} are the pressures within the two cells on either side of the common face, and $\hat{J}_f$ contains the influence of the velocities in these cells. The term d_f is a function of the average of the momentum equation coefficients for the cells on either side of face f. Once a solution is obtained, the cell pressure and the face flux are corrected using

$$p = p^* + \lambda p' \tag{3.28}$$

where p^* is the initial pressure field, p' is the cell pressure correction, and λ is the relaxation factor for the pressure correction. In order to solve the above equations, phase fraction, density and viscosity relations are taken into consideration as follows

$$\frac{\partial \alpha_k}{\partial t} + \nabla \cdot \boldsymbol{U}\alpha_k = 0 \tag{3.29}$$

$$\rho = \sum_k \rho_k \alpha_k \qquad \mu = \sum_k \mu_k \alpha_k \tag{3.30}$$

where the density and viscosity of the mixture are linearly interpolated.

All the key model parameters are summarized in Table 3.1. For the grooved plate simulation, the MRF is applied. The interface between the moving and surrounding stationary volumes needs special treatment to satisfy the continuity equation.

Two-phase wet clutch simulations become difficult when the fluid is dispersed at a

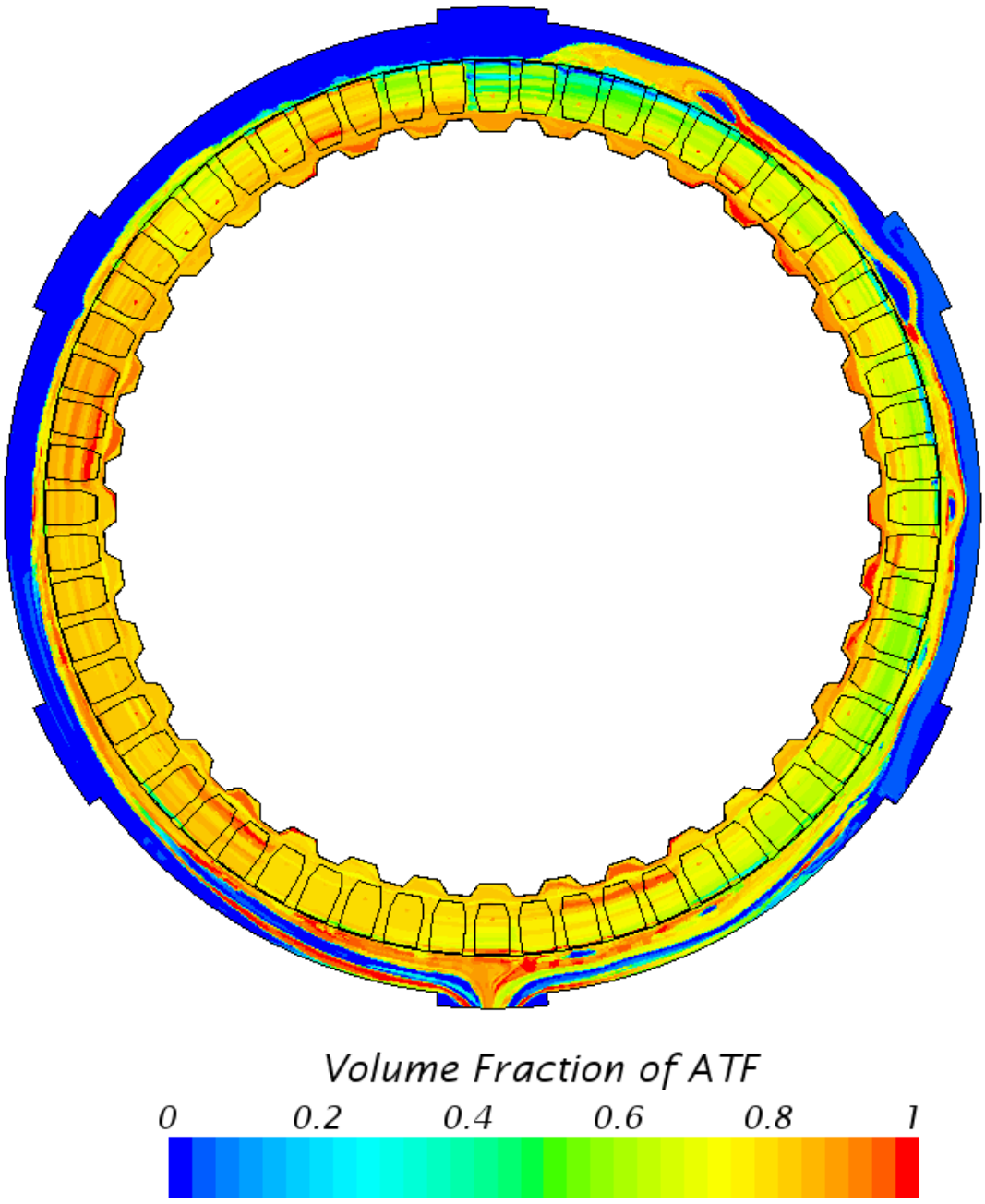

Figure 3.11: Phase fraction plot at 400 rpm

Table 3.1: Model setup parameters

Model parameters	**Value**
Clutch plate inner radius	92.4 mm
Clutch plate outer radius	104.3 mm
Outer structure inner radius	113.8 mm
Clearance	0.25 mm
Density of the ATF	828.6 kg/m^3
Dynamic viscosity of ATF oil	0.025 $Pa \cdot s$
ATF oil supply flow rate	0.2 L/min per interface
Cell layers across the interface	10

high rotational speed. A phase fraction contour plot is shown in Figure 3.11. It is not straightforward to choose an appropriate time step and mesh size to achieve numerical convergence and stability. In order to capture the flow pattern with a clearance of about 0.25 mm, the element size needs to be much smaller. The convergence behavior also depends on the boundary and initial conditions. A sensitivity study was conducted to identify the simulation parameters for both transient and steady-state solvers.

3.3.1 Time Step Investigation

An explicit integration scheme requires the Courant number, $\boldsymbol{C}_r$, to be smaller than 1 as the necessary condition for stability. In other words, the time step must be smaller than the time needed for a fluid particle to travel through a single cell. Thus, the faster the plate motion is, the smaller the time step must be. Figure 3.12 compares phase fraction contour plots from two simulations with different time steps. When the time step is 20 µs, $\boldsymbol{C}_r$ remains less than 1 for a rotational speed of 200

rpm. The simulation converges at each time step, and agrees well with the test data. The Courant number $\boldsymbol{C}_r$ becomes greater than 1 for a time step of 50 µs. Thus, a fluid particle can travel over multiple cells at each time step. The viscous terms in the momentum equation, and numerical dissipation added by the SIMPLE algorithm keep the numerical solution from catastrophic failure. However, the simulation produces non-accurate results and fails to conserve mass and momentum, although the phase fraction contour plot may appear reasonable at a first glance.

To further illustrate the effects of the time step size, simulation results based on 3 different values are shown in Figure 3.13. When the speed is 100 rpm, the results are the same regardless of the time step size. Note that the Courant numbers remain below 1 for all three time step sizes. As the rotational speed increases, the Courant number also increases according to Equation (3.25). The simulation with a 50 µs time step cannot produce the same results as 10 µs and 20 µs at 200 rpm, since the corresponding Courant number is larger than 1. As the rotating speed reaches 400 rpm, the corresponding Courant number for 20 µs becomes greater than 1, as illustrated in Figure 3.12. The results does not necessarily converge to the right solution. Therefore, as the speed keeps rising, a smaller time step should be chosen in the simulations. Since there is better guide for selecting the proper size of the time step, we use the Courant number as a criterion in order to ensure proper convergence in mass, momentum and phase fraction.

3.3.2 Boundary Conditions

The actual boundary conditions for a wet clutch pack is not clearly understood because of the difficulty in monitoring flow and pressure around clutch plates within a transmission system. Accordingly, various assumptions are employed for boundary conditions based on the clutch design geometry and assumed flow path. These consist of the description of flow properties such as flow rate, velocity and phase fraction,

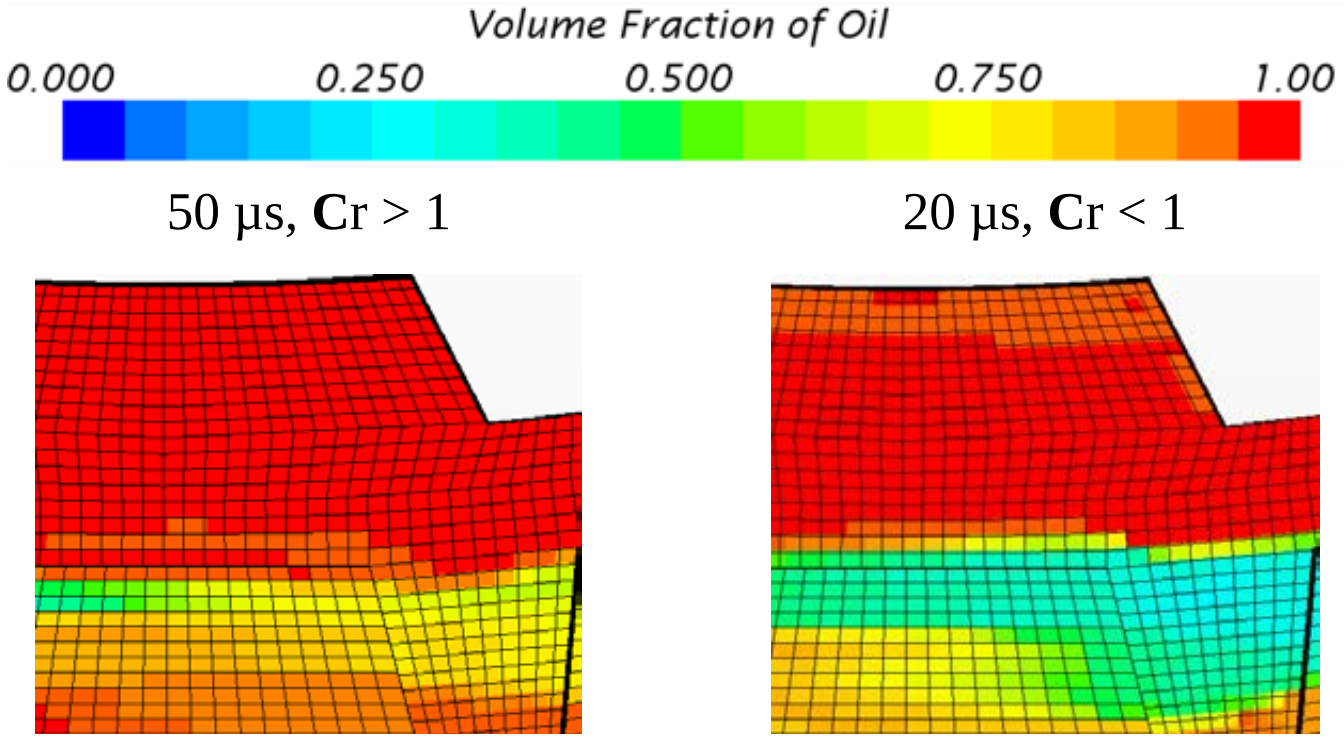

Figure 3.12: Phase fraction contour plot with different Courant number

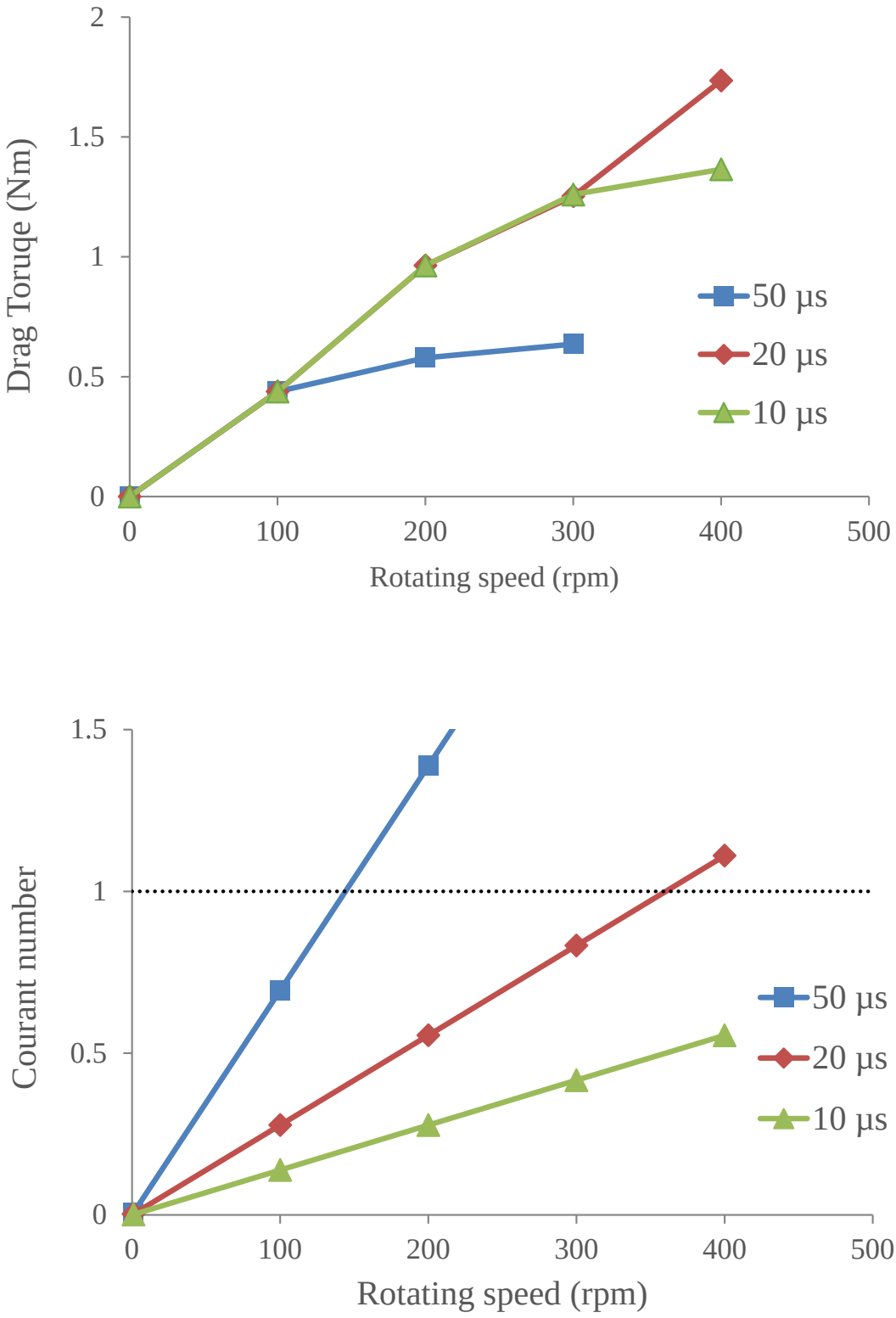

Figure 3.13: Effects of time steps on simulations

which is the volumetric percentage of the ATF within the mixture. At the inner radius illustrated in Figure 3.9, it is assumed that there is a continuous ATF supply. The phase fraction of the inlet flow is 1, and the velocity component satisfies the prescribed flow rate. At the air inlet, the phase fraction is 0, which means the boundary is open to the atmosphere. A mixture of ATF and air exits through the drainage holes. A Neumann boundary condition, specifically zero gradient, is used to prescribe the phase fraction or pressure boundary condition at the drainage holes.

Simplified simulations were conducted to assess the effects of boundary conditions as summarized in Table 3.2. Specifically, the rotating speeds are set to 0 for the clutch geometry in Figure 3.9. Six ATF inlet holes and four side drainage holes are closed in order to further simplify the geometry. Initially, the domain is full of the ATF with no air. As time elapses, the fluid within the domain drains due to gravity.

Table 3.2: Assessment of boundary conditions

Combinations	Boundaries	Velocity	Pressure	Phase fraction
(a)	Top air inlet	unspecified	Zero pressure	0
	Drainage hole	unspecified	Zero pressure	1
(b)	Top air inlet	unspecified	Zero pressure	0
	Drainage hole	unspecified	Zero gradient	1
(c)	Top air inlet	unspecified	Zero pressure	0
	Drainage hole	unspecified	Zero pressure	Zero gradient

In order to highlight the effect of the boundary conditions in the simulations, extra nodes, which are often referred to as ghost nodes, are added outside the physical

boundary, as shown in Figure 3.14(a). These ghost nodes are used to interpolate the boundary conditions. A zero-gradient phase fraction indicates that the difference between the ghost and boundary nodes is zero, which ensures uniform flow at the boundary. If there is a reversal of flow, its phase fraction is thus the same as the ghost cell flow. Figure 3.14(b) shows the simulation results after 1 second at the air inlet near the top, and the drainage hole at the bottom for the clutch geometry shown in Figure 3.9. The phase fraction and the pressure at the air inlet are set equal to 0. For the drainage holes at the bottom of the outer structure, the phase fraction and the pressure are given a zero gradient, and the flow is allowed to develop by itself during the simulation.

When the pressure boundary conditions at the bottom drainage hole is set to zero gradient, the time for the ATF to drain out completely is shorter than the time calculated from the analytical solution. This is due to the gradient boundary condition at the top of the domain. If zero phase fraction is applied at the boundary, the flow entering from the exit hole consists of pure air with a zero phase fraction, thus allowing the mixture to exit. This discontinuity results in the presence of air near the drainage hole, creating a non-physical situation as shown in Figure 3.14 (c).

3.3.3 Initial Conditions

When a transient solver is utilized for open clutch simulation, both results and convergence behaviors depend on the initial conditions. A number of simulations were conducted to evaluate the effects of the initial conditions. When the rotating speed is small, for example 100 rpm, simulations are relatively insensitive to the selection of initial conditions. However, when the rotating speed becomes higher, the simulation shows dependency on the initial phase fraction within the clutch interface.

Figure 3.15 shows the change of the phase fraction within the interface. When the initial phase fraction is less than 1, for example, 0.5, 0.6 and 0.7, the phase

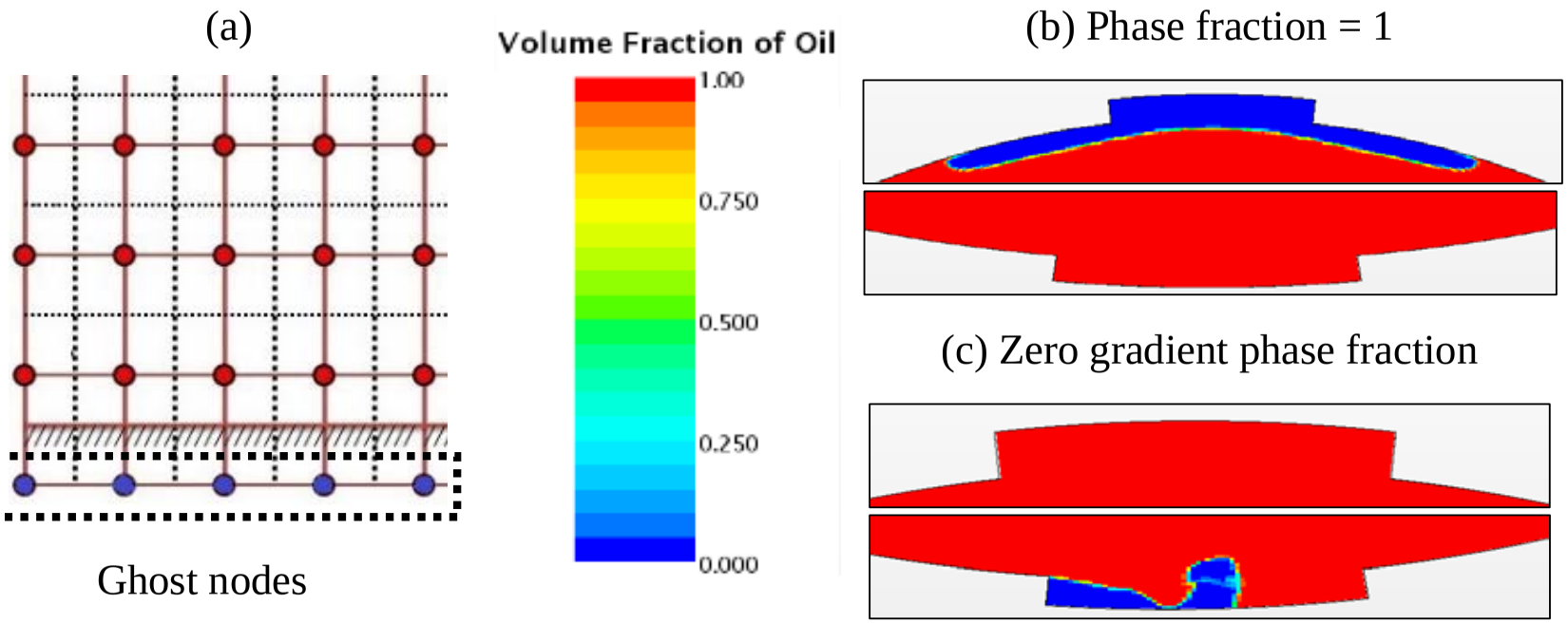

Figure 3.14: Effects of boundary conditions on simulations

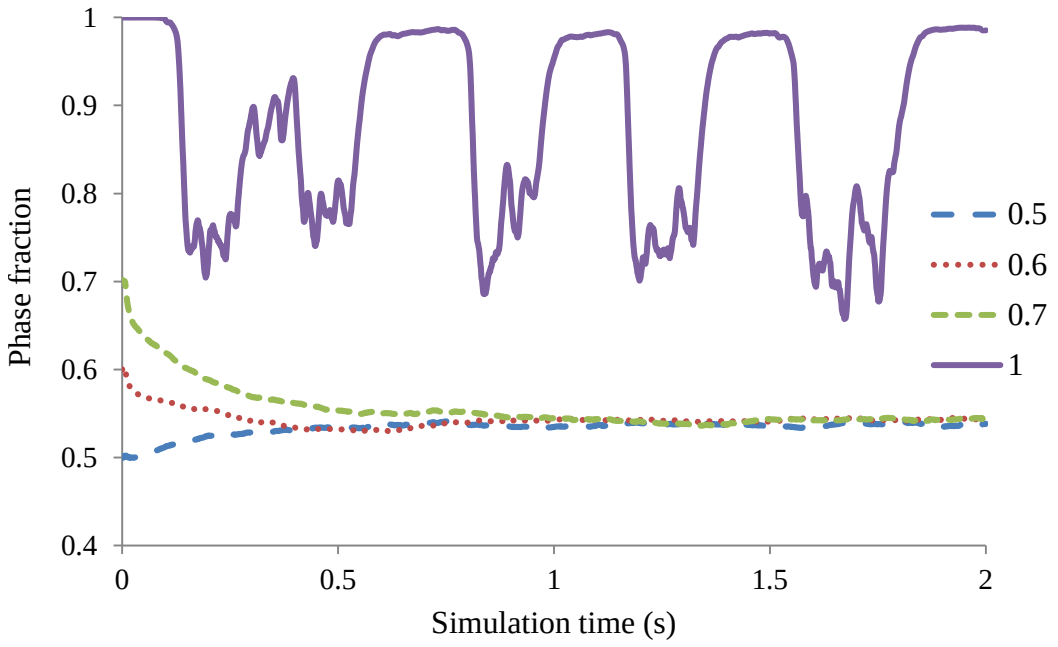

Figure 3.15: Assessment of initial conditions at 300 rpm

fraction converges to the same value in all three cases. However, when the initial phase fraction is set to 1, the results oscillate with no converged solution.

3.3.4 Assessment of Inner Iteration

For a transient solver, inner iterations are required at each time step to find a converged flow velocity and pressure field. For open clutch simulations, the time step can be in the order of 10^{-5} seconds. Thus, a large number of inner iterations significantly increases the computational cost. Three levels of inner iterations are investigated for the residuals after running the model for one second, and the residuals are shown in Figure 3.16.

Figure 3.16 shows the residual change within two time steps, and the jump on each curve indicates that the simulation enters a new time step. Using 5 inner iterations, convergence is achieved within a given time step. For 10 inner iterations, the computation further reduces the residuals while 20 inner iterations indicate a marginal

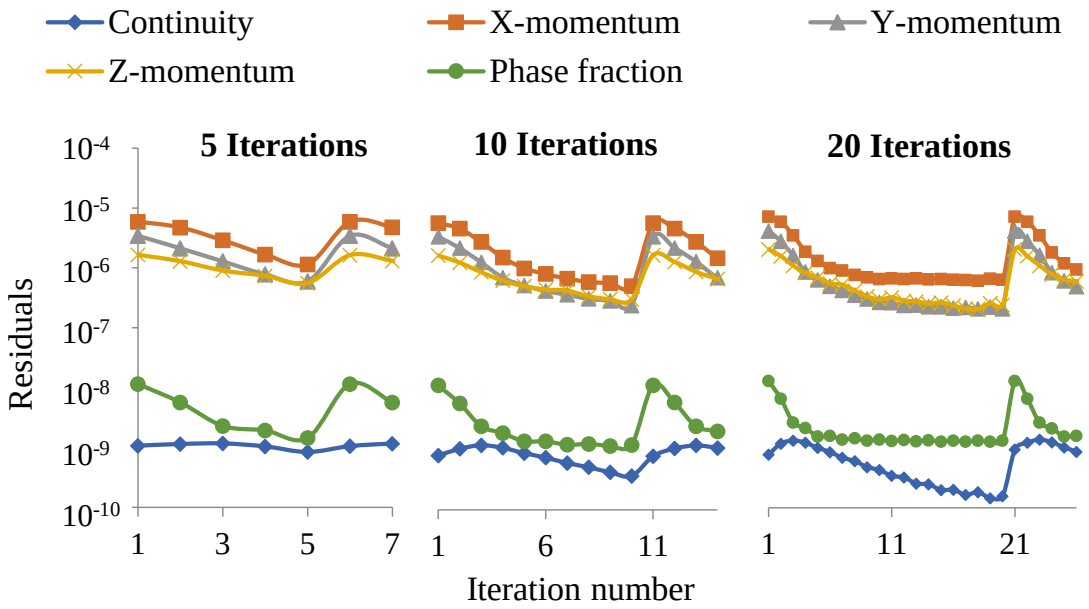

Figure 3.16: Assessment of inner iterations

improvement. For all simulations in this thesis, 10 inner iterations are used in order to achieve a balance of accuracy and computational efficiency.

3.3.5 Relaxation Factor Selection

The effects of the relaxation factors are examined through simulations. Most cases with over-relaxation factors lead to numerical instability. In particular, it becomes difficult to maintain mass and momentum balance when the phase fraction becomes smaller. Figure 3.17 shows the simulation results with different relaxation factors for the VOF method at different speeds. The smaller relaxation factors do not necessarily exhibit stable behaviors for 300 rpm cases. A relaxation factor of 0.6 or 0.7 provides the best behavior, achieving convergence after 10000 iterations. For higher speeds at 600 rpm, values of 0.5 and 0.6 provide smoother results.

Different relaxation factors would also have an effect on the behavior of the numerical solution. Figure 3.18 displays the comparison of phase fraction convergence behaviors for different pressure relaxation factors. The results are smooth and stable.

However, the examination of the mass balance between the inlet and outlet boundaries reveals significant differences, as summarized in Table 3.3. The values of 0.2, 0.3 and 0.4 can maintain the mass balance to a small difference. In other cases, the interface between the ATF and air phase becomes smeared. As a result, it becomes difficult to separate different phases and apply the corresponding physical properties. Mass conservation cannot be satisfied under this condition.

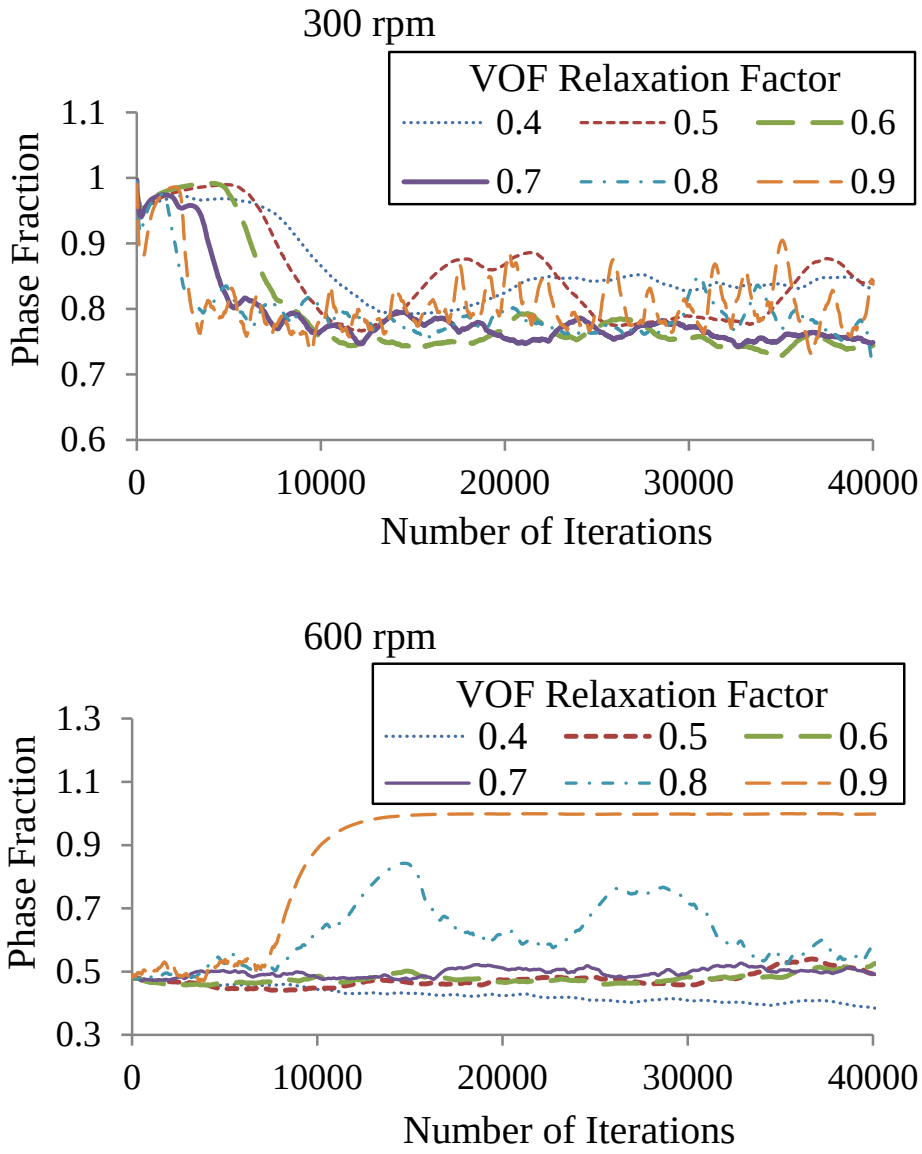

Figure 3.17: Assessment of VOF relaxation factors for shaped groove plate

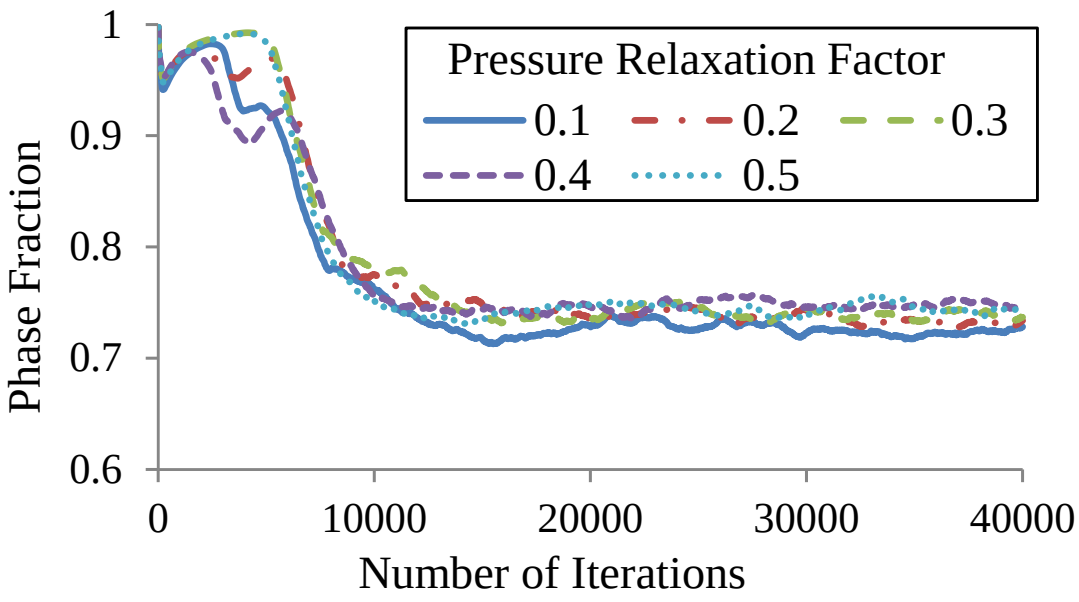

Figure 3.18: Assessment of pressure relaxation factors for shaped groove plate

Table 3.3: Effect of differential pressure relaxation factors

$\lambda_{pressure}$	Q_{in}(kg/s)	Q_{out}(kg/s)	ΔQ(kg/s)
0.1	2.76×10^{-3}	2.64×10^{-3}	1.21×10^{-4} (4.38 %)
0.2	2.76×10^{-3}	2.74×10^{-3}	1.89×10^{-5} (0.682 %)
0.3	2.76×10^{-3}	2.75×10^{-3}	1.25×10^{-5} (0.452 %)
0.4	2.76×10^{-3}	2.75×10^{-3}	1.29×10^{-5} (0.468 %)
0.5	2.76×10^{-3}	2.63×10^{-3}	1.27×10^{-4} (4.59 %)

The choice of relaxation factors can be different based on both plate geometry and flow conditions. Figure 3.19 shows a comparison of the results at 300 rpm with a radial groove pattern. In this case, a value of 0.5 provides a stable result, which is different from the shaped groove plate.

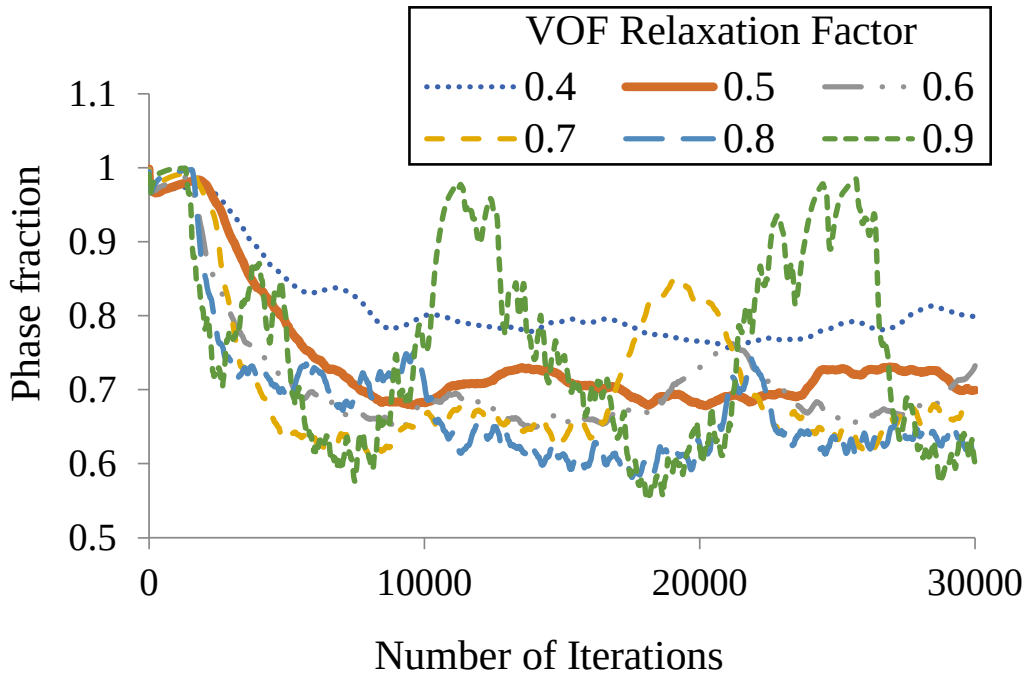

Figure 3.19: Assessment of VOF relaxation factors for radial groove plate at 300 rpm

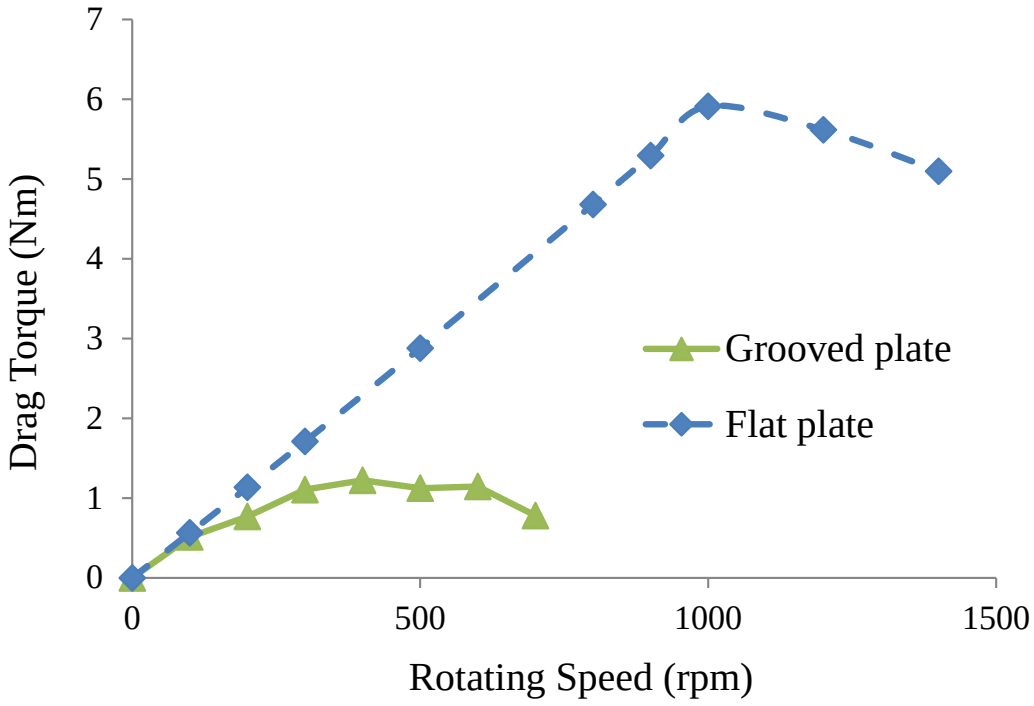

Figure 3.20: Simulation results for shaped grooved and flat plate

Figure 3.20 shows simulation results for a shaped grooved and a flat plate. The drag torque from the flat plate is much higher than that from the grooved plate, which is consistent with the real trend. Since the grooves provide additional conveyance for the ATF to exit from the clearance, the aeration would take place at a really small speed. The peak drag torque for a flat plate occurs at a higher speed, and the peak drag torque is higher than that of the grooved plate.

3.4 Experimental Study

3.4.1 Drag Test

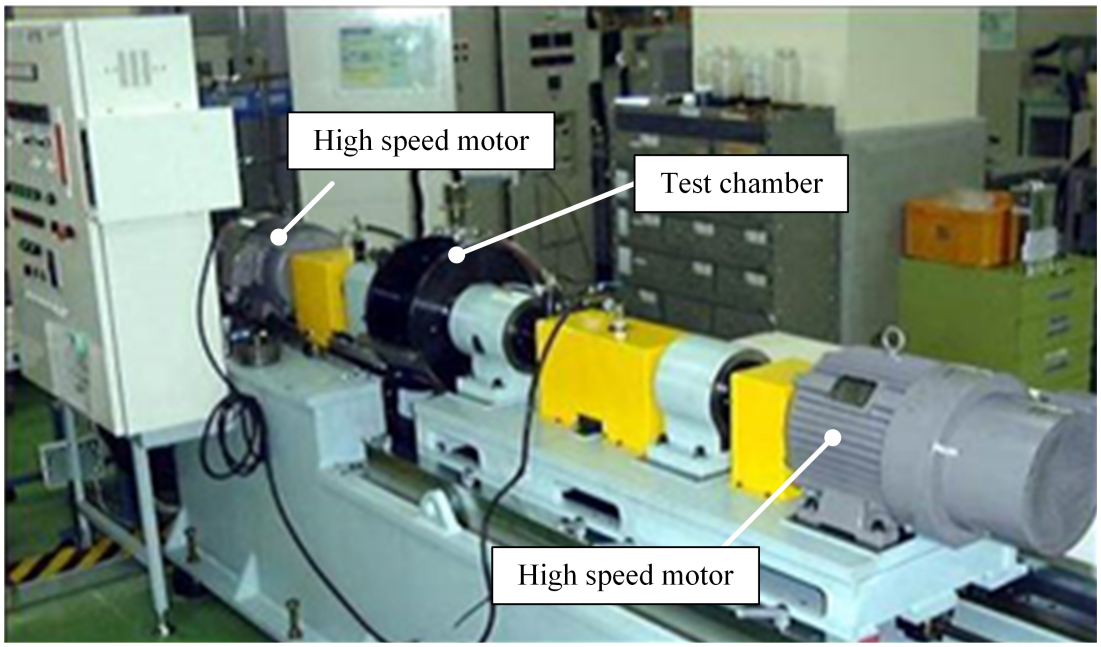

Figure 3.21: Clutch drag torque tester

Drag torque measurements were conducted on a clutch bench tester, shown in Figure 3.21, for validating the CFD model. A complete clutch pack, which includes 3 friction plates and 4 separator plates, is mounted in the test chamber. One of the motors spins the friction plates mounted on the hub, while separator plates remain stationary. A controlled amount of ATF is supplied through the center shaft into

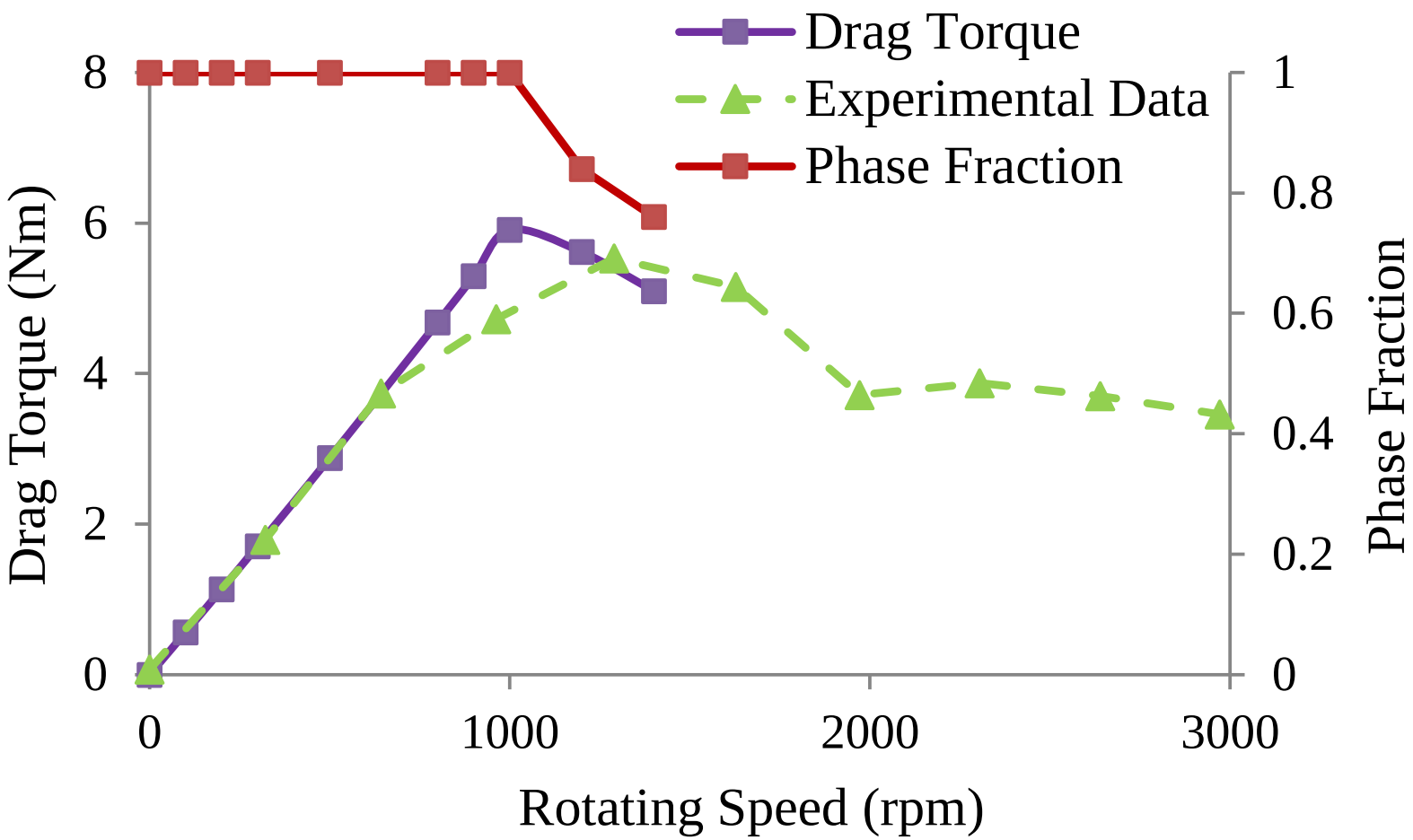

Figure 3.22: Simulation results vs. test data for flat plate

frictional interfaces.

Figure 3.22 shows the drag torque comparison between experimental data and simulation results for a flat friction plate with no grooves. The steady state solver is employed in the simulation. The simulation result for a single interface is multiplied by 6 to represent a total drag torque for a complete clutch pack assuming that all the interfaces between the plates are identical, i.e. generating the same drag torque, and the fluid temperature remains the same throughout the pack. The figure also shows the volumetric average phase fraction from the simulation. The agreement is good for regime (I) (illustrated in Figure 1.4) where an ATF film is maintained in the interface. The peak torque level and corresponding speed are in agreement within 1 Nm and 300 rpm, respectively. Though it is difficult to verify, it is considered that non-uniform distribution of plate positions within the pack and local heating of the ATF in the experimental set up contribute to the observed differences.

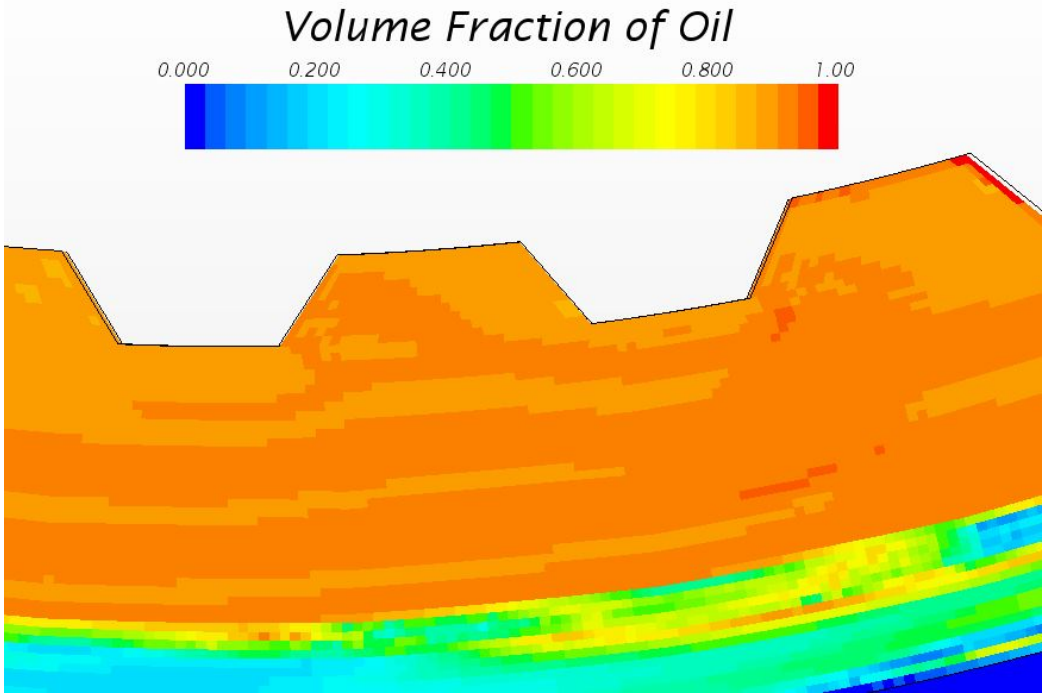

Figure 3.23: Phase fraction contour plot for flat plate simulation at 1400 rpm

When the slip speed becomes larger than 1400 rpm in the case corresponding to

regime (II), the flow pattern becomes complex and dispersed. It becomes increasingly difficult to achieve mass balance due to a non-converged phase fraction. Figure 3.23 shows the phase fraction contour plot at 1400 rpm. The phase fraction drops to 0 at the outer edge of the clutch plate, indicating the presence of air. A finer mesh or smaller time step can be selected to improve the convergence behavior at a higher computational effort.

Drag torque measurements for a shaped groove plate are shown in Figure 3.24. Compared to the flat plate, the flow pattern for a grooved plate is very different due to the presence of the grooves. Grooves provide additional channels for the ATF to move across the plate surface quickly, allowing air entrainment at a relatively low speed. Also, the grooves reduce the effective surface area of friction material where the ATF becomes sheared. Accordingly, the peak torque occurs at a lower speed, and its magnitude is much smaller than the peak torque for the flat plate. The CFD simulation not only captures the overall trend, but also provides a physical insight into the drag torque generation process. Specifically, drag torque is transmitted through fluid pressure acting on groove walls in addition to viscous shear over the friction material surface. In this thesis, the former is referred to as pressure torque, which does not exist for a non-grooved flat plate where the entire surface area is parallel to the rotational direction. Figure 3.25 shows the pressure torque and the viscous torque exerted on the friction plate (FP) and separator plate (SP), respectively. Due to the conservation of angular momentum, the drag torque on the flat separator plate is larger than that of the friction plate with grooves.

Figure 3.26 shows the pressure distribution within a groove at 500 rpm. The pressure on one side of the groove is much larger than the pressure on the other side due to fluid-structure interaction. Fluid recirculation takes place inside the groove due to the pressure difference, creating a complex flow pattern.

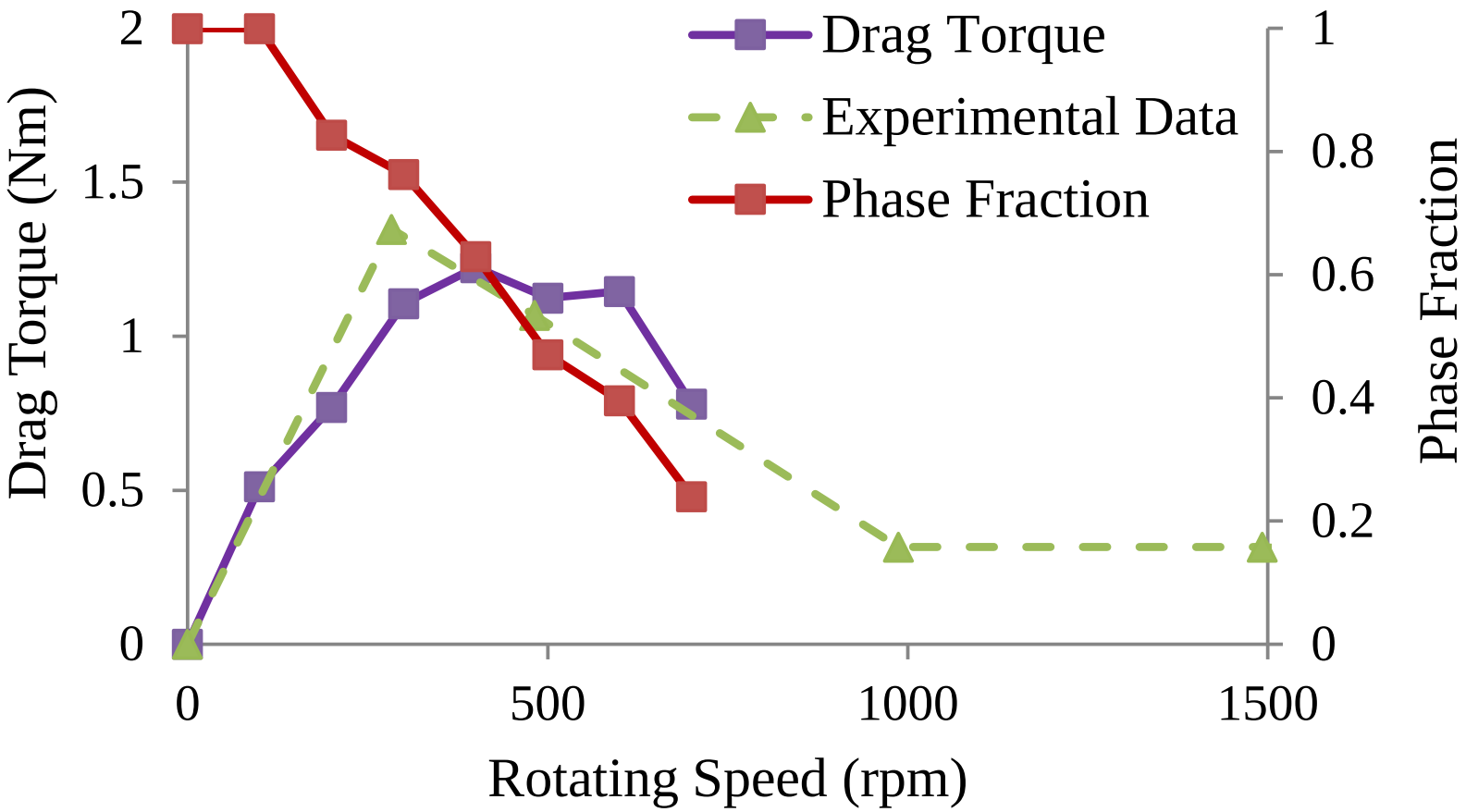

Figure 3.24: Simulation results vs. test data for groove plate

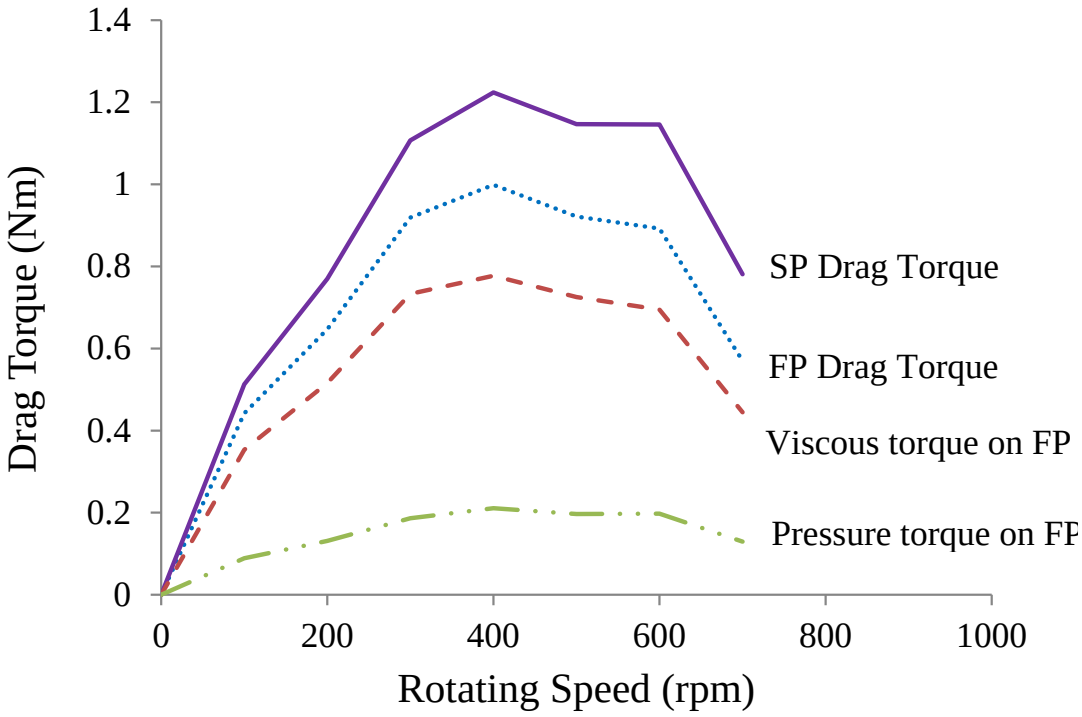

Figure 3.25: Viscous torque vs. pressure torque for grooved clutch plate

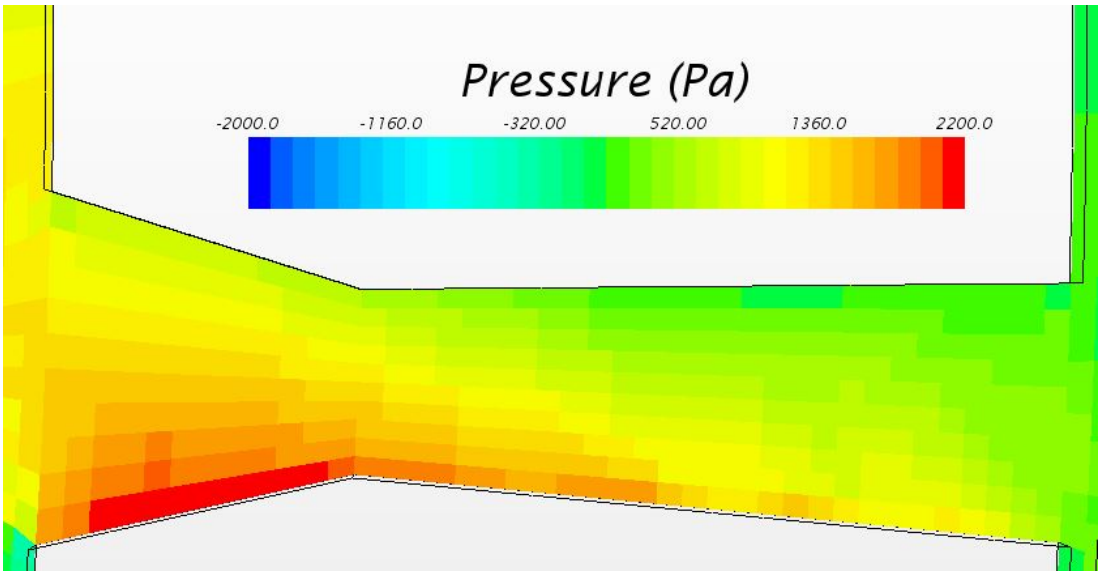

Figure 3.26: Pressure contour plot in the groove at 500 rpm

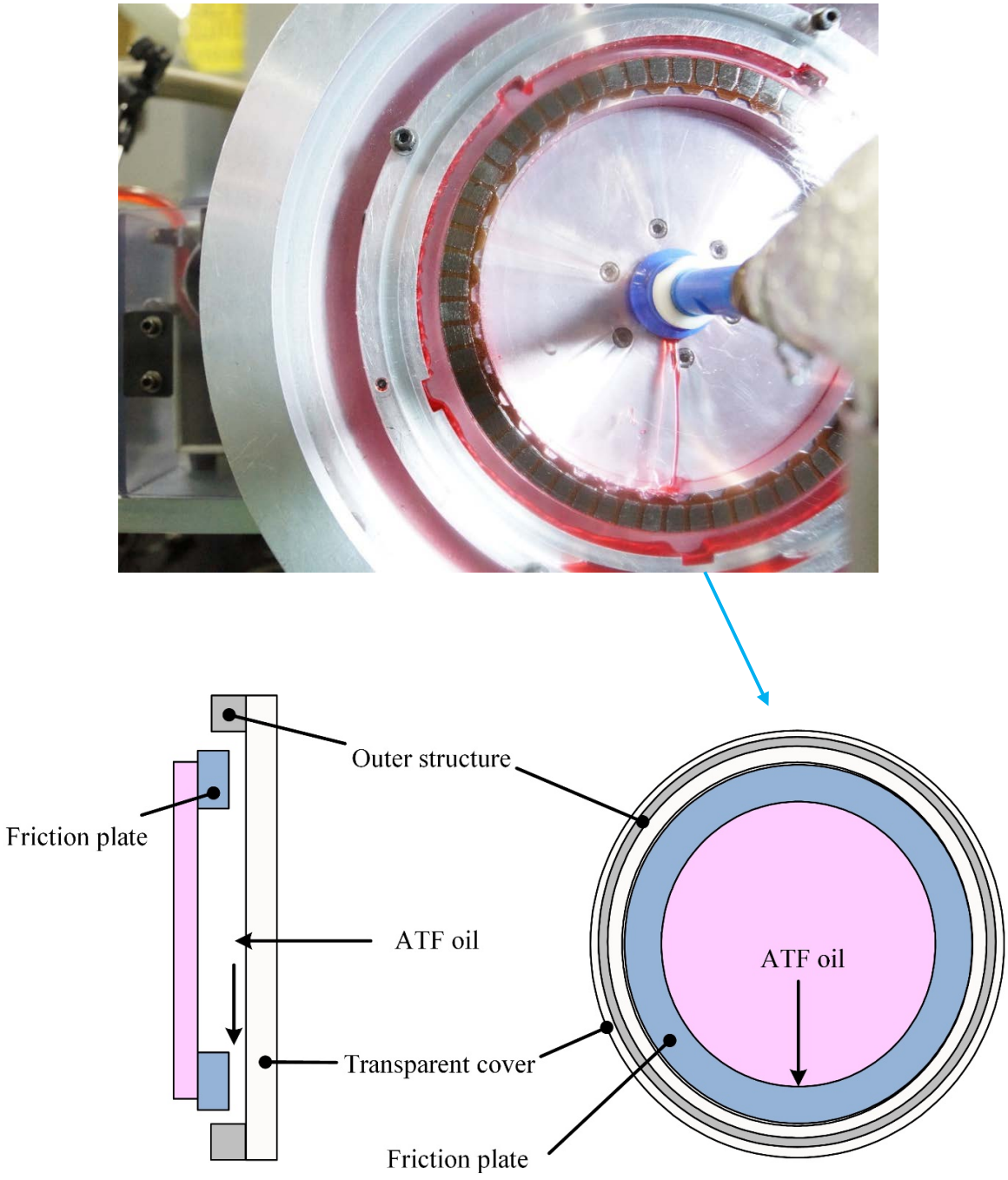

Figure 3.27: Photo and schematic drawing of visualization test stand

3.4.2 Visualization Test

The visualization test fixture in Figure 3.27 is utilized to observe the air-fluid behavior at the clutch frictional interface as a function of rotational speed. A clutch plate is mounted on a hub which is connected to an electric motor. The ATF flows out from a tube at the center of the test head to the frictional interface. As the plate rotates, the ATF is distributed and covers the entire surface where air-ATF flow patterns are observed through a transparent cover. The cover has the same function as the separator plate in a real transmission. Because of gravity, after lubricating the whole plate surface, the oil flows downward, and exits through the drainage hole at the bottom before returning to the oil pump. There is an outer structure outside of the clutch plates, which simulates the effect of the transmission housing, and creates realistic flow conditions around the clutch plate sample. The outer structure is screwed to the transparent front cover plate of the visualization test stand. A high speed camera is used to capture the fluid behavior and interface conditions during the tests. The setting of the visualization test is summarized in Table 3.4.

Table 3.4: Visualization test setup

Input data	**Value**
Clutch friction material inner radius	50.9 mm
Clutch friction material outer radius	60.5 mm
Clearance per plate	0.2 mm
Density of ATF oil	$828.6\,\mathrm{kg/m^3}$
Dynamic viscosity of ATF oil	$0.025\,\mathrm{Pa \cdot s}$
ATF oil supply flow rate	80 cc/min per interface
Number of clutch plate	1

Table 3.5 shows the comparison of the images from the high speed camera and

corresponding simulation results as a function of slipping speeds. At 200 rpm, a large air bubble appears within the groove. This is because the grooves provide a large flow area as compared to the friction material surface, promoting air entrainment. As the rotating speed increases from 200 rpm to 400 rpm, air bubbles break up and become dispersed inside the grooves. The dispersed air spreads to the friction material surfaces as the rotating speed further increases. At 700 rpm, air appears as streaks, covering the entire friction plate surface. A phase fraction value is estimated from the image at each speed based on the surface area fraction covered by the ATF, as indicated in Table 3.5. The CFD simulation results corresponding to each speed condition capture the way air is spreading over the surface as a function of rotational speed. In the simulations, phase fractions are presented as a volumetric average of the ATF within the whole interface, instead of surface area covered by the ATF. Though the definition is different, the phase fractions agree well between simulations and image analyses, demonstrating a satisfactory performance by the CFD model.

Table 3.5: Comparison between visualization test and CFD simulations

Speed	Photos from visualization test	Contour plots from simulation
	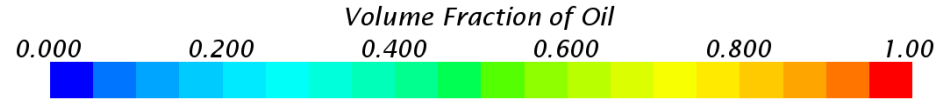	
200 rpm	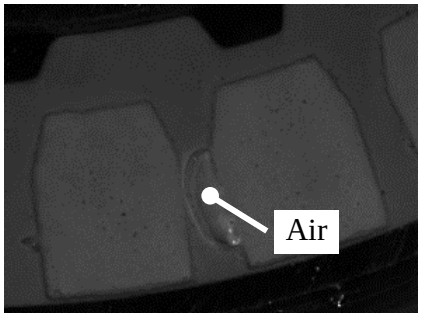	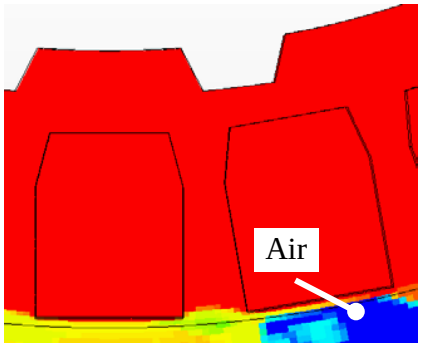
Phase fraction	0.97	0.99
300 rpm	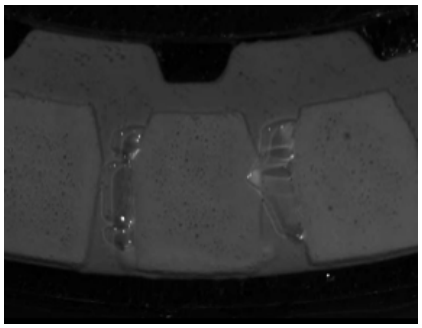	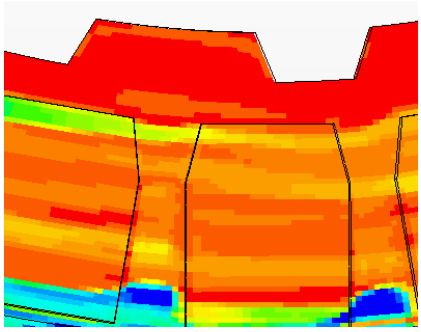
Phase fraction	0.91	0.92
400 rpm	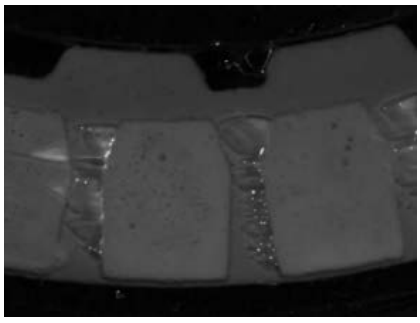	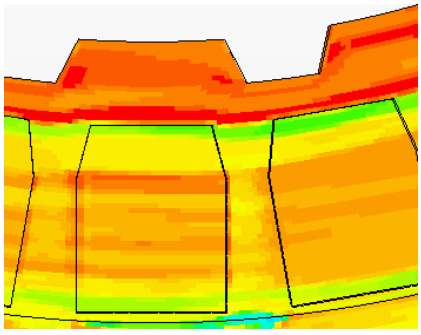
Phase fraction	0.87	0.85

Speed	Photos from visualization test	Contour plots from simulation
		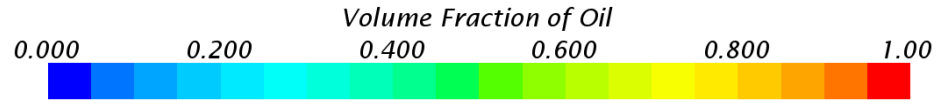
500 rpm	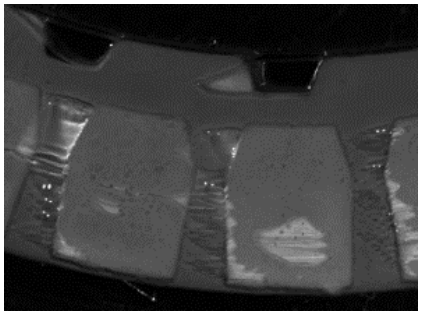	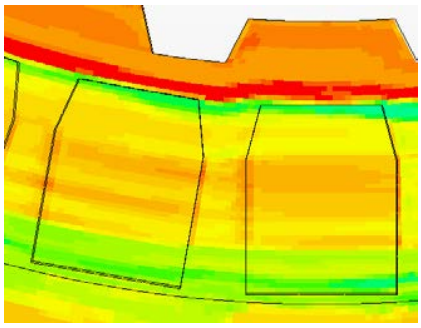
Phase fraction	0.77	0.80
700 rpm	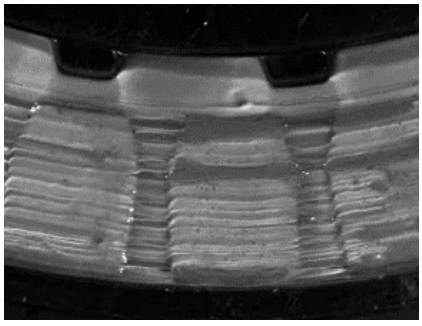	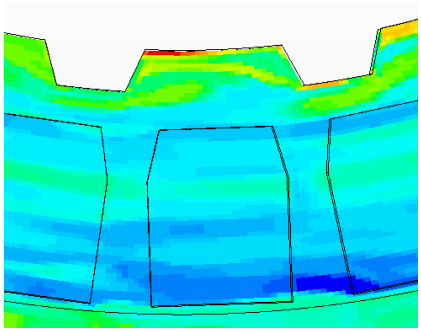
Phase fraction	0.63	0.57

CHAPTER IV

Statistical Modeling of Clearance Distribution

Among all design factors, clearance is one of the most important features that affect the drag torque. In the previous chapter, one of the basic assumptions was that the plates are uniformly distributed within the clutch pack. In reality, however, the clutch plates continuously move back and forth in the axial direction. Given the same total clearance, the distribution of the gaps can be different at any time, affecting the drag torque behavior. In this chapter, a statistical method is developed for modeling the distribution of the plates in a clutch pack. The proposed method employs order statistics to represent dynamically-changing plate positions. A simulation study is conducted to investigate the effects of plate movement on open clutch drag in the slip region where ATF is present at the interface. It is shown that the model can predict the difference in drag torque with or without fixed clutch plates. The simulation results compare satisfactorily with experimental data.

Figure 4.1 shows the experimental observation of drag torque behavior with free or fixed separator plates. For the free separator plate case, the plate can move freely in the axial direction. For the fixed separator plate case, which is shown schematically in Figure 4.2, the distance between the separator plates is fixed by spacers. In Figure 4.1, the peak drag torque from the fixed separator plates is considerably smaller than that from the free separator plates. Limiting the movement of separator plates

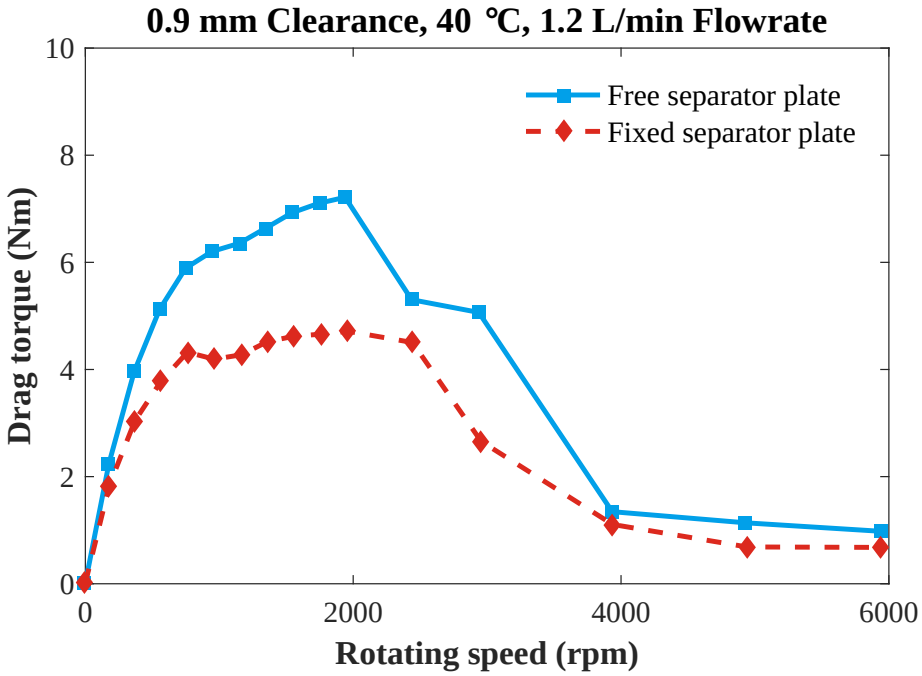

Figure 4.1: Drag torque curve for free and fixed separator plates cases

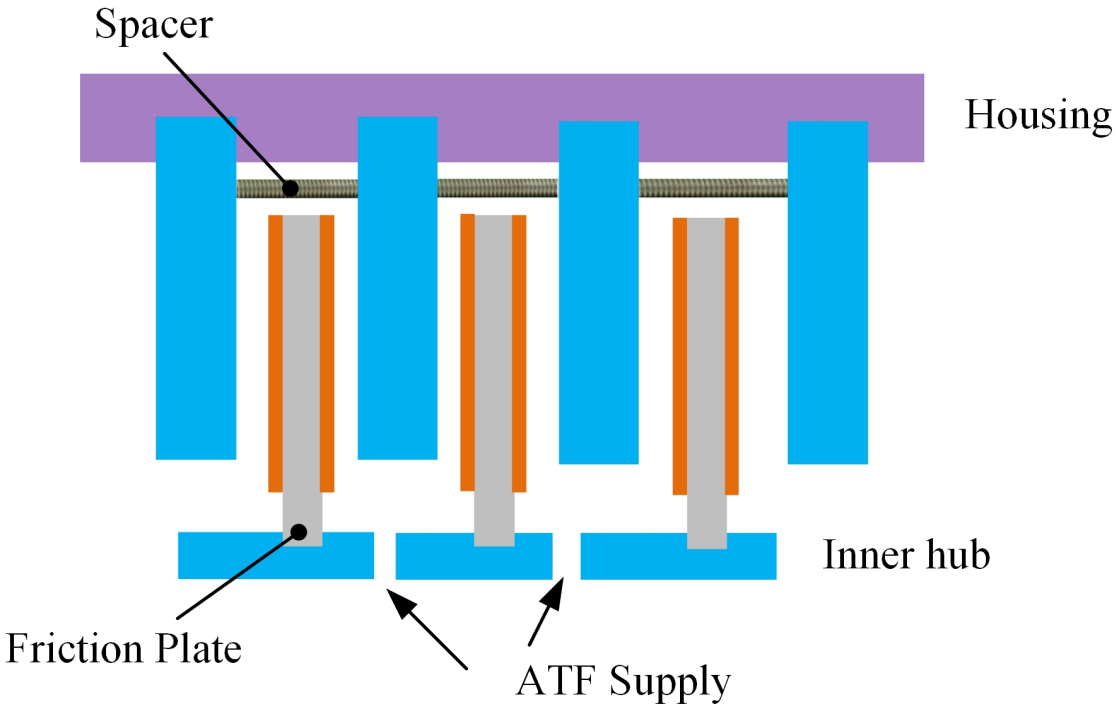

Figure 4.2: Fixed separator plates with spacer

without changing the total clearance results in an overall drag torque reduction. This phenomenon has been widely recognized by the automotive industry for years without a firm theoretical understanding. In this section, a statistical method is employed, coupled with a viscous flow clutch model, to provide analytical insight into a complex interaction between plate movement and fluid behavior.

In this section, the focus is placed on the small rotating speed range where the flow in the interface is considered to be single phase. A statistical method is introduced to account for varying clutch plate positions, coupled with a simple viscous drag model described by Equation (3.17). However, the proposed statistical method can be extended to higher speed ranges with the inclusion of a suitable drag torque model. For example, at higher speeds, the proposed statistical method can be coupled with the previous two-phase CFD model to calculate the drag torque numerically.

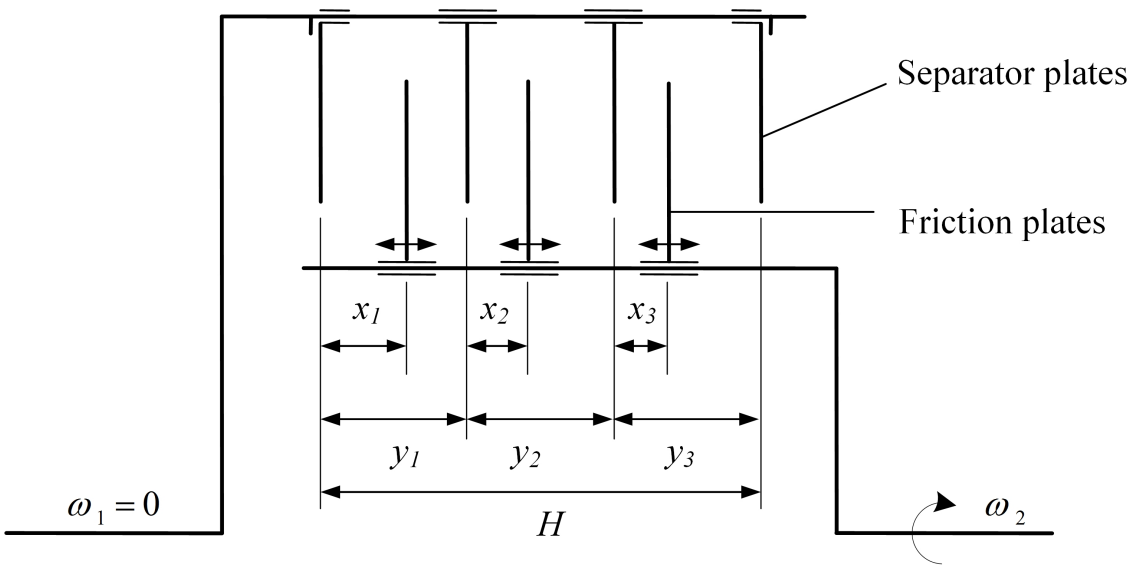

Figure 4.3: Clutch pack modeling geometry

The statistical model of non-uniform clearance distribution between the plates in a clutch pack is developed for the geometry shown in Figure 4.3. There are three friction plates and four separator plates. To simplify the model, the plates are as assumed

to have zero thickness. The fluid flowing between the clutch plates is assumed to be of single-phase and isothermal. The separator plates are assumed to be stationary, and friction plates rotate at a constant speed, ω_2. The total clutch clearance is H. Individual clearances are randomly generated, following a particular probability density function (PDF), such that the sum of these random numbers is equal to the total clearance H.

4.1 Random Number Generation Method

Once the individual clearances are available, the analytical solution can be applied to calculate the drag torque for each interface separately. Thus, the total drag torque for the clutch pack is the sum of the drag torques for all the clutch interfaces. The physical properties of the clutch plates and ATF are summarized in Table 4.1.

Table 4.1: Summary of physical parameters

Rotating speed	1000 rpm
Kinematic viscosity of ATF	7.48×10^{-3} kg/(m· s)
Friction lining outer radius	104.3 mm
Friction lining inner radius	92.4 mm

The fundamental assumption in this analysis is that the clearance is represented with a beta distribution. Its probability density function is shown below (*Ross* (2014), *Norman et al.* (1994))

$$f(x_1) = \frac{(x-a)^{p-1}(c-x)^{q-1}}{(c-a)^{p+q-1}B(p,q)} \tag{4.1}$$

where p and q are shape parameters, such that p & $q > 0$. The parameters a and

c represent lower and upper bounds for individual clearances, such that $a \leq x \leq c$. $B(p, q)$ is a normalization constant which ensures that the total probability integrates to 1. The reasons for choosing the beta distribution are:

1. The beta distribution is continuous and bounded. This is consistent with the actual distribution for clutch clearances.

2. The beta distribution requires only two shape parameters to generate a PDF that is suitable for representing clutch clearances.

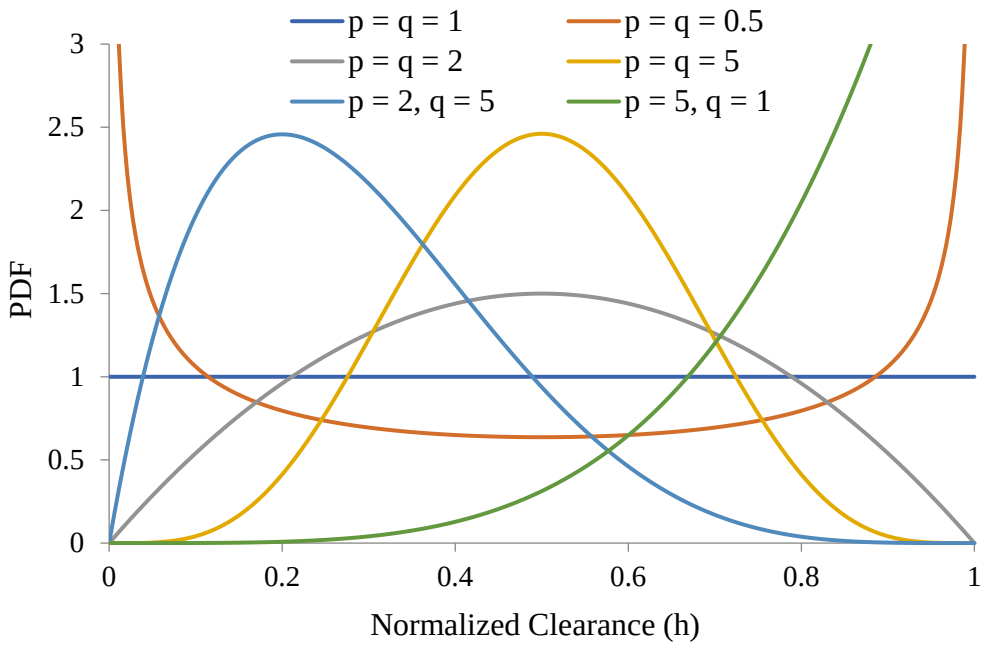

Figure 4.4: Beta distribution with different shape parameters

Figure 4.4 shows several beta distributions with different shape parameters. The clearance has been normalized by the total pack clearance. The normalized clearance can assume any value between zero and one. Figure 4.4 illustrates that when $p = q$, the distribution is symmetric. Otherwise, the shape is skewed. If $p = q = 1$, the beta distribution becomes identical to the uniform distribution. As the shape parameters become larger, the shape of the beta distribution becomes taller and

thinner, which describes a plate movement within a narrower range. As $p = q \to \infty$, the beta distribution becomes the Dirac delta function anchored at the mid-point of the distribution with a probability equal to 1. In this case, all the plates in the clutch pack are uniformly distributed.

After the shape parameters are determined, the gaps can be numerically generated. Approximately one million random numbers (gaps) were generated for each distribution in this study.

4.1.1 Single Gap Analysis

For single gap analysis, two sets of distributions are numerically generated: the first set consists of gaps varying between 0 and 1 mm, and the second one of gaps varying between 0 and 0.5 mm. The drag torque value is calculated by Equation (3.17). The gap statistics are summarized in Figures 4.5 and 4.6 with the analytical PDF curve, which is shown as a solid line. Both Figure 4.5 and 4.6 show that the shape of the distribution closely follows the analytical curve.

When generating gaps between 0 and 0.5 mm, the probability of a gap larger than 0.5 mm is zero, which is shown in Figure 4.6. In both cases, the relative frequency is calculated from the statistical data of the one million random gaps. The average gap and drag torque values are summarized in Table 4.2. The first column corresponds to the range of each gap, and the second column shows the type of beta distribution that was used to generate the random numbers. The third column lists the average value of one million gaps, and the fourth column is the average drag torque from one million gaps. Table 4.2 shows that the average drag torque is distinct for different distributions, i.e. sensitive to plate movement patterns. When the shape parameter is small, the distribution is symmetric and similar to that of a uniform distribution. The plate can move freely without constraint, and there is a high probability to achieve a small gap. The drag torque from this small gap leads to a large average

Distribution	Average Clearance	Relative Frequency
$\alpha = \beta = 1.01$	0.5 mm	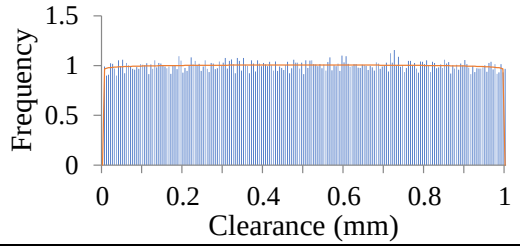
$\alpha = \beta = 2$	0.5 mm	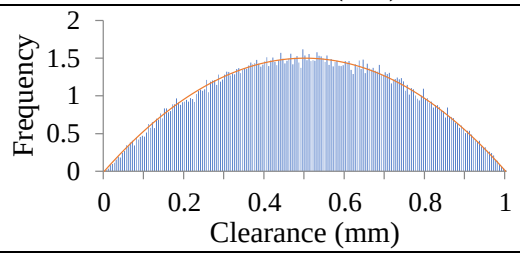
$\alpha = \beta = 5$	0.5 mm	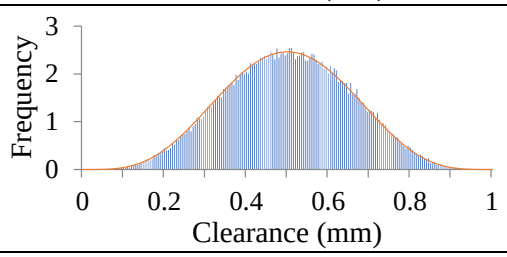
$\alpha = 2, \beta = 6$	0.25 mm	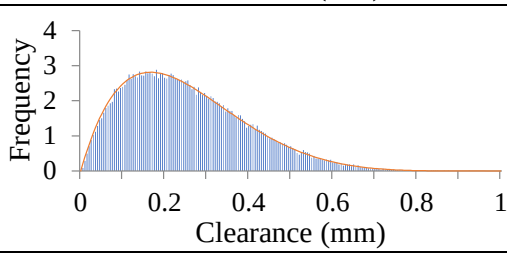
$\alpha = 6, \beta = 2$	0.75 mm	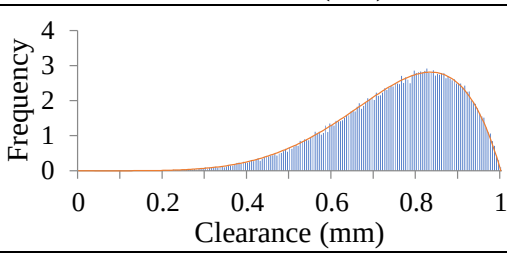
Double Peak	0.5 mm	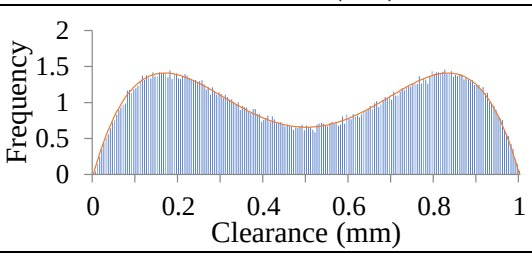

Figure 4.5: Gap statistics for a single gap with 1.0 mm clearance

Distribution	Average Clearance	Relative Frequency
$\alpha = \beta = 1.01$	0.25 mm	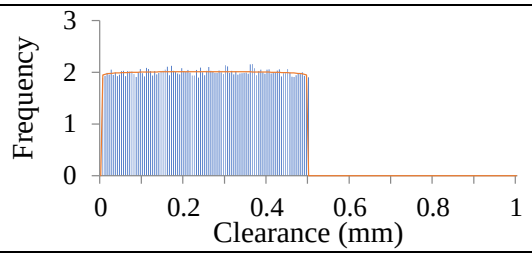
$\alpha = \beta = 2$	0.25 mm	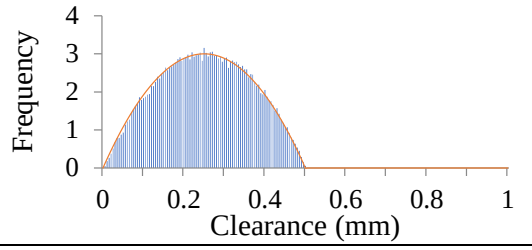
$\alpha = \beta = 5$	0.25 mm	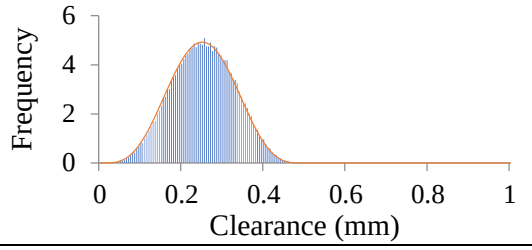
$\alpha = 2, \beta = 6$	0.125 mm	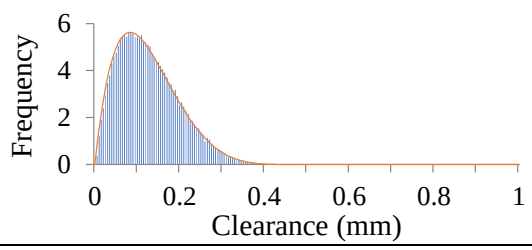
$\alpha = 6, \beta = 2$	0.375 mm	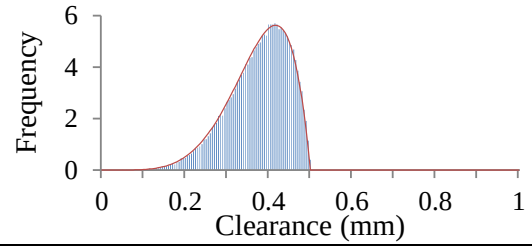
Double Peak	0.25 mm	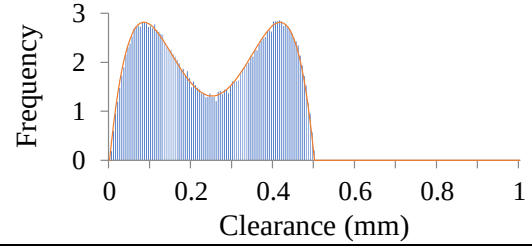

Figure 4.6: Gap statistics for a single gap with 0.5 mm clearance

drag torque. When the shape parameter becomes large, the distribution is narrower, thus the plate moves within a relatively limited range. The probability to achieve a small gap becomes lower, and the average drag torque becomes smaller. For the same distribution, a smaller gap leads to a larger drag torque, and this trend agrees with the analytical drag torque equation since the drag torque is inversely proportional to the clearance.

Table 4.2: Effects of gap distribution on drag torque

Clearance		Avg. Gap (mm)	Torque (Nm)
0 - 0.5 mm	$\alpha = \beta = 1.01$	0.250	7.54
	$\alpha = \beta = 2$	0.250	1.14
	$\alpha = \beta = 5$	0.250	0.862
	$\alpha = 2, \beta = 6$	0.125	2.66
	$\alpha = 6, \beta = 2$	0.375	0.536
	Double Peak	0.250	1.60
0 - 1.0 mm	$\alpha = \beta = 1.01$	0.500	3.77
	$\alpha = \beta = 2$	0.500	0.571
	$\alpha = \beta = 5$	0.500	0.431
	$\alpha = 2, \beta = 6$	0.250	1.33
	$\alpha = 6, \beta = 2$	0.750	0.268
	Double Peak	0.500	0.798

Distribution	First Gap	Second Gap	Total
$\alpha = \beta = 1.01$	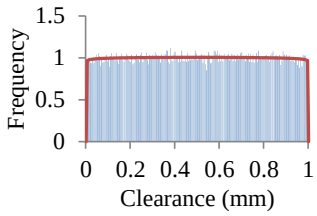	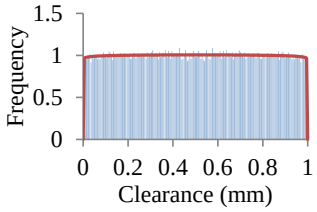	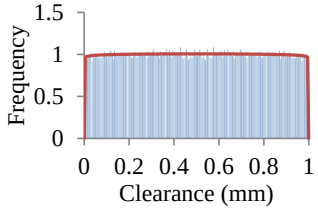
$\alpha = \beta = 2$	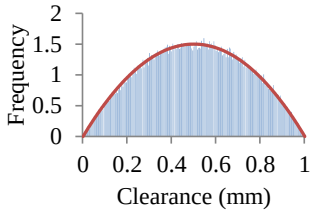	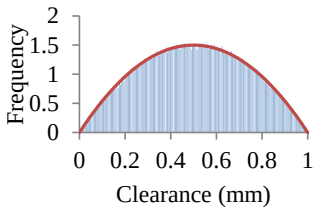	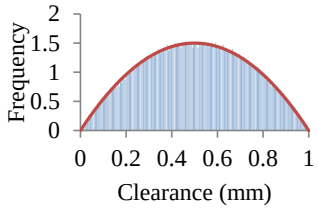
$\alpha = \beta = 5$	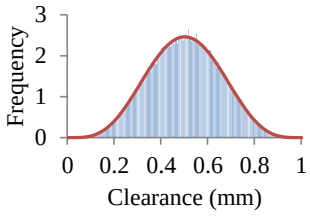	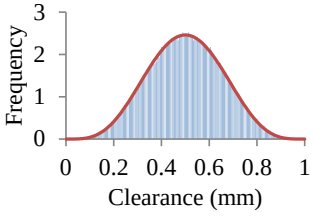	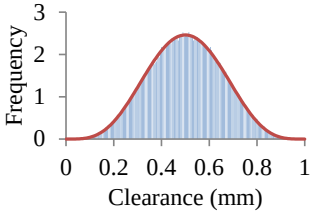
$\alpha = 2, \beta = 6$	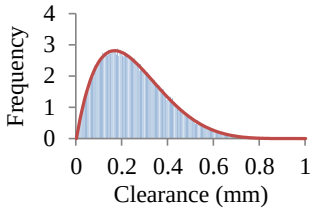	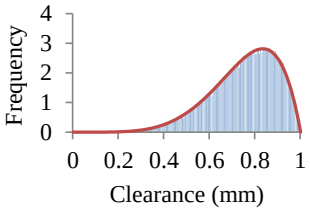	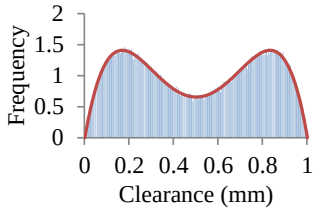
$\alpha = 6, \beta = 2$	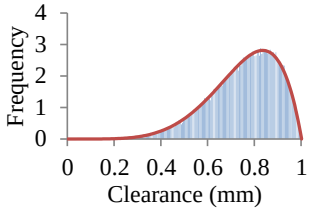	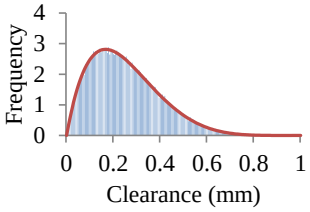	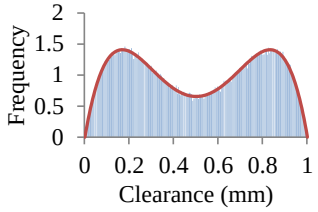
Double peak	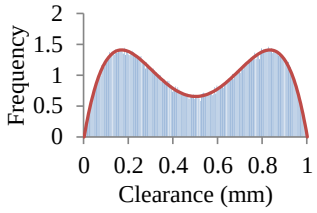	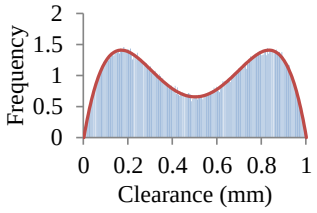	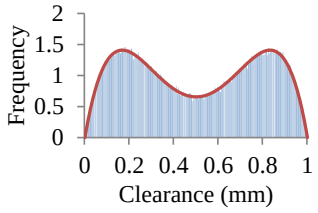

Figure 4.7: Gap statistics for two gaps with 1.0 mm clearance

4.1.2 Two Gaps Analysis

For fixed separator plate cases, the configurations for fixed separator plate is the same with that shown in Figure 4.3. In this case, the separator plates are constrained by space screws, such that the distances between the separator plates are identical, i.e. $y_1 = y_2 = y_3 = H/3$. The three friction plates follow the same analysis. The two gaps between two adjacent separator plates are taken into consideration. The friction plate can move axially between their neighboring separator plates, and the statistical variables x_i can each take any values between 0 and y_i. For a particular value of x_i for the first gap, the second gap would be $y_i - x_i$. The first and second gaps are generated simultaneously, and approximately two million random numbers (gaps) were generated for each gap for each different distribution. The first, second

Table 4.3: Gap distribution effects on drag torque for fixed separator plates

Clearance		Avg. Gap (mm)	Total Torque (Nm)
0 - 0.5 mm	$\alpha = \beta = 1.01$	0.250	8.95
	$\alpha = \beta = 2$	0.250	2.29
	$\alpha = \beta = 5$	0.250	1.73
	$\alpha = 2, \beta = 6$	0.250	3.19
	$\alpha = 6, \beta = 2$	0.250	3.20
	Double Peak	0.250	3.20
0 - 1.0 mm	$\alpha = \beta = 1.01$	0.500	4.47
	$\alpha = \beta = 2$	0.500	1.15
	$\alpha = \beta = 5$	0.500	0.862
	$\alpha = 2, \beta = 6$	0.500	1.60
	$\alpha = 6, \beta = 2$	0.500	1.60
	Double Peak	0.500	1.60

and total gaps are summarized separately, and the statistics are shown in Figure 4.7.

In Figure 4.7, the gap statistics are summarized together with the analytical PDF curve. For symmetric distributions, the statistics for the first and second gap are the same, indicating that these two adjacent gaps follow the same distribution. Two sets of distributions are generated with different upper bounds: 0.5 mm and 1.0 mm. The drag torque value is calculated by the analytical solution, which is Equation (3.17). The average gap and drag torque values are summarized in Table 4.3. The drag torque is the total drag torque from two gaps. Compared with the drag torques obtained from single gap showing in Table 4.2, the drag torque is larger. For $\alpha = 2 \,\&\, \beta = 6$, $\alpha = 6 \,\&\, \beta = 2$ and the double peak cases, since the behavior for total gaps are the same, the average gap and average torque values are almost identical.

4.1.3 Clutch Pack Analysis

In this section, the focus is placed on the behavior of the whole clutch pack. The same clutch pack configuration is assumed, as shown in Figure 4.3. For the fixed separator plate case, the two adjacent gaps can follow the same distribution. However, for the clutch pack, the gaps may not follow the same distribution, and a new method based on order statistics (*Ross* (2014), *Norman et al.* (1994)) is used to generate all the gaps independently.

Let $X_1, X_2, \cdots, X_n$ be random variables. Let $X_{(1)}$ denote the smallest of the X_s. $X_{(2)}$ is the next smallest, and so on, such that

$$X_{(1)} \leq X_{(2)} \leq \cdots \leq X_{(n)}$$

This relabeling of the X_i corresponds to arranging them in increasing order, as shown in Figure 4.8 for one particular ordering of five values $X_1, X_2, \cdots, X_5$.

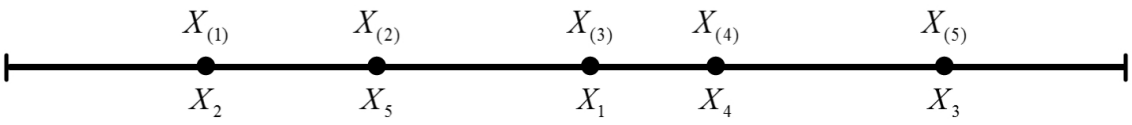

Figure 4.8: Illustration of order statistics

Notice that

$$X_{(1)} = min(X_1, X_2, \cdots, X_n)$$
$$X_{(n)} = max(X_1, X_2, \cdots, X_n)$$

In general, $X_{(k)}$ is called the k^{th} order statistics of X_1, X_2, $\cdots$, X_n. In this case, $X_{(k)}$ is the location of each plate in the clutch pack. The first and last separator plates are fixed, as shown in Figure 4.9. In order to have six gaps, the total clearance needs to be subdivided into 6 pieces. The length of each piece represents the corresponding gap. There should be 5 random numbers to represent the cuts, which are also the positions of the plates in between. After computing these positions, the friction and separator plates are placed one by one into the corresponding coordinates.

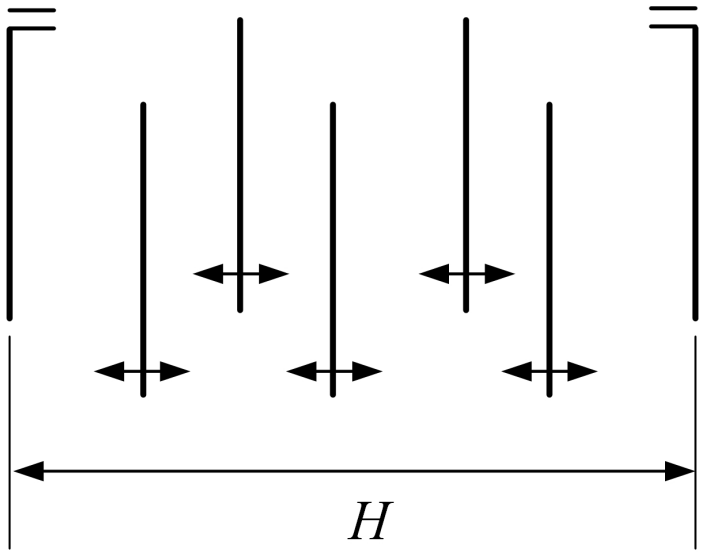

Figure 4.9: Schematic representation of the clutch pack

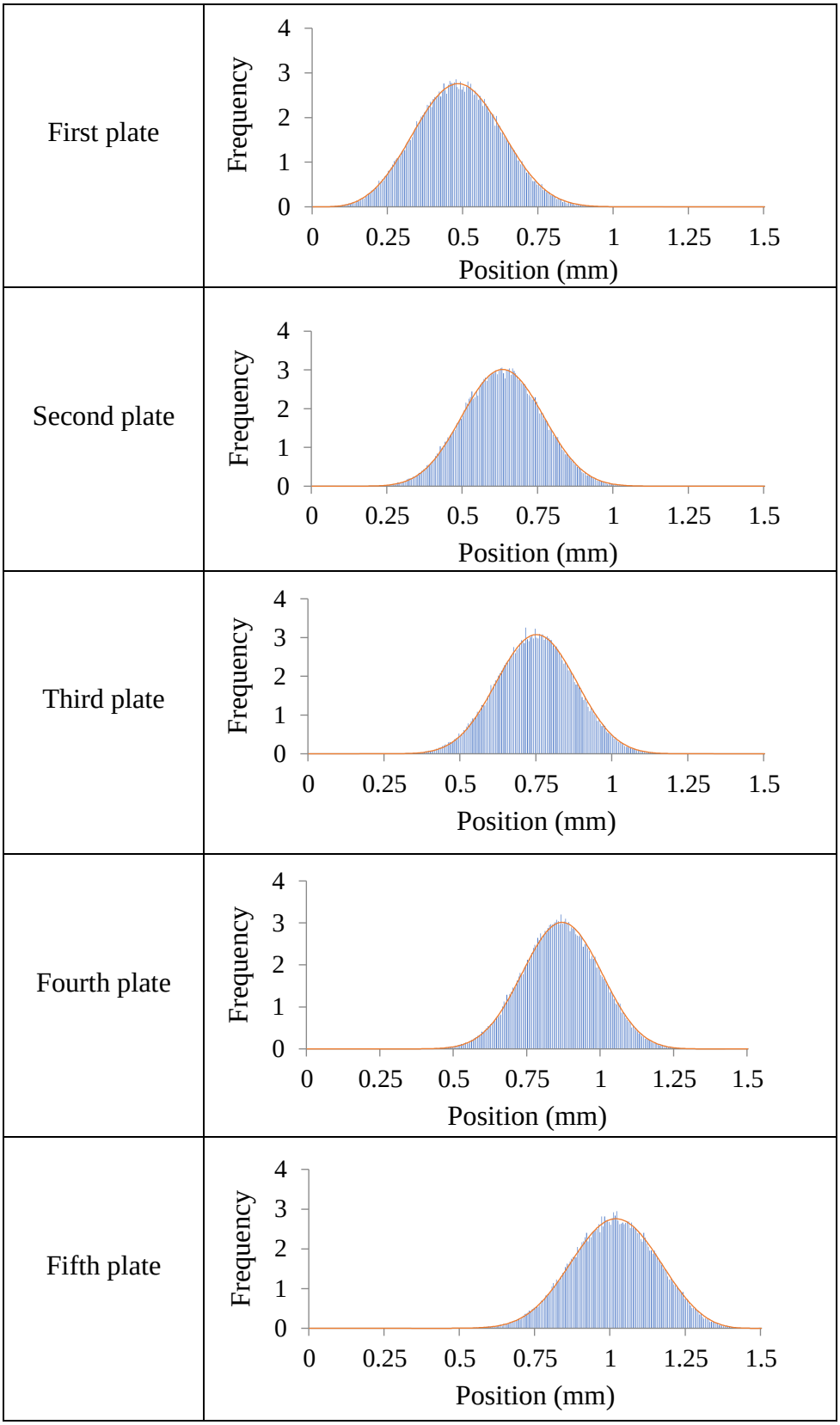

Figure 4.10: Summary of the plate location distribution

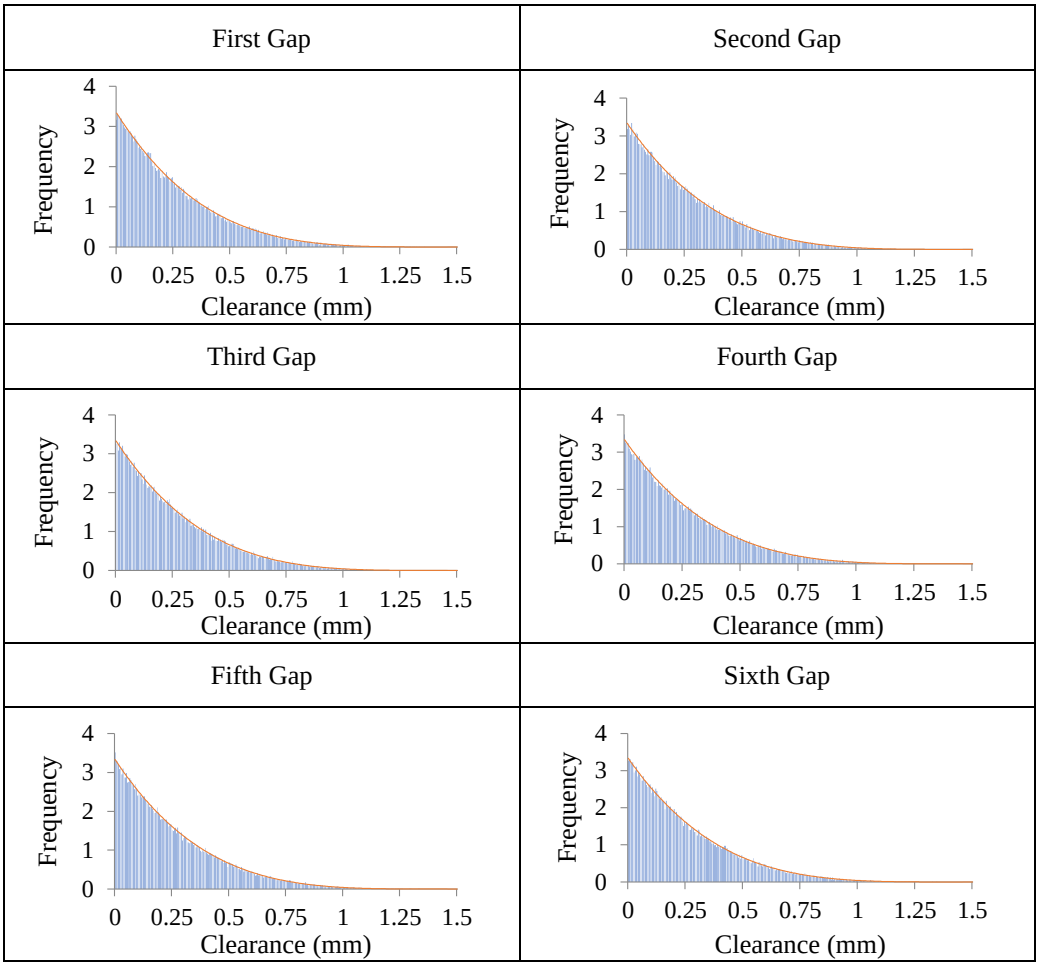

Figure 4.11: Gap behavior in the clutch pack with uniform distribution

First, assuming that the positions of these plates follow a uniform distribution, the location of each plate can be anywhere between the first and last separator plate. One of the properties of order statistics is that if X_1, X_2, $\cdots$, X_n follow a uniform distribution, $X_{(k)}$ follow a beta distribution with shape parameter $(k, n-k+1)$. Therefore, all the pieces are expected to have the same length. Figure 4.10 shows the distribution of the plates in between, and Figure 4.11 shows the distribution of each gap. It is assumed that the total clearance for the clutch pack is 1.5 mm, hence the average gap would be 0.25 mm. The analytical PDF curve for each distribution is shown as a solid line. It is obvious that each plate follows a different distribution,

which is actually a beta distribution. The distance between adjacent plates represents the gap. Each gap follows the same distribution, and the average gap length is the same.

In an alternative scenario, if all the plates follow a beta distribution, the gap distributions are significantly different, as shown in Figure 4.12. Note that the first and the last gap, the second and the fifth gap, and the third and the fourth gap follow the same distribution. The expected length of each gap is different as well. The difference between two order statistics is difficult to calculate. For the second, third, fourth and fifth gap, an analytical PDF is not available.

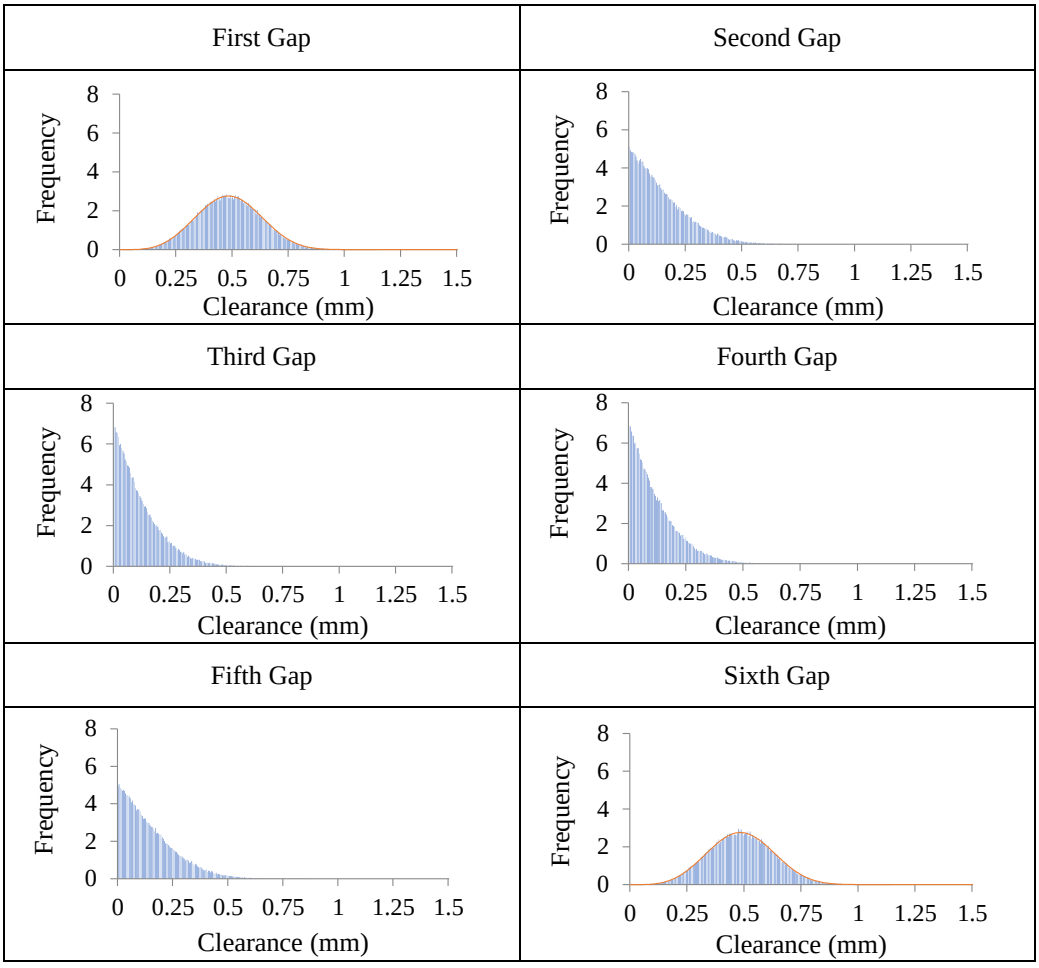

Figure 4.12: Behavior of each gap in the clutch pack with beta distribution

The statistics of all the gaps are summarized in Table 4.4. The first column is the clearance for the clutch pack. The second column is the distribution of the position of each clutch plate. A constant gap represents the situation when all the plates are fixed and uniformly distributed. The third column is the total drag torque for the whole clutch pack. Table 4.4 shows that regardless of the distribution followed by the plates, the drag torque is larger than the uniformly distributed case, indicating that the plate movement has a large impact on the drag torque.

Table 4.4: Summary of statistics for whole clutch pack model

Total clearance	Distribution type	Total drag torque (Nm)
1.5 mm	Constant gap	4.6
	Uniform distribution	92.5
	Beta distribution	57.8
3.0 mm	Constant gap	2.3
	Uniform distribution	64.6
	Beta distribution	32.8

4.2 Analytical Method

The effect of plate movement can also be studied analytically. The analysis can be divided into two parts: Fixed separator plate model and free separator plate model. The configurations for these two cases are the same as the random number generation method shown in Figure 4.3.

4.2.1 Fixed Separator Plate Model

In the fixed separator plate model, the separator plates are constrained by space screws, such that the distances between the separator plates are identical, i.e. $y_1 = y_2 = y_3 = H/3$. The three friction plates can move axially between their neighboring separator plates, and the statistical variables x_1, x_2 and x_3 can each take any values between 0 and y_1, y_2, and y_3, respectively. The three friction plates follow the same analysis. For a particular value of x_1 for the first two gaps, the drag torque acting on both sides of the first friction plate can be calculated as follows:

$$M_1(x_1) = \frac{\mu\omega_2\pi}{2x_1}(R_{out}^4 - R_{in}^4) + \frac{\mu\omega_2\pi}{2(y_1 - x_1)}(R_{out}^4 - R_{in}^4) \tag{4.2}$$

where x_1 is the gap between the first separator plate and the first friction plate, and y_1 is the distance between the first and second separator plates. The PDF of the first friction plate location, x_1, is described by a particular distribution, for example, the beta distribution. The expected value of the drag torque acting on both sides of the first friction plate can be obtained by integrating the product of the drag torque at gap x_1 and the corresponding probability of x_1, as follows

$$\overline{M}_1(y_1) = \int_0^{y_1} M_1(x_1) \cdot f(x_1) \cdot dx_1 \tag{4.3}$$

For example, if the shape parameters of the beta distribution are given as $p = 2$ and $q = 2$, the integral in Equation (4.3) can be evaluated as follows

$$\overline{M}_1(y_1) = \frac{6\mu\omega_2\pi}{2y_1^3} \int_0^{y_1} \Big(\frac{1}{x_1} + \frac{1}{y_1 - x_1}\Big) x_1(y_1 - x_1)dx_1 = \frac{3\mu\omega_2\pi}{y_1}(R_{out}^4 - R_{in}^4) \tag{4.4}$$

Equation (4.4) shows that the integration eliminates the variable x_1, thus the expected value of the drag torque is a function of y_1 only, which is the distance between the

first and the second separator plates. This indicates that the expected drag torque is higher in the case of a non-uniform clearance distribution than that in the case of a uniform clearance distribution where $x_1 = y_1/2$:

$$\frac{\overline{M}_1(y_1)}{\overline{M}_1(x_1 = \frac{y_1}{2})} = \frac{3}{2} \tag{4.5}$$

Since the three friction plates follow the same analysis, the expected value of the total drag torque of the clutch pack can be expressed as follows

$$\overline{M} = 3\overline{M}_1(y_1) \tag{4.6}$$

The shape parameters of the beta distribution are assumed to be equal, i.e. $p = q$. The ratio of the clutch pack drag torques with non-uniform and uniform clearance distributions can be generally derived for positive integer $p \geq 2$ values as follows

$$\begin{aligned}\frac{3\overline{M}_1(y_1)}{3M_1(x_1 = \frac{y_1}{2})} &= \frac{\frac{\mu\omega_2\pi}{2}\left(R_{out}^4 - R_{in}^4\right)\int_0^{y_1}(\frac{1}{x_1} + \frac{1}{y_1 - x_1})\frac{x_1^{p-1}(y_1 - x_1)^{p-1}}{B(p,p)y_1^{2p-1}}dx_1}{\frac{\mu\omega_2\pi}{2}(R_{out}^4 - R_{in}^4)\frac{4}{y_1}} \\ &= \frac{y_1^{3-2p}}{4B(p,p)}\int_0^{y_1}\left(x_1y_1 - x_1^2\right)^{p-2}dx_1 \end{aligned} \tag{4.7}$$

By expanding the beta function, Equation (4.7) can be further simplified, as follows

$$\frac{3\overline{M}_1(y_1)}{3M_1(x_1 = \frac{y_1}{2})} = \frac{(2p-1)!}{4(p-1)!(p-1)!}\sum_{k=0}^{p-2}\frac{(-1)^k}{p-1+k}\frac{1}{k!(p-2-k)!} = \frac{2p-1}{2p-2} \tag{4.8}$$

Equation (4.8) shows that the ratio for drag torque of non-uniform and uniform gap distribution is a function of the shape parameter p. The corresponding plot is shown in Figure 4.13.

When $p = 2$, the plate moves freely at a relative wide range, and the torque

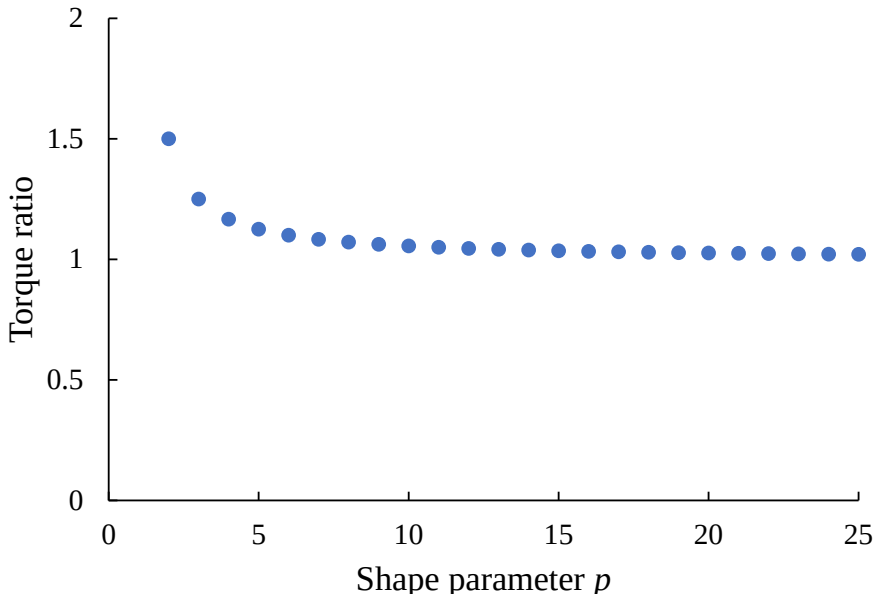

Figure 4.13: Relationship between torque ratio and shape parameter p

achieves its maximum value. As the shape parameter p increases, the friction plate moves in a relatively limited range, and the drag torque becomes smaller. As p approaches infinity, the plate becomes uniformly distributed, and the drag torque ratio approaches 1. Furthermore, if the drag torque ratio is obtained from experimental measurements, the shape parameters can be back calculated through Equation (4.8), assuming that the gaps follow the beta distribution. Then, an accurate distribution function becomes available.

4.2.2 Free Separator Plate Model

The free separator plate model is based on the same geometrical geometry as the fixed separator plate model, but without spacer screws. In this case, both the friction and separator plates can move freely in the axial direction.

The generalized formulation of Equation (4.3) provides the expected value of the drag torque acting on both sides of the i^{th} friction plate, $\overline{M_i}(y_i)$, for the given statistical distributions of the location of the friction plates, $f(x_i|y_i)$, and for the given

instantaneous value of the distance between the separator plates, y_i, as follows

$$\begin{aligned}\overline{M}_i(y_i) &= \int_0^{y_i} M_i(x_i) \cdot f(x_i \mid y_i) \cdot dx_i \\ &= \int_0^{y_i} \frac{\mu\omega_2\pi}{2}\Big(R_{out}^4 - R_{in}^4\Big)\Big(\frac{1}{x_i} + \frac{1}{y_i - x_i}\Big)\frac{(x_i - 0)^{p-1}(y_i - x_i)^{q-1}}{B(p,p)\, y_i^{p+q-1}} dx_i \end{aligned} \tag{4.9}$$

where $i = 1, 2, 3$. This equation is the same as the fixed separator plate model except y_i is no longer constant. Additionally, $f(x_i|y_i)$ is the conditional probability of x_i within [0, y_i] corresponding to a specific value of y_i. It can be shown upon integration that the expected value of the drag torque becomes independent of the x_i variables as a function of the y_i variables only. Practically, the problem of studying six random gaps in the clutch pack is hereby reduced to a three-gap system, as shown in Figure 4.14.

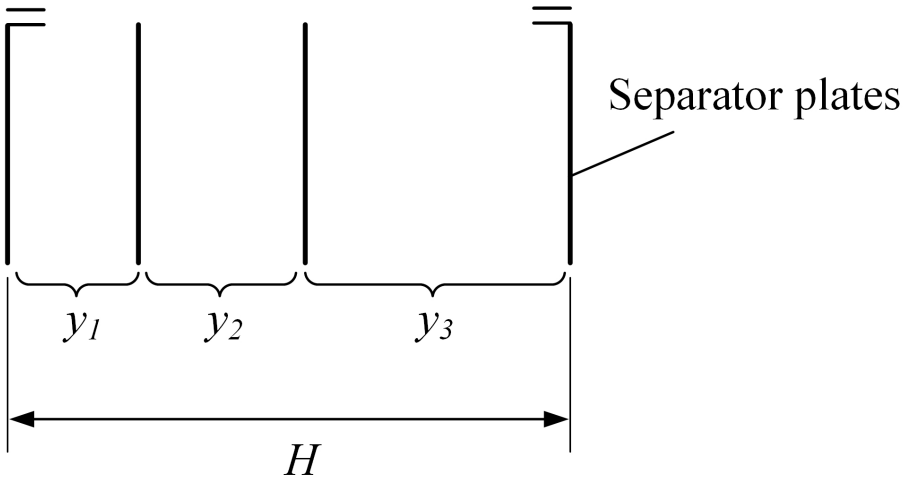

Figure 4.14: Model simplification from six gaps to three gaps

The free separator plate model treats the distances y_i distances between the separator plates as variables following certain statistical distributions. Following a similar approach, a new statistical variable is defined as $y_{1+2} = y_1 + y_2$. The expected value of

the total drag torque acting on the first two friction plates, for a given y_{1+2} distance, is formulated as follows

$$\overline{M}_{1+2}(y_{1+2}) = \int_0^{y_{1+2}} \Big(\overline{M}_1(y_1) + \overline{M}_2(y_{1+2} - y_1)\Big) f(y_1|y_{1+2}) dy_1 \tag{4.10}$$

Here the y_1 variable can take any values between 0 and y_{1+2}, and the $\overline{M}_1$ and $\overline{M}_2$ torques are functions of the y_1 and $y_2 = y_{1+2} - y_1$ distances, respectively. The conditional probability of y_1 within $[0, y_{1+2}]$ for a specific value of y_{1+2} is given by $f(y_1|y_{1+2})$. After integration, the y_1 variable is eliminated, and the $\overline{M}_{(1+2)}$ torque becomes a function of the y_{1+2} variable only. In this way, the system of three random gaps, (y_1, y_2, y_3) is reduced to a system of two gaps, (y_{1+2}, y_3). Similarly, the expected value of the drag torque acting on all three friction plates for a given instantaneous total pack clearance of y_{1+2+3} can be obtained as follows

$$\overline{M}_{1+2+3}(y_{1+2+3}) = \int_0^{y_{1+2+3}} \Big(\overline{M}_{1+2}\big(y_{1+2}\big) + \overline{M}_3\big(y_{1+2+3} - y_{1+2}\big)\Big) f(y_{1+2}) dy_{1+2} \tag{4.11}$$

In Equation (4.11), the y_{1+2} variable can assume any values between 0 and y_{1+2+3}, and the $\overline{M}_3$ torque is a function of the distance $y_3 = y_{1+2+3} - y_{1+2}$. The probability of y_{1+2} within $[0, y_{1+2+3}]$ for a specific value of y_{1+2+3} is given by $f(y_{1+2})$. Following integration, the y_{1+2} variable is eliminated, and the $\overline{M}_{1+2+3}$ torque becomes a function of the y_{1+2+3} variable only. In a clutch pack with free separator plates, the instantaneous value of the total clearance, y_{1+2+3}, can also change in time as the clutch plates move axially. Lastly, in order to calculate a time-averaged drag torque considering the changes in y_{1+2+3} described by the probability density function $f(y_{1+2+3})$, the

expected value of the drag torque for the whole clutch pack can be written as follows

$$\overline{M} = \int_0^H \overline{M}_{1+2+3}\big(y_{1+2+3}\big) \cdot f\big(y_{1+2+3}\big) \cdot dy_{1+2+3} \tag{4.12}$$

Combining these equations produces the expected value of the drag torque for the whole clutch pack. In order to calculate the expected drag torque, the probability density functions $f(x_1|y_1)$, $f(x_2|y_{1+2} - y_1)$, $f(y_1|y_{1+2})$, $f(x_3|(y_{1+2+3} - y_{1+2}))$ and $f(y_{1+2})$ need to be known. As discussed previously, the beta distribution provides a suitable and flexible way for describing the probability of the clutch plate locations. For defining a particular beta distribution, the shape parameters and the range of the statistical variable should be specified. In the order statistics example discussed previously, the probability of all clutch plate locations was always defined within the range that represents the total pack clearance between 0 and y_{1+2+3}. Therefore, the functions $f(x_i)$ and $f(y_i)$ are marginal distributions that provide the probability for the plate locations with no dependence on any other variables. However, the probability density functions in Equation (4.12) have to be defined within the intervals that correspond to the relevant integration limits, considering that the interval boundaries are statistical variables, and therefore can vary according to their own probability density functions. Thus, the x_1, x_2, x_3 and y_1 variables are described by conditional probabilities within their new variable ranges. Additionally, the shape parameters are determined in such a way that the distributions of the variables defined within the integration limits are the same as the distributions defined within the total pack clearance between 0 and y_{1+2+3}. This approach accounts for the dependencies of the statistical variables representing the distances between the clutch plates, and allows every gap in the clutch pack to assume any values between 0 and y_{1+2+3} while the sum of all six gaps is always equal to y_{1+2+3}. The parameters that define the probability density functions are summarized in Table 4.5.

Table 4.5: Probability density function parameters

PDF	Upper and lower limits	Shape parameters
$f(x_1\|y_1)$	$[0,\ y_1]$	$(p,\ p)$
$f(x_1\|y_{1+2}-y_1)$	$[0, y_{1+2}-y_1]=[0, y_2]$	$(p,\ p)$
$f(y_1\|y_{1+2})$	$[0,\ y_{1+2}]$	$(2p,\ 2p)$
$f(x_3\|y_{1+2+3}-y_{1+2})$	$[0, y_{1+2+3}-y_{1+2}]=[0, y_3]$	$(p,\ p)$
$f(y_{1+2})$	$[0,\ y_{1+2+3}]$	$(4p,\ 2p)$

The detailed derivation process can be found in the appendix. In some cases, for example when $p = 2$, Equation (4.12) can be evaluated in a closed form as follows:

$$\overline{M}_{1+2+3}(y_{1+2+3}) = 33\frac{\mu\omega_2\pi(R_{out}^4 - R_{in}^4)}{y_{1+2+3}} \tag{4.13}$$

It was found that the average of the clutch pack drag torques calculated from multiple random number sets agrees well with Equation (4.13). For $p = 2$, the ratio of the drag torque of a clutch pack with non-uniform and uniform gap distributions between the plates can be expressed as follows:

$$\frac{\overline{M}_{1+2+3}(y_{1+2+3})}{M_{uniform}} = \frac{11}{6} \tag{4.14}$$

Compare with Equation (4.8) and (4.14),

$$\frac{\overline{M}_{free}}{\overline{M}_{fixed}} = \frac{11/6}{3/2} = \frac{11}{9} \approx 1.2 \tag{4.15}$$

It is obvious that the drag torque is larger in the free separator plates case than that with fixed separator plates.

Compared with the random number generation method, the analytical approach provides further insight to visualizing the plate movement. However, when the distribution becomes more complex, an analytical solution may not be possible, thus the random number generation method becomes the practical choice.

In the application of this proposed statistical method, the drag torque ratio between the fixed and free separator plate cases can be obtained from a bench test. The same ratio can also be calculated through the statistical method for the same temperature and slip speed conditions. Therefore, the parameter p can be uniquely determined from the measured torque ratio. The probability density function that describes the plate motion can then be estimated using the computed parameter p. Notice that this approach may require the parameter p to be a real number instead of an integer. Alternatively, a different baseline probability density function may be required to calibrate the model with experimental measurements.

Table 4.6: Sample specifications and test conditions for drag test

Inner hub rotational speed (rpm)	0 - 6,000
ATF temperature (°C)	40, 120
ATF flow rate (L/min)	0.6, 1.2
Total clearance for clutch pack (mm)	0.9, 1.8
Facing dimensions (mm)	184.8 - 208.6
Groove pattern	No groove
Number of plates	3 friction and 4 separator plate

4.3 Experimental Study

Experiments were also conducted at the Dynax R&D test facility to characterize drag torque for both the free and fixed separator plate (SP) cases. The sample specifications and test conditions are shown in Table 4.6.

For each test case, the total clearances between the plates are varied while keeping all other parameters constant. The drag torque ratios are calculated for different rotating speeds, and the results are shown in Figure 4.15 for various test conditions and parameters. Figure 4.15(a) shows the results for a 1.8 mm total clearance at a temperature of 120 °C. When the rotating speed increases, the drag torque ratio remains nearly constant at approximately 1.2. This value is very close to the ratio calculated by the analytical method, indicating that the plate motion can be described by the beta distribution with a shape parameter $p = 2$. Figure 4.15(b) shows the torque ratio for the same temperature, but with a smaller clearance. The torque ratio is around a value of 1.3, which is also very close to the value provided by the analytical solution. In Figure 4.15(c), the torque ratio is larger, i.e., around 1.4. Therefore, a different shape parameter value, for example $p = 3$, can be used to describe the motion of the plates under this test condition. A possible explanation is that when the temperature is low, the viscosity of the ATF increases, thus the reaction force between the plates in the axial direction is larger. As a result, the axial motion of the plates is constrained, and the plates stay within a relatively narrower range of positions.

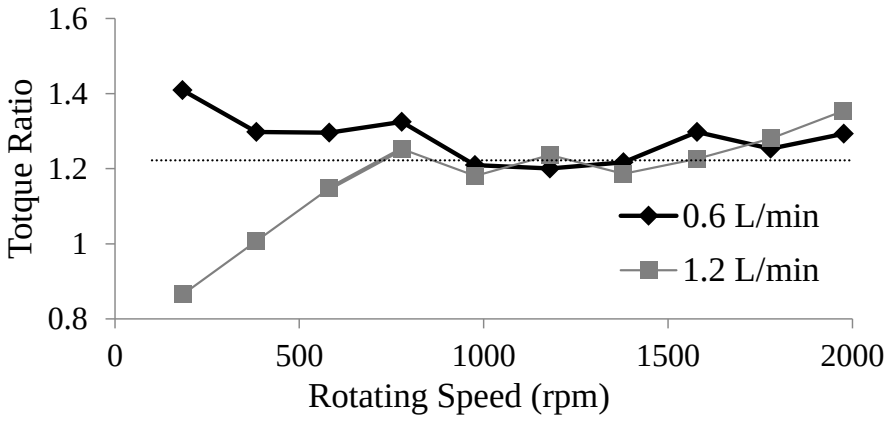

(a) 120 °C, 1.8 mm clearance

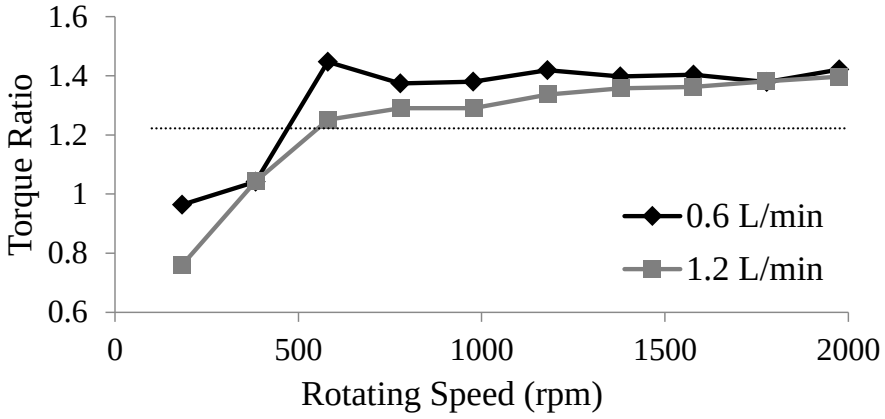

(b) 120 °C, 0.9 mm clearance

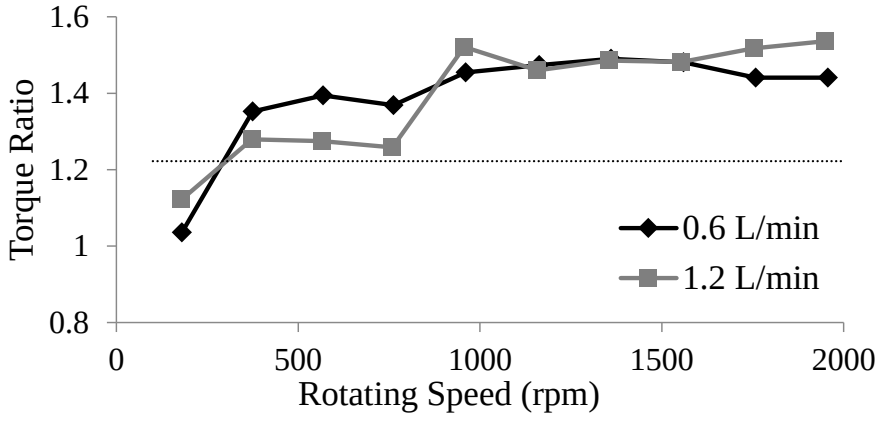

(c) 40 °C, 0.9 mm clearance

Figure 4.15: Drag torque ratio for different test conditions

CHAPTER V

Engagement Modeling

In this chapter, a CFD analysis of hydrodynamic behavior for the clutch engagement process is conducted under realistic shift conditions. A baseline squeeze film model is constructed based on the finite-volume method, coupled with an iterative scheme. The iterative scheme allows use of the actuator piston force as an input to the computation of oil film change while ensuring force balance at very time step. The model also explicitly accounts for the effects of the plate mass on the squeeze film process. The baseline model is validated with analytical solutions. Sub-models are developed to capture the porous media flow and asperity contact phenomena within the engagement process. An advanced bench test is conducted using in-vehicle clutch slip and pressure profiles for specifically replicating the torque and inertia phases of shifting. It is shown that the CFD model together with advanced clutch bench testing provide a valuable insight into in-vehicle clutch engagement behaviors.

5.1 Baseline Squeeze Film Model

For the engagement process, the differential equation governing the pressure distribution in fluid film lubrication is known as the Reynolds equation. A simplified Reynolds equation using cylindrical coordinates was derived by *Hamrock et al.* (2004)

and *Hori* (2006), and can be written as follows

$$\frac{\partial}{\partial r}\Big(\frac{rh^3}{12\mu}\frac{\partial p}{\partial r}\Big) = r\frac{\partial h}{\partial t} \tag{5.1}$$

where r is the radius of the clutch plate, h is the film thickness or the clearance between the two plates, p is the fluid pressure, and μ is the ATF viscosity. Note that Equation (5.1) only considers the squeeze motion in the z direction.

5.1.1 Mathematical Model

To simplify the derivation process, the boundary conditions for pressure at both the inner and outer radii are known.

$$p(r_1) = p_1 \qquad p(r_2) = p_2$$

Integration of Equation (5.1) once, and division by r yields

$$rh^3\frac{\partial p}{\partial r} = 6\mu r^2\frac{\partial h}{\partial t} + C_1 \tag{5.2}$$

$$h^3\frac{\partial p}{\partial r} = 6\mu r\frac{\partial h}{\partial t} + C_1/r \tag{5.3}$$

Then, integrating again, we get the pressure distribution, as follows

$$p = \frac{1}{h^3}\Big(3\mu r^2\frac{\partial h}{\partial t} + C_1\ln r + C_2\Big)$$

Following substitution of the corresponding boundary conditions, the pressure distribution can be written as follows

$$p = \frac{3\mu}{h^3}\frac{\partial h}{\partial t}(r^2 + \beta_1\ln r + \beta_2) + \eta_1\ln r + \eta_2 \tag{5.4}$$

$$\beta_1 = -\frac{r_1^2 - r_2^2}{\ln r_1 - \ln r_2} \qquad \eta_1 = \frac{p_1 - p_2}{\ln r_1 - \ln r_2}$$
$$\beta_2 = \frac{r_1^2 \ln r_2 - r_2^2 \ln r_1}{\ln r_1 - \ln r_2} \qquad \eta_2 = -\frac{p_1 \ln r_2 - p_2 \ln r_1}{\ln r_1 - \ln r_2}$$

During the engagement process, let us assume that a quasi-steady state is achieved, which means that the applied force F_{app} is balanced by the internal force generated within the interface, i.e. F_{fluid}. Hence

$$F_{app} = F_{fluid} = \int_{r_1}^{r_2} 2\pi p r dr = 2\pi \int_{r_1}^{r_2} \Big[\frac{3\mu}{h^3}\frac{\partial h}{\partial t}(r^2 + \beta_1 \ln r + \beta_2) + \eta_1 \ln r + \eta_2\Big] r dr \quad (5.5)$$

After rearranging Equation (5.5), the squeeze film velocity can be expressed as follows

$$\frac{F_{app}}{2\pi} = \frac{3\mu}{h^3}\frac{\partial h}{\partial t} M + \frac{A}{2\pi} \quad (5.6)$$

$$\frac{\partial h}{\partial t} = \frac{h^3 F_{app}}{6\pi\mu}\frac{1}{M} - \frac{h^3 A}{6\pi\mu}\frac{1}{M} \quad (5.7)$$

where

$$M = \frac{1}{4}(r_2^4 - r_1^4) + \beta_1\big[\frac{1}{2}(r_2^2 \ln r_2 - r_1^2 \ln r_1) - \frac{1}{4}(r_2^2 - r_1^2)\big] + \frac{1}{2}\beta_2(r_2^2 - r_1^2)$$
$$A = 2\pi\Big\{\eta_1\big[\frac{1}{2}(r_2^2 \ln r_2 - r_1^2 \ln r_1) - \frac{1}{2}(r_2^2 - r_1^2)\big] + \frac{1}{2}\eta_2(r_2^2 - r_1^2)\Big\}$$

Integrating Equation (5.7) by separation of variables, leads to

$$h^{-3} dh = \Big(\frac{F_{app}}{6\pi\mu}\frac{1}{M} - \frac{A}{6\pi\mu}\frac{1}{M}\Big) dt \quad (5.8)$$

$$\int_0^h h^{-3} dh = \int_0^t \Big(\frac{F_{app}}{6\pi\mu}\frac{1}{M} - \frac{A}{6\pi\mu}\frac{1}{M}\Big) dt \quad (5.9)$$

Theoretically, the applied force can be arbitrary. However, to simplify the derivation process, the force is assumed to follow some particular pattern, for example, a linear

or sinusoidal force profile, i.e.

$$F_{app} = a \times t + b$$

$$F_{app} = a \times sin[b(t-c)] + d$$

If the force profile is linear, we can rearrange the variables, so that the film thickness h can be expressed as follows

$$h = \Big[\frac{1}{h_0^2} - \frac{at^2}{6\pi\mu M} + \frac{At}{3\pi\mu M} - \frac{bt}{3\pi\mu M}\Big]^{-1/2} \tag{5.10}$$

where h_0 is the initial film thickness. If the force profile has a sinusoidal distribution, the film thickness h can be expressed as follows

$$h = \Big[\frac{1}{h_0^2} + \frac{\frac{1}{b}a \times cos[b(t-c)] - \frac{1}{b}a \times cos[bc]}{3\pi\mu M} + \frac{At}{3\pi\mu M} - \frac{dt}{3\pi\mu M}\Big]^{-1/2} \tag{5.11}$$

Figure 5.1 shows the squeeze film behavior for both linear and sinusoidal force profiles under zero pressure boundary conditions ($p_1 = p_2 = 0$). The initial thickness of the ATF film is the same. Based on these applied forces, the behavior of the film thickness rate of change, and squeeze film velocity are found to be quite different. The analytical solution of the squeeze film equation provides a simple, yet valuable means to investigate the clutch behavior, at least for the purpose of a trend analysis. Later the analytical solution can also be used to validate the accuracy of the CFD simulations.

5.1.2 Squeeze Film Motion with Rotation

To simulate the clutch engagement process, we assume that the top plate is rotating with speed ω, and the bottom plate is stationary, which is the same as in the open clutch model. The velocity distributions for radial and tangential directions are

$$F_{app} = 120 \times t$$

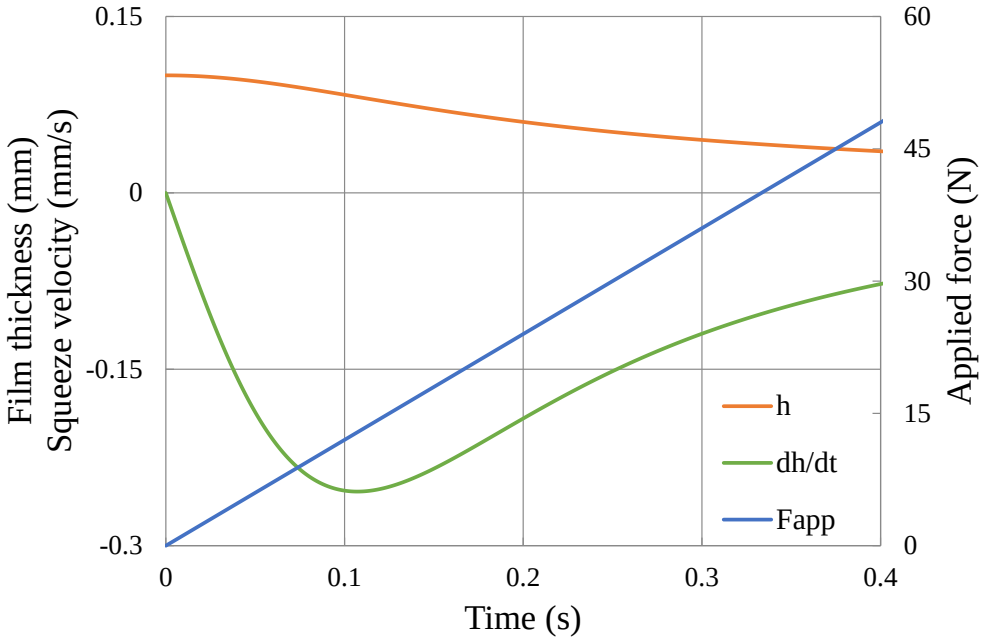

$$F_{app} = 24 \times \sin\left[\frac{5\pi}{2}\left(t - \frac{1}{5}\right)\right] + 24$$

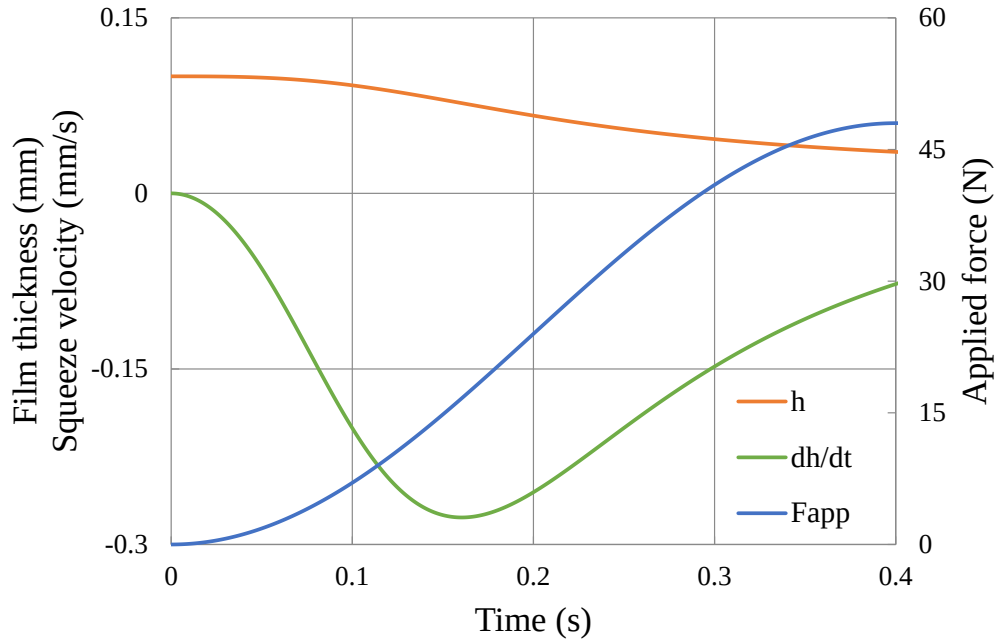

Figure 5.1: Analytical solution for engagement process with zero pressure boundary

the same as the open clutch case, which are shown in Equation (3.7) and (3.9). The only difference is that the clearance h is not constant. The continuity equation in cylindrical coordinates are shown below.

$$\frac{1}{r}\frac{\partial}{\partial r}(r\rho v_r) + \frac{1}{r}\frac{\partial}{\partial \theta}(\rho v_\theta) + \frac{\partial}{\partial z}(\rho v_z) = 0 \tag{5.12}$$

Integrating the continuity equation in the z direction, and division by ρ yields

$$\begin{aligned} \frac{1}{r}\frac{\partial}{\partial r}\Big(\int_0^h r v_r dz\Big) + (w_a - w_b) &= 0 \\ \frac{\partial}{\partial r}\Big(\frac{rh^3}{12\mu}\frac{\partial p}{\partial r} + r\Phi_R\Big) = r(w_b - w_a) &= r\frac{\partial h}{\partial t} \end{aligned} \tag{5.13}$$

Compare with Equation (5.1), Equation (5.13) has an additional term $r\Phi_R$ within the partial derivative, where Φ_R is given by

$$\Phi_R = \int_0^h \Big[\frac{\rho}{\mu r}\Big(\frac{z}{h}\int_0^h\int_0^z v_\theta^2 dz dz - \int_0^z\int_0^z v_\theta^2 dz dz\Big)\Big]dz = -\frac{\rho r\omega^2}{\mu}\frac{h^3}{40} \tag{5.14}$$

We can rearrange the terms in Equation (5.13) to obtain

$$\begin{aligned} \frac{\partial}{\partial r}\Big(\frac{rh^3}{12\mu}\frac{\partial p}{\partial r}\Big) &= r\frac{\partial h}{\partial t} - \frac{\partial}{\partial r}(r\Phi_R) \\ \frac{\partial}{\partial r}\Big(\frac{rh^3}{12\mu}\frac{\partial p}{\partial r}\Big) &= r\frac{\partial h}{\partial t} + \frac{\rho r\omega^2}{\mu}\frac{h^3}{20} \end{aligned} \tag{5.15}$$

Next, recall the boundary condition at the inner and outer radii, i.e.

$$p(r_1) = p_1 \qquad\qquad p(r_2) = p_2$$

Then, the solution of the Equation (5.15) can be written as follows

$$p = \underbrace{\frac{3\mu}{h^3}\frac{\partial h}{\partial t}(r^2 + \beta_1 \ln r + \beta_2) + \eta_1 \ln r + \eta_2}_{\text{pressure due to squeeze film}} + \underbrace{\frac{3}{20}\rho\omega^2(r^2 + \beta_1 \ln r + \beta_2)}_{\text{pressure due to rotation}} \tag{5.16}$$

$$\beta_1 = -\frac{r_1^2 - r_2^2}{\ln r_1 - \ln r_2} \qquad \eta_1 = \frac{p_1 - p_2}{\ln r_1 - \ln r_2}$$

$$\beta_2 = \frac{r_1^2 \ln r_2 - r_2^2 \ln r_1}{\ln r_1 - \ln r_2} \qquad \eta_2 = -\frac{p_1 \ln r_2 - p_2 \ln r_1}{\ln r_1 - \ln r_2}$$

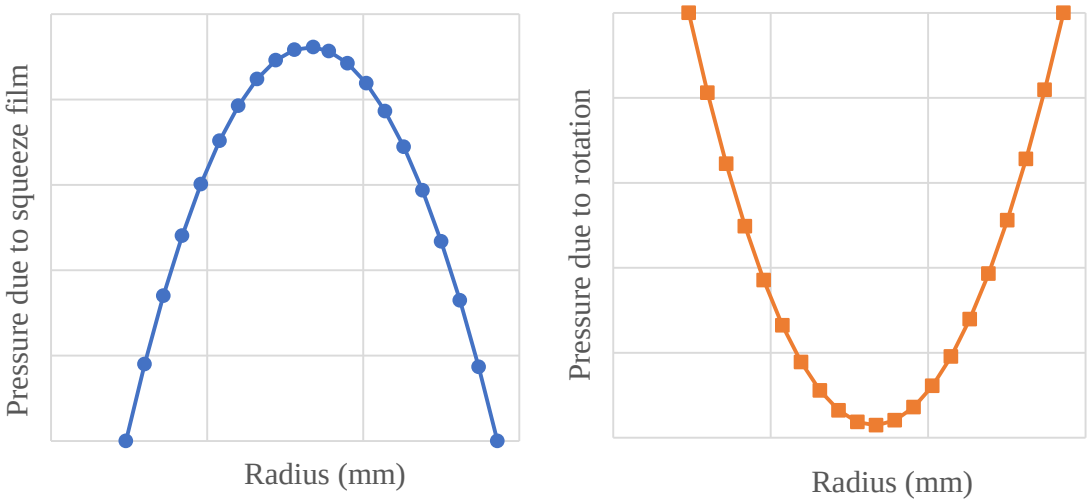

Figure 5.2: Pressure decompositions

The pressure field in Equation (5.16) contains two parts: one part is due to the squeeze film process, and the other part is due to the rotation or centrifugal force, which is shown in Figure 5.2. The pressure generated due to the squeeze film process, pushes the ATF out through both the inner and outer radii. The maximum pressure occurs at the middle of the plates. This pressure is exactly the same with the result shown in the previous section. The pressure generated due to rotation is the centrifugal pressure, pumping the ATF from the inner to the outer radius, which is discussed in the open clutch chapter. The total pressure is the sum of these two components. The centrifugal pressure dominates if the rotational speed is large. If the applied

force is large, the squeeze film pressure would dominate the total pressure.

5.2 Iterative Scheme

For modeling squeeze film flow, the CFD code requires knowledge of the moving disk's position, either as its velocity or displacement. However, in a real transmission operation, the applied force is used to control the dynamic behavior of the clutch during the engagement process. To utilize the force input, an iterative scheme was developed (*Cho et al.* (2011), *Cho* (2012)) that allows the use of force as an input for the clutch engagement simulation.

The fundamental assumption is that the flow is under quasi-steady state conditions (*Sanni* (1997)), thus the external force F_{app} and the internal fluid force F_{fluid} are balanced during every time step of the solution. The flow chart for the iterative scheme is shown in Figure 5.3. At every time step, a velocity is provided by the model, usually as a result of the previous time step. By using this velocity, the model predicts for the flow at the next time step, thus obtaining the pressure and velocity fields. After a converged result is achieved, the model calculates the internal force within the interface. The two forces are not balanced unless the film thickness is correct. To correct the tentative thickness, a relative error is defined to ensure a force balance, as follows

$$e(t,i) = \frac{F_{app} - F_{fluid}}{F_{app}} \tag{5.17}$$

where $e(t,i)$ is the relative error at time t and iteration i. If the magnitude of F_{app} is larger than that of F_{fluid}, $e(t,i)$ is positive. This means that the current squeeze velocity is small and needs to increase, which results in reducing the film thickness, thus increasing the internal force to satisfy the force balance.

As shown in Figure 5.3, if the relative error is larger than the minimum error

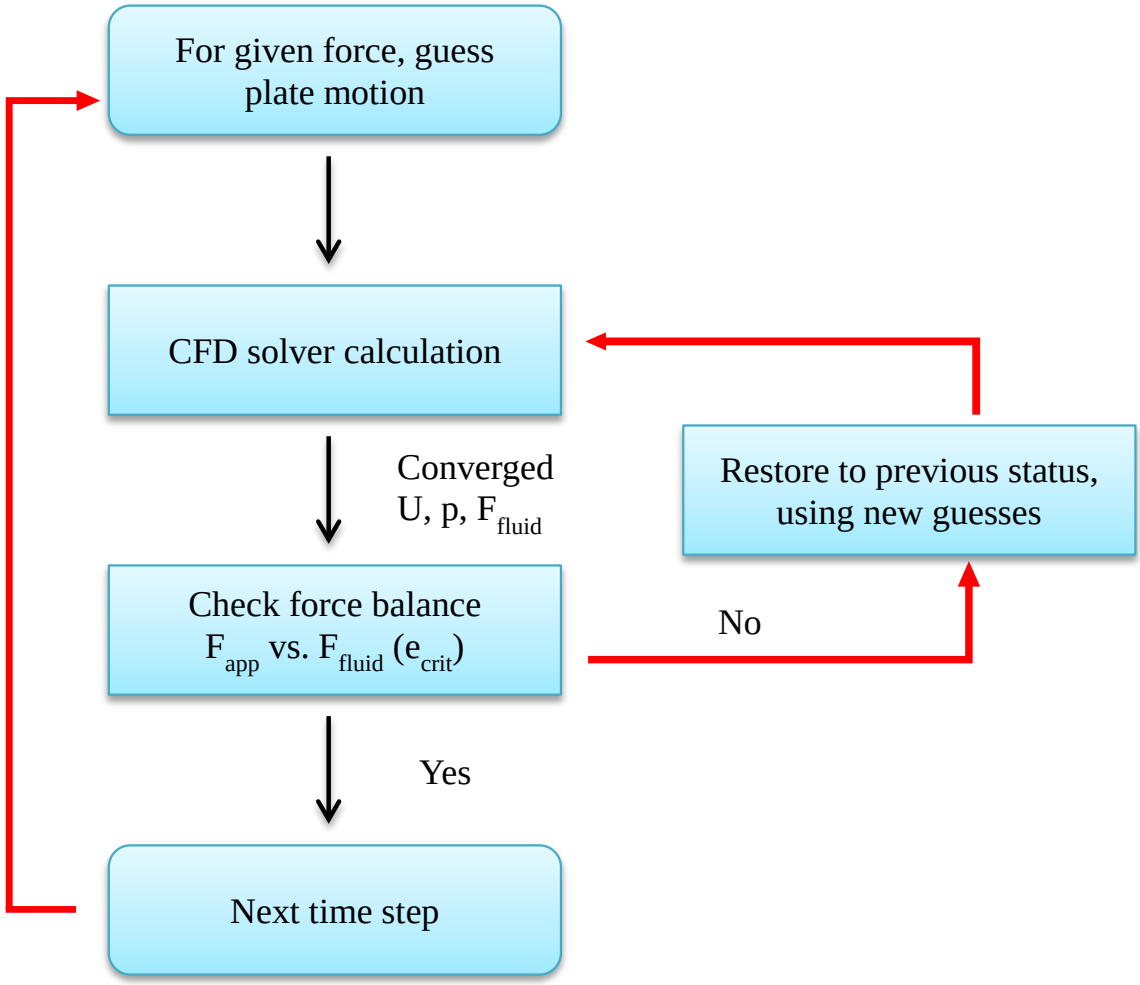

Figure 5.3: Iterative scheme flow chart

criteria e_{crit}, all variables are reset to the status of the previous time level. A new velocity is needed, which can be obtained by the Newton-Raphson method. The new velocity at time t and iteration $i+2$ can be computed using information from the previous iterations i and $i+1$. The new squeeze velocity $v(t, i+2)$ is given by

$$v(t,i+2) = -\frac{v(t,i+1) - v(t,i)}{e(t,i+1) - e(t,i)} e(t,i+1) + v(t,i+1) \tag{5.18}$$

The squeeze velocity $v(t)$ at each time step is an input parameter for a moving

wall boundary condition. The internal force F_{fluid} caused by $v(t)$ has to balance F_{app} during each time step by satisfying the relative error criteria e_{crit}. If a force balance is achieved, the simulation proceeds to the next time step, otherwise the iterations continue until reaching a force balance.

5.2.1 Baseline Squeeze Film Model

The analytical solution described in the previous section is used to validate the CFD model. Figure 5.4 shows the comparison between simulation results and the analytical solution, with a linear force profile applied. Figure 5.4 shows that the simulation results agree well with the analytical solution for the squeeze velocity and film thickness change. It shows that the CFD model has the capability to predict the engagement behavior.

More simulations were conducted with different rotating speeds and geometries. The results are shown in Figure 5.5 and 5.6. For the no-groove plate, a high rotating speed accelerates the squeeze film process. This is due to the strong pumping effect. A high rotating speed pumps the fluid out quickly, which accelerates the squeezing of the film.

For the grooved plate, the rotation drives the fluid within the grooves, resulting in a strong fluid structure interaction, and generating a large pressure within the grooves. Due to this large hydrodynamic pressure, the moving plate tends to rise when the applied force is weak, at the very beginning of the squeeze process. This phenomenon occurs when the rotating speed is large and the applied force is small. Such a behavior cannot be experienced in a real transmission since the attached hardware prevents the plate form moving in the opposite direction. In the model, however, this reverse movement delays the squeeze film process, leading to a longer engagement time. On the other hand, this phenomenon provides further insight into the fluid behavior, and enables simulations of higher fidelity.

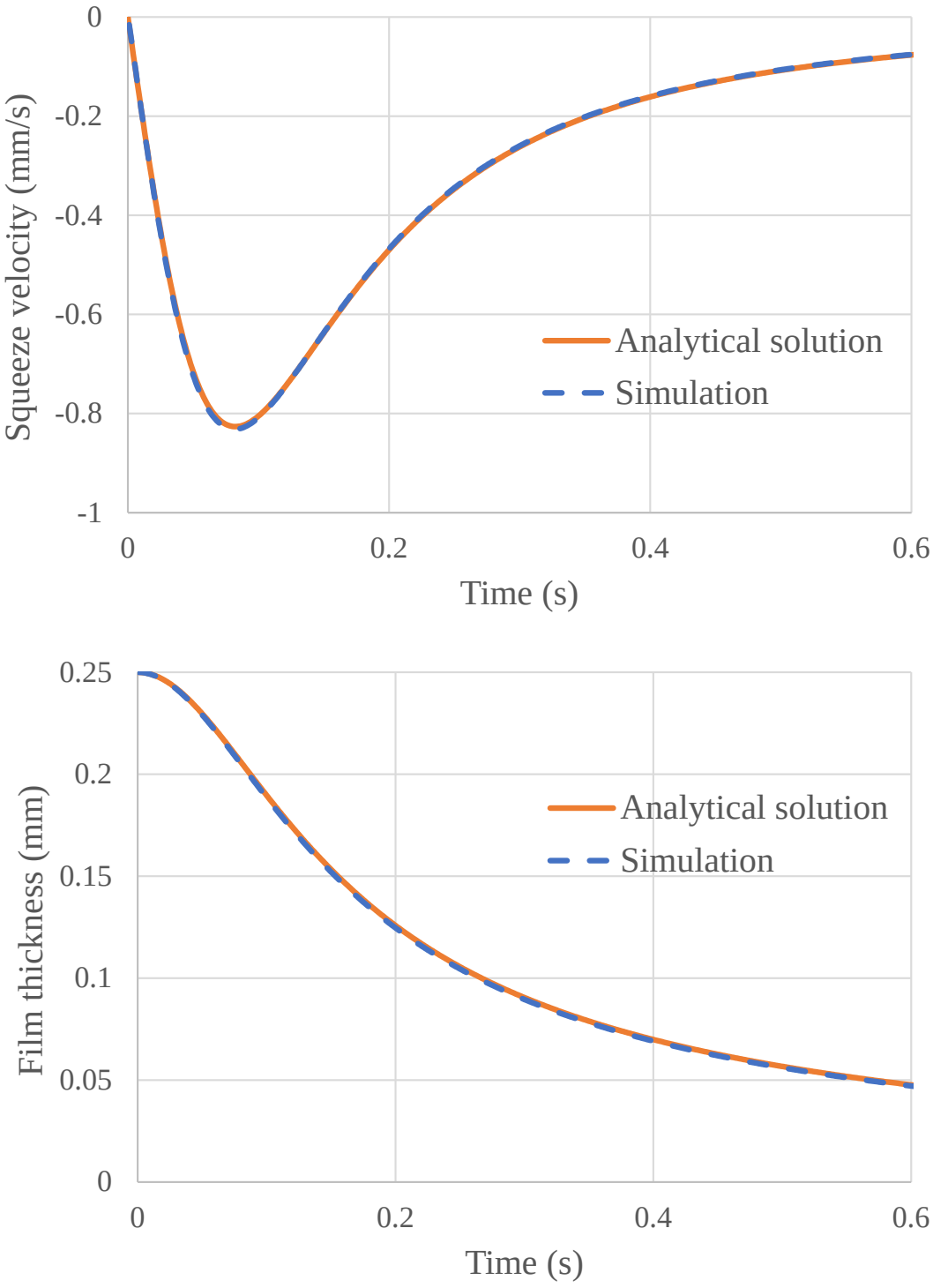

Figure 5.4: Validation of CFD tool with analytical solution for engagement process

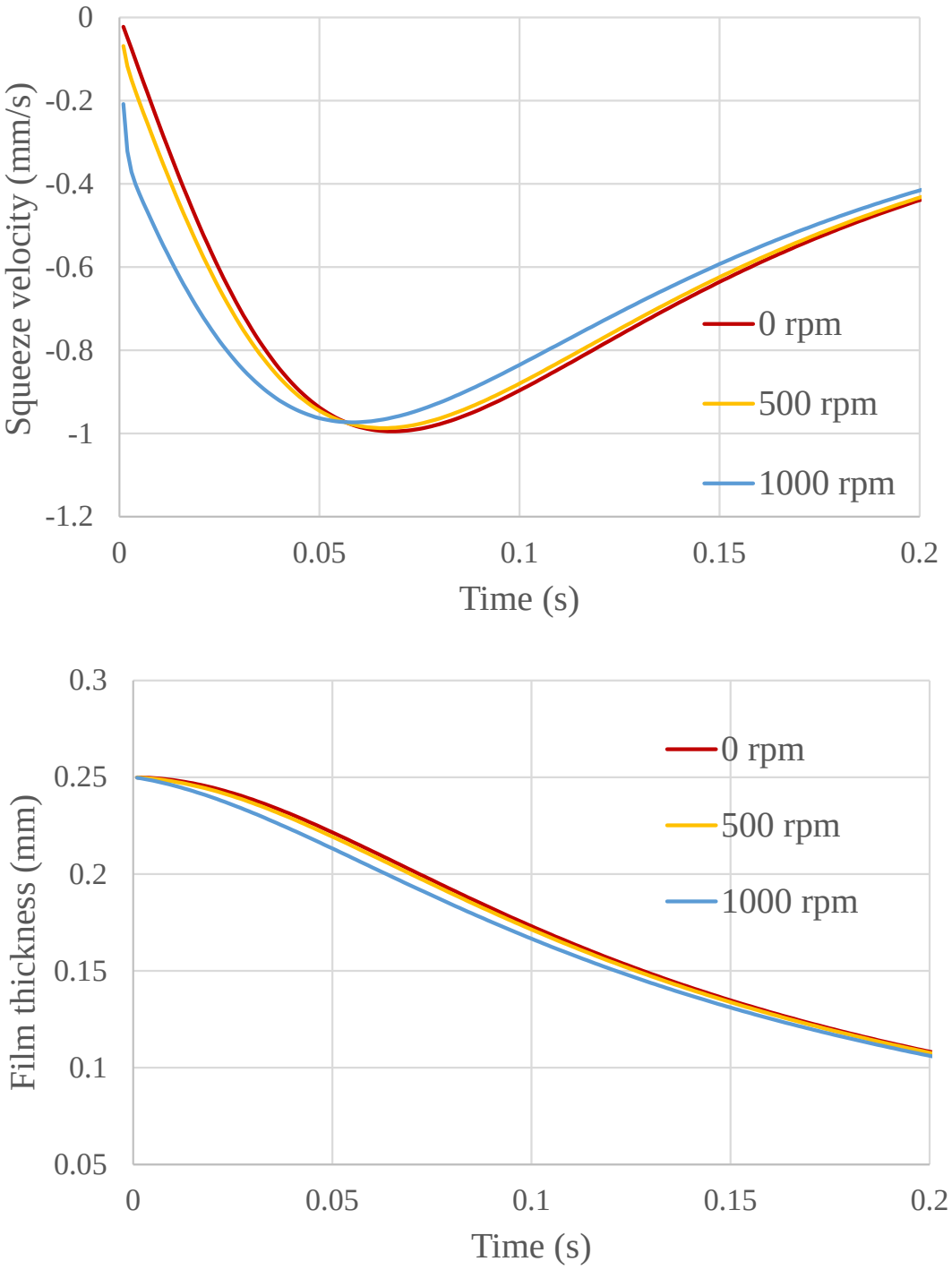

Figure 5.5: Simulation results for no groove plate

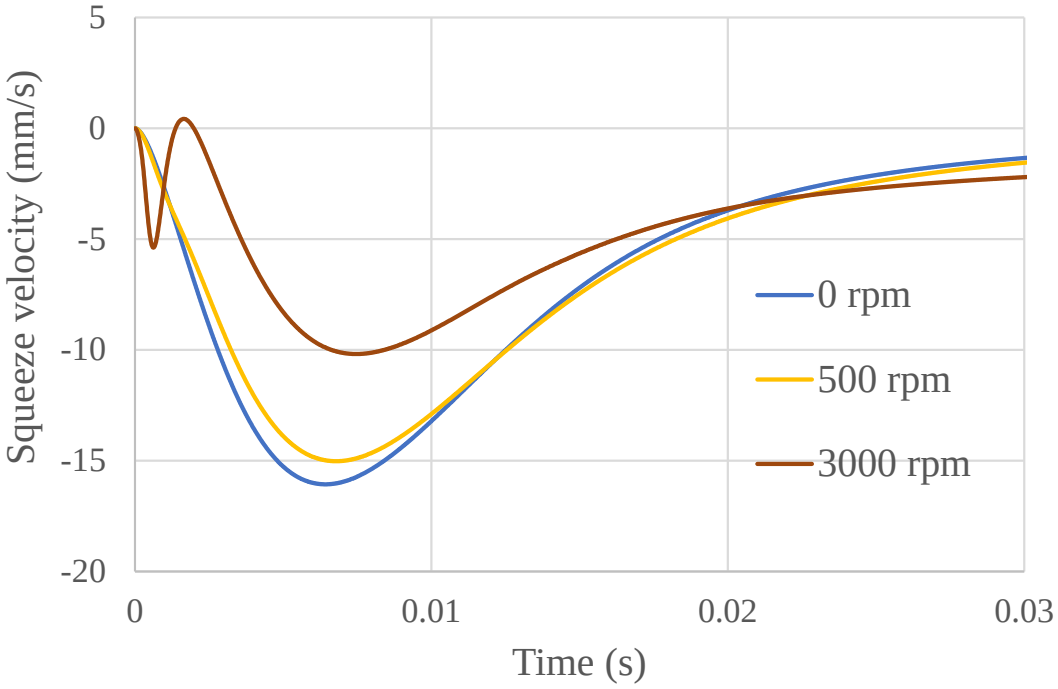

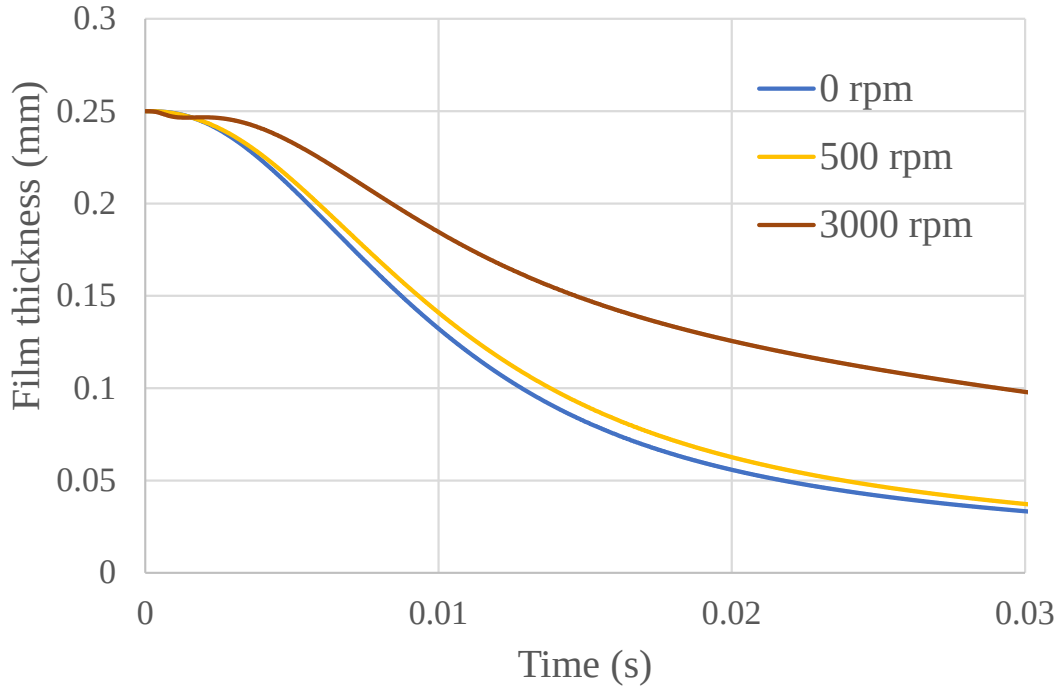

Figure 5.6: Simulation results for grooved plate

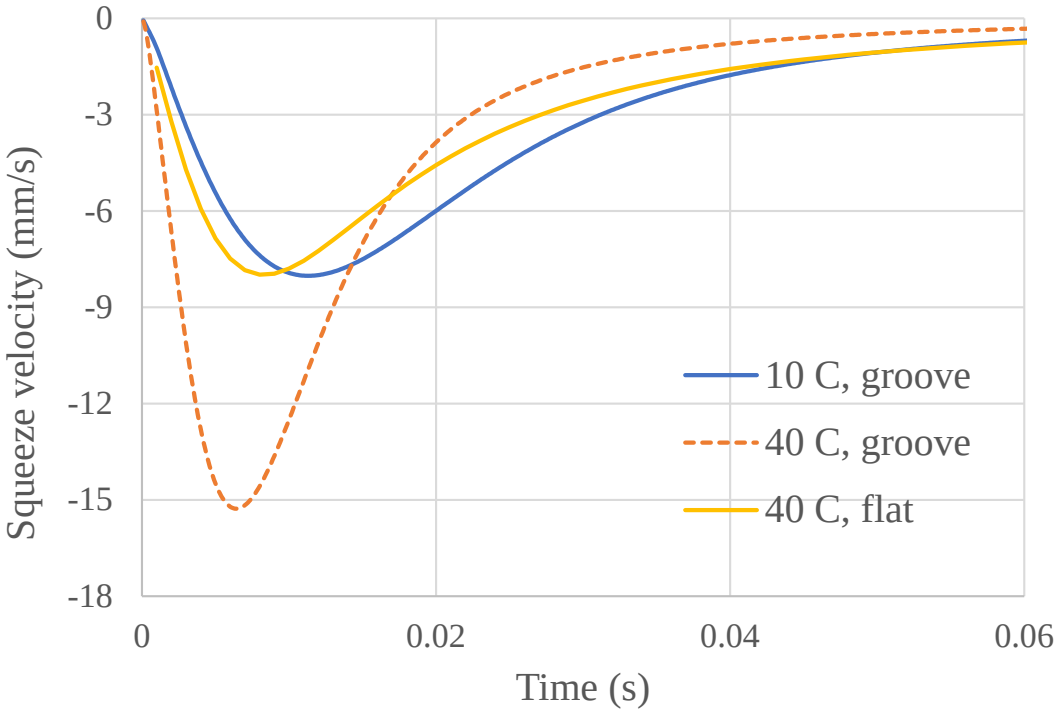

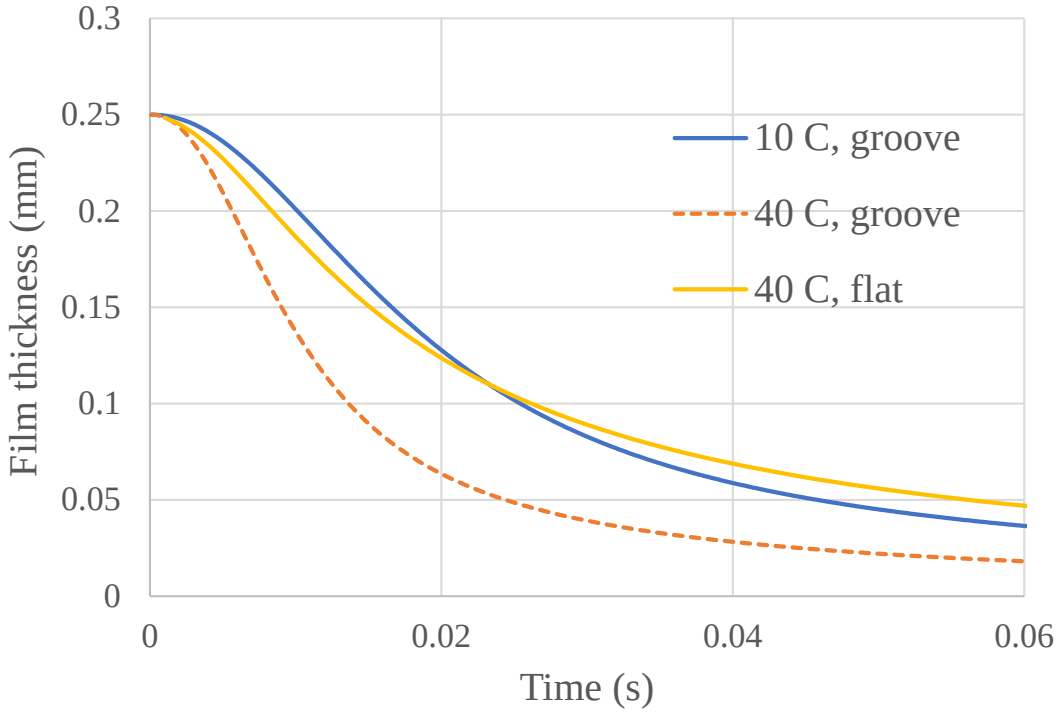

Figure 5.7: Comparison with different geometry and temperature

Computational tests were conducted between no-groove and grooved plates under different temperatures, and the results are summarized in Figure 5.7. Under the same temperature, 40 °C, the squeeze film process is faster for a grooved plate. This is because grooves provide additional channels for the fluid to evacuate from the interface, which accelerates the engagement process. For the same grooved plate, the engagement behavior is temperature dependent. Specifically, the squeeze film process is faster for higher temperatures. This is due to the change of the ATF viscosity. At higher temperature, the viscosity of the ATF is smaller, thus it is easier for the ATF to flow out of the interface, leading to a shorter engagement time.

5.2.2 Pressure Characterization

Pressure contour plots for a grooved plate are shown in Figure 5.8. The pressure plotted in Figure 5.8 is the kinematic pressure, which is defined as the ratio of pressure to density, p/ρ. At the very beginning of the engagement process, rotation dominates the pressure behavior, as a large hydrodynamic pressure is observed within the grooves. As the distance between the friction and separator plates becomes smaller, squeeze film motion dominates the pressure behavior, and the maximum pressure shifts from the groove area to friction material surface. At the end of the squeeze film process, the rotation speed is reduced to zero. The pressure within the grooves vanishes, and the maximum pressure occurs at the center of the friction material surfaces.

A further investigation of the pressure distribution at the friction material patches was conducted under different conditions. A 3D plot was generated, which is shown in Figure 5.9. Similar to Figure 5.8, the maximum pressure takes place at the center of the friction material patch. The pressure distribution can be decomposed into the

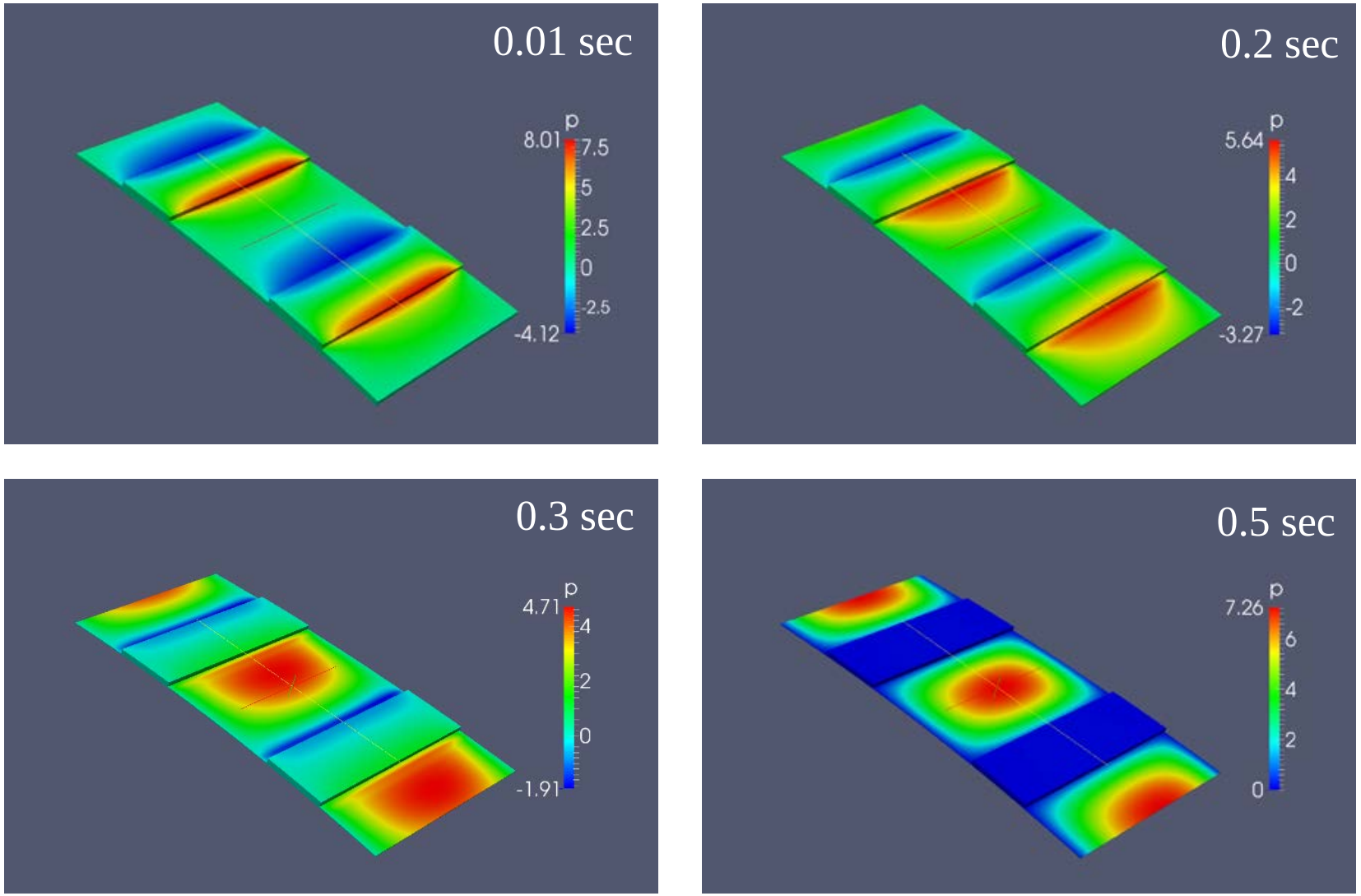

Figure 5.8: Pressure contour plots for different time

radial and circumferential directions, as follows

$$P = A(F, h) \cdot R(r) \cdot \Theta(\theta) \tag{5.19}$$

where $R(r)$ and $\Theta(\theta)$ are the normalized pressure components in the radial and circumferential directions, respectively. Here we assumed that the pressure distribution in the radial and circumferential directions are only a function of radius r, and circumferential angle θ, independently. $A(F, h)$ is the magnitude of the pressure, determined by the applied force, and the film thickness. $A(F, h)$ can be tunned within the integration of the pressure over the friction material patch to balance the applied force. This analytical expression for the pressure distribution can be used to approximate the pressure obtained from the CFD simulation to achieve a faster solution for the control of the automatic transmission, and when CFD results are not available.

The pressure distributions in the radial and circumferential directions at different rotation speeds and film thicknesses are summarized in Figure 5.10, 5.11, 5.12 and 5.13. In Figure 5.10 and 5.11, the normalized radial pressure distributions are plotted for different rotating speeds and film thicknesses. It can be concluded that the shapes for the radial pressure distributions are parabolic, and that they are independent of the rotating speeds and film thicknesses. Thus, the pressure distribution is only a function of the radius r. In Figure 5.12, the normalized circumferential pressure distributions are plotted for different film thicknesses, specifically for 0 and 500 rpm. It can be seen that the circumferential pressure distribution depends strongly on the rotating speed. When the rotating speed is low, the shape of the pressure distribution is parabolic. When the rotating speed is high, the shape of the pressure distribution changes from parabolic towards a linear distribution. The same behavior can be seen in Figure 5.13. When the rotating speed is zero, the pressure distribution is parabolic. As the speed increases beyond 1000 rpm, the shape becomes linear. In this case, the

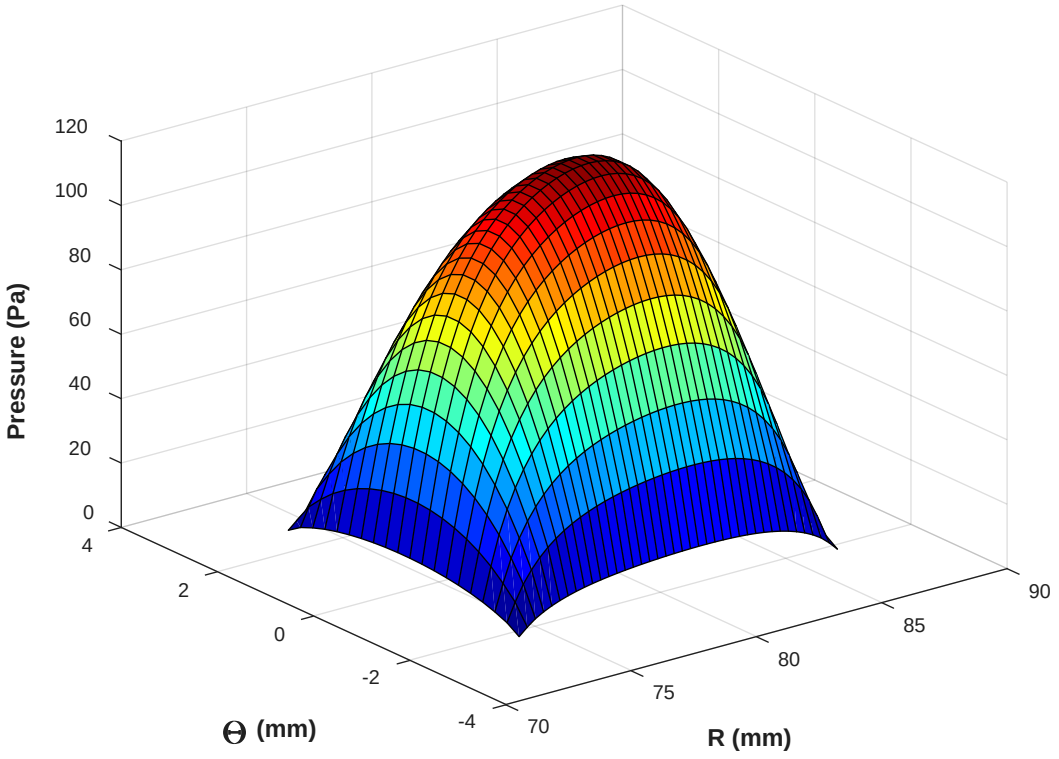

Figure 5.9: 3D pressure contour plot at non-groove area

total pressure distribution can be expressed as follows

$$P = A(F, h) \cdot R(r) \cdot \Theta(\theta, \omega) \tag{5.20}$$

The pressure distribution obtained from the previous simulations can be used to quickly predict the clutch behavior, with an accurate representation of grooves, when a CFD model is not available. The prescribed pressure distributions, coupled with a simple model, can save significant computational time, and allow the engagement process to be predicted in real time.

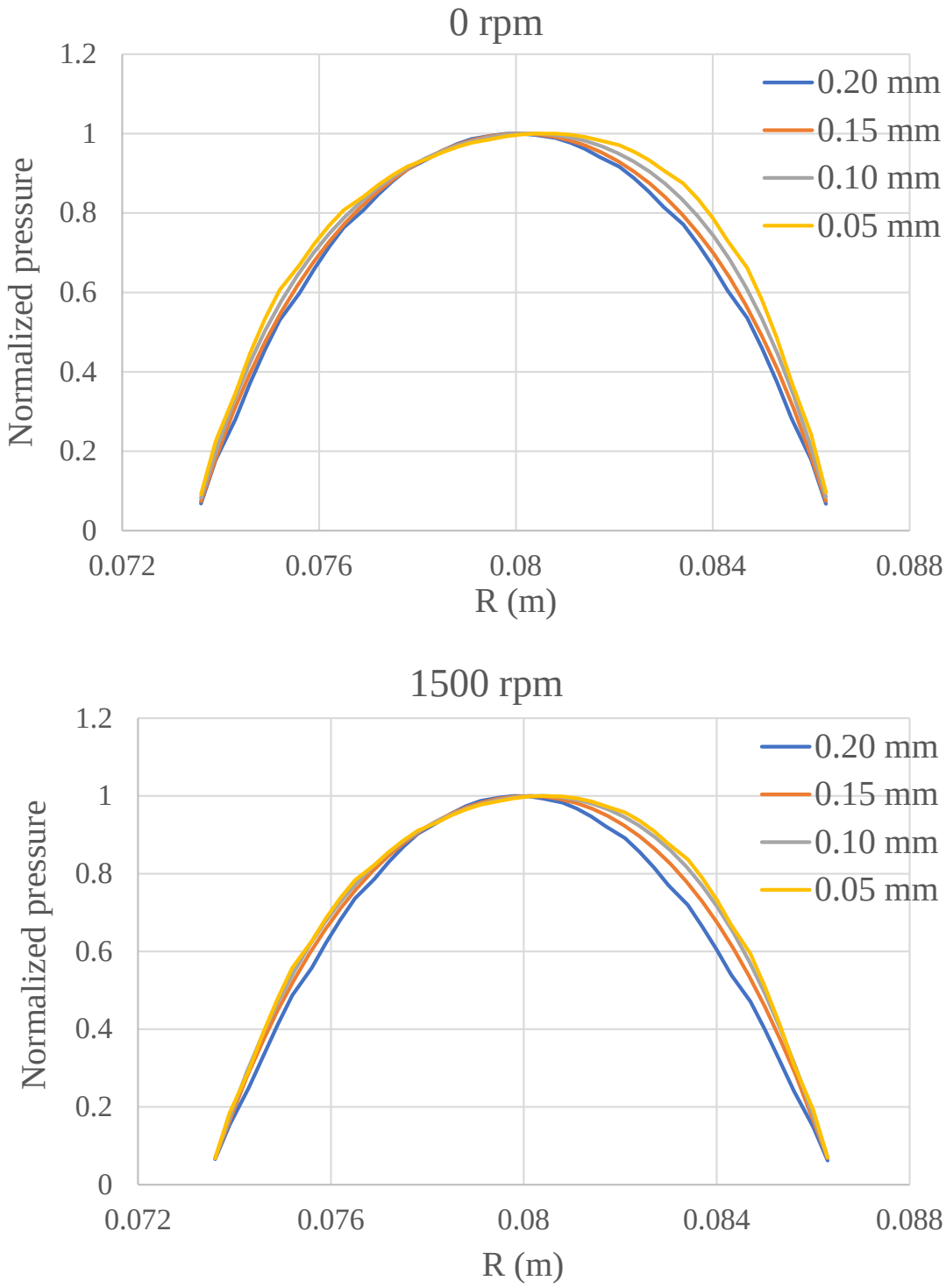

Figure 5.10: Normalized radial pressure distribution for different rotational speeds

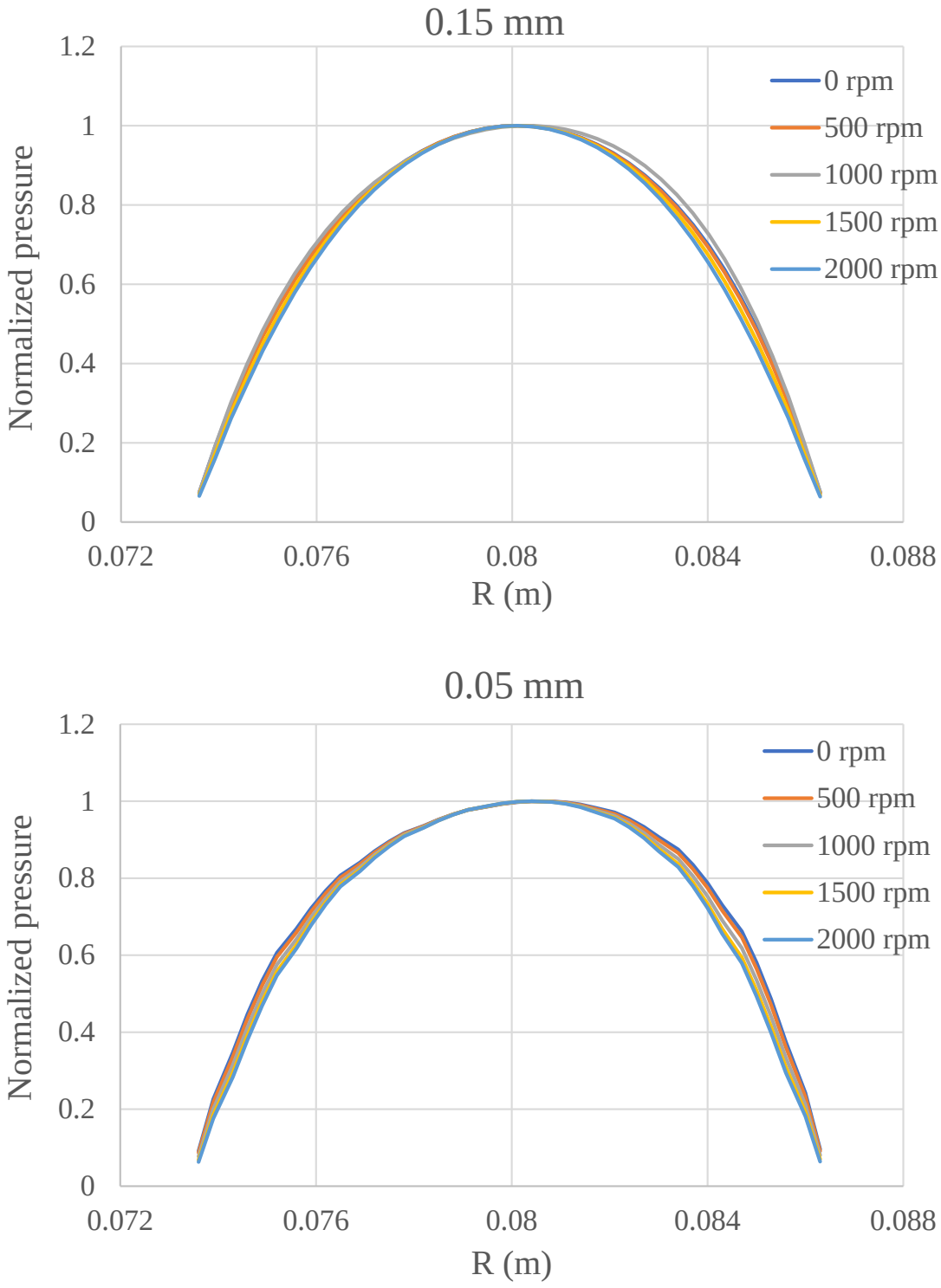

Figure 5.11: Normalized radial pressure distribution for different film thicknesses

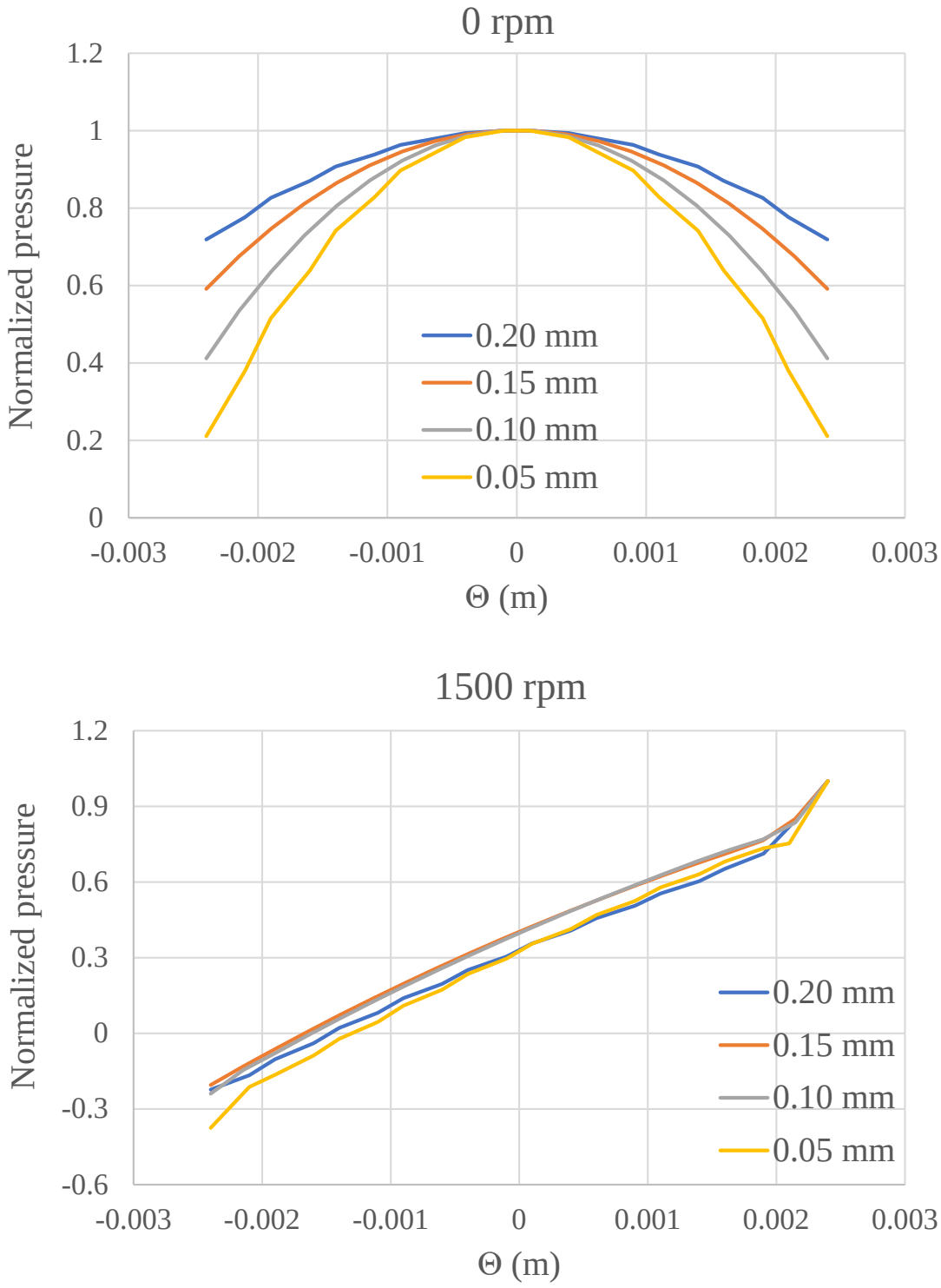

Figure 5.12: Normalized circumferential pressure distribution for distinct rotational speeds

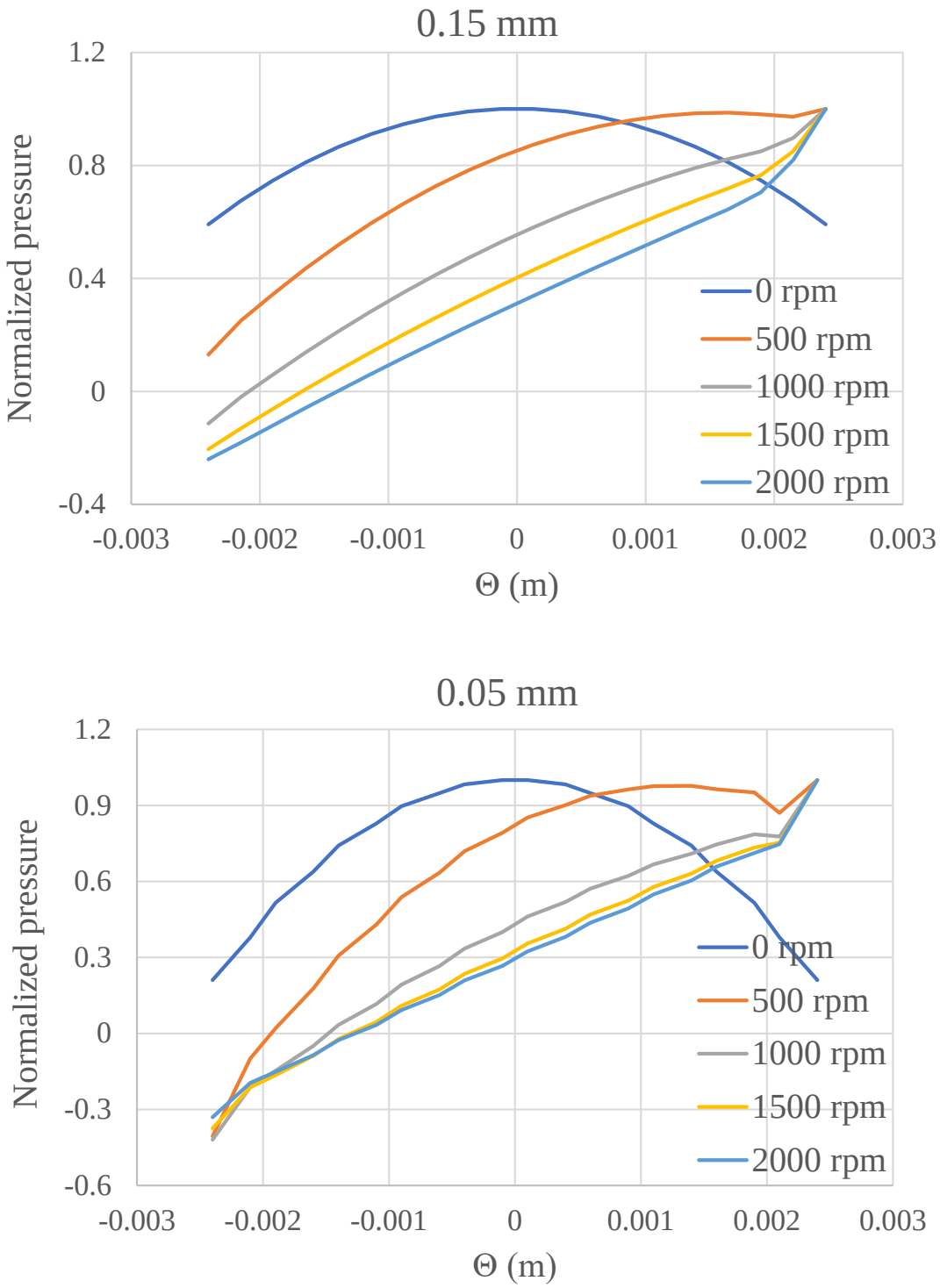

Figure 5.13: Normalized circumferential pressure distribution for distinct film thicknesses

5.2.3 Plate Mass Treatment

For for a grooved plate with a small applied force, the hydrodynamic pressure forces the friction plate to rise. To include this behavior in the model, the plate mass must be taken into consideration, so that the inertia of the plate could prevent it from separating. By including the plate mass, the original iterative scheme needs to be modified, and the changes are summarized in Table 5.1. When the plate mass is taken into consideration, the difference between applied force and internal fluid stresses generates an acceleration of the friction plate. Thus, the calculations of the squeeze velocity and film thickness change need to be adjusted accordingly. The results are summarized in Figure 5.14. The differences in the squeeze film process between a massless plate and one with mass occur at the very beginning of the simulation. By including the plate mass, the reverse motion of the plate is successfully eliminated. As the squeeze process proceeds, the difference between the applied force and the internal fluid stress becomes small, leading to a vanishing acceleration, and the effect of including the plate mass becomes insignificant. Eventually, the results converge to the same film thickness, however, the path that leads them to convergence is different.

Table 5.1: With and without including plate mass

	Without plate mass	With plate mass
Force balance	$F_{app} = F_{fluid}$	$F_{app} - F_{fluid} = ma$
Squeeze velocity	v	$v + at$
Film thickness change	$h_0 - v\Delta t$	$h_0 - v\Delta t - \frac{1}{2}a(\Delta t)^2$

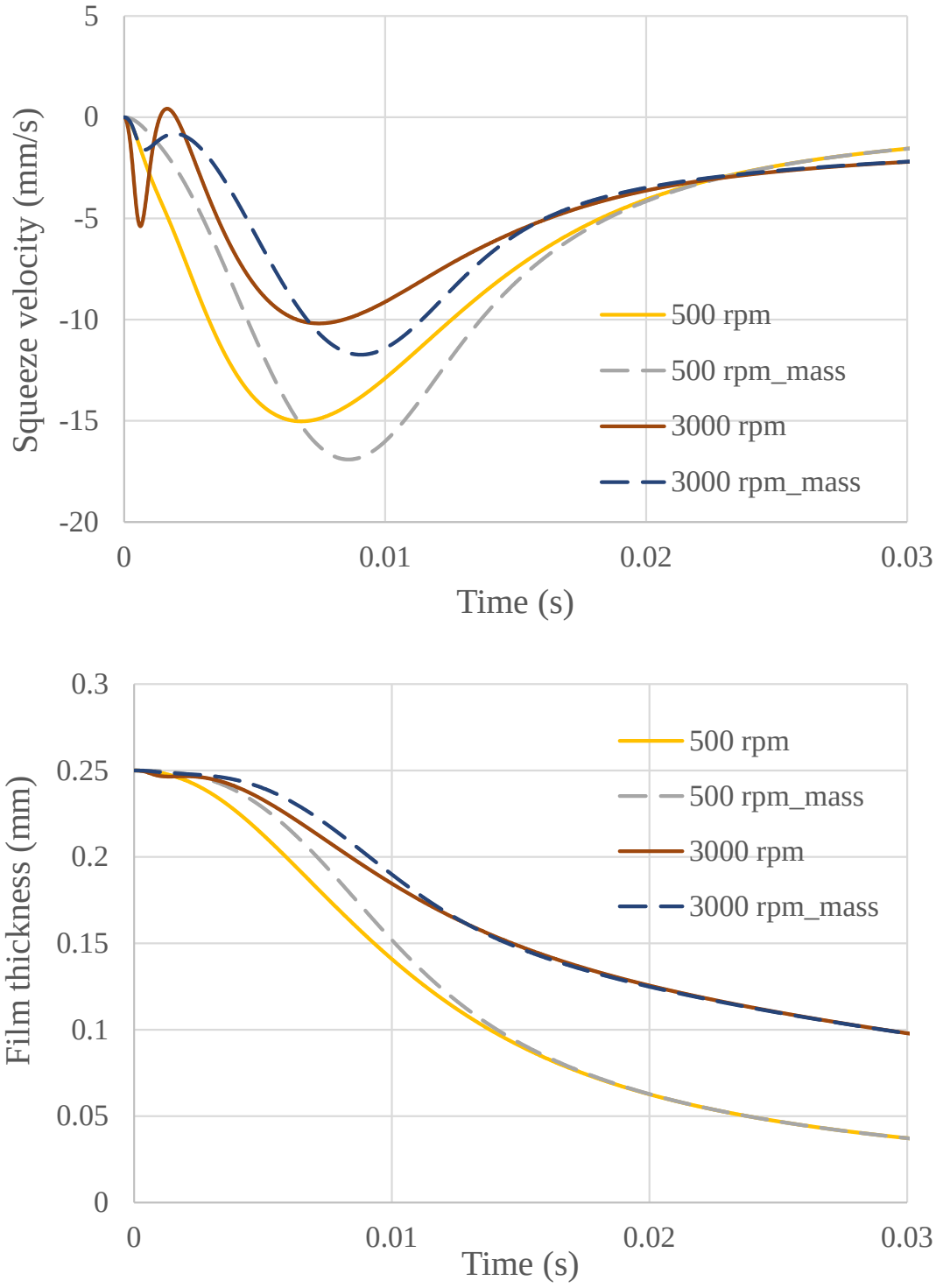

Figure 5.14: Comparison with and without taking plate mass into consideration

5.3 Heat Transfer

As mentioned in the previous section, during the engagement process, large quantities of heat are generated due to the viscous shear and asperity contact. Therefore, the temperature of the fluid within the interface increases. The density and viscosity of the ATF change, which affects the viscous torque and engagement time. The rise of the temperature also affects the functionality of the clutch plate. Therefore, it is critical to include the heat transfer process during the engagement process.

The heat generated during the engagement can be written as follows (*Davis et al.* (2000))

$$Q_s = \mu u \frac{\partial u}{\partial z} + r p_{con} \omega \mu_f \tag{5.21}$$

where Q_s is the heat flux density, μ is the fluid viscosity, u is the tangential velocity, p_{con} is the asperity contact pressure, ω is the angular velocity, and μ_f is the friction coefficient. The asperity contact pressure p_{con} will be described in in the next section, dealing with the asperity contact. In Equation (5.21), the first term corresponds to the heat flux due to the viscous shear while the second term accounts for the heat generated by the contact of the separator and friction plates. There are two mechanisms for the heat to transfer within the system: conduction and convection. The heat exchange that occurs within the clearance and the porous media is due to convection. The heat transferred through the separator plate and to the outer housing of the clutch is due to conduction. The conduction process is expressed as as follows

$$\rho C \frac{\partial T}{\partial t} = k\Big[\frac{1}{r}\frac{\partial}{\partial r}\Big(r\frac{\partial T}{\partial r}\Big) + \frac{\partial^2 T}{\partial z^2}\Big] \tag{5.22}$$

where C is the specific heat capacity, k is the thermal conductivity, T is the local

temperature. Similarly, the convection can be written as follows

$$q = h_T \Delta T \qquad h_T = f(k, L) \tag{5.23}$$

where the heat transfer coefficient h_T is a function of the thermal conductivity and the flow rate. In the present analysis, we will assume that h_T can be represented by an average value over the surface of the plate.

The boundary conditions at the interface are defined in Figure 5.15. Since the ATF is continuously supplied, the temperature at the inlet is assumed to be constant. Therefore, a Dirichlet boundary condition is used to describe the constant temperature at the inlet. Since large quantities of heat are generated on the surface of the separator plate, due to asperity contact, the temperature of the plate increases. The porous material lining on the friction plate is assumed to be adiabatic,thus the temperature gradient on the friction lining is set equal to zero. For the outlet, the evacuating flow removes heat from the interface, thus the flux can be estimated based on the temperature difference between the separator plate surface and the continuous fluid. However, since the temperature of the separator plate is changing, the heat flux at the outlet is also changing, depending on the temperature of the separator plate.

Since both the viscosity μ and density ρ of the ATF are functions of the temperature, empirical equations are used to interpolate μ and ρ in the heat transfer model, as shown in Figure 5.16. The density of the ATF can be interpolated linearly by a simple equation given by

$$\rho = -0.0007 \times T + 0.86 \tag{5.24}$$

Since the viscosity has a non-linear dependence on the temperature, the data has to be interpolated in piece-wise fashion by three empirical equations in the corre-

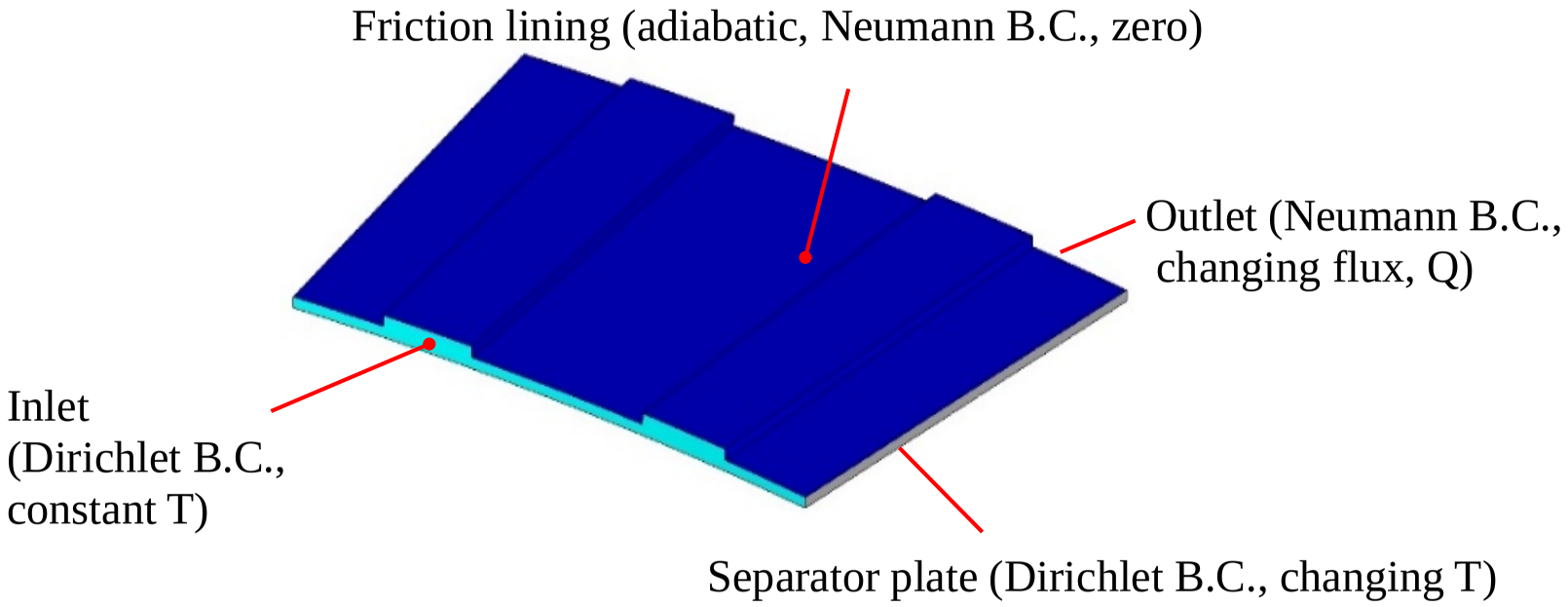

Figure 5.15: Boundary conditions for heat transfer model

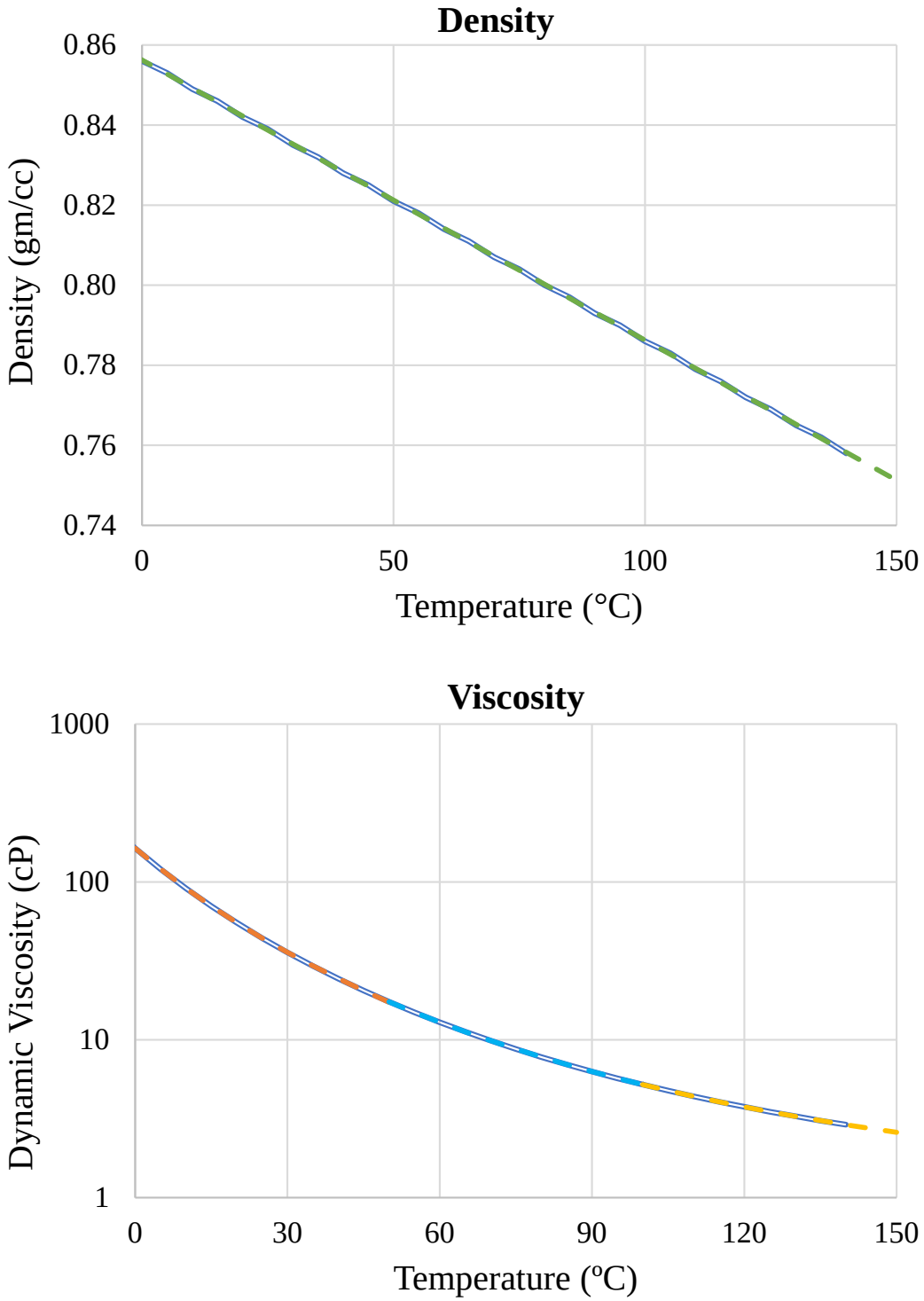

Figure 5.16: Physical properties interpolation for different temperature

sponding temperature ranges, as follows

$$\mu = \begin{cases} 92 \times e^{-0.088 \times T} + 71 \times e^{-0.029 \times T} & 0 \leq T \leq 50 \\ 104 \times e^{-0.049 \times T} + 16 \times e^{-0.013 \times T} & 50 \leq T \leq 100 \\ 67 \times e^{-0.034 \times T} + 5.6 \times e^{-0.0063 \times T} & 100 \leq T \leq 150 \end{cases} \tag{5.25}$$

5.4 Porous Media

The friction lining is made of a porous material. The characteristics of the friction material affect the engagement behavior significantly. During the engagement process, the ATF can enter and leave the friction lining freely, which is shown in Figure 5.17. The porous material provides additional conveyance for the ATF to flow through the interface between the two plates, which accelerates the engagement process.

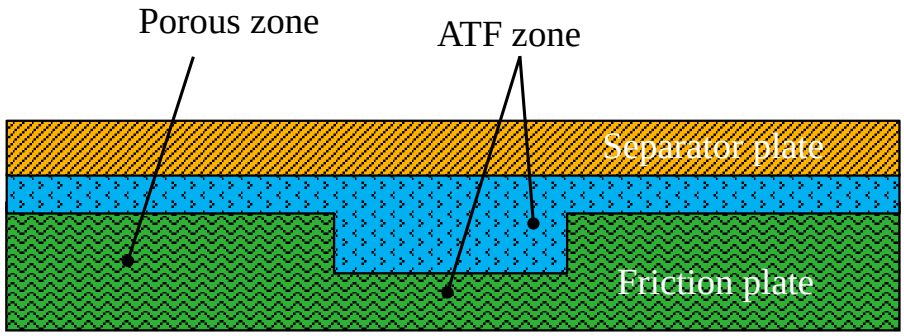

Figure 5.17: Schematic drawing for porous media zone within clutch pack

In OpenFOAM, the porous media flow is handled as a source term that is added to the equation of conservation of momentum, as follows

$$\frac{\partial}{\partial t}(\gamma \rho u_i) + u_j \frac{\partial}{\partial x_j}(\rho u_i) = -\frac{\partial p}{\partial x_i} + \mu \frac{\partial \tau_{ij}}{\partial x_j} + S_i \tag{5.26}$$

where γ is the porosity, and τ_{ij} is the shear stress. The value of γ should be between 0 and 1, indicating the range from impermeable to completely porous material. The

source term, S_i, consists of a viscous loss term and an inertial loss term, which is written as follows

$$S_i = -\Big(\mu D_{ij} + \frac{1}{2}\rho|u_{kk}|F_{ij}\Big)u_i \tag{5.27}$$

where D_{ij} is the viscous resistance, and F_{ij} is the inertial resistance. The resistance is defined as the reciprocal of the permeability of the friction material. This equation is known as the Darcy-Forchheimer Equation (*Bejan* (1984)). In the case of simple homogeneous porous media, it becomes

$$S_i = -\Big(\mu D + \frac{1}{2}\rho|u_{jj}|F\Big)u_i \tag{5.28}$$

where D_{ij} and F_{ij} are represented by the scalars D and F. In laminar flow, the pressure drop is proportional to the velocity, and F is assumed to be equal to zero. If the convective acceleration and diffusion are also negligible, Equation (5.26) becomes Darcy's Law, i.e.

$$\nabla p = -\mu D\vec{v} = -\frac{\mu}{\alpha}\vec{v} \tag{5.29}$$

where α is the permeability of the friction lining.

5.5 Asperity Contact

As the film thickness, i.e. the distance between the plates becomes smaller, asperity contact takes place. The surface roughness becomes very important in the characterization of clutch behavior. The flow regime changes from hydrodynamic lubrication to partial lubrication, and the torque is transferred through both viscous

shear and asperity contact, i.e.

$$T_{total} = T_{fluid} + T_{con} \tag{5.30}$$

where T_{total} is the total transferred torque, T_{fluid} is the torque transferred through viscous shear, and T_{con} is the torque transferred through asperity contact. The clutch applied force, F_{app}, is balanced against the sum of the fluid force, F_{fluid}, and the asperity contact force, F_{con}, during the engagement process, i.e.

$$F_{app} = F_{fluid} + F_{con} \tag{5.31}$$

The asperity contact torque is obtained by using Coulomb's friction model, by integrating the asperity contact pressure, p_{con}, over the entire frictional area, as follows

$$T_{con} = \int_{A_n} \mu_f r p_{con} dA \tag{5.32}$$

where μ_f is the friction coefficient, and A_n is the nominal contact area of the friction plate. The typical approach to calculating the asperity contact pressure, p_{con}, is based on the real contact area A_r, assuming that there is a linear relationship between A_n and A_r (*Natsumeda and Miyoshi* (1994))

$$p_{con} = \beta \frac{A_r}{A_n} \tag{5.33}$$

where the proportional constant β is determined empirically.

5.5.1 Compressive Testing

A compression tester is used to study the elastic behavior of the friction lining. The friction plate is compressed by the actuator at a prescribed load. The total thickness

of the friction plate is measured for each load condition. The elastic modulus of the friction material is then determined as the ratio of the surface pressure to the compression rate. In this study, the friction plate is subjected to loads between 3 N to 19000 N in steps, corresponding to a surface pressure ranging from 0.001 MPa to 4.6 MPa on the friction material.

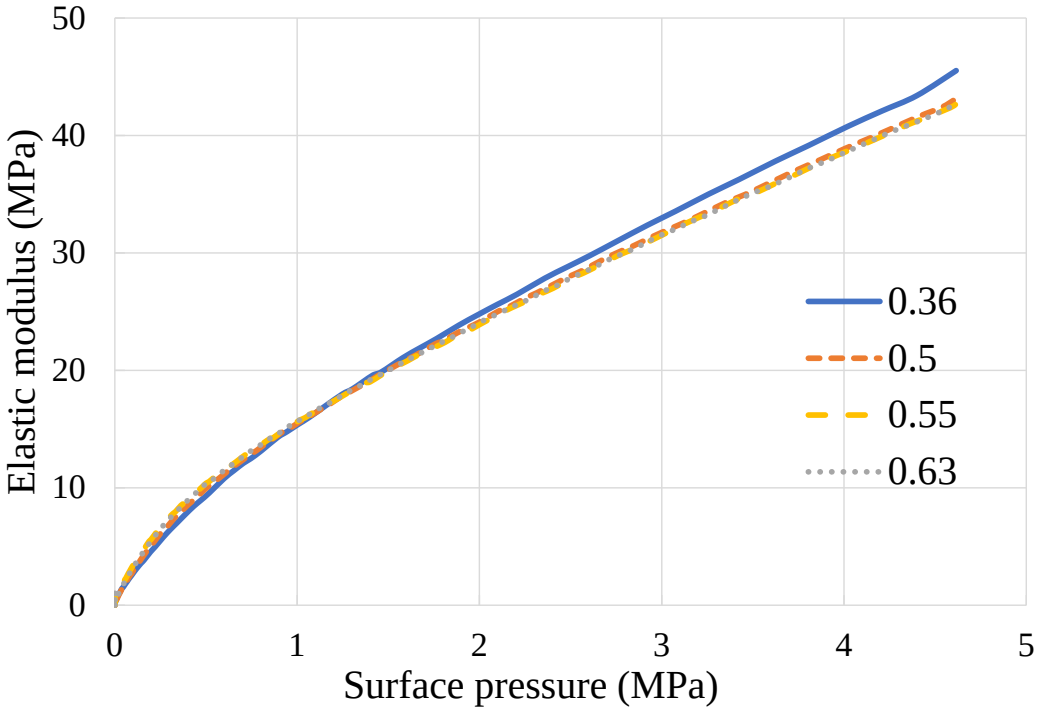

Figure 5.18: Elastic modulus for friction materials with different thickness

Figure 5.18 shows the variation of the elastic moduli for different thicknesses of friction linings with respect to surface pressure. The elastic moduli curves remain similar, indicating that the compression rate is not sensitive to the material thickness. The measurements also shows that the micro-structure of the friction lining is homogeneous, and is independent of the thickness. Note that the elastic modulus increases to 45 MPa within the pressure range that corresponds to a typical operating condition during the clutch engagement process.

5.5.2 Surface Roughness Characterization

The surface roughness of the friction material can be measured by using a profilometer. The stylus of the profilometer moves across the friction material over the asperities, and the vertical motion of the stylus is recorded in the form of electrical signals. The specifications of the profilometer are shown in Table 5.2. The vertical resolution of the stylus measurements indicates the smallest height that the profilometer can measure accurately. The horizontal resolution indicates the smallest horizontal distance between the data points, and is defined by the scan length and speed.

Table 5.2: Specification of profilometer

Scan speed	0.03 mm/s
Sampling interval	0.15 µm
Sampling frequency	200 Hz
Horizontal resolution	0.15 µm
Vertical resolution	0.02 µm

Two different friction plate samples are used to study the surface profiles of the friction material. One is a brand new plate sample, the other corresponds to a used sample, after completing 200 break-in cycles on a SAE #2 tester. After the break-in period, the friction lining becomes smoother than that of a brand new plate. Repeated measurements are conducted in both the radial and circumferential directions. The blue region represents the friction lining, and the gray area corresponds to the groove. The surface is traced in 13 circumferential and 9 radial directions, as shown in Figure 5.19.

Figure 5.20 shows an example of the surface measurement data for the brand new plate. The data is utilized to analyze statistically the distribution of asperity

heights. The nominal surface is selected so that the mean of the measurements is zero (*Hamrock et al.* (2004))

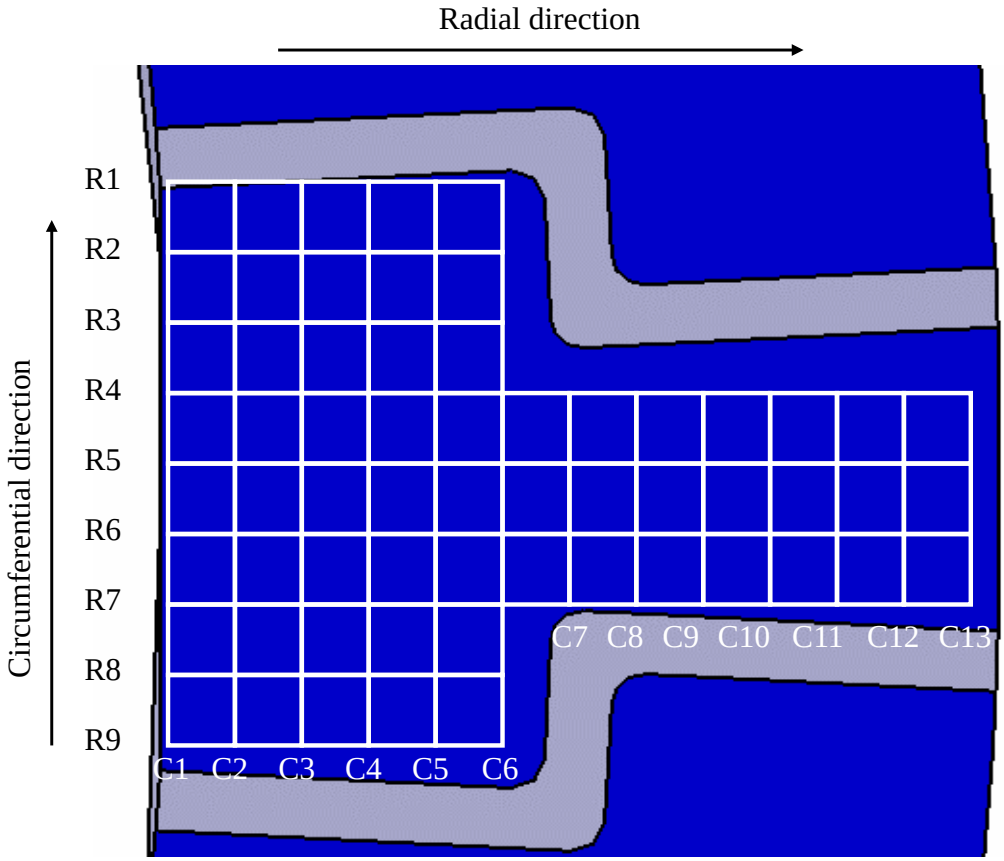

Figure 5.19: Friction material sample for surface profile measurements

The asperity measurement data are plotted in Figure 5.21 in the form of a PDF. The top figure shows the plate data after break-in while the bottom figure corresponds to the brand new plate. A positive value indicates that the asperity is above the nominal surface while a negative value indicates a fissure in the surface. The figure also shows the distribution of asperities when all the measurements are combined. The data show that the distributions in the radial and circumferential directions are similar, which implies that the distributions are direction independent. As expected, larger asperities are removed during the repeated break-in cycles. The highest asper-

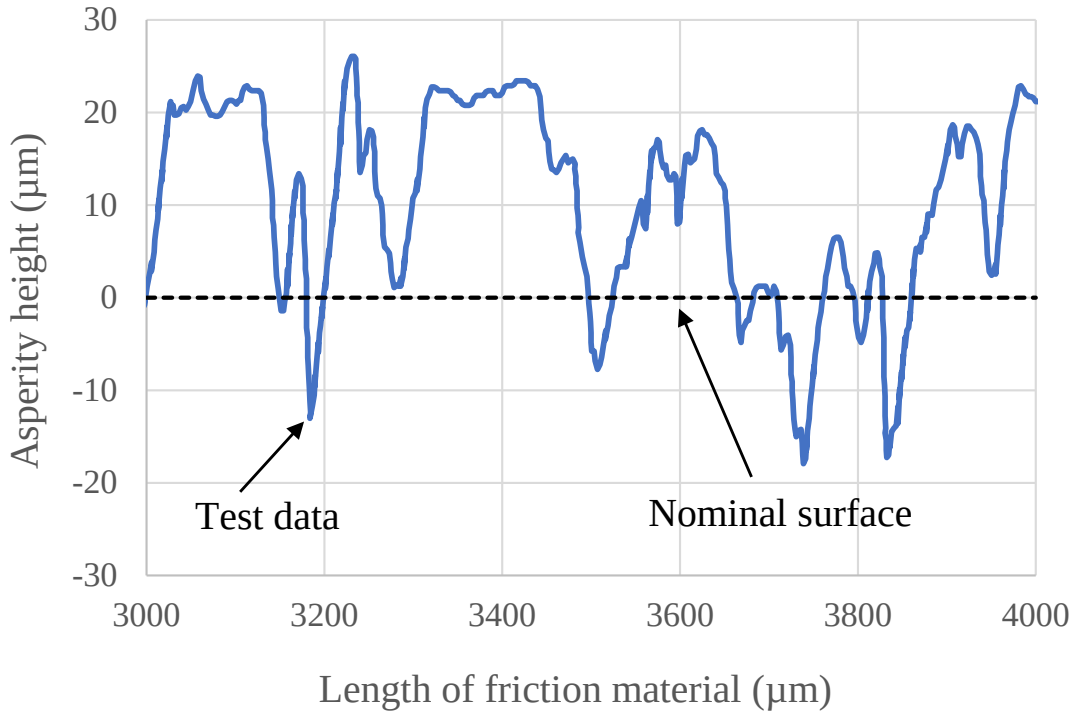

Figure 5.20: Profilometer measurements on a new friction material

ities of broken-in plates are approximately 20 µm, which is significantly lower than those of new plates, which are approximately 30 µm. The deepest fissures are the same for both plates, and are found to approximately 50 µm. The overall shape of the distribution has a pronounced asymmetry, which can be represented by the kernel distribution.

In order to better characterize the new and broken-in clutch plates, center line differences, R_a, and standard deviations, σ, are calculated using Equations (5.34) and (5.35) from the combined test data sets, and are summarized in Table 5.3. The values of R_a and σ of the broken-in plate are significantly smaller than those of the new plate, which is consistent with the results shown in Figure 5.21. The PDF obtained from Figure 5.21 will be used in the next section to obtain the relationship between the

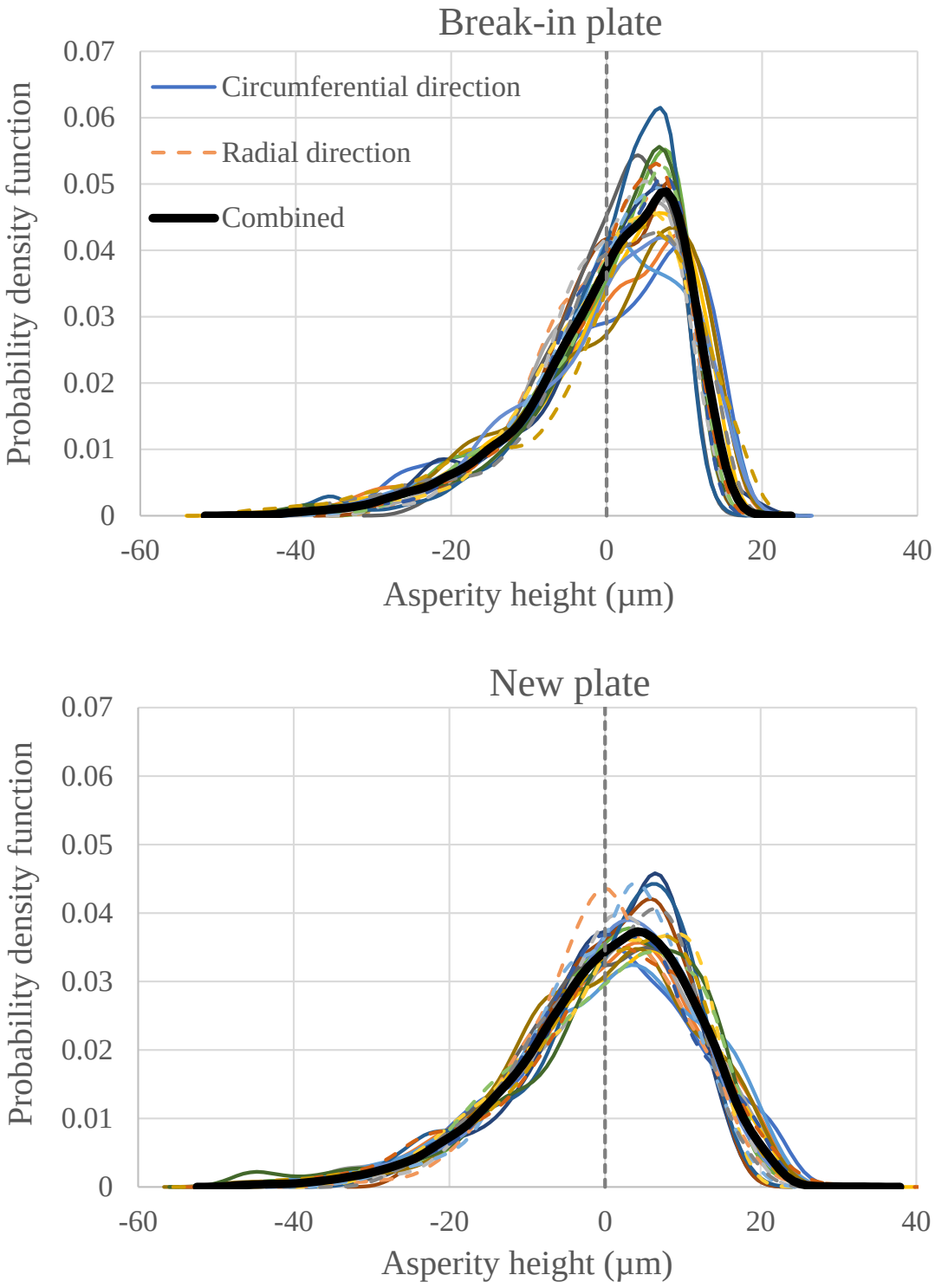

Figure 5.21: PDF of asperity heights for new and break-on friction plate

asperity height and real contact area.

$$R_a = \frac{1}{n}\sum_{i=1}^{n}|z_i| \tag{5.34}$$

$$\sigma^2 = \frac{1}{n-1}\sum_{i=1}^{n}(z_i - \overline{z})^2 \tag{5.35}$$

Table 5.3: Surface parameters for new and break-in plates

Surface parameters	New plate	Break-in plate
R_a (μm)	8.99	7.84
σ (μm)	11.39	10.04

5.5.3 Real Contact Area Measurements

The rough surface of the friction material results in a small real contact area against the separator plate, as compared to the nominal surface area A_n. The real contact area, A_r, is important for determining the contact pressure and the asperity torque. A prism measuring device for contact area quantification is used to measure the real contact area, as illustrated in Figure 5.22.

The prism measuring device is actuated by an air cylinder that applies a load to the friction plate. The displacement of the prism is used to determine the distance between the bottom surface of the prism and the friction plate. A LED light source is projected on one surface of the prism, and the refracted light is captured in the form of an image through a microscope. The portion of the prism in contact with the asperities does not reflect the projected light completely, and results in darker spots. Th rest of the sample reflects the light, thus forming lighter areas. The raw image is then digitized to generate a black and white picture. The ratio of the black pixels to the total number of pixels gives the real contact area of the friction material.

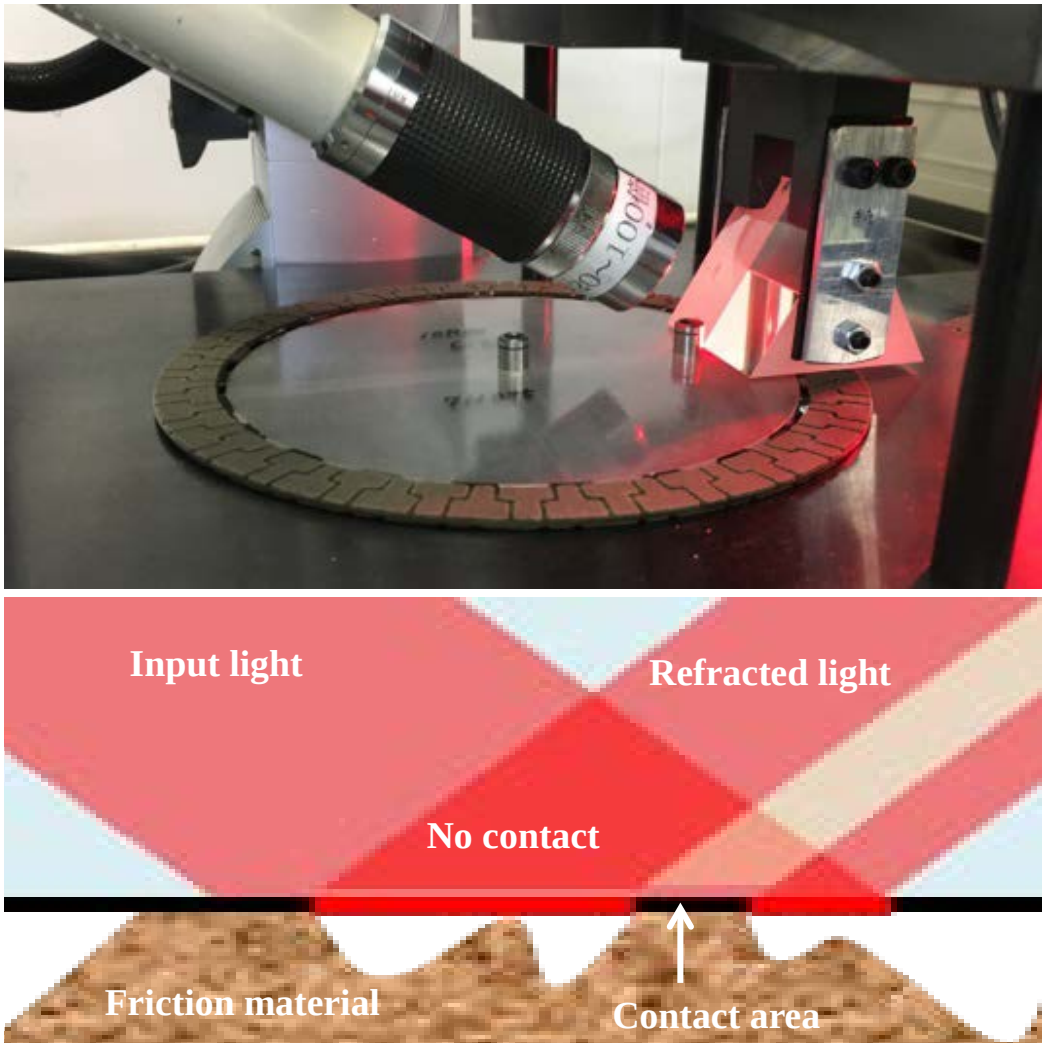

Figure 5.22: Optical Measurements of real contact area on prism device

The digitized images in Figure 5.23 show real contact areas of the friction material under 0.5 and 3.0 MPa. It is obvious that the real contact area increases with the applied pressure. Comparing the circled regions in the figure, the area (A) of the asperities that are already in contact does not appear to change significantly, even when the pressure becomes six times larger. This can be attributed to the porous structure of the friction lining. A further examination of the images shows that the elastic deformation of the entire friction material structure appears to have a first-order effect on the real contact area change, by bringing more asperities into

0.5 MPa

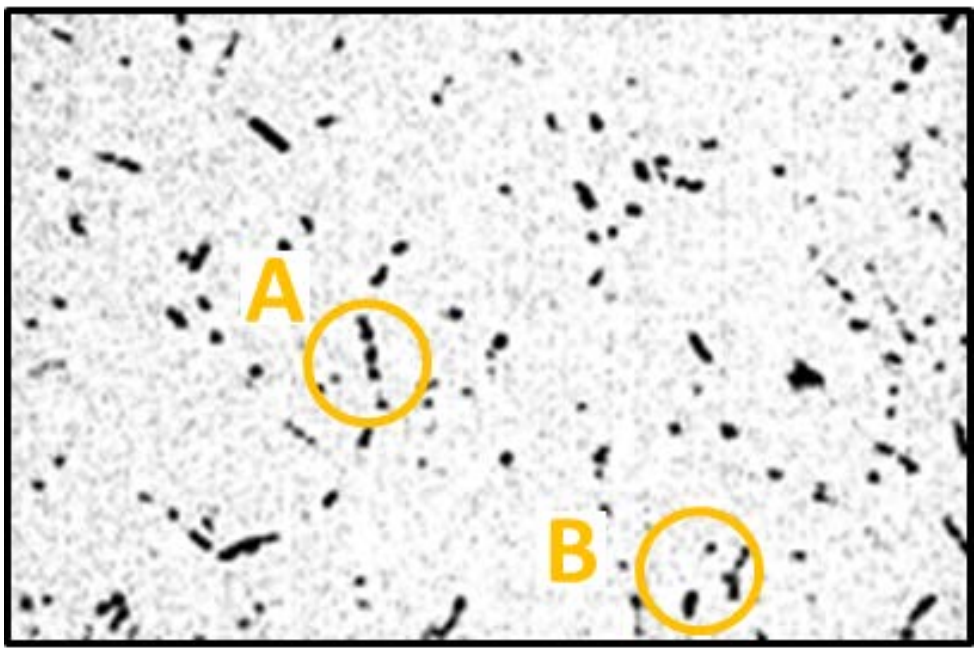

3.0 MPa

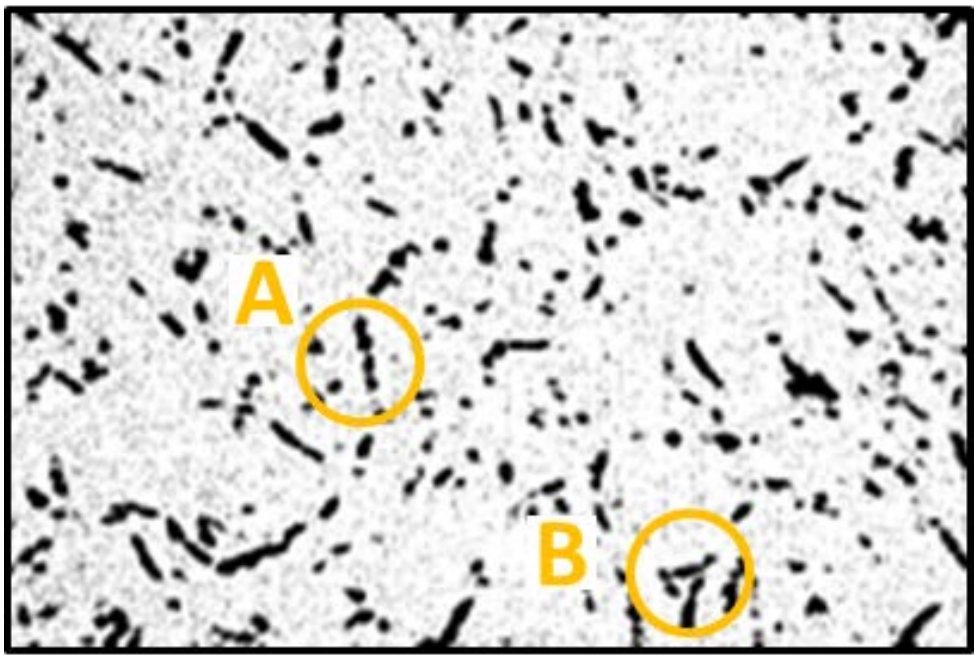

Figure 5.23: Digitized images of real contact are at two different surface pressures

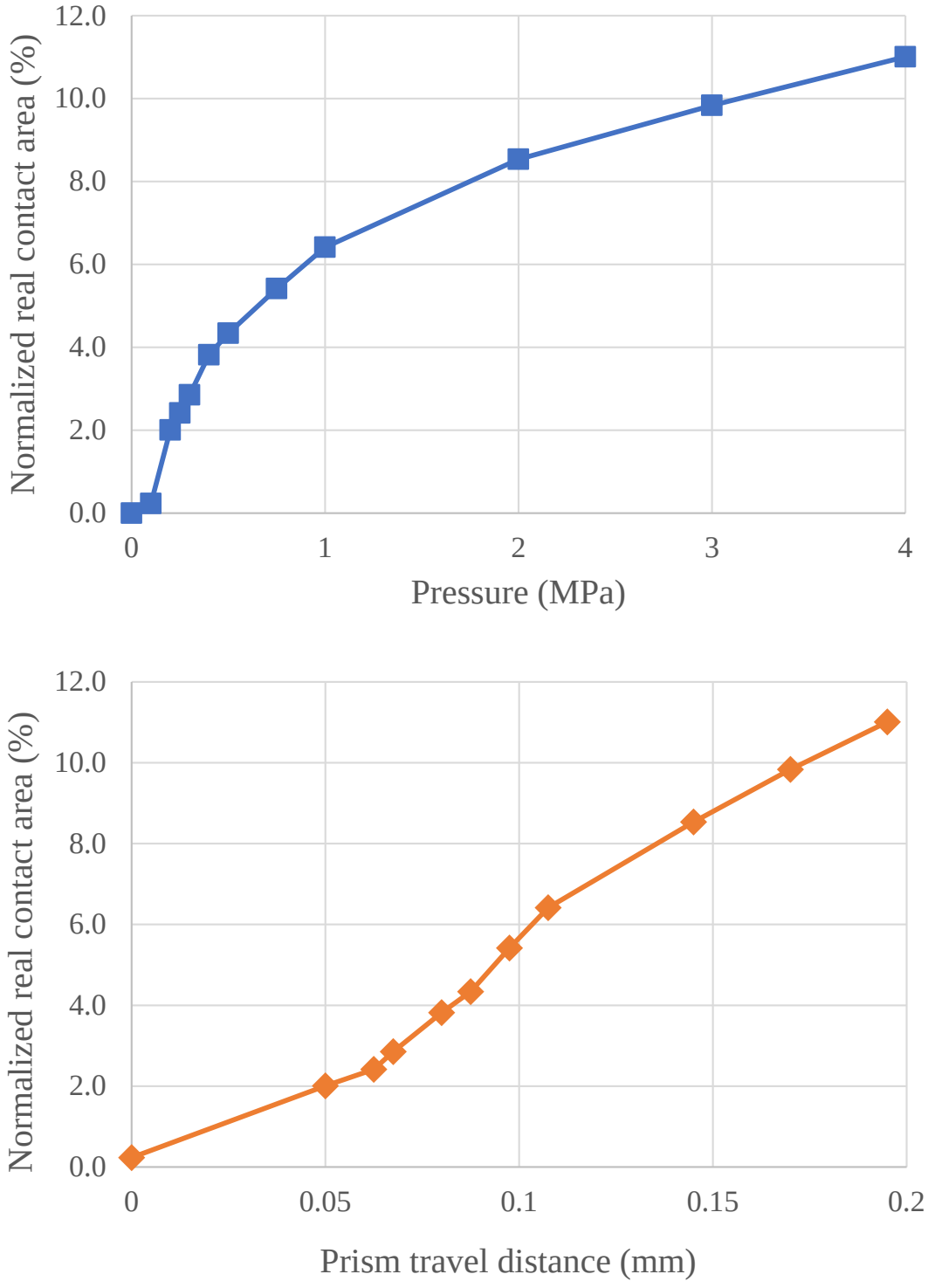

Figure 5.24: Normalized real contact area with respect to surface pressure and prism travel distance

contact under loaded conditions, as observed in (B), instead of the deformation of asperities. The real contact area as a function of the applied load recorded on the prism measurement device is shown in Figure 5.24. The real contact area is shown as a function of the applied pressure and the prism travel distance. When coupled with the surface roughness measurements, the relationship between the pressure, real contact area, and prism travel distance becomes the foundation of the empirical asperity contact model .

5.5.4 Empirical Asperity Contact Model

To add the asperity contact process to the baseline squeeze film CFD model, a relationship is required between the asperity contact pressure, p_{con}, the real contact area, A_r, and the nominal gap or the film thickness, h, between the two plates.

The real contact area measurements provide the relationship between the real contact area, A_r, and the asperity contact pressure, p_{con}, which is shown in Figure 5.24. Although the prism travel distance is measured, the film thickness,h, is not directly observable in the prism device. In order to find the relationship between p_{con}, A_r, and h, the real contact area measurements and surface roughness measurements must be combined.

Figure 5.25 defines the key parameters that are used in the empirical asperity contact model. Let the nominal distance between the separator and friction plates be denoted by $h(L)$, where L is the load. The nominal surface of the friction material is where the mean height of the asperities is zero, as previously defined in Figure 5.20. The nominal thickness of the friction lining, $H_n(L)$, is the distance between the nominal surface and the surface of the core of the friction plate. The total distance between the separator plate and the surface of the core plate of the friction plate is defined by $H_p(L)$. Since there are two layers of friction materials attached to each side of the core friction plate, $H_p(L)$ represents half of the prism travel distance under

a given load L.

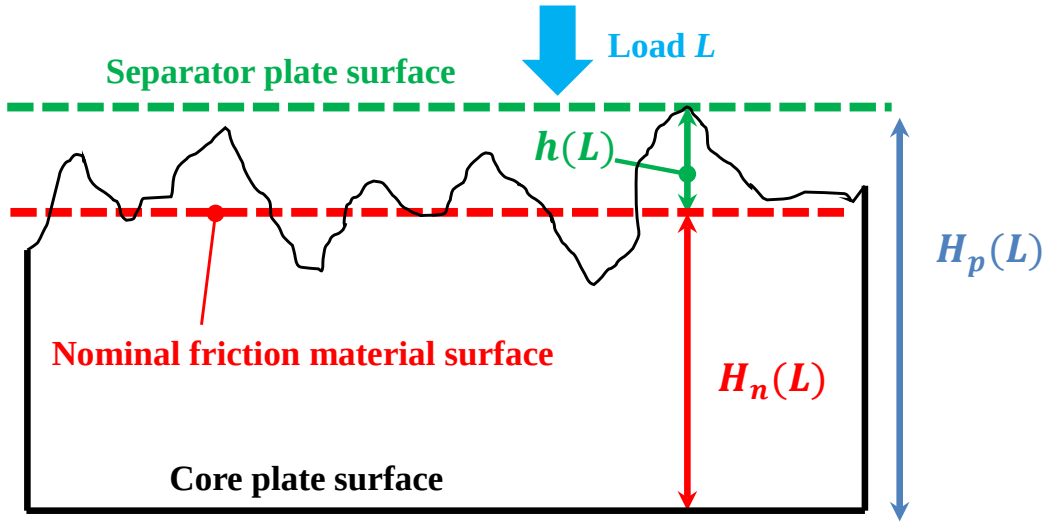

Figure 5.25: Asperity contact model parameters

Consider two load values L_i and L_j, such that $L_i < L_j$. The dependent variables for the two loads can be expressed as $h(L_i)$, $H_n(L_i)$, $H_p(L_i)$, and $h(L_j)$, $H_n(L_j)$, $H_p(L_j)$, respectively, for the following relations. Hence

$$h(L_i) = H_p(L_i) - H_n(L_i) \tag{5.36}$$

$$h(L_j) = H_p(L_j) - H_n(L_j) \tag{5.37}$$

According to the elasticity moduli characterization in Figure 5.18, the deformation of the friction material structure is insensitive to the overall thickness, H_p, i.e. the ratio of h to H_n. Thus, the rate of thickness change is considered to be uniform across the friction material, resulting in the following linear equation

$$\frac{\Delta h(L_{ij})}{h(L_i)} = \frac{\Delta H_p(L_{ij})}{H_p(L_i)} \tag{5.38}$$

where $\Delta h(L_{ij}) = h(L_j) - h(L_i)$, and $\Delta H_p(L_{ij}) = H_p(L_j) - H_p(L_i)$. Equation (5.38)

can be rearranged as follows

$$\Delta H_p(L_{ij}) = \frac{H_p(L_i)}{h(L_i)}\Big(\Delta h(L_{ij})\Big) = \frac{\Delta h(L_{ij})}{k} \tag{5.39}$$

$$\xi = \frac{H_p(L_i)}{h(L_i)} \tag{5.40}$$

where ξ is defined as a scaling factor that determines the effective thickness of the asperity layer with respect to the friction material of thickness H_p. This scaling factor can be empirically estimated by combing the surface profile measurements and the contact area measurements.

A kernel distribution is used to fit the PDF of surface asperity measurements in Figure 5.21. The kernel distribution is defined as follows

$$F_n(x) = \frac{1}{n \times BW}\sum_{i=1}^{n} K\Big(\frac{x - x_i}{BW}\Big) \tag{5.41}$$

where n is the sample size, x_i is the data sample from the distribution, $K(\cdot)$ is the kernel smoothing function that integrates to 1, and $BW = 1.17$ is the bandwidth. This PDF is used to estimate the number of asperities that come into contact under general load conditions.

When a wet clutch is actuated, a load is applied between the friction and separator plates. As the nominal distance, $h(L)$, between the plates decreases, more and more asperities come into contact. The area under the PDF, integrated between h and ∞, gives the total number of asperities, N, (normalized) in contact at a given gap, h, between the plates. The function that calculates N can be described by

$$N(h) = 7.93 \times 10^{-5} \times h^4 + 3.70 \times 10^{-3} \times h^3 - 0.037 \times h^2 - 3.91 \times h + 49.3 \tag{5.42}$$

As the distance h decreases, the number of asperities in contact, N, increases. The

real contact area, A_r, is characterized as a function of pressure, p_{con}, as well as H_p, as shown in Figure 5.26. The real contact area as a function of H_p can then be represented in the following form

$$A_r(H_p) = -1.20 \times 10^{-7} \times H_p^4 + 4.30 \times 10^{-5} \times H_p^3 - 3.70 \times 10^{-2} \times H_p^2 - 0.003 \times H_p + 8.97 \tag{5.43}$$

Using Equations (5.39), Equation (5.43) can be expressed as a function of the nominal

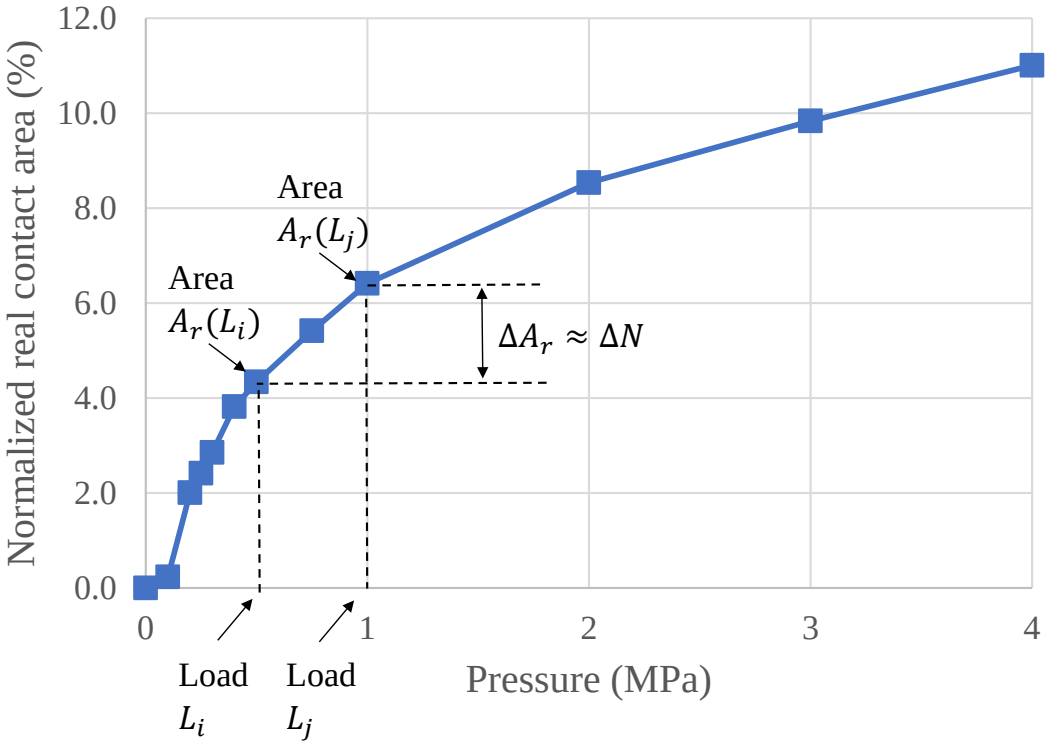

Figure 5.26: Normalized real contact area as a function of pressure

surface distance, h, as follows

$$A_r(h) = -1.20 \times 10^{-7} \times (h \times \xi)^4 + 4.30 \times 10^{-5} \times (h \times \xi)^3 - 3.70 \times 10^{-2} \times (h \times \xi)^2 - 0.003 \times (h \times \xi) + 8.97 \tag{5.44}$$

As previously discussed, it is unlikely that the friction material deforms significantly upon contact under load conditions due to the large elastic modulus. The microscopic image also supports the fact that the contact area increases due to an increase in the number of asperities in contact, as shown in Figure 5.23. As a first approximation, it is assumed that the real contact area increases in proportion to the number of asperities in, contact under load conditions. Hence, in a normalized expression, we can write

$$\Delta A_r \approx \Delta N \tag{5.45}$$

Equation (5.45) can be integrated over asperity height, i.e.

$$\Delta = \int_{h_1}^{h_2} (N - A_r) dh = 0 \tag{5.46}$$

where the values h_1 and h_2 are chosen to be the minimum and maximum gap when plates are in contact. Substituting the Equations (5.43) and (5.44) into Equation (5.46), Δ is obtained as a function of k, as follows

$$\Delta = 6.50 \times 10^{-2} \times \xi^3 - 1.35 \times \xi^2 + 6.00 \times \xi + 2.02 \tag{5.47}$$

The function Δ is minimized to obtain the scaling factor $\xi = 14.0$. The scaling factor is then used to express the real contact area, A_r, and the contact pressure, p_{con}, as a function of the distance between the plates, h, which are shown in Equations (5.48) and (5.49), respectively. Hence

$$A_r = 0.0603 \times h^3 - 2.06 \times h^2 + 21.4 \times h - 60.9 \tag{5.48}$$

$$p_{con} = 0.12 \times h^2 - 3.46 \times h + 25.1 \tag{5.49}$$

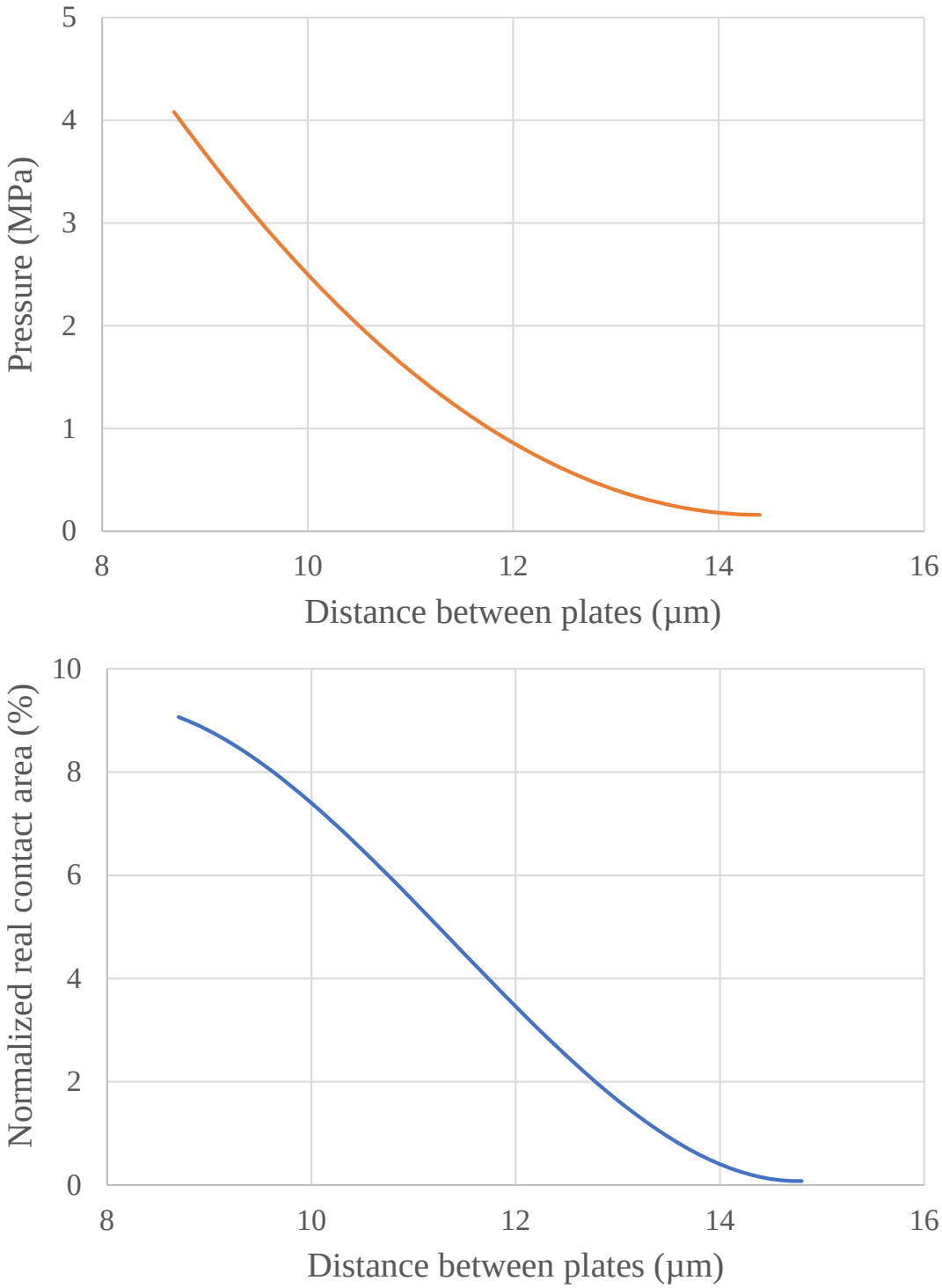

Figure 5.27: Empirical asperity contact model

These two relationships constitute the empirical asperity contact model, representing actual friction material characteristics, which are plotted in Figure 5.27 for the region that is critical for modeling clutch engagement behavior. This asperity model can be utilized to compute the real contact area and asperity pressure as a function of nominal distance between the friction and separator plates. It can be integrated with the baseline hydrodynamic model to provide actual representation of asperity contact behavior for enabling high fidelity transmission shift simulations.

5.6 Model Validation

5.6.1 Slip Test

An engagement bench test was conducted in the Research and Development Center of F.C.C. Corporation in Hamamatsu, Japan, to validate the performance of the CFD model. The test conditions are summarized in Table 5.4. An advanced slip tester is utilized, which is shown in Figure 5.28. A complete clutch module, which includes 2 friction plates and 3 separator plates, is mounted in the test chamber. The motor spins the friction plates, while the separator plates remain stationary. A controlled amount of ATF is supplied through the center shaft into the frictional interfaces. One of the benefits of using this tester is that a complete clutch assembly can be installed to realistically duplicate the clutch engagement stroking mechanism.

The clutch behavior is first examined empirically in a test vehicle. The bench tests are conducted using the in-vehicle clutch slip and pressure profiles for specifically replicating the torque and inertia phases of shifting, and duplicating the real clutch engagement control strategy, which is shown in Figure 5.29. There are three different sets of profiles to represent the three distinct throttle positions. For higher throttle positions, the corresponding speed and pressure values are larger. The shape of these profiles are adjusted to make it easy to input to the tester, and eliminate some

Table 5.4: Test conditions for engagement bench test

Sampling frequency (Hz)	1,000
Clutch pack clearance (mm)	0.4, 0.8
Friction lining inner and outer radii (mm)	73.5, 86.5
Temperature at inlet (°C)	0, 50, 100
ATF flow rate (cc/min)	200, 500, 800
Groove pattern	Flat, T-shape groove
Number of plates	2 Friction and 3 Separator plates

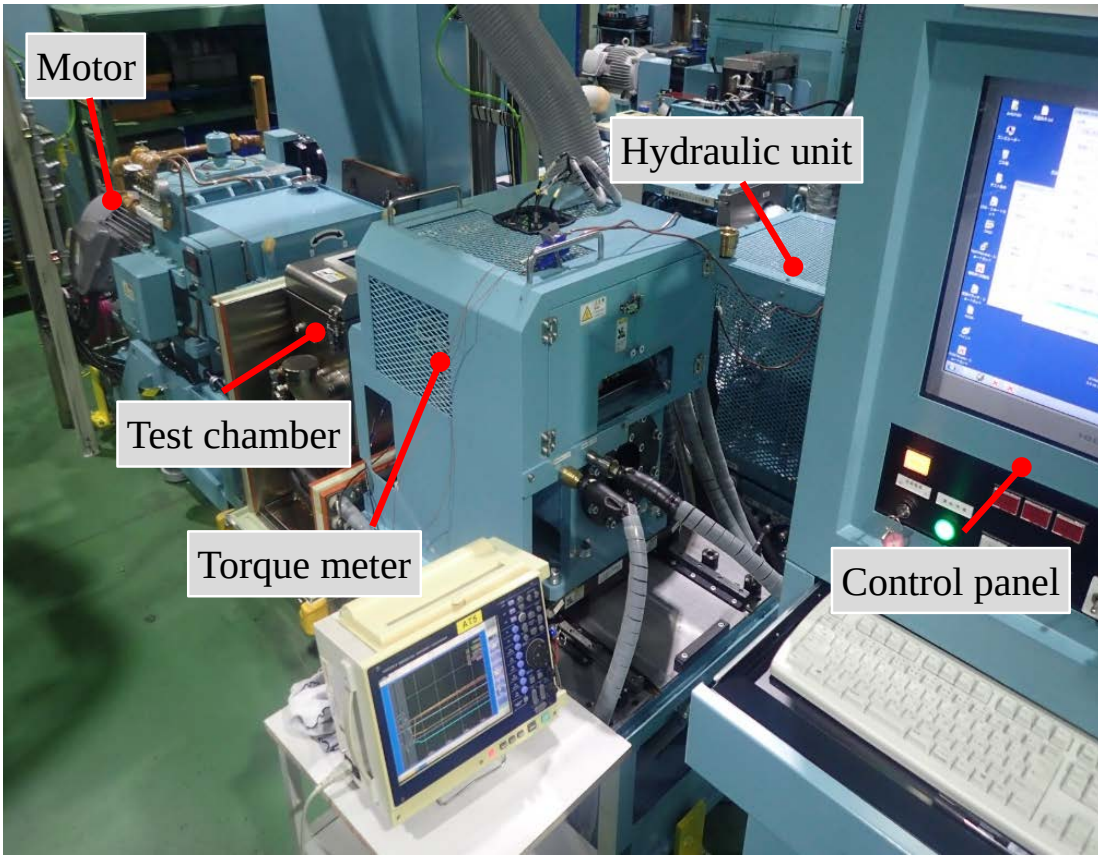

Figure 5.28: Engagement bench tester - slip tester

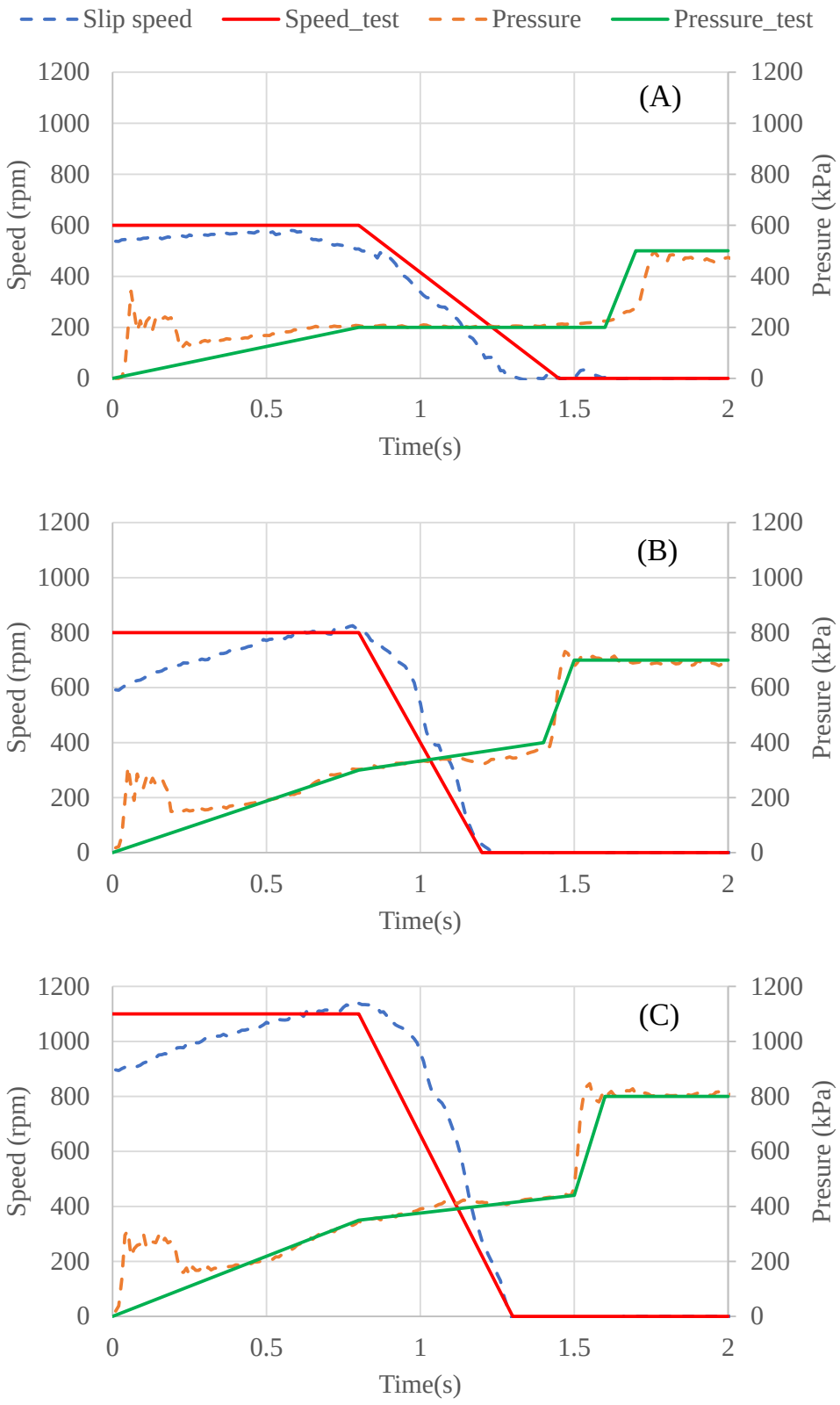

Figure 5.29: Slip speed and pressure profiles for advanced bench tests

unnecessary noise.

Some of the bench test results are summarized in Figures 5.30 and 5.31. In Figure 5.30, the clutch behavior is examined under low throttle position with different temperatures. The measurements show that the clutch behavior is temperature dependent, which is due to the viscosity change under different temperatures. The viscosity of the ATF is different at 0 °C and 100 °C. At 0 °C, the viscosity of the ATF is larger, thus the torque before stroking is larger than that at 100 °C. At 100 °C, the viscosity is smaller, and offers little resistance to the stroking process, hence the engagement process starts at a relative early time, compared to that at 0 °C. Finally, Figure 5.31 shows the results corresponding to different groove patterns. They also have an effect on the clutch behavior. Grooves provide additional conveyance for the ATF to evacuate from the interface, which accelerates the engagement process.

In both Figure 5.30 and 5.31, the pressure applied to the piston is increasing monotonically. However, the torque rise occurs at different times. This indicates that potentially there are other forces acting on the piston that oppose the stroke motion. It is assumed that this unknown force may be due the friction of the rubber seal between the piston and the chamber. To validate this assumption, attempts were made to measure and characterize the seal drag force.

5.6.2 Seal Drag Model

In the current clutch module test, there are two seal rings for the clutch piston, one on the outer radius, and the other on the inner radius. The nominal dimensions are shown in Figure 5.32. The seal drag force is characterized using a low speed spin test conducted on the same bench model. The friction plates are rotating at 5 rpm, and the piston is stationary. The applied pressure is increased gradually in order to capture the initial torque rise, which is shown in Figure 5.33. The piston overcomes the return spring force and the seal drag needed to push the plates together, causing

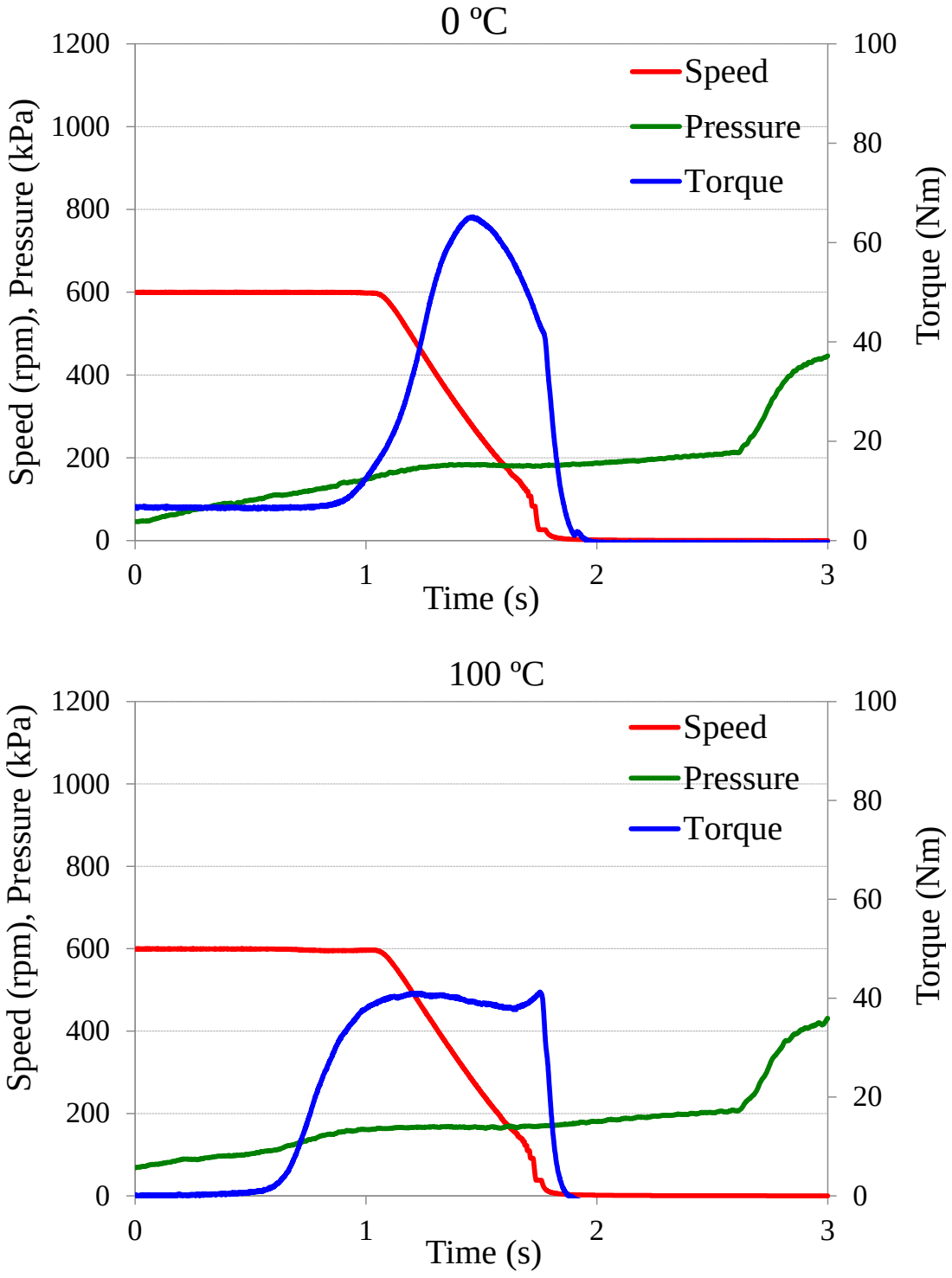

Figure 5.30: Bench test results for flat plate at different temperatures with 200 cc/min flow rate and 0.4 mm clutch pack clearance

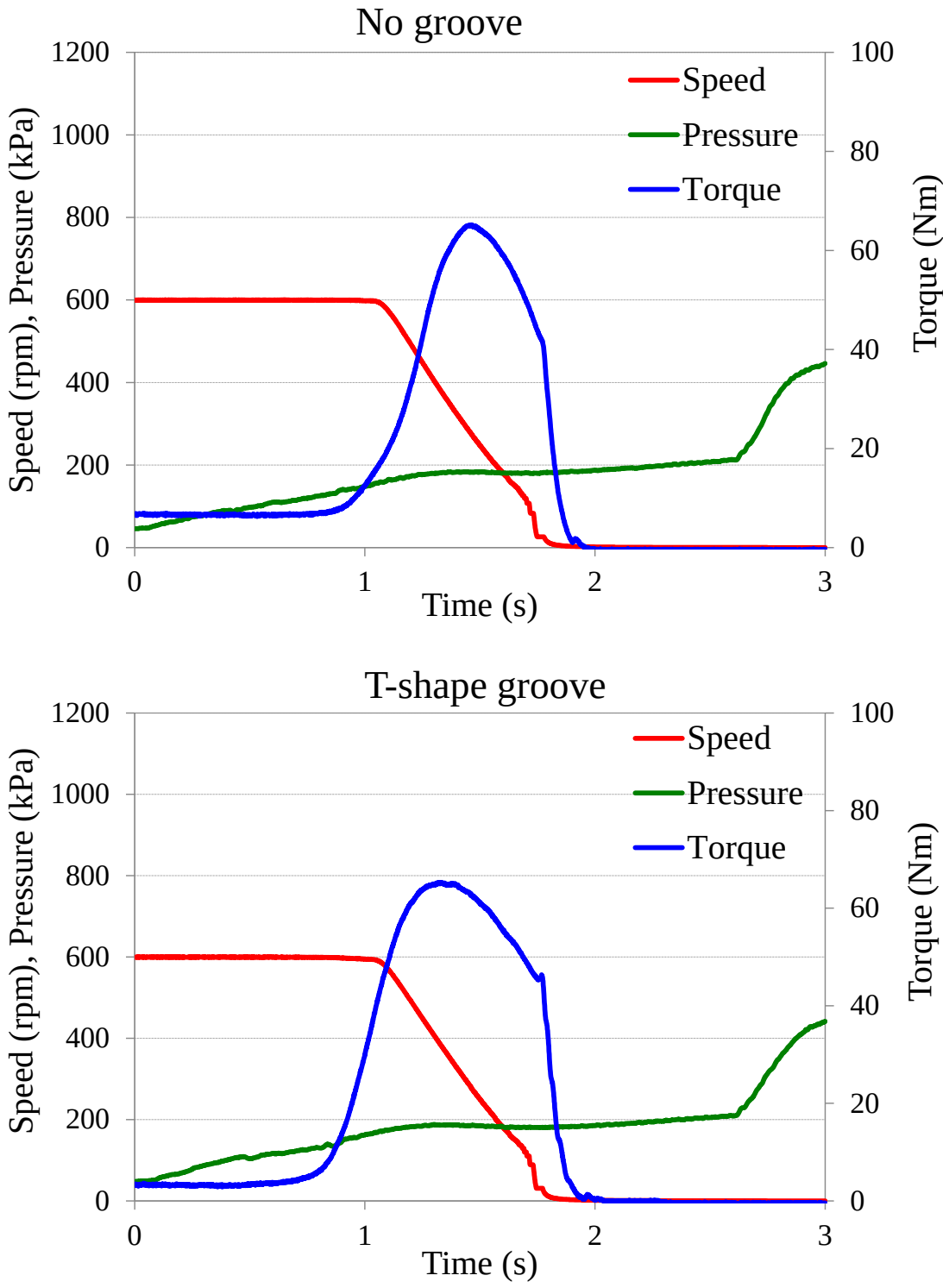

Figure 5.31: Bench test results for different groove patterns at 0 °C with 200 cc/min flow rate and 0.4 mm clutch pack clearance

a torque rise. The actual return spring force is measured, and subtracted form the piston force to calculate the seal drag, which is written as follows

$$\begin{aligned} \text{Seal drag force} &= \text{Piston force} - \text{Return spring force} \\ &= 901 - 692 = 209\ N \end{aligned} \tag{5.50}$$

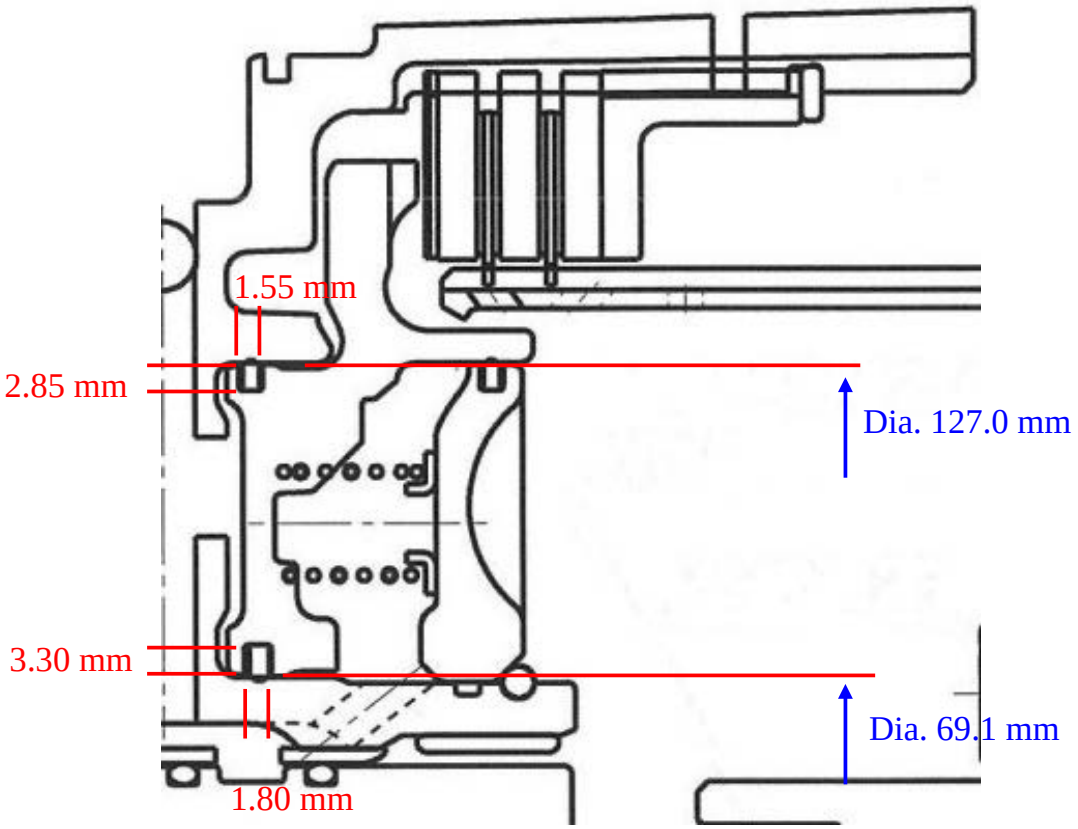

Figure 5.32: Basic seal design parameters in clutch pack

Note that the 209 N seal drag force represents the static friction. During the piston stroking process, the seal drag varies as a function of applied pressure. Thus, the seal drag should increase with respect to the applied pressure. Toward the end of stroking (around 40 µm), the seal drag diminishes quickly. The deformation of the seal rings can accommodate a finite film thickness change without sliding at the very end, thus reducing the contribution to the seal drag.

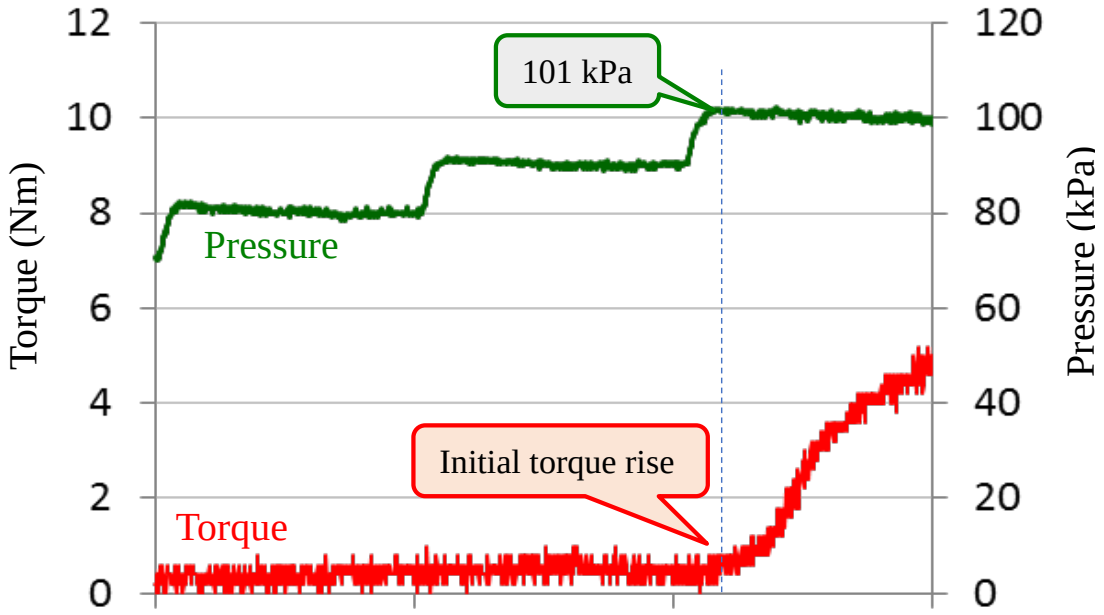

Figure 5.33: Seal drag force characterization

This can be verified by a simple calculation of the seal deformation during stroking. The piston force profile of the low throttle position is utilized as an example, which is shown in Figure 5.30 and 5.31. At time $t = 1.0\,s$, the applied pressure is approximately 150 kPa. The elastic modulus, E, for the seal ring is 10.0 MPa. For the rings at inner and outer radii, we may assume that they have the same compression, which is Δl mm. Then, the strain ϵ_{ID}, stress σ_{ID}, and force F_{ID} acting on the inner seal ring are as follows

$$\epsilon_{ID} = \frac{\Delta l}{1.80}$$

$$\sigma_{ID} = E \cdot \epsilon = \frac{\Delta l}{0.18}\ \text{MPa}$$

$$F_{ID} = \sigma_{ID} \times A_{ID} = \frac{\Delta l}{0.18}\ \text{MPa} \times 716.37\,\text{mm}^2 \tag{5.51}$$

Similarly, the strain ϵ_{OD}, stress σ_{OD}, and force F_{OD} acting on the outer seal ring are

as follows

$$\epsilon_{OD} = \frac{\Delta l}{1.55}$$

$$\sigma_{OD} = E \cdot \epsilon = \frac{\Delta l}{0.155}\ \text{MPa}$$

$$F_{OD} = \sigma_{OD} \times A_{OD} = \frac{\Delta l}{0.155}\ \text{MPa} \times 1137.10\,\text{mm}^2 \tag{5.52}$$

Therefore, the applied pressure force acting on the piston is balanced by the inner and outer seal rings, i.e.

$$p \times A_{piston} = F_{ID} + F_{OD}$$

$$\Delta l = 0.118\ \text{mm} \tag{5.53}$$

At time $t = 1.0\,s$, the film thickness of a single interface is 0.035 mm, and the total clearance for the clutch pack with 4 interfaces should be 0.14 mm, which is consistent with film thickness back-calculated from the test data.

Since the changing seal drag during the stroking process cannot be measured directly, a seal drag model is developed to predict the seal drag behavior. The net force acting on the piston can be back-calculated through the film thickness change by Equation (5.9). The difference between the applied force and the back-calculated force should be equal to the seal drag. Assuming that the seal drag has a linear relationship with the applied force, a straight line may be used to fit the seal drag, as shown in Figure 5.34. As previously discussed, at approximately $1\,s$, the deformation of the seal can accommodate a finite film thickness change without sliding to the very end. Then, the seal drag diminishes quickly, and drops to 0. Although the preceding analysis was based on the low throttle position, the same methodology can be used for other cases as well, therefore the seal drag model can be incorporated in the overall

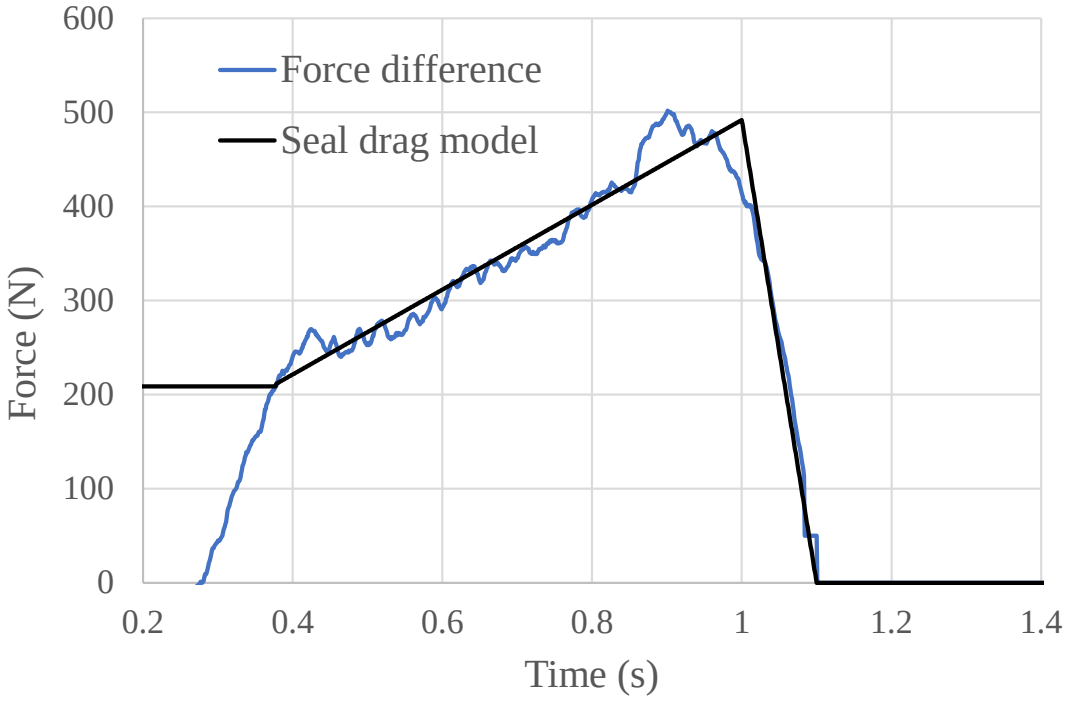

Figure 5.34: Seal model to capture the seal change within stroking process

clutch model.

After obtaining the seal drag, the net force applied to the piston can be calculated by subtracting the return spring force and the seal drag. The net force and slip speed profiles are used as input to the engagement model, and the simulation results are compared with the test data, as shown in Figure 5.35. The applied force is filtered by a low-pass filter to remove some of the noise. The Coulomb friction model, commonly used in clutch design, is also shown for comparison. The Coulomb friction model assumes that the torque is transferred through pure friction, utilizing the Coulomb friction force to calculate the torque transferred between the plates. The Coulomb friction torque has a linear dependence on the input force. It can be seen that the Coulomb friction model cannot capture the hydrodynamic behavior during the engagement process.

Compared with the Coulomb friction model, the initial slope of the CFD results

agrees well with the test data, which means the model successfully captures the hydrodynamic behavior of a wet clutch. At around $t = 1.2\,s$, after the rotating speed drops, the asperity contact takes place. In the current model, the asperity contact is set to be turned on when the film thickness of the ATF is smaller than $18\,\mu m$. After asperity model is triggered, the total torque is the sum of the hydrodynamic and asperity contact torque. At the end of the simulation, the torque drops to zero. The reason is that there is no relative rotation, and no torque transfer between the two plates.

For pattern B, the rotating speed and apply force increase. There is a small difference at the very beginning. This is due to the noise from the data acquisition system. The small bump on the simulation results correspond to the bump on the applied force. If the bump on the force curve is eliminated, the bump on the simulation results would disappear. As the apply force increases, the asperity contact takes place at an early time, before the rotating speed drops, which leads to a larger peak torque.

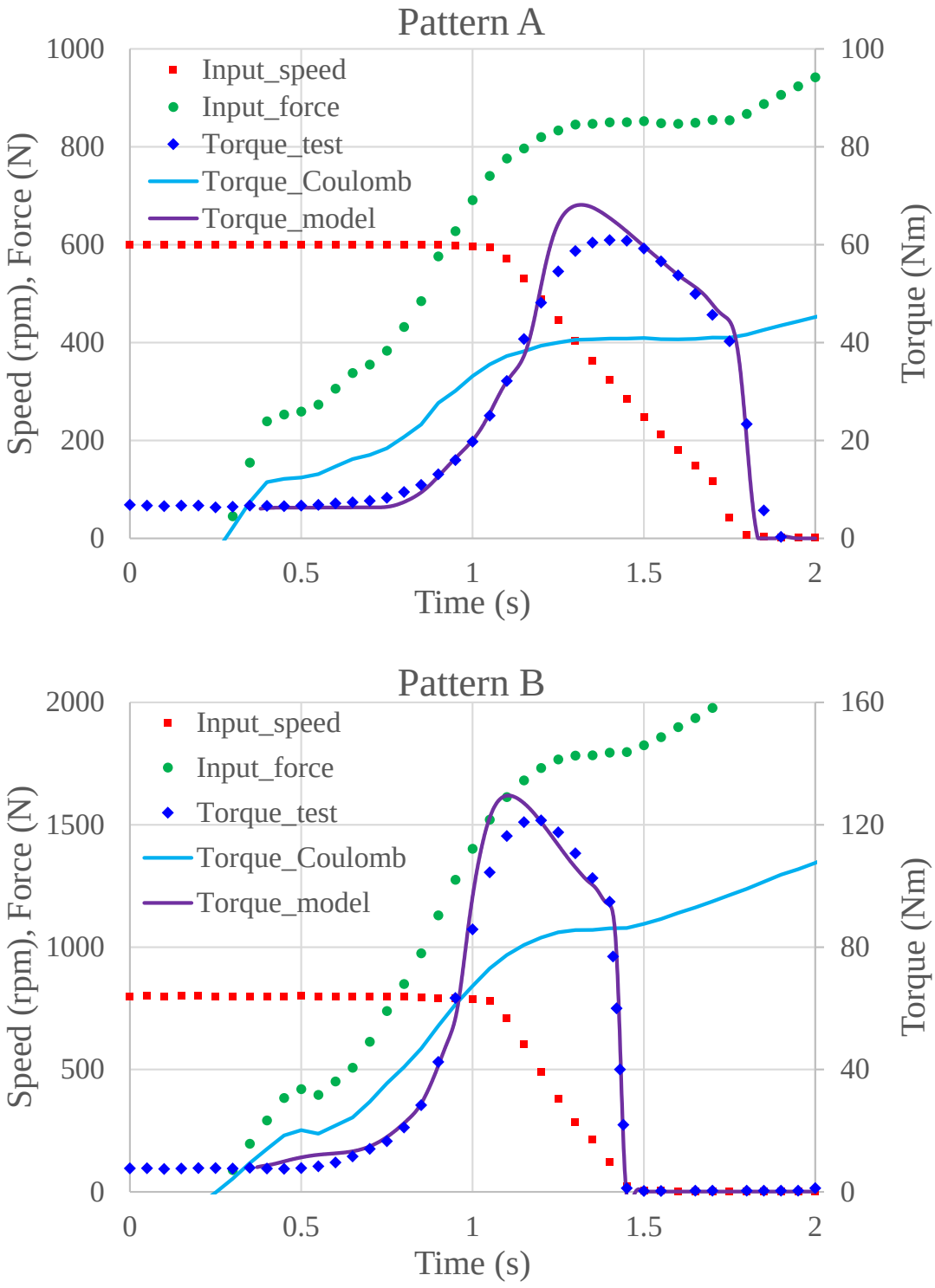

Figure 5.35: Simulation results vs. test data for flat plate for low and medium throttle positions

CHAPTER VI

Conclusions

6.1 Summary and Conclusions

In this research, a multi-physics model is developed to predict the dynamic behavior of a wet clutch in an automatic transmission system. The prediction and control of clutch dynamics are of major significance in fuel efficiency, thus optimal operational characteristics are sought to reduce drag and improve shifting quality. The research is motivated by the need to better understand the physics occurring in a wet clutch system. The model simulates clutch operations under open, and engagement conditions. The present work overcomes previous limitations by constructing comprehensive CFD models under different conditions. The physics of wet clutch behavior involves two-phase flow or ATF and air, fluid structure interactions, rotating frames, asperity contact, heat transfer, porous media flow, dynamic meshing, etc.

The main contributions of this dissertation are:

1. A single-phase model with SRF is developed to study drag torque behavior at low speeds. The characteristics of an open clutch represent a complicated problem that it not easily explained. The model is validated with analytical solutions. The results of single-phase model show a large hydrodynamic pressure within the grooves of the friction plate. Though the application of the single-

phase model is limited, it can be used to study the effect of different design parameters. (Chapter 3)

2. A two-phase CFD model with MRF is developed for investigating open clutch drag torque behavior. The model includes detailed design features to capture the complexity of fluid-structure interactions, and to reflect real working conditions in the transmission system. A series of studies is conducted to evaluate the number of inner iterations, time steps, and initial and boundary conditions in terms of convergence behavior. Selecting appropriate settings is critical for achieving mass and momentum balance in a dispersed two-phase flow towards stable convergence. The models capability is validated with clutch drag test data. The model successfully captures the time and magnitude of the peak drag torque while accounting for key design features such as groove and drainage geometry. The total drag torque is decomposed into viscous and pressure elements to quantify the torque transfer mechanisms for a given groove design. Interface visualization tests are conducted to investigate fluid-structure interactions as a function of rotational speed. The use of the VOF method in the model captures the overall aeration process, as observed in the validation tests. The CFD model offers physical insight into complex open clutch behaviors, and provides a valuable means for drag improvement, complementing hardware-based clutch design processes. (Chapter 3)

3. A statistical method for determining the distribution of clearances in a wet clutch pack is presented. The predictive ability of the method is validated with bench test data. The drag torque from a uniform gap distribution can be calculated either by a statistical or an analytical method. The drag torque of a non-uniform gap distribution can be measured experimentally. Thus, the ratio of the experimental and analytical torques can be calculated. Shape parame-

ters of the beta distribution can be back-calculated from this torque ratio to determine the probability density function that describes the plate motion statistically. Alternatively, a different probability density function may be utilized for the model calibration with experimental data. Finally, the computed probability density function yields an analytical representation of the plate motion to provide a physical insight into open clutch drag torque behavior. The same statistical methodology can be extended to higher speed ranges, where single-phase flow in no longer a valid assumption for drag torque analysis. This can be accomplished by coupling the present statistical method with the multi-phase CFD model, thus eliminating the need for an analytical solution. (Chapter 4)

4. The clutch engagement process is modeled using the open clutch solution as an initial condition. A squeeze film model is developed, coupled with an iterative scheme. The iterative scheme allows use of the actuator piston force as an input to the computation of ATF film change while ensuring force balance at every time step. The model also explicitly accounts for the effects of the plate mass on the squeeze film process. The results are validated using analytical solutions under the influence of various boundary conditions. Based on transient CFD simulations, a numerical analysis is conducted to provide physical insight into temperature dependent torque characteristics. The flow through the porous friction material is simulated using Darcy's law. Mechanical contact is simulated based on the asperity contact model. The heat generation and exchange at the interface are captured by a heat transfer model. Subsequently, these models are combined with the squeeze-film flow model to create an integrated clutch engagement model. The clutch behavior is first examined empirically in a test vehicle. An advanced bench test is conducted using in-vehicle clutch slip and pressure profiles for specifically replicating the torque and inertia phases of shifting. It is shown that the CFD model together with advanced clutch bench

testing provide a valuable insight to in-vehicle clutch engagement behaviors. (Chapter 5)

5. An empirical asperity model is developed based on the examination of friction material properties. The wet clutch friction material is examined in detail for its contact behavior under various load conditions. The surface roughness measurements show that the asperity height distribution is asymmetric, and represented by the kernel distribution. The test data show that the real contact area is proportional to the number of asperities that come into contact, as the material structure deforms during engagement. The model can be utilized to compute the real contact area and pressure as a function of nominal distance between the friction and separator plates. The asperity model can be integrated with the squeeze film model, providing actual representation of asperity contact behavior for enabling high fidelity transmission shift simulations. (Chapter 5)

During the development of the model, the influence of each component of the model on wet clutch operation is studied independently. The results of this study provide physical insight into complex fluid interactions for wet clutches. This model can be integrated in a shape optimization study to optimize the number and shape of grooves for fuel efficiency and shift quality.

6.2 Future Research

The present work overcomes previous limitations by constructing a comprehensive computational fluid dynamics model for multiphase flow in a non-inertial frame. However, there are other areas that need further investigation.

First, a parametric study of wet clutch design factors presents an unlimited horizon for future work. These include the optimal plate dimensions, pattern of grooves and plate waviness, the physical properties of the friction material, the ATF properties,

etc. By applying the present open clutch model, an optimal design can be found to further reduce the energy loss in an automatic transmission, and improve fuel efficiency.

Second, the present model is based on a simplified two-plate system. This should be extended to include the complete clutch pack. The complete model requires an increased computational effort, but it will eliminate unknown noise factors, and should provide more comprehensive results.

Third, the empirical asperity contact model is obtained through the combination of real contact area measurements and surface roughness measurements. To make this model more reliable, the contact area measurement device should be redesigned to include the capability to measure the film thickness at the same time. Also, different friction materials should be studied to make the model more versatile.

Finally, the computational effort needed by the CFD model is very large. Without a high performance computer, it would be impossible to obtain the results shown in this thesis within a reasonable time. It is also impossible to employ the present CFD model in real time simulations. Therefore, research on further acceleration of the model, and development of approximate but equally consistent models for use in real-time control of an automatic transmission would be desirable.

APPENDIX

APPENDIX A

Conditional Probability

The parameters listed in Table 4.5 can be obtained using the definition of conditional probability and Bayes' theory, i.e.

$$P(A|B)P(B) = P(A \cap B) = P(B \cap A) = P(B|A)P(A) \tag{A.1a}$$

$$P(A|B) = \frac{P(B|A)P(A)}{P(B)} \tag{A.1b}$$

where the conditional probability of event A, given the occurrence of event B, is denoted by $P(A|B)$. The probability of the joint of events A and B by $P(A \cap B)$. $P(B|A)$ is the conditional probability of event B, given the occurrence of event A. $P(A)$ and $P(B)$ are the marginal (or unconditional) probabilities of events A and B, respectively. In the case of clutch pack modeling, $f(x_1|y_1)$ can be considered as the conditional probability of variable x_1 within the range $[0,\ y_1]$, given that y_1 takes a particular value according to its own marginal probability density function $f(y_1)$, which is defined within the entire sample space of $[0,\ y_{1+2+3}]$. Similarly, $f(y_1|x_1)$ is the conditional probability of variable y_1 within the range $[x_1,\ y_{1+2+3}]$, given that x_1 takes a particular value according to its own marginal probability density function $f(x_1)$, which is defined within the range of $[0,\ y_{1+2+3}]$. Then the Bayes theorem can

be applied as follows

$$f(x_1|y_1) = \frac{(x_1-0)^{p-1}(y_1-x_1)^{p-1}}{B(p,p)(y_1-0)^{2p-1}} = f(y_1|x_1)f(x_1)\frac{1}{f(y_1)}$$
$$= \frac{(y_1-x_1)^{p-1}(y_{1+2+3}-y_1)^{4p-1}}{B(p,4p)(y_{1+2+3}-x_1)^{5p-1}} \frac{x_1^{p-1}(y_{1+2+3}-x_1)^{5p-1}}{B(p,5p)y_{1+2+3}^{6p-1}} \frac{B(2p,4p)y_{1+2+3}^{6p-1}}{y_1^{2p-1}(y_{1+2+3}-y_1)^{4p-1}} \tag{A.2}$$

The shape parameters of the marginal beta distributions $f(x_1)$ and $f(y_1)$ are given according to the order statistics as $(p,\ 5p)$ and $(2p,\ 4p)$, respectively. For the conditional beta distributions $f(x_1|y_1)$ and $f(y_1|x_1)$, the shape parameters are determined by pairing the exponentiation terms in Equation (A.2) and assigning the same exponents to the same base expressions. In order to verify the validity of Equation (A.2), first all the exponentiation terms should be cancelled out, then the following relationship containing the beta functions needs to be proved

$$\frac{B(p,p)\ B(2p,4p)}{B(p,4p)\ B(p,5p)} = 1 \tag{A.3}$$

Equation (A.3) can be rewritten using the following property of the beta function where p and q are positive integers, i.e.

$$B(p,q+1) = B(p,q)\frac{q}{p+q} \tag{A.4}$$

By applying the rule shown in Equation (A.3) multiple times, and using the fact that the beta function is symmetric or $B(p,q) = B(q,p)$, the beta functions in Equation

(A.4) can be expressed as follows

$$B(p,4p) = B(p, p + \underbrace{1+1+\cdots+1}_{3p}) = B(p,p)\prod_{n=0}^{3p-1}\frac{p+n}{2p+n} \tag{A.5}$$

$$B(p,5p) = B(p, p + \underbrace{1+1+\cdots+1}_{4p}) = B(p,p)\prod_{n=0}^{4p-1}\frac{p+n}{2p+n} \tag{A.6}$$

$$B(2p,p) = B(p,2p) = B(p, p + \underbrace{1+1+\cdots+1}_{p}) = B(p,p)\prod_{n=0}^{p-1}\frac{p+n}{2p+n} \tag{A.7}$$

$$\begin{aligned} B(2p,4p) &= B(2p, p + \underbrace{1+1+\cdots+1}_{3p}) \\ &= B(2p,p)\prod_{n=0}^{3p-1}\frac{p+n}{3p+n} = B(p,p)\prod_{n=0}^{p-1}\frac{p+n}{2p+n}\prod_{n=0}^{3p-1}\frac{p+n}{3p+n} \end{aligned} \tag{A.8}$$

Combining Equations (A.3) - (A.8) yields the following relationship

$$\frac{B(p,p)B(p,p)\prod_{n=0}^{p-1}\frac{p+n}{2p+n}\prod_{n=0}^{3p-1}\frac{p+n}{3p+n}}{B(p,p)\prod_{n=0}^{3p-1}B(p,p)\prod_{n=0}^{4p-1}\frac{p+n}{2p+n}} = 1 \tag{A.9}$$

After cancelling out all $B(p,p)$ terms and rearranging, we obtain

$$\prod_{n=0}^{p-1}\frac{p+n}{2p+n}\prod_{n=0}^{3p-1}\frac{p+n}{3p+n} = \prod_{n=0}^{4p-1}\frac{p+n}{2p+n}\prod_{n=0}^{3p-1}\frac{p+n}{2p+n} \tag{A.10}$$

Equation (A.10) can be rearranged further. It can be shown that the left and right sides of this equation are equal in the following way

$$\prod_{n=0}^{p-1}\frac{p+n}{2p+n}\prod_{n=0}^{3p-1}\frac{2p+n}{3p+n} = \prod_{n=p}^{4p-1}\frac{p+n}{2p+n}\prod_{n=0}^{p-1}\frac{p+n}{2p+n} = \prod_{n=0}^{3p-1}\frac{p+n+p}{2p+n+p}\prod_{n=0}^{p-1}\frac{p+n}{2p+n} \tag{A.11}$$

The shape parameters obtained in Equation (A.2) are also confirmed by random number samples. It can be shown that after generating random numbers for the

y_1 variable according to $f(y_1)$ marginal distribution within the range of [0, y_{1+2+3}], and generating random samples for the x_1 variable according to $f(x_1|y_1)$ conditional distribution within the range of [0, y_1], the x_1 samples follow a beta distribution that is identical to the $f(x_1)$ marginal distribution within the range of [0, y_{1+2+3}].

The above process can be used to determine the shape parameters for the other probability density functions from Table 4.5, as follows

$$\begin{aligned} f\big(x_2|(y_{1+2}-y_1)\big) &= \frac{(x_2-0)^{p-1}\big((y_{1+2}-y_1)-x_2\big)^{p-1}}{B(p,p)(y_{1+2}-y_1)^{2p-1}} \\ &= f\big((y_{1+2}-y_1)|x_2\big)f(x_2)\frac{1}{f(y_{1+2}-y_1)} \\ &= \frac{\big((y_{1+2}-y_1)-x_2\big)^{p-1}\big(y_{1+2+3}-(y_{1+2}-y_1)\big)^{4p-1}}{B(p,4p)(y_{1+2+3}-x_2)^{5p-1}} \\ &\times \frac{(x_2-0)^{p-1}(y_{1+2+3}-x_2)^{5p-1}}{B(p,5p)(y_{1+2+3}-0)^{6p-1}} \\ &\times \frac{B(2p,4p)(y_{1+2+3}-0)^{6p-1}}{\big((y_{1+2}-y_1)-0\big)^{2p-1}\big(y_{1+2+3}-(y_{1+2}-y_1)\big)^{4p-1}} \end{aligned} \tag{A.12}$$

$$\begin{aligned} f(y_1|y_{1+2}) &= \frac{(y_1-0)^{2p-1}(y_{1+2}-y_1)^{2p-1}}{B(2p,2p)(y_{1+2}-0)^{4p-1}} = f(y_{1+2}|y_1)f(y_1)\frac{1}{f(y_{1+2})} \\ &= \frac{(y_{1+2}-y_1)^{2p-1}(y_{1+2+3}-y_{1+2})^{2p-1}}{B(2p,2p)(y_{1+2+3}-y_1)^{4p-1}} \\ &\times \frac{(y_1-0)^{2p-1}(y_{1+2+3}-y_1)^{4p-1}}{B(2p,4p)(y_{1+2+3}-0)^{6p-1}} \\ &\times \frac{B(4p,2p)(y_{1+2+3}-0)^{6p-1}}{(y_{1+2}-0)^{4p-1}\big(y_{1+2+3}-y_{1+2}\big)^{2p-1}} \end{aligned} \tag{A.13}$$

$$
\begin{aligned}
f\big(x_3|(y_{1+2+3}-y_{1+2})\big) &= \frac{(x_3-0)^{p-1}(y_{1+2+3}-y_{1+2}-x_3)^{p-1}}{B(p,p)(y_{1+2+3}-y_{1+2}-0)^{2p-1}} \\
&= f\big((y_{1+2+3}-y_{1+2})|x_3\big)f(x_3)\frac{1}{f(y_{1+2+3}-y_{1+2})} \\
&= \frac{(y_{1+2+3}-y_{1+2}-x_3)^{p-1}\big(y_{1+2+3}-(y_{1+2+3}-y_{1+2})\big)^{4p-1}}{B(p,4p)(y_{1+2+3}-x_3)^{5p-1}} \\
&\times \frac{(x_3-0)^{p-1}(y_{1+2+3}-x_3)^{5p-1}}{B(p,5p)(y_{1+2+3}-0)^{6p-1}} \\
&\times \frac{B(2p,4p)(y_{1+2+3}-0)^{6p-1}}{(y_{1+2+3}-y_{1+2}-0)^{2p-1}\big(y_{1+2+3}-(y_{1+2+3}-y_{1+2})\big)^{4p-1}}
\end{aligned}
\tag{A.14}
$$

$$
f(y_{1+2}) = \frac{(y_{1+2}-0)^{4p-1}(y_{1+2+3}-y_{1+2})^{2p-1}}{B(4p,2p)(y_{1+2+3}-0)^{6p-1}} \tag{A.15}
$$

The marginal probability of the distance between any two clutch plates in the pack, $f(g)$, can be determined according to the realtionship below, which was very useful during the derivation of Equations (A.2) and (A.12) - (A.15)

$$
f(g) = \frac{g^{j-i-1}(y_{1+2+3}-g)^{6p-1-j+i}}{B(j-i,6p-j+i)y_{1+2+3}^{6p-1}} \tag{A.16}
$$

Here $g = X_{(j)} - X_{(i)}$, where $j > i$, $i = 0 \ldots 5p$, $j = 1p \ldots 6p$, and $X_{(k)}$ is the k^{th} order statistic of the random varibale X_k that is uniformly distributed within interval [0, y_{1+2+3}], $k = 1 \ldots 6p-1$. Equation (A.16) is utilized when formulating the marginal probability density function for $f(x_2)$, $f(x_3)$, $f(y_{1+2}-y_1)$ and $f(y_{1+2+3}-y_{1+2})$.

BIBLIOGRAPHY

BIBLIOGRAPHY

Aphale, C. R. (2007), Drag reduction at low and high reynolds numbers., Ph.D. thesis, University of Michigan.

Aphale, C. R., J. Cho, W. W. Schultz, S. L. Ceccio, T. Yoshioka, and H. Hiraki (2006), Modeling and parametric study of torque in open clutch plates, *Journal of tribology*, *128*(2), 422–430.

Aphale, C. R., W. W. Schultz, and S. L. Ceccio (2010), The influence of grooves on the fully wetted and aerated flow between open clutch plates, *Journal of Tribology*, *132*(1), 011,104.

Batchelor, G. K. (1951), Note on a class of solutions of the navier-stokes equations representing steady rotationally-symmetric flow, *The quarterly journal of mechanics and applied mathematics*, *4*(1), 29–41.

Behzadi, A., R. Issa, and H. Rusche (2004), Modelling of dispersed bubble and droplet flow at high phase fractions, *Chemical Engineering Science*, *59*(4), 759–770.

Bejan, A. (1984), Convection heat transfer. john wiley & sons, new york., *Convection heat transfer. John Wiley & Sons, New York.*

Berger, E., F. Sadeghi, and C. Krousgrill (1996), Finite element modeling of engagement of rough and grooved wet clutches, *Journal of Tribology*, *118*(1), 137–146.

Berger, E., F. Sadeghi, and C. Krousgrill (1997), Analytical and numerical modeling of engagement of rough, permeable, grooved wet clutches, *Journal of Tribology*, *119*(1), 143–148.

Cho, J. (2012), A multi-physics model for wet clutch dynamics, Ph.D. thesis, University of Michigan.

Cho, J., N. Katopodes, N. Kapas, and Y. Fujii (2011), CFD modeling of squeeze film flow in wet clutch, *Tech. rep.*, SAE Technical Paper.

Cochran, W. (1934), The flow due to a rotating disc, in *Mathematical Proceedings of the Cambridge Philosophical Society*, vol. 30, pp. 365–375, Cambridge University Press.

Davis, C. L., F. Sadeghi, and C. M. Krousgrill (2000), A simplified approach to modeling thermal effects in wet clutch engagement: analytical and experimental comparison, *Journal of tribology*, *122*(1), 110–118.

Fish, R. L. (1991), Using the SAE #2 machine to evaluate wet clutch drag losses, *Tech. rep.*, SAE Technical Paper.

Fluent, A. (2009), 12.0 theory guide, *Ansys Inc*, *5*.

Froslie, L. E., T. Milek, and R. Smith (1960), Automatic transmission friction elements, *Tech. rep.*, SAE Technical Paper.

Fujii, Y., W. Tobler, and T. Snyder (2001a), Prediction of wet band brake dynamic engagement behaviour part 1: mathematical model development, *Proceedings of the Institution of Mechanical Engineers, Part D: Journal of Automobile Engineering*, *215*(4), 479–492.

Fujii, Y., W. Tobler, and T. Snyder (2001b), Prediction of wet band brake dynamic engagement behaviour part 2: Experimental model validation, *Proceedings of the Institution of Mechanical Engineers, Part D: Journal of Automobile Engineering*, *215*(5), 603–611.

Fujii, Y., N. Kapas, and J.-W. Tseng (2014), Clutch wet, *Encyclopedia of Automotive Engineering*.

Gao, H., G. Barber, and H. Chu (2002a), Friction characteristics of a paper-based friction material, *International Journal of Automotive Technology*, *3*(4), 171–176.

Gao, H., G. Barber, and M. Shillor (2002b), Numerical simulation of engagement of a wet clutch with skewed surface roughness, *Journal of Tribology*, *124*(2), 305–312.

Gorin, A., and M. Shilyaev (1976), Laminar flow between rotating disks, *Fluid Dynamics*, *11*(2), 219–224.

Greenwood, J., and J. P. Williamson (1966), Contact of nominally flat surfaces, in *Proc. R. Soc. Lond. A*, vol. 295, pp. 300–319, The Royal Society.

Hamrock, B. J., S. R. Schmid, and B. O. Jacobson (2004), *Fundamentals of fluid film lubrication*, CRC press.

Hashimoto, H., S. Wada, and Y. Murayama (1984), The performance of a turbulent-lubricated sliding bearing subject to centrifugal effect, *Trans. Jpn. Soc. Mech. Eng., Ser. C*, *49*(446), 1753–1761.

Hays, D. F. (1963), Squeeze films for rectangular plates, *Journal of Basic Engineering*, *85*(2), 243–246.

Hori, Y. (2006), *Hydrodynamic lubrication*, Springer Science & Business Media.

Hou, S., J. Hu, and Z. Peng (2017), Experimental investigation on unstable vibration characteristics of plates and drag torque in open multiplate wet clutch at high circumferential speed, *Journal of Fluids Engineering*, *139*(11), 111,103.

Hu, J., Z. Peng, and S. Yuan (2009), Drag torque prediction model for the wet clutches, *Chinese Journal of Mechanical Engineering*, *22*(2), 238.

Hu, J., Z. Peng, and C. Wei (2012), Experimental research on drag torque for single-plate wet clutch, *Journal of Tribology*, *134*(1), 014,502.

Hu, J., S. Hou, and C. Wei (2018), Drag torque modeling at high circumferential speed in open wet clutches considering plate wobble and mechanical contact, *Tribology International*.

Iqbal, S., F. Al-Bender, B. Pluymers, and W. Desmet (2013a), Experimental characterization of drag torque in open multi-disks wet clutches, *SAE International Journal of Fuels and Lubricants*, *6*(2013-01-9073), 894–906.

Iqbal, S., F. Al-Bender, B. Pluymers, and W. Desmet (2013b), Mathematical model and experimental evaluation of drag torque in disengaged wet clutches, *ISRN Tribology*, *2013*.

Iqbal, S., F. Al-Bender, B. Pluymers, and W. Desmet (2014), Model for predicting drag torque in open multi-disks wet clutches, *Journal of Fluids Engineering*, *136*(2), 021,103.

Iqbal, S., F. Al-Bender, A. P. Ompusunggu, B. Pluymers, and W. Desmet (2015), Modeling and analysis of wet friction clutch engagement dynamics, *Mechanical Systems and Signal Processing*, *60*, 420–436.

Jang, J., and M. Khonsari (1999), Thermal characteristics of a wet clutch, *Journal of tribology*, *121*(3), 610–617.

Jang, J., M. Khonsari, and R. Maki (2011), Three-dimensional thermohydrodynamic analysis of a wet clutch with consideration of grooved friction surfaces, *Journal of Tribology*, *133*(1), 011,703.

Jen, T.-C., and D. J. Nemecek (2008), Thermal analysis of a wet-disk clutch subjected to a constant energy engagement, *International Journal of Heat and Mass Transfer*, *51*(7-8), 1757–1769.

Kato, Y. (1993), Fuel economy improvement through tribological analysis of the wet clutches and brakes of an automatic transmission, *Proceedings of JSAE, 1993*.

Kim, S., and S. Shim (2017), Modeling of heat transfer for a wet multi-plate clutch based on empirical data, *Proceedings of the Institution of Mechanical Engineers, Part D: Journal of Automobile Engineering*, p. 0954407017733184.

Kitabayashi, H., C. Y. Li, and H. Hiraki (2003), Analysis of the various factors affecting drag torque in multiple-plate wet clutches, *Tech. rep.*, SAE Technical Paper.

Levy, H., K. Loewy, and E. Lenz (1970), Temperature distribution on disk clutches in machine tools, *Annals of the CIRP*, *67*, 239–250.

Li, H., Q. Jing, and B. Ma (2013), Modeling and parametric study on drag torque of wet clutch, in *Proceedings of the FISITA 2012 world automotive congress*, pp. 21–30, Springer.

Lloyd, F. A. (1974), Parameters contributing to power loss in disengaged wet clutches, *Tech. rep.*, SAE Technical Paper.

Madhavan, J., G. Pandit, M. Barnholt, and R. Suppiger (2012), Application of simulation based methods in development of wet clutch system, *Tech. rep.*, SAE Technical Paper.

Mansouri, M., M. Holgerson, M. Khonsari, and W. Aung (2001), Thermal and dynamic characterization of wet clutch engagement with provision for drive torque, *Journal of tribology*, *123*(2), 313–323.

Matsch, L., and W. Rice (1968), An asymptotic solution for laminar flow of an incompressible fluid between rotating disks, *Journal of Applied Mechanics*, *35*(1), 155–159.

Mellor, G., P. Chapple, and V. Stokes (1968), On the flow between a rotating and a stationary disk, *Journal of Fluid Mechanics*, *31*(1), 95–112.

Miao, L., X. Li, X. Cheng, and R. Chen (2017), The simulation analysis of fluid internal characteristics of wet clutch during the engaging process, in *Mechatronics and Automation (ICMA), 2017 IEEE International Conference on*, pp. 2045–2050, IEEE.

Miyagawa, M., M. Ogawa, Y. Okano, H. Hara, S. Sasaki, and K. Okui (2009), Numerical simulation of temperature and torque curve of multidisk wet clutch with radial and circumferential grooves, *Tribology Online*, *4*(1), 17–21.

Moore, D. (1965), A review of squeeze films, *Wear*, *8*(4), 245–263.

Natsumeda, S., and T. Miyoshi (1994), Numerical simulation of engagement of paper based wet clutch facing, *Journal of tribology*, *116*(2), 232–237.

Norman, L., S. Kotz, and N. Balakrishnan (1994), *Continuous Univariate Distributions*, Wiley.

Ompusunggu, A. P., T. Janssens, F. Al-Bender, P. Sas, and H. Van Brussel (2011), Engagement behavior of degrading wet friction clutches, in *Advanced Intelligent Mechatronics (AIM), 2011 IEEE/ASME International Conference on*, pp. 271–276, IEEE.

Pahlovy, S. A., S. F. Mahmud, M. Kubota, M. Ogawa, and N. Takakura (2016), New development of a gas cavitation model for evaluation of drag torque characteristics in disengaged wet clutches, *SAE International Journal of Engines*, *9*(2016-01-1137), 1910–1915.

Patir, N., and H. Cheng (1978), An average flow model for determining effects of three-dimensional roughness on partial hydrodynamic lubrication, *Journal of lubrication Technology*, *100*(1), 12–17.

Patir, N., and H. Cheng (1979), Application of average flow model to lubrication between rough sliding surfaces, *Journal of Lubrication Technology*, *101*(2), 220–229.

Poncet, S., R. Schiestel, and M.-P. Chauve (2005), Centrifugal flow in a rotor-stator cavity, *Journal of Fluids Engineering*, *127*(4), 787–794.

Razzzaque, M. M., and T. Kato (1999), Effects of a groove on the behavior of a squeeze film between a grooved and a plain rotating annular disk, *Journal of tribology*, *121*(4), 808–815.

Ross, S. M. (2014), *Introduction to probability models*, Academic press.

Sanni, S. (1997), Unsteady squeeze film between rectangular plates, *Wear*, *213*(1-2), 98–102.

Savage, S. (1964), Laminar radial flow between parallel plates, *Journal of Applied Mechanics*, *31*(4), 594–596.

Schade, C. (1971), Effects of transmission fluid on clutch performance, *Tech. rep.*, SAE Technical Paper.

Serre, E., E. Tuliszka-Sznitko, and P. Bontoux (2004), Coupled numerical and theoretical study of the flow transition between a rotating and a stationary disk, *Physics of Fluids*, *16*(3), 688–706.

Stewartson, K. (1953), On the flow between two rotating coaxial disks, in *Mathematical Proceedings of the Cambridge Philosophical Society*, vol. 49, pp. 333–341, Cambridge University Press.

Szeri, A., S. Schneider, F. Labbe, and H. Kaufman (1983), Flow between rotating disks. part 1. basic flow, *Journal of Fluid Mechanics*, *134*, 103–131.

Takagi, Y., Y. Okano, M. Miyagawa, and N. Katayama (2011a), Combined numerical and experimental study on drag torque in a wet clutch, in *ASME-JSME-KSME 2011 Joint Fluids Engineering Conference*, pp. 2425–2430, American Society of Mechanical Engineers.

Takagi, Y., et al. (2011b), Effect of two-phase flow on drag torque in a wet clutch, *Journal of Advanced Research in Physics*, *2*(2).

Ting, L. (1975), Engagement behavior of lubricated porous annular disks. part i: squeeze film phasesurface roughness and elastic deformation effects, *Wear*, *34*(2), 159–172.

Wang, P., N. Katopodes, and Y. Fujii (2017a), Statistical modeling of plate clearance distribution for wet clutch drag analysis, *SAE International Journal of Passenger Cars-Mechanical Systems*, *11*(2017-01-2446).

Wang, P., N. Katopodes, and Y. Fujii (2017b), Two-phase MRF model for wet clutch drag simulation, *SAE International Journal of Engines*, *10*(2017-01-1127).

Winchell, F., and W. Route (1961), Ratio changing the passenger car automatic transmission, *Tech. rep.*, SAE Technical Paper.

Wu, H. (1970), Squeeze-film behavior for porous annular disks, *Journal of Lubrication Technology*, *92*(4), 593–596.

Wu, H. (1971), The squeeze film between rotating porous annular disks, *Wear*, *18*(6), 461–470.

Wu, W., Z. Xiong, J. Hu, and S. Yuan (2015), Application of CFD to model oil–air flow in a grooved two-disc system, *International Journal of Heat and Mass Transfer*, *91*, 293–301.

Xiang, X., and J. M. Kremer (2001), A simplified close form approach, for slipping clutch thermal model, *Tech. rep.*, SAE Technical Paper.

Yang, Y., R. C. Lam, Y. F. Chen, and H. Yabe (1995), Modeling of heat transfer and fluid hydrodynamics for a multidisc wet clutch, *Tech. rep.*, SAE Technical Paper.

Yuan, S., K. Guo, J. Hu, and Z. Peng (2010), Study on aeration for disengaged wet clutches using a two-phase flow model, *Journal of Fluids Engineering*, *132*(11), 111,304.

Yuan, S., Z. Peng, and C. Jing (2011), Experimental research and mathematical model of drag torque in single-plate wet clutch, *Chinese Journal of Mechanical Engineering-English Edition*, *24*(1), 91.

Yuan, Y., P. Attibele, and Y. Dong (2003), CFD simulation of the flows within disengaged wet clutches of an automatic transmission, *Tech. rep.*, SAE Technical Paper.

Yuan, Y., E. A. Liu, J. Hill, and Q. Zou (2007), An improved hydrodynamic model for open wet transmission clutches, *Journal of Fluids Engineering*, *129*(3), 333–337.

Zagrodzki, P. (1985), Numerical analysis of temperature fields and thermal stresses in the friction discs of a multidisc wet clutch, *Wear*, *101*(3), 255–271.

Zagrodzki, P. (1990), Analysis of thermomechanical phenomena in multidisc clutches and brakes, *Wear*, *140*(2), 291–308.